UNIVERSITY OF OXFORD

ST JOHN'S COLLEGE

DOCTORAL THESIS

Inkjet Printing of Liquid Crystals and Polymer Composites for Novel Thin-Film Optical Elements

---

Author:

Ellis PARRY

Supervisors:

Dr. Stephen MORRIS

Dr. Alfonso CASTREJÓN-PITA

Soft Matter Photonics Group

and

Fluid Dynamics Group

Department of Engineering Science

Hilary Term, 2020

Abstract

Inkjet Printing of Liquid Crystals and Polymer Composites for Novel Thin-Film Optical Elements

by Ellis PARRY

This thesis investigates the drop-on-demand inkjet printing of liquid crystal (LC)inks, from drop formation and deposition, through to substrate selection. Inkjet printing is a particularly attractive fabrication method as it is a precise, scalable and highly cost-effective additive manufacturing process. These benefits, along with the ability to deposit pico-liter volumes of particulate suspensions, viscous and complex fluids, have led to inkjet printing being considered as an attractive alternative fabrication technique in a range of established fields such as the display, pharmaceutical and bioengineering industries. However, the unique considerations of using liquid crystalline inks, such as their anisotropic properties and alignment criteria is barely touched in the literature. This thesis describes the design and build of an inkjet printing system capable of depositing a range of different functional inks such as LCs and polymer solutions. Drop generation of a nematic LC in a piezoelectric printhead and the role of different printing substrates on the final droplet configuration is considered in detail. This knowledge is used to fabricate novel, variable-focus microlens arrays that can be deposited as pre-programmable arrays on to a variety of different substrates. The unique properties of inkjet printing are then leveraged to describe two new methods of producing patterned, single layer polymer dispersed LC films. A prototype switchable, patterned polymer-dispersed LC film, produced by inkjet printing, is demonstrated. This work shows the feasibility of inkjet printing LC and polymer formulations and has important technological implications in the manufacturing of small and large area, polymer dispersed LC films for a variety of applications.

Acknowledgements

First of all, I would like to extend my gratitude and appreciation to my supervisors. Thank you Steve M. for inviting me to join the group, what an adventure it has been! Thank you for being a good man and a caring supervisor. Thank you Alfonso for your guidance, friendship and brightening some of the darker times in the basement lab. To Steve E, thank you for your wisdom, the story and how to present. I appreciate you all for showing me tolerance and patience toward my often unconventional working style...

To the stalwarts of SMP and the people who have made my PhD a time to cherish. Dave, I have found the constant evolution of your desk a fascination to behold. Thanks for the laughs, the zaphooning, an appreciation of ergonomics, the memories. To John, I'm so glad you decided to change groups! Thank you for our eclectic discussions, your friendship, our unforgettable time in California. To Chloe, my construction partner, my partner in crime and my partner in life, thanks for the support, encouragement and constant faith in me when I have none.

To Jia-de, Waqas, Julien and Taimoor, and Lake, thank you all for your company and companionship over the years. I wish you all the very best in your PhDs and life beyond.

To all my friends at college, Pusey Street, the chef, Battlefields and green tea. The Saints, neumind, Woodstock and 111. To Ian and Tara, the comradeship, phall and epic times. Thank you all for making my time at Oxford so enjoyable and memorable.

Finally, I wish to extend my love and gratitude to my dearest support team back home. My mum, who, despite having literally no idea what I do, has given me endless encouragement and unfaltering confidence. My dad, who brings me back to earth with a cheeky nandos and cinema. Claire, for her wisdom humor and company. To Luke, my inspiration to be the best I can be and to see the positive in life, always.

"When one tugs at a single thing in nature, he finds it attached to the rest of the world."

John Muir

Publications

1. E. Parry et al. “Drop-on-Demand Inkjet Printing of Thermally Tunable Liquid Crystal Microlenses”. In: *Advanced Engineering Materials* 20.3 (2018). ISSN: 14381656. DOI: 10.1002/adem.201700774

2. E. Parry et al. “Formation of Radial Aligned and Uniform Nematic Liquid Crystal Droplets via Drop-on-Demand Inkjet Printing into a Partially-Wet Polymer Layer”. In: *Optical Materials* 80 (2018), pp. 71–76. ISSN: 09253467. DOI: 10.1016/j.optmat.2018.04.038

3. E. Parry et al. "Inkjet Printing of Patterned Polymer Dispersed Liquid Crystal Films", *in preparation*

Presentations

National

1. "Inkjet Printing of Optically Active Fluids", 22nd Merck CASE Conference, Hampshire, April 2016 (Oral - awarded best first year presentation)
   “Drop-on-Demand Printing of Optically Active Fluids”, Photon16 Conference, Leeds, 2016 (Poster)
   "Inkjet Printing of Liquid Crystals for Photonic Applications", 23rd Merck CASE Conference, Hampshire, April 2016 (Oral - awarded best second year presentation)

2. “Drop-on-Demand Ink-jet Printing of Liquid Crystal Microlens Arrays”, Oxford Photonics Day, Oxford, October 2017 (Poster - awarded first prize)

3. "Inkjet Printing of Liquid Crystals for Photonic Applications", 24th Merck CASE Conference, Hampshire, April 2016 (Oral - awarded best third year presentation)

4. “Inkjet Printing of Liquid Crystals in the Formation of Optical Temperature Sensors” , Oxford Photonics Day, Oxford, April 2018 (Poster, awarded second prize)

International

1. "Drop-on-Demand Ink-jet Printing of Liquid Crystals and the Fabrication of Tuneable Microlens Arrays", ECLC, Moscow, Russia, 2017 (Oral)

2. "Drop-on-Demand Ink-jet Printing of Tunable Liquid Crystal Microlens Arrays", OLC conference, Sao Paulo, Brazil, 2017 (Oral)

3. "Drop-on-Demand Printing of Liquid Crystal Composites for Photonics Applications", SPIE Photonics West, San Francisco, USA, 2018 (Oral)

4. "Inkjet Printable Liquid Crystals for Tunable Micro-Optical Elements", ILCC, Kyoto, Japan, 2018 (Oral)

Patents

1. E.Parry, A. A. Castrejón-Pita, S. J. Elston, S. M. Morris, "Polymer Dispersed Liquid Crystals", GB patent application 1819634.5, filed 30.11.2018

Contents

List of Figures

List of Tables

List of Abbreviations

AC	**A**lternating **C**urrent
ADC	**A**nalog-to-**D**igital **C**onverter
AMOLED	**A**ctive-**M**atrix **O**rganic **L**ight **E**mitting **D**iode
CCD	**C**harge **C**oupled **D**evice
CIJ	**C**ontinuous **I**nk**J**et
DAQ	**D**ata **A**c**Q**uisition
DC	**D**irect **C**urrent
DMSO	**D**i**M**ethyl **S**ulf**O**xide
DoD	**D**rop-**O**n-**D**emand
IJP	**I**nk**J**et **P**rinting
LC	**L**iquid **C**rystal
LCD	**L**iquid **C**rystal **D**isplay
LED	**L**ight **E**mitting **D**iode
OLED	**O**rganic **L**ight **E**mitting **D**iode
PBG	**P**hotonic **B**and **G**ap
PDLC	**P**olymer **D**ispersed **L**iquid **C**rystal
PEDOT	**P**oly(3,4-**E**thylene**D**i**O**xy**T**hiophene)
PEI	**P**oly**E**thylen**I**mine
PID	**P**roportional, **I**ntegral, **D**erivative
POM	**P**olarised (it) **O**ptical **M**icroscopy
PSS	**P**oly**S**tyrene **S**ulfonate
PTFE	**P**oly**T**etra**F**luoro**E**thylene
PVA	**P**oly(**V**inyl **A**lcohol)
PWM	**P**ulse **W**idth **M**odulation
TTL	**T**ransistor-**T**ransistor **L**ogic
UV	**U**ltra **V**iolet
QD	**Q**uantum **D**ot

List of Symbols

$\boldsymbol{D}$	Displacement field	C/m^2
De		
$\boldsymbol{E}$	Electric field strength	V/m
Er	Ericksen number	Dimensionless
f_d	Free energy density of elastic deformation	J/m^3
f_e	Free energy density of the electric field	J/m^3
f_s	Surface free energy density	J/m^3
F_d	Free energy of elastic deformation	J
F_e	Free energy of the electric field	J
F_s	Surface free energy	J
K	Single elastic constant approximation	N
$K_{11/22/33}$	Splay/Twist/Bend Frank elastic constants	N
L	Characteristic length scale	m
$\hat{\boldsymbol{n}}$	LC director	unit vector
n	Refractive index	Dimensionless
n_{avg}	Average refractive index	Dimensionless
n_e	Refractive index	Dimensionless
n_o	Refractive index	Dimensionless
Δn	Birefringence	Dimensionless
Oh	Ohnsorge number	Dimensionless
R	Radius	m
Re	Reynold number	Dimensionless
S	Scalar Order Parameter	Dimensionless
S_{eq}	Equilibrium spreading coefficient	Dimensionless
T_{iso}	Isotropic temperature	°C
W	Anchoring strength	J/m^2
W_θ	Polar anchoring strength	J/m^2
W_ϕ	Azimuthal anchoring strength	J/m^2
We	Weber number	Dimensionless
$\hat{\varepsilon}$	Dielectric tensor	F/m
ε_0	Permittivity of free space	F/m
ε_r	Relative permittivity	Dimensionless
$\varepsilon_\parallel$	Parallel dielectric permittivity	F/m
$\varepsilon_\perp$	Perpendicular dielectric permittivity	F/m
$\Delta\varepsilon$	Dielectric anisotropy	F/m
γ	Interfacial tension	N/m
γ_1	Rotational viscosity	Pa.s
λ	Wavelength	m
η	Dynamic viscosity	Pa.s
ρ	Density	kg/m^3
σ	Surface tension	N/m
τ_{rise}	Rise time	s

τ_{decay}	Decay time	s

Chapter 1

Introduction

Modern manufacturing processes are continually driven by increased automation, miniaturisation, reduced production times and reduced cost. This has led to numerous alternative manufacturing methods being considered across industries. Out of them, inkjet printing has emerged as a promising fabrication technique due to its precision, high-throughput and rapid prototyping abilities. In the last two decades, development of ever more functional inks and substrates has led to inkjet technology finding applications far outside of its traditional industries of graphics and textiles. This thesis investigates the inkjet printing of liquid crystals and polymer composites, from drop formation and substrate interactions, through to thin-film optical device fabrication.

This introductory chapter provides a background to the field of inkjet printing, with a focus on its use of functional materials as inks. An outline of the motivations for this investigation is provided, along with the structure and content of the remaining chapters in the thesis.

1.1 Inkjet Printing

Throughout history, printing has served as a means to automate the generation of potentially complex and large scale patterns. Early printing methods, today referred to as 'contact printers', required casts of pages or lines to be laboriously made specific to the document to be printed. The first example of automating direct deposition of ink dates back to 1867 when Lord Kelvin patented the syphon

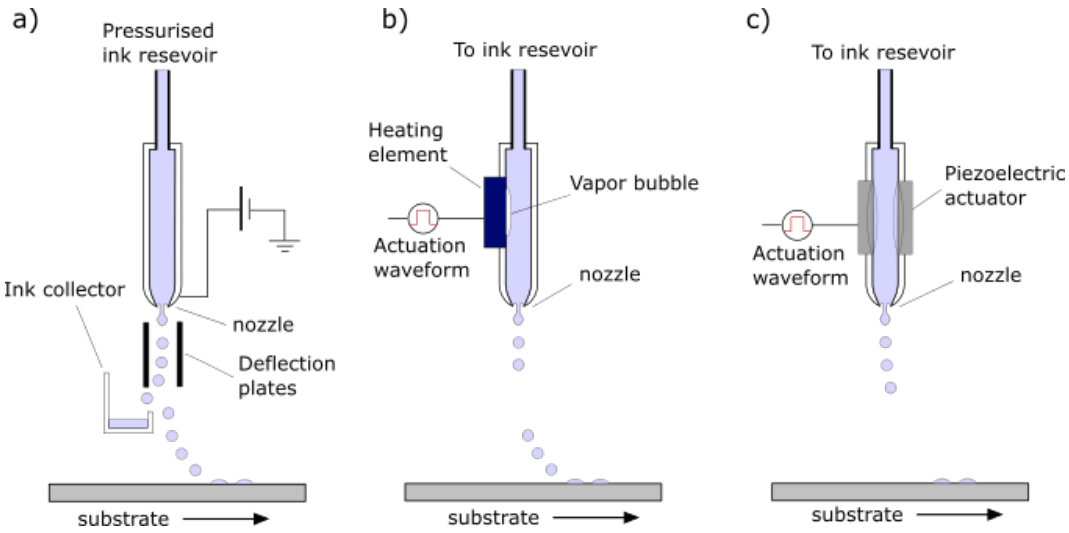

FIGURE 1.1: a) Continuous Inkjet (CIJ) printer where the placement of droplets is controlled using charged deflection plates. b) Drop-on-Demand (DoD) inkjet printer using thermal expansion to generate droplets. c) DoD inkjet printer using deformation of a piezoelectric actuator to generate droplets.

recorder [3]. The machine was used to record telegraph messages as a continuous trace on paper. A syphon pump was used to generate a jet of fluid from a moveable nozzle that could be deflected by an electric field.

In 1948, Rune Elmqvist of Siemens patented what is today regarded as the first practical inkjet printer. The 'mingograph', which was used to record cardiograms, was based on the spontaneous break-up of a jet of fluid into individual droplets. This phenomena was theoretically described by Rayleigh and is referred to now as the Plateau-Rayleigh instability [4]. However, it was Richard Sweet from Stanford University whose inventions would eventually lead to the first wide-spread use of successful inkjet printers. He demonstrated that an acoustic wave could be applied to the nozzle orifice to generate a continuous stream of individual droplets [5]. The resulting patent was acquired by the A. B. Dick Company, who in 1968 produced the first ever commercial inkjet printer called the Videojet 9600.

Continuous inkjet printing (CIJ) refers to inkjet systems that are based on the spontaneous break-up of a continuous jet of fluid into a stream of droplets. Steering the stream of droplets in-flight determines the positioning and deposition of the individual droplets onto a substrate. This is done by applying a voltage to the nozzle such that the generated droplets leave the nozzle partially charged and

are then steered using charged deflector plates. A collector is positioned so that suitably deflected droplets will not strike the substrate (in some instances, the ink can also be recycled). This process, illustrated by Figure 1.1a, is almost identical to that invented by Richard Sweet back in 1965. Droplet diameters typically range from 50-150 μm with drop generation frequencies between 20-60 kHz. CIJ systems are potentially wasteful due to the continuous deposition of ink and their use is generally limited to commercial, large-scale coding and marking applications.

The other category of inkjet technology is known as drop-on-demand (DoD). In DoD systems, a selected number of drops are generated as required using a pressure wave induced in the printhead. The pressure wave can be generated using a number of techniques with each offering distinct benefits. The first commercial DoD printer was developed by Canon in 1979. Figure 1.1b illustrates the operating principle of a thermal DoD inkjet printer. The technology utilises a heating element to rapidly vaporise a small amount of ink. The expansion and subsequent collapse of the vapour pocket causes a pressure wave that ejects a droplet from the nozzle. Thermal DoD inkjet systems are reliable, easily miniaturised and are still used in many desktop printers today. However, the requirement to vaporise the ink along with the thermal cycling involved severely limits the range of compatible inks, making the method particularly unsuitable for printing functional materials.

Piezoelectric DoD printing utilises the mechanical deformation of a piezoelectric element in response to an electric field. The resulting pressure wave is used to generate droplets, as shown in Figure 1.1c. Similar to thermal DoD printing, droplet generation frequencies typically range from 1-20 kHz, with droplet diameters in the order of 10-150 μm. There is a high degree of control over the driving waveform and thus the resulting pressure wave, which enables high control of droplet volumes and velocities. Moreover, inks are limited only by the ability to generate droplets, making the method highly suitable for the deposition of many functional fluids and particulate suspensions.

A third method of DoD printing worth noting is electrostatic or electrohydrodynamic inkjet printing. Droplet generation is driven by an electric field between

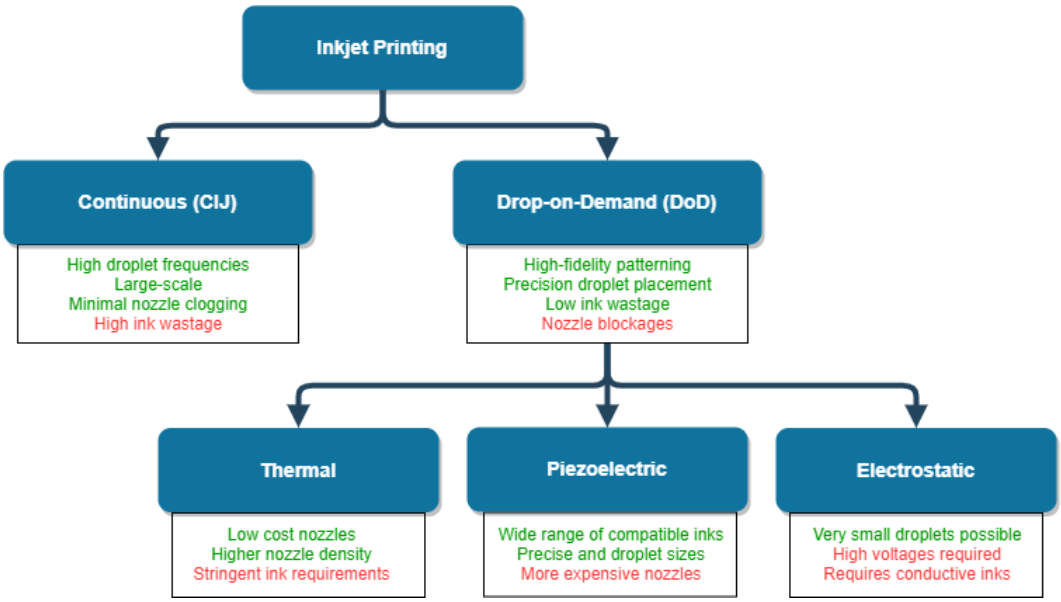

FIGURE 1.2: Comparison of the major inkjet printing technologies.

the nozzle and the printing substrate. The electric field causes mobile ions in a polarisable liquid to migrate to the liquid surface. The electrostatic repulsion of the ions causes the fluid ligament to narrow. A critical field strength leads to the generation of a droplet that is projected towards the grounded substrate. At high field strengths, the technique can generate droplets as small as 240 nm [6]. However, this method is requires the inks to be conductive.

1.2 Inkjet Printing of Functional Materials

The most common uses of DoD inkjet systems are still in the fields of graphic printing and textiles. However, the increased availability of functional materials in the form of inks, alongside the constant demand for ever more affordable fabrication techniques has led to inkjet printing becoming a versatile tool across a number of industries [7]. Figure 1.2 compares different inkjet printing technologies. Out of them, piezoelectric DoD has emerged as the most suitable method for printing functional materials. The unparalleled efficiency of the technique and the ability to accurately position pico-litre volumes of a wide-range of fluids has seen applications in the manufacturing of displays, printed electronics, tissue engineering, pharmaceuticals, bioengineering and 3D-printed components [8, 9,

10, 11, 12].

Inkjet printing has become a major enabler in the cost-effective production of micro-optical elements and thin-film optoelectronic devices [13, 14]. IDTechEx Research has predicted the printed, flexible and organic electronics market will grow from $31.7 billion in 2018, to $77.3 billion in 2029 [218]. The majority of this market involves the fabrication of low-cost flexible OLEDs (Organic Light Emitting Diode), an area which inkjet printing has been heavily invested in. Other major contributions include the fabrication of printed and flexible sensors, and optoelectronic devices such as organic solar cells, transparent electrodes and color filters for liquid crystal displays (LCD) [15, 16, 17].

The piezoelectric inkjet printing of light-emitting polymer layers has enabled the cost-effective manufacturing of large-area OLED displays [18, 18]. LEDs with emitting layers based on quantum dot (QD) formulations have also been demonstrated [19, 20]. In addition to material deposition, inkjet technology also has the potential to enhance device architectures. For instance, DuPont Displays have developed active matrix OLED (AMOLED) displays that no longer require polymer walls to separate pixels. This is done by depositing a continuous jet of fluid across a patterned wetting and non-wetting substrate, resulting in continuous lines of emitting material in place of pixels [21].

The deposition of conductive polymers such as poly(3,4-ethylenedioxythiophene) polystyrene sulfonate (PEDOT:PSS) has been successfully achieved using inkjet printing [22, 23]. Such films are usually produced using methods such as vacuum evaporation that involve multiple steps and masks. Inkjet printing allows for reduced fabrication costs and higher yields. PEDOT and other similar coumpounds are used in a wide range of optoelectronic devices including OLEDs, LEDs, solar cells and electronic paper, for both protection and as transparent conducting films [24, 25].

1.2.1 Liquid Crystals

A class of functional fluid that has only recently been considered as a candidate for inkjet printing are liquid crystals (LCs). LC molecules possess unique electro-optic properties and exhibit different LC phases. The most common phase

used in current technology being the so-called 'nematic' phase (see Chapter 2 for background and theory of LCs). Due to the huge success of nematic LCs as functional components in flat-panel displays, LC research has been historically focussed on display applications.

To date, the use of LCs as functional inkjet printing inks has not been widely explored. The inkjet printing of LCs to produce mono-disperse LC droplets has been demonstrated [26]. Formulations of LCs were deposited using inkjet printing to form optical humidity sensors [27, 28] and miniature lasing cavities [29]. The inkjet printing of polymer and elastomer LCs has been used to fabricate responsive actuators [30, 31]. More recently, the use of LCs doped with nanoparticles as inks was explored for anti-counterfeiting purposes [32]. The most established application of inkjet printing LCs is the single-drop filling method, used to deposit the LC in the manufacturing of LCDs [33]. Although the inkjet printing of a LC is fundamental to the aforementioned studies, there is little reference to the procedure, challenges and opportunities of inkjet printing LCs in the literature.

This thesis represents the first body of work to explore in detail the inkjet printing of LCs, from drop-formation to possible device fabrication. The goals of this investigation are enumerated as follows:

1. Design a bespoke DoD inkjet printing system for LC and polymer deposition
2. Conduct a comprehensive analysis of optimal printing conditions
3. Characterise the effect of different substrates on LC droplets
4. Fabricate a proof-of-concept LC microlens
5. Fabricate patterned polymer-dispersed liquid crystalline films

1.3 Thesis Structure and Aims

Chapter two examines the relevant LC theory. The unique microscopic opto-electrical properties and the macroscopic ordering of LCs is described, along with

LC molecular anchoring and hydrodynamic behaviour. There is particular emphasis on LC droplets in terms of possible director configurations and optical signatures.

Chapter three discusses several experimental techniques used throughout this thesis. A major component of this involves the design and build of a highly versatile and low-cost inkjet printing system. The bespoke system is capable of printing and analysing the droplet properties of a range of different fluids. The hardware and software components are explained in sufficient detail to inform readers wishing to develop a similar printing system. Finally, a description of the various image-analysis programs used to extract droplet properties both during printing and after deposition onto the substrate is provided.

Chapter four is concerned with the inkjet printing of a nematic LC and considers the parameters that are of importance for reliably forming uniform droplets. The mechanism of droplet generation in a piezoelectric DoD printhead is described in detail. The effect of different printing parameters, such as temperature and driving voltage, on the resulting drop volume and velocity is discussed. Finally, a procedure for determining the optimal waveform for a given printhead and functional ink is presented.

Chapter five investigates the role that different substrates play on the resulting LC droplet or film. The droplet impact, wetting and spreading behaviour of a nematic LC onto glass, polymer and liquid substrates is presented. The effect of the printing process on the LC director alignment, which is instrumental to LC device fabrication, is shown for conventional and non-conventional substrates. The generation of radially aligned nematic droplets that do not require any specialist substrate treatment is demonstrated. Finally, optimal substrates for homeotropic, planar and radial aligned droplets are identified.

Chapter six demonstrates how the inkjet printing system that has been developed can be used to produce bespoke LC microlens arrays. The LC microlenses are highly uniform with a focal length that can be tuned by varying the temperature. The chapter moves on to consider encapsulation of such a lens before demonstrating a proof-of-concept, fast-switching and fully-encapsulated, polymer-dispersed LC microlens.

Chapter seven builds upon the inkjet printing of LC and prepolymer formulations introduced in the previous chapter to investigate two novel methods of producing patterned polymer-dispersed LC films. Inkjet allows for efficient fabrication of polymer-dispersed LC films that can be uniquely patterned within a single layer. The feasibility of each fabrication method is discussed in details. The chapter concludes with the optical characterisation of a patterned polymer-dispersed LC film produced via inkjet printing.

Finally, chapter eight brings together the main conclusions and contributions presented throughout this investigation. Due to the exploitative and multi-disciplinary nature of this thesis, many different ideas and concepts have been considered. This chapter summarises several possible directions for future work and serves as an aid and guide for future researchers operating this field.

Chapter 2

Liquid Crystals

2.1 Background

Liquid crystals (LCs) are a unique class of quasi-crystalline material that have the ability to self-assemble into regular and/or periodic structures, whilst being able to flow like a fluid [214]. It is believed that Austrian botanist, Friedrich Reinitzer was the first to observe a liquid crystalline state when studying the melting point of the material cholesteryl benzoate back in 1888 [34]. It was his friend and colleague Otto Lehmann who coined the term liquid crystal, and was the first to discover the anisotropic optical nature of the material [35].

For much of the 20th century, the field of LCs persisted as a relatively small area of scientific curiosity. This was until 1964 when the first ever LCD was demonstrated, marking the first major application of the technology and a sign of developments to come. Using dynamic mode scattering technology, LCDs began to carve out a niche in small-size displays used in pocket watches and calculators. The first thin 'large-area' LCD (then just 14-inches) was demonstrated in 1988 using active-matrix, thin-film-transistor technology. This spawned a new industry - flat-panel display, which is projected to reach 206 billion dollars in 2025 (Allied Market Research). In the late 80's, LCs became a center of scientific and industrial research, with major contributions coming from all over the world and a Nobel Prize being awarded to Pierre-Gilles de Gennes in 1991.

Due to the success of LCDs, there has been a historic focus on display applications. However, this research also developed a solid scientific understanding of this complex class of materials. Today, unlike 30 years ago, LCs are just one type

of flat-panel display technology. Their former dominance of the industry that they created being usurped by LED- and OLED-based displays. As a result, the modern LC community has diversified its research into new and exciting applications of LCs. These range from the self-assembly of nano-particles, LC elastomers and 'soft robots', optical/bio sensors, smart windows and many more [36, 37, 38, 39].

2.1.1 Liquid Crystal Phases

LCs can possess both the symmetry and order of a crystalline solid, whilst being able to flow like a fluid. A LC exhibits a thermodynamic mesophase, in which the constituent molecules have a degree of macroscopic orientation and/or positional order. If this mesophase appears over a range of temperatures between the solid and liquid phase, it is referred to as thermotropic LC. On the other hand, a LC with a mesophase that is determined by the concentration of a host solvent is referred to as a lyotropic LC [214].

An example of an organic thermotropic LC - pentyl-cyanobiphenyl (5CB) is shown in Figure 2.1a. The two phenyl rings are rigidly linked and form the backbone of the molecule, while the hydrocarbon terminal group is flexible. As with many organic LCs, 5CB has a permanent dipole and the direction of the dipoles will average to zero in the bulk material. The molecule will rotate about its long axis such that the volume it sweeps out can be approximated by a cylinder, as shown in Figure 2.1b. A molecule of this type is effectively uniaxial, with a single axis of symmetry indicated by the dotted line. This type of long, rod-shaped LC molecule is known as a uniaxial calamitic LC. 5CB is the dominant constituent component of the LC blend E7, which is used extensively throughout this thesis and characterised in §3.2.

The phase a LC takes is dependent on the molecular structure, shape, mixture composition, as well as the temperature (in a thermotropic LC). Some of the most common and stable mesophases are the nematic, smectic and columnar phases. There are many other more complex phases such as the cholesteric, smectic and blue phases. Figure 2.1c shows an example of the possible phases a thermotropic calamitic LC may undergo as it is heated. At low temperatures, a crystalline solid

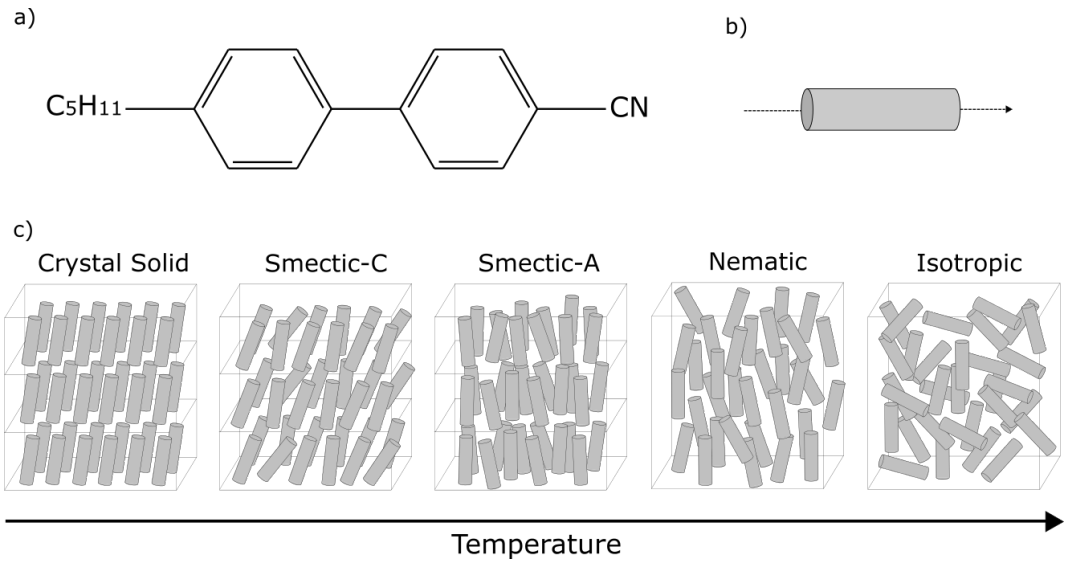

FIGURE 2.1: a) Chemical structure of the liquid crystal molecule 5CB. b) Cylindrical representation of a calamitic LC molecule. c) Schematic examples of common phases of a thermotropic calamitic LC.

phase is formed. In this phase there exists both orientational and positional ordering of the LC molecules, which undergo almost zero diffusion. The degree of macroscopic order reduces as the material is heated. The temperature above which the LC forms an isotropic fluid is known as the clearing, or isotropic temperature (T_{iso}).

Unlike the calamitic LC shown in Figure 2.1, a columnar (or discotic) LC can form a columnar phase at low temperatures in addition to having solid crystalline and isotropic phases (some discotic LCs also possess a nematic phase). Note that this thesis is concerned with thermotropic calamitic LCs only and thus further discussion is limited to this type of LC.

2.1.2 Nematic Liquid Crystals

The nematic phase is the simplest LC phase whereby the LC molecules have no positional order but exhibit a macroscopic preferential orientation as they diffuse in the sample. The macroscopic preferential orientation is called the LC director and is denoted by the unit vector $\hat{\boldsymbol{n}}$. As seen in Figure 2.2a, the unit vector $\hat{\boldsymbol{a}}$ points in the direction of the long axis of a single LC molecule and is defined by the polar and azimuthal angles θ and ϕ, with the z-axis chosen such that it

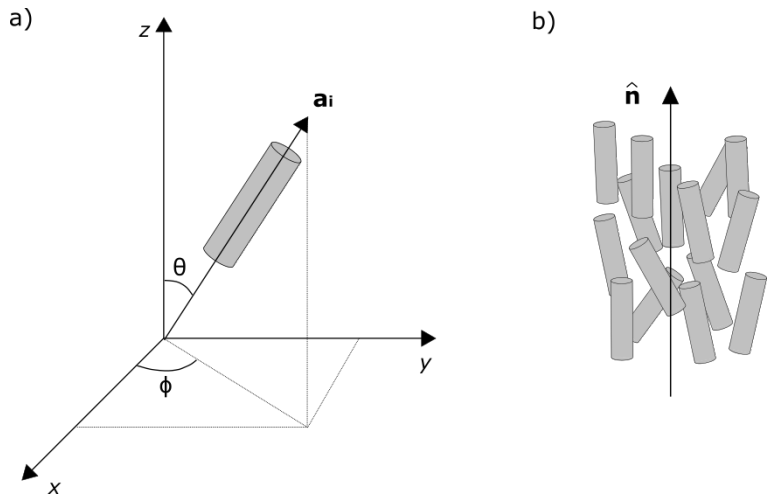

FIGURE 2.2: a) Orientation of a single LC molecule oriented at an angle θ from the direction of the LC director, $\hat{\boldsymbol{n}}$. b) Average orientation of a large number of molecules defined by the LC director $\hat{\boldsymbol{n}}$.

is parallel to $\hat{\boldsymbol{n}}$. It is noted that uniaxial LCs have no preferred orientation in the azimuthal direction, allowing the orientation of a LC to be described with a single angle: θ.

The LC director $\hat{\boldsymbol{n}}$ points in the average direction of a large number of molecular orientations $\boldsymbol{a_i}$. This is shown diagrammatically in Figure 2.2b. The LC molecules are uniaxial and, even for LCs with a permanent dipoles, there will be an equal number of LC molecules oriented parallel and anti-parallel to $\hat{\boldsymbol{n}}$, thus $\hat{\boldsymbol{n}} \equiv -\hat{\boldsymbol{n}}$. The presence of the nematic phase can be determined using polarised optical microscopy (POM) which is discussed in Section 2.3.2.

2.1.3 Order Parameter

An order parameter is used to quantify the degree of orientational order in a nematic sample. It is defined such that it is zero in the isotropic, unordered phase, and non-zero in ordered phases. For a uniaxial LC (whose orientation is independent of ϕ), the orientation state of the LC molecules can be described by a distribution function $f(\theta)\, d\Omega$, where $d\Omega = sin\theta d\theta$ is the small solid angle. Rather than using the full distribution function $f(\theta)$, it is convenient to use a single numerical parameter to quantify the degree of orientational order.

For uniaxial LCs, such a parameter is given by taking the average of the second-order Legendre polynomial [213, 40, 41]:

$$S = \frac{1}{2}\langle(3cos^2\theta - 1)\rangle = \int_0^\pi f(\theta)\frac{1}{2}(3cos^2\theta - 1)d\Omega \Big/ \int_0^\pi f(\theta)d\Omega \ , \tag{2.1}$$

where $\langle\rangle$ indicates the spatial and temporal average. For a perfect solid crystalline ordering, $S = 1$, whilst for fully isotropic liquids, $S = 0$. The nematic phase will typically have an order parameter $0.3 < S < 0.8$ [42].

In the isotropic phase, the LC transforms into an isotropic liquid. At this temperature, a vial of LC appears clear to the naked eye (where the clearing temperature gets its name). This simple observation can be used to determine the nematic-isotropic phase transition for LC sample. More rigorous determination of the order parameter can be carried out using optical techniques such as the Haller method, which requires determination of the density and refractive indices [43, 44, 222]. A qualitative assessment of the LC phase can be done using polarised optical microscopy discussed in more detail in Section 2.3.3.

2.1.4 Order Parameter and Temperature

The order parameter depends strongly on the temperature of the LC sample. As the temperature is raised, the corresponding increase in kinetic energy of the LC molecules leads to a loss of orientational order. Figure 2.3 shows how the order parameter for thermotropic nematic LC varies with temperature. The discontinuity at T_{iso} indicates the phase transition from the nematic to isotropic phase. This is a first order phase transition which occurs rapidly and often nucleates from impurities and/or defects in the liquid crystalline structure.

2.2 Dielectric Properties

The dielectric and diamagnetic properties of LCs are inherently anisotropic. LCs are generally assumed to be non-conductive with very high resistances ($\approx 10^{10}\Omega$) and dipole moments that can be induced by external fields. For fields below

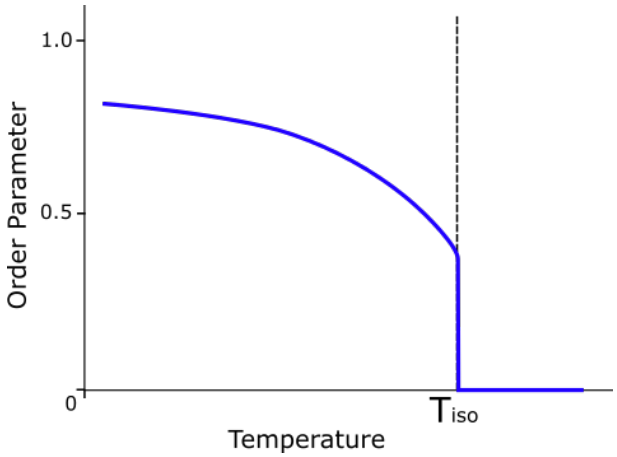

FIGURE 2.3: Typical plot of the scalar order parameter for a thermotropic liquid crystal.

optical frequencies, the dielectric permittivity is given by Maxwell's relation:

$$\boldsymbol{D} = \hat{\boldsymbol{\varepsilon}} \cdot \boldsymbol{E}\,, \tag{2.2}$$

where $\hat{\boldsymbol{\varepsilon}}$ is the dielectric tensor, $\boldsymbol{D}$ is the displacement field and $\boldsymbol{E}$ is the electric field. Note that $\varepsilon = \varepsilon_o \varepsilon_r$, where ε_o and ε_r is the permittivity of free space and the relative permittivity, respectively. For a uniaxial nematic LC, the dielectric tensor is:

$$\hat{\boldsymbol{\varepsilon}} = \begin{bmatrix} \varepsilon_\perp & 0 & 0 \\ 0 & \varepsilon_\perp & 0 \\ 0 & 0 & \varepsilon_\parallel \end{bmatrix},$$

where $\varepsilon_\perp$ and $\varepsilon_\parallel$ are the dielectric permittivity perpendicular and parallel to the LC director ($\hat{\boldsymbol{n}} = [0,0,1]$), respectively. The majority of LCs, and all those used in this thesis, possess positive dielectric anisotropy ($\varepsilon_\parallel > \varepsilon_\perp$). The dielectric anisotropy is defined as: $\Delta\varepsilon = \varepsilon_\parallel - \varepsilon_\perp$.

Taking into account the LC director, the displacement $\boldsymbol{D}$ can be written in the following form:

$$\boldsymbol{D} = \varepsilon_\perp \boldsymbol{E} + (\varepsilon_\parallel - \varepsilon_\perp)(\hat{\boldsymbol{n}} \cdot \boldsymbol{E})\hat{\boldsymbol{n}}\,. \tag{2.4}$$

The electrostatic energy density, f_e is:

$$f_e = -\int_0^E \boldsymbol{D} \cdot d\boldsymbol{E} = -\frac{1}{2}\varepsilon_\perp (\boldsymbol{E} \cdot \boldsymbol{E}) - \frac{\Delta\varepsilon}{2}(\hat{\boldsymbol{n}} \cdot \boldsymbol{E})^2\,. \tag{2.5}$$

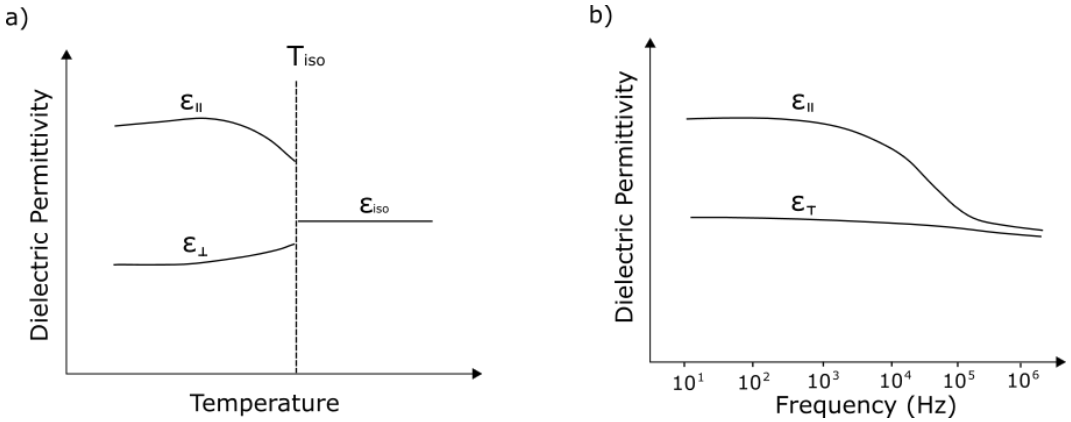

FIGURE 2.4: Figure showing the typical dielectric permittivity response of a uniaxial nematic LC with positive dielectric anisotropy. a) Temperature dependence of the dielectric permittivity as the LC is heated through the isotropic temperature (T_{iso}). b) DC and low-frequency dependence of the dielectric permittivity for a LC with positive dielectric anisotropy.

The dielectric energy is dependent on the orientation of the LC director relative to the applied electric field. As the left-hand term in Equation 2.5 is independent of the director $\hat{\boldsymbol{n}}$, its contribution to dielectric coupling can be neglected such that the dielectric free energy simplifies to:

$$f_e = -\frac{\Delta\varepsilon}{2}(\hat{\boldsymbol{n}} \cdot \boldsymbol{E})^2 \,. \tag{2.6}$$

From Equation 2.6, and for a LC with positive dielectric anisotropy ($\Delta\varepsilon > 0$), the electric free-energy density is minimised when the director is aligned parallel or anti-parallel to the applied field. Thus, the LC will tend to align parallel to the applied electric field. On the other hand, LCs with negative dielectric anisotropy will tend to align perpendicular to the applied field.

The dielectric constants are strongly dependent on temperature and the frequency of the applied field [214]. Figures 2.4a) and b) show typical behaviour of a uniaxial LC with positive dielectric anisotropy. Both $\varepsilon_\perp$ and $\varepsilon_\parallel$ show normal Debye type relaxation in the frequency range 1-10^{10} Hz [214]. Dual-frequency LCs have the unique property of the dielectric anisotropy ($\Delta\varepsilon$) changing sign at a particular cross-over frequency. However, such LCs are not discussed further as they are not used in any of the investigations presented.

2.2.1 Refractive Index

The refractive index is a dimensionless number that defines the speed at which light propagates in a non-magnetic medium. For a material with a relative permittivity, ε_r, it is defined as:

$$n = \sqrt{\varepsilon_r}\,. \tag{2.7}$$

At optical frequencies (typically above 10^{10} Hz), $\varepsilon_{\parallel} > \varepsilon_{\perp}$[214]. There is no dipole effect induced in the molecules at optical frequencies, however, their dielectric anisotropy remains due to the molecular polarizability. Therefore, LCs are birefringent with optical behaviour characterised by two refractive indices called the ordinary (n_o) and extraordinary (n_e) refractive indices[1]. Figure 2.5 shows the optical indicatrix for a uniaxial LC. The birefringence of a LC is defined as:

$$\Delta n = n_e - n_o\,. \tag{2.8}$$

The average refractive index, corresponding to the refractive index of the LC material in the isotropic phase (neglecting any temperature dependence) is: $n_{avg} = (n_e + 2n_o)/3$.

Depending on the director orientation, orthogonal components of polarized light incident to the LC material will become out of phase. The thickness and birefringence of LC device dictates the degree to which orthogonal components of light will emerge out of phase, allowing nematic LCs to be used as wavelength dependent quarter and half-wave plates. This phenomenon is known as optical retardation and is responsible for the beautiful and descriptive patterns seen when viewing LCs under crossed-polarisers.

2.2.2 Dependency on Temperature, Order and Wavelength

The birefringence of a LC is temperature dependent. The Haller approximation is often used to determine the birefringence for temperatures below the clearing temperature [44]:

$$\Delta n(T) = (\Delta n)_o (1 - T/T_{iso})^{\beta}\,, \tag{2.9}$$

[1]There are in fact three orthogonal refractive indices. However, two of them are very similar and denoted the ordinary refractive index n_o.

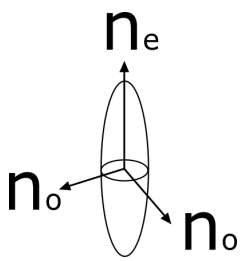

FIGURE 2.5: Optical inicatrix of a uniaxial LC showing the ordinary (n_o) and extraordinary (n_e) refractive indices relative to the local director $\hat{\boldsymbol{n}}_r$.

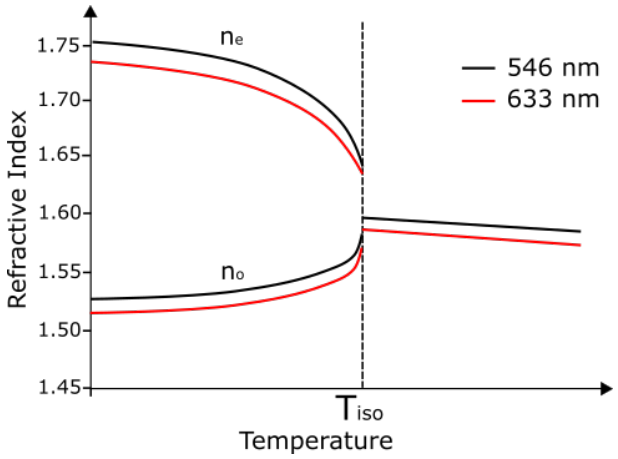

FIGURE 2.6: Temperature dependency of the refractive indices for the nematic LC 5CB at $\lambda = 546$ and $\lambda = 633$ nm (adapted from [42]).

where $(\Delta n)_o$ is the birefringence of the LC in the crystalline state and the exponent β is a material constant (β=0.16-0.24 for 5-8CB LCs [45]). Figure 2.6 shows the temperature dependency of the refractive indices at two different wavelengths for the nematic LC 5CB. The dependency of the refractive indices on the wavelength of light can be modelled by using the extended Cauchy equations or the Three-band model [219, 46]. The two-coefficient Cauchy model is:

$$n_{e,o} = A_{e,o} + \frac{B_{e,o}}{\lambda^2}\,, \tag{2.10}$$

where the coefficients $A_{e,o}$ and $B_{e,o}$ must be determined by measuring the refractive indices at two known wavelengths.

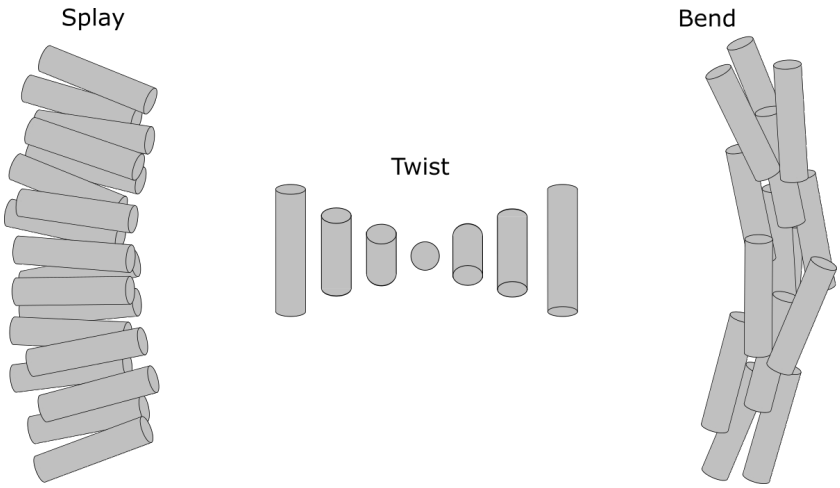

FIGURE 2.7: Diagram of the three main types of deformation in a LC material.

2.3 Elastic Properties

The free energy of a nematic LC is at a minimum when the material is unconstrained and in thermodynamic equilibrium. However, akin to a crystalline solid, a LC experiences strain and deformation when subject to external forces or competing boundary conditions. Such deviations from the unconstrained state cause changes to the director $\hat{\boldsymbol{n}}$. Continuum theory takes a macroscopic view (larger than 1μm), whereby these deviations are considered continuous, elastic and come with an associated energetic penalty. Figure 2.7 shows the three main types of deformation used to describe the distortion of a LC - which can be a combination of these fundamental deformations.

Splay deformation is characterised by the divergence of the director $(\boldsymbol{\nabla} \cdot \hat{\boldsymbol{n}})$, twist is characterised by $(\hat{\boldsymbol{n}} \cdot \boldsymbol{\nabla} \times \hat{\boldsymbol{n}})$, and bend is characterised by $(\hat{\boldsymbol{n}} \times \boldsymbol{\nabla} \times \hat{\boldsymbol{n}})$. The local elastic free energy density is given by the Frank-Oseen equation [47, 48]:

$$f_d = f_{splay} + f_{twist} + f_{bend} \,,$$

$$= \frac{1}{2}\left[K_{11}(\boldsymbol{\nabla} \cdot \hat{\boldsymbol{n}})^2 + K_{22}(\hat{\boldsymbol{n}} \cdot \boldsymbol{\nabla} \times \hat{\boldsymbol{n}})^2 + K_{33}(\hat{\boldsymbol{n}} \times \boldsymbol{\nabla} \times \hat{\boldsymbol{n}})^2\right] \,, \tag{2.11}$$

where K_{11}, K_{22} and K_{33} are the splay, twist and bend Frank elastic constants, respectively and are on the order of 1-20 pN [214, 211]. It is most common

for $K_{33} > K_{11} > K_{22}$. For example, the LC 5CB has: $K_{11} = 0.64 \times 10^{-11}$ N, $K_{22} = 0.3 \times 10^{-11}$ N, $K_{33} = 1 \times 10^{-11}$ N. There is also saddle-splay and splay-bend deformations (K_{24} and K_{13} respectively). However, these are often neglected in order to simplify analysis and are henceforth only referenced qualitatively [49, 50]. The total elastic energy F_d, over a volume V, is then given by:

$$F_d = \int_V f_d \, dV \, . \tag{2.12}$$

Note that the reasoning behind the subscript d is due to the elastic energy associated with distortion and is used to avoid confusion with other free energies introduced later. In order to qualitatively describe the LC director, Equation 2.11 is often simplified using the one-constant approximation: $K_{11} = K_{22} = K_{33} = K$, where K is taken as the largest elastic constant K_{33} (for 5CB $K = 10^{-11}$ N)[42]. The elastic free energy density then becomes:

$$f_d = \frac{1}{2} K \left[(\boldsymbol{\nabla} \cdot \hat{\boldsymbol{n}})^2 + (\boldsymbol{\nabla} \times \hat{\boldsymbol{n}})^2 \right] \, . \tag{2.13}$$

2.3.1 Anchoring

LC molecules tend to align with a preferential orientation at a surface or interface. The most common anchoring conditions encountered are:

Homeotropic alignment where the director $\hat{\boldsymbol{n}}$ is perpendicular to the interface. A homeotropic aligned LC cell is shown in Figure 2.8a.

Uniform planar alignment is shown in Figure 2.8b. The director $\hat{\boldsymbol{n}}$ is mostly parallel to the interface, often deviating by an angle referred to as the pre-tilt, and with a preferential in-plane orientation.

Random Planar The director $\hat{\boldsymbol{n}}$ lies parallel to the interface but at an arbitrary in-plane orientation, which may vary spatially across the substrate.

Degenerate Planar The director $\hat{\boldsymbol{n}}$ again lies parallel to the substrate. However, many (or all possible) in-plane orientations of the director are accommodated for.

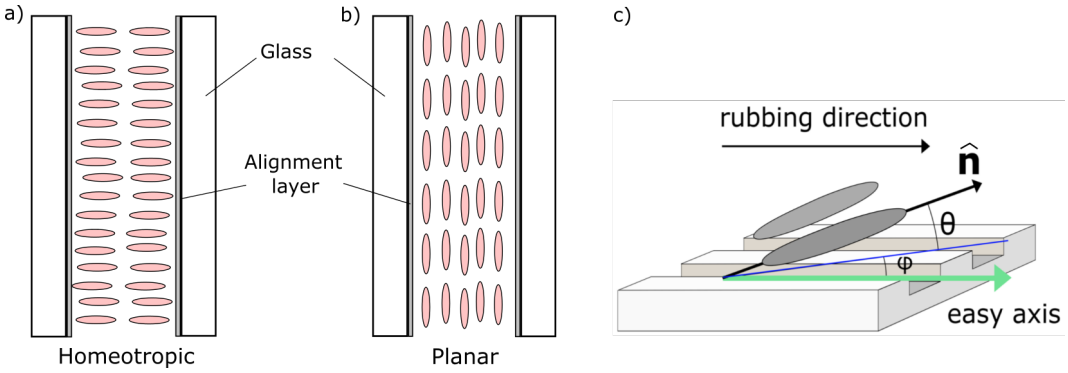

FIGURE 2.8: Schematic illustration of a homeotropic (a) and planar (b) aligned LC cell. c) Schematic representation of a nematic LC molecule aligned on a rubbed polymer alignment layer, showing the polar angle (θ), azimuthal angle (ϕ) and easy axis. The rigid grooves are a simplified mechanical representation of the supposed alignment of the polymer chains which occurs during the rubbing.

Often, it is common for substrates to exhibit random planar anchoring with a degree of degeneracy, for example untreated ground-glass and many (untreated) polymers such as Polyvinyl alcohol (PVA). The mechanism of the alignment of the interface is usually a balance between steric interactions, interfacial chemistry and the associated elastic energy of the LC director [51]. Typical planar LC cells comprise of polyimide, or similar polymer layer, which is rubbed in a particular direction. The rubbing process aligns the polymer chains of the substrate in the rubbing direction and promotes planar anchoring with the director oriented parallel to the rubbing direction. Homeotropic anchoring is often achieved via the use of surfactants or detergents such as lecithin.

The preferred orientation of the director $\hat{\boldsymbol{n}}$ at an interface is referred to as the easy axis as it represents the most energetically favourable orientation of the LC molecules at the substrate. This is shown in Figure 2.8c, which also shows the pre-tilt angle (θ). In reality, the director may not be aligned with the easy axis due to the orientation of the bulk LC or the application of external forces. Any misalignment to the easy axis incurs an associated energy penalty which can be described by a surface free energy density [52]:

$$f_s = \frac{1}{2} W_\theta \, sin^2(\theta - \theta_o) + \frac{1}{2} W_\phi \, sin^2(\phi - \phi_o) \, , \tag{2.14}$$

where θ and ϕ are the polar (or pre-tilt) and azimuthal angles of the LC molecules at the interface. Similarly, θ_o and ϕ_o are the polar and azimuthal angles of the easy axis. The constants W_θ and W_ϕ are the anchoring energies describing the strength of the anchoring at the interface. Typically $W_{\theta/\phi}$ have a magnitude ranging between 10^{-7} to 10^{-3} Jm^{-2} [53, 54]. Often, f_s can be approximated by the single constant Rapini-Papoular equation:

$$f_s = \frac{1}{2} W \, sin^2\theta \, . \tag{2.15}$$

Configurations commonly encountered in this thesis are LC/air, LC/water and LC/polymer interfaces. Many LCs, including E7, show strong homeotropic alignment at an air interface in the order of 10^{-4} Jm^{-2} [54]. In the absence of surfactants, these LCs form random degenerate planar alignment at the interface with water. The LC/polymer interface depends upon the chemical composition of the polymer as well its state of polymerisation.

2.3.2 LC Defects and Microscope Textures

Section 2.3 describes continuous variations to the director field. However, this is often not the case due to topological defects and disclinations present in the sample [220]. Considering a 2D case in the x-y plane, the local director field, $\boldsymbol{n}(\boldsymbol{r})$ can be described by a single angle ϕ: $\boldsymbol{n}(\boldsymbol{r}) = [cos\phi, sin\phi, 0]$. Using the single elastic constant, K, and assuming the only contributions to the free energy are due to elastic deformation, minimizing Equation 2.13 leads to a solution in the form:

$$\phi(x, y) = s \, tan^{-1}\left(\frac{x}{y}\right) + \phi_0 \, , \tag{2.16}$$

where ϕ_0 is a constant and $s = 0, \pm\frac{1}{2}, \pm 1, \pm\frac{3}{2}, \ldots$. The solution $s = 0$ corresponds to a uniform director with a constant $\mathbf{n}$ oriented at an angle ϕ_0. However, the solutions $s = \pm\frac{1}{2}$ and $s = \pm 1$, correspond to a director field which varies around a singularity at $x = y = 0$ (where the director is undefined). In the literature the term s is called the defect 'strength'. Higher strength disclinations $\mid s \mid$ are possible, however, they are unstable and do not persist unless the LC is doped or held

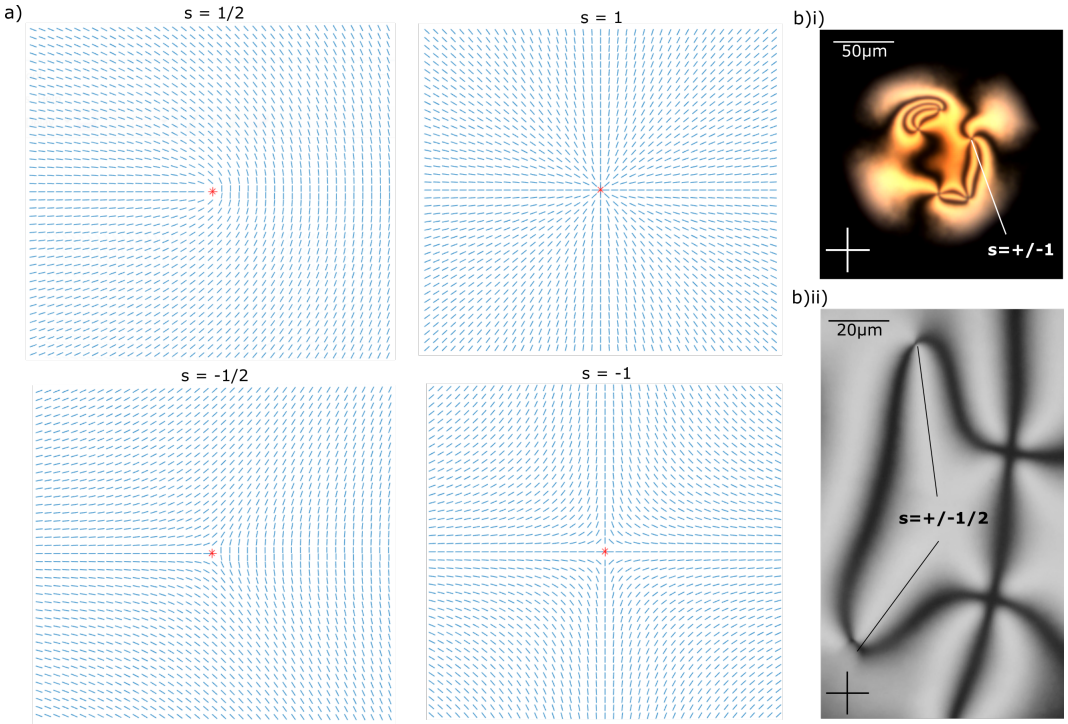

FIGURE 2.9: a) 2-D plots of the director field around the four possible topological defects, produced using MATLAB. b)i) Example of a nematic LC droplet on a degenerate planar substrate (wet PVA) and a homeotropic top LC/air interface. b)ii) Example of a nematic LC sample with non-uniform LC alignment showing the characteristic schlieren texture (b)ii) has been reproduced with permission [56], other figures have been taken by the author of this thesis). The strength of the defects are indicated on the figures.

at lower temperatures [55]. Figure 2.9 show MATLAB plots for each of the four possible defect structures with $\phi_0 = 0$. A disinclination line, which is observed in practise, can be thought of as extending the 2D director representations shown in Figure 2.9 in the z-direction.

2.3.3 Microscope Textures

Polarized Optical Microscopy (POM - described experimentally in §3.3.1) is a convenient means to determine the phase, LC director and the presence of any defects in a LC sample. The disclination lines described above can be observed using POM and appear as thread-like structures , in fact the name 'nematic' comes from the Greek word for 'thread'. The sample is viewed between crossed polarisers using a microscope in transmission mode. As described in §2.2.1, linearly

polarised light passing through a nematic LC can experience two different refractive indices depending on the orientation of the LC director relative to the polarisation and propagation direction of the light. The top polariser (the analyser) is placed at 90°to the bottom polariser, such that the sample will only appear bright if its polarisation has been changed - light passing thought the sample has interacted with both n_o and n_e. On the other hand, the sample will appear dark if the LC director is parallel or perpendicular to the bottom polariser - light passing though the sample has interacted with n_e only. Additionally, the sample will appear dark if the LC director is co-axial to the trajectory of incident light - light passing through the sample interacts with n_o only.

Figure 2.9b)i) shows an oblate nematic droplet with five instances of $s = \pm 1$ defects. Characteristic of such defects, four dark brushes are seen to propagate from a central point. The dark brushes indicate the LC director is parallel or perpendicular to the polariser. Figure 2.9b)ii) is an example of a nematic displaying two $s = \pm\frac{1}{2}$ defects which are indicated on the figure (and two ± 1 defects that aren't labelled). It is noted that Figure 2.9a is a 2D representation, whereas Figure 2.9b are 3D POM images. However, due to uniform anchoring of the LC at the top and bottom interfaces and the LC layer being very thin (≈ 5 μm), the 2D defects identified are still observed.

2.3.4 Nematic Droplets

Throughout this thesis, LC's confined in the form of droplets will be considered. These are commonly, but not limited to, spherical and hemispherical configurations. This section will outline the common LC director configurations observed in spherical droplets. These configurations are well-studied and will form a good basis when discussing results in the following Chapters. The four most commonly observed director configurations are shown schematically in Figure 2.10, along with the corresponding POM images. The LC director configuration a droplet assumes depends on the drop radius, magnitudes of the elastic coefficients, anchoring conditions at the interface and the anchoring strengths [57].

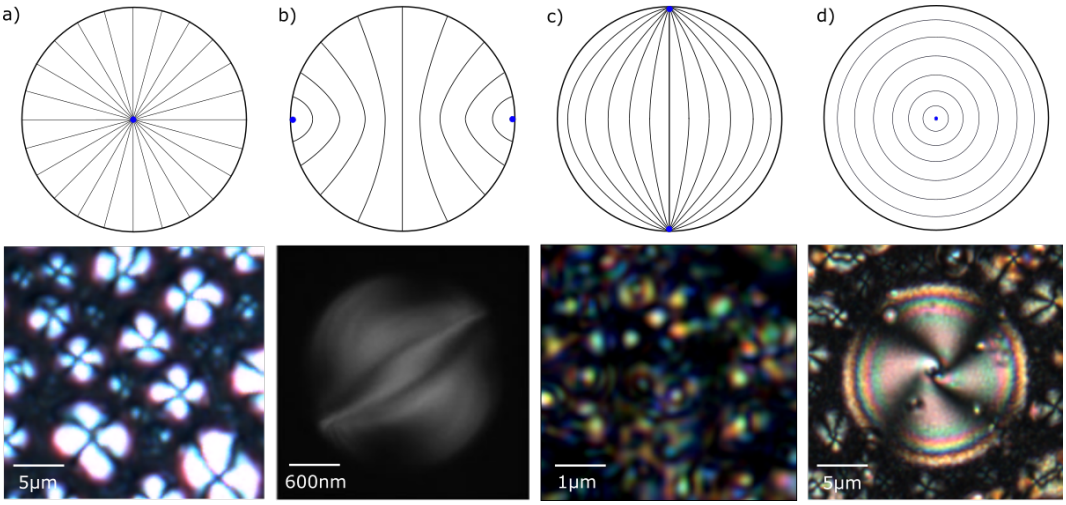

FIGURE 2.10: Schematic representations (i) and polarised microscopy images (ii) of the director profile in nematic droplets: a) Radial, b) Axial, c) Bipolar, d) Concentric. The polarised microscopy images were taken by the author of the thesis apart from b)ii), which was reproduced with permission [59].

Radial Radial configuration, shown in Figure 2.10a, has a single point-defect in the centre of the droplet, often referred to as a hedgehog defect. This is akin to the $s = 1$ defect shown in Figure 2.9. However, in the spherical geometry the defect is stable as a point defect only. The radial configuration is typically stable in larger droplets (diameter approximately $\geq 3\mu$m), where the droplet is subject to homeotropic anchoring conditions at the droplet surface [58].

Axial An axial LC director configuration is shown in Figure 2.10b. Similarly to radial alignment, it occurs with homeotropic anchoring conditions. However, it is stable in smaller droplets (diameter approximately $\leq 3\mu$m) [58]. There are no defect structures present at low anchoring strengths. However, when subject to strong homeotropic anchoring conditions, defect structures akin to the $s = \frac{1}{2}$ are present at the blue points indicated in Figure 2.10. This forms an equatorial disclination in three dimensions.

Bipolar A bipolar configuration is shown in Figure 2.10c. This configuration is stable when subject to planar anchoring conditions and is observed over a large range of droplet diameters [58]. The bipolar configuration is characterised by

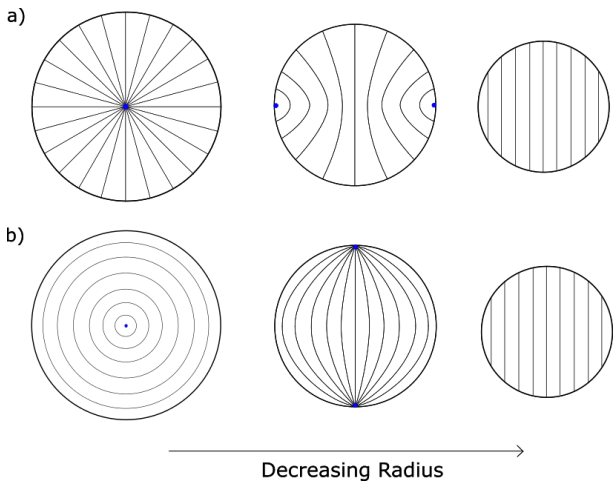

FIGURE 2.11: Schematic representation of the size-dependent droplet morphologies for: a) Homeotropic anchoring at the droplet surface. b) Planar anchoring at the droplet surface.

two-point defects at its poles, called boojums, which are analogous to the hedgehog defect ($s = 1$).

Concentric A concentric configuration is shown in Figure 2.10d. Such configuration has a defect line in its axis akin to the $s = -1$ defect shown in Figure 2.9. It is noted that such configuration is only observed when the bend-splay ratio K_{33}/K_{11} is less than unity [58].

As stated, the size of the droplet plays a key role in determining the morphology of the droplet. Historically, analysis of nematic droplets used the one-elastic approximation (Equation 2.13). Using this model, the elastic energy of the droplet is found to be proportional to KR, and the surface anchoring scales with WR^2, where W is the anchoring strength and R is the droplet radius. This leads to the expectation that the LC director profile in droplets with $R < K/W$ will be free of strain [60, 50]. Using typical values for the elastic constant and anchoring strength ($K = 10^{-11}$ Nm, $W = 5\text{x}10^{-5}$ J/m^2), this predicts that droplets with a diameter less than $\approx 1\mu$m will be free of strain.

Figures 2.11a and b show typical size dependent droplet morphologies for droplets subject to homeotropic and planar anchoring conditions. It is noted that, in general, larger droplets will satisfy surface anchoring conditions and incur an elastic energy penalty associated with deformation of the LC director. On the

other hand, smaller droplets tend to satisfy elastic deformation of the LC director and instead incur a surface energy penalty. More recently, the significance of the saddle-splay elastic constant (K_{24}) in determining the droplet morphology has been recognised [61].

The type of LC droplet can often be determined using polarised optical microscopy (see Section 2.2.1). However, unless the droplet has spherical symmetry, the resulting POM images will be dependent on the orientation of the droplet. For example, the POM images of droplets in a bipolar configuration can vary greatly (as seen in Figure 2.10c). However, droplets in a radial (or concentric) configuration will possess very similar POM signatures (as seen in Figure 2.10a).

2.4 Nematic Hydrodynamics

Much of this thesis is concerned with the bulk macroscopic flow of a nematic LC and how this may affect the inkjet printing of such a fluid. An appreciation of the hydrodynamic behaviour of a LC is also required to understand fundamental concepts, such as the reorientation of the LC director in response to an applied electric field. This section describes some basic LC nemato-hydrodynamics underpinning the chapters to follow.

Although nematic LCs appear to flow like a conventional Newtonian fluid, they exhibit different hydrodynamic behaviour that is dependent on the orientation of the LC director relative to the direction of flow. Moreover, there is a mutual coupling between the direction of flow and the LC director. The anisotropic nature of LC viscosity is described physically by three different viscosity coefficients. Each coefficient describes the viscous behaviour of the LC in three characteristic configurations of the LC director $\hat{\boldsymbol{n}}$ with respect to the direction of the flow velocity v and the gradient ∇v.

Miesowicz was the first to experimentally determine the different viscosity coefficients. He used a strong magnetic field to orient the LC before measuring the viscosity between two moving parallel plates [62]. The three LC director configurations relating to the different measurable viscosity coefficients, known as the Miesowizc coefficients, are shown in Figure 2.12. The coefficient η_1 describes

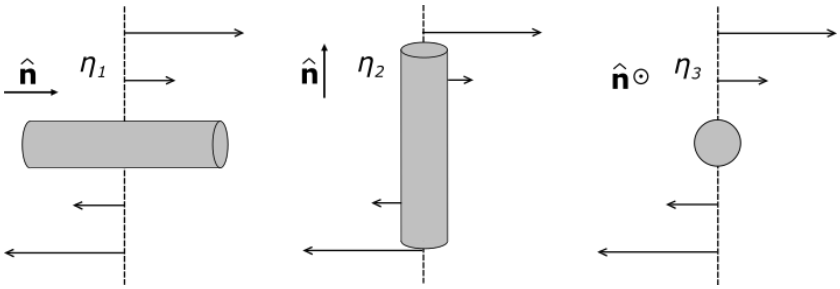

FIGURE 2.12: Diagram showing the three director-flow configurations relating to the Miesowicz viscosity coefficients.

the viscosity when $\hat{\boldsymbol{n}}$ is parallel to the flow $\boldsymbol{v}$. η_2 is the viscosity coefficient when $\hat{\boldsymbol{n}}$ is parallel to the gradient ∇v, and η_3 is the viscosity coefficient when $\hat{\boldsymbol{n}}$ is perpendicular to both $\boldsymbol{v}$ and ∇v.

The three Miesowicz viscosities are a ratio of the shear force over flow velocity, analogous to the definition of flow viscosity for an isotropic fluid. In addition to these three viscosities, there is a fourth which only exists in anisotropic fluids, known as the rotational viscosity, γ_1. This viscosity describes the ratio of the viscous torque acting on the director and the resulting angular velocity of $\hat{\boldsymbol{n}}$.

In addition to experimental determination of the viscous coefficients produced by Miezowicz, a complete theoretical analysis based on continuum theory using a viscous stress tensor was undertaken by Ericksen [63], Leslie [64, 65] and Parodi [66]. The viscous stress tensor contains six elements (α_i) named the Leslie coefficients. In this approach, a general viscosity $\eta(\theta, \psi)$ is described for any director orientation:

$$\eta(\theta,\psi) = \alpha_1 sin^2\theta\, cos^2\theta\, cos^2\psi + \frac{1}{2}\left(-\alpha_2 sin^2\theta\, cos^2\psi + \alpha_3 cos^2\theta + \alpha_4 + \alpha_5 sin^2\theta\, cos^2\psi + \alpha_6 cos^2\theta\right) . \tag{2.17}$$

The angles θ and ψ relative to the flow $\boldsymbol{v}$ and gradient ∇v, are indicated in Figure 2.13a. The relationship between the Leslie coefficients and the Miezowicz viscosities can be found from Equation 2.17 by choosing values of θ and ψ relating to the

three cases in Figure 2.12:

$$\begin{aligned}\eta_1 &= \frac{1}{2}(\alpha_3 + \alpha_4 + \alpha_6) \\ \eta_2 &= \frac{1}{2}(-\alpha_2 + \alpha_4 + \alpha_5) \\ \eta_3 &= \frac{1}{2}\alpha_4 \,.\end{aligned} \tag{2.18}$$

With the rotational viscosity given by:

$$\gamma_1 = \alpha_3 - \alpha_2 \,. \tag{2.19}$$

The Leslie viscosity coefficients and Miesowicz viscosities relate to a specific flow and LC alignment configuration. In the case of inkjet printing, the alignment of the bulk LC is unknown inside the printhead chamber. The flow velocity v and gradient ∇v is non-trivial and highly variable over the evolution of droplet generation. Furthermore, full characterisation of the viscosity coefficients has not been undertaken for many LCs, making it unpractical to determine an exact anisotropic viscosity for all possible configurations encountered during inkjet printing. However, the rotational viscosity, γ_1, is well characterised due to its significance in LCD display switching. The rotational viscosity has a magnitude that lies within the range of the Miesowicz viscositis, for 5CB: $\eta_1 < \gamma_1 < \eta_1, \eta_3$ [67]. Thus, the rotational viscosity is used throughout this thesis to characterise different printing regimes.

2.4.1 Flow-Alignment in Liquid Crystals

The direction and gradient of flow relative to the LC director not only affects the viscosity, but also the director orientation itself. The flow defined in the left and middle configurations of Figure 2.12 would create a reorienting torque on the LC molecules and thus change the director $\hat{\boldsymbol{n}}$. From Equations 2.18, it is seen that the torques generated in these two cases relate to the coefficients α_3 and α_2. An equilibrium orientation of $\hat{\boldsymbol{n}}$ which lies in the shearing plane can be obtained by balancing the torques:

$$\theta = tan^{-1}\sqrt{\frac{\alpha_3}{\alpha_2}}\,, \tag{2.20}$$

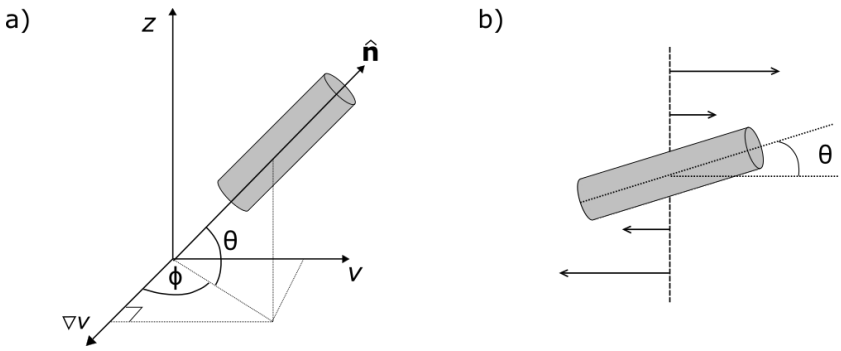

FIGURE 2.13: a) Schematic showing the angles θ and ψ relative to the direction of flow $\boldsymbol{v}$ and the gradient of flow ∇v. b) Schematic showing the steady director orientation of a flow-aligning LC subject to a shearing flow.

where θ is the angle between the director $\hat{\boldsymbol{n}}$ and the direction of flow, shown in Figure 2.13b. Flow aligning LCs have a positive ratio α_3/α_2 and thus Equation 2.20 has a real solution. Most nematic LCs, fall into this category, with typical value of θ between 5-15°, such that the director has a tendency to align approximately parallel with the direction of flow [68, 69].

In many cases, the alignment generated by the flow will compete with the director of the bulk LC, or any alignment imposed by interfacial boundaries or applied fields. As discussed in Section 2.3, any resulting distortion will incur an elastic energetic penalty. The Ericksen number is a dimensionless parameter that gives the ratio of viscous torque over the elastic distortion and is used to quantify the flow-aligning affects in a LC system:

$$Er = \frac{\eta v L}{K}, \tag{2.21}$$

where η is the viscosity, v is the flow velocity, K is an elastic constant and L is the relevant length scale, such as the cell thickness, channel or droplet diameter. Exactly which viscosity coefficient and elastic constant to use in Equation 2.21 depends on the configuration being analysed. However, flow alignment is concerned with α_3 and α_2, so the rotational viscosity γ_1 (which is often well-characterised for a LC) is suitable to use. The elastic constant relevant to the imposed elastic deformation should be used. However, as the Erickson number is used to qualitatively determine the governing alignment mechanism, the

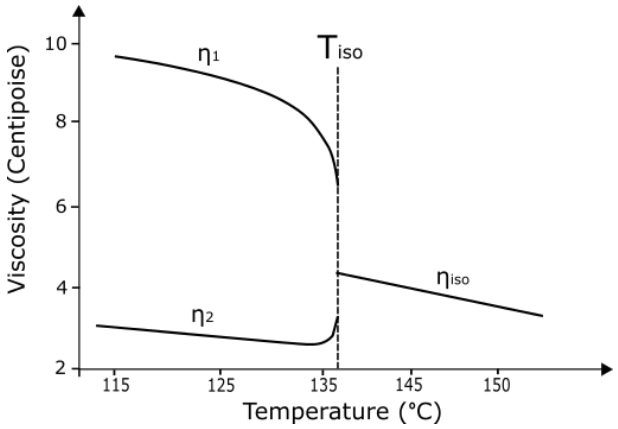

FIGURE 2.14: Viscosity-Temperature dependence for the nematic LC PAA, where η_1 and η_2 are two of Miezowicz viscosities. As a reference, water has a dynamic viscosity of 0.9cP at room temperature. Note that the figure has been adapted from Porter et al. [70] and the values should be used for qualitative purposes only.

single-constant elastic approximation: $K_{11} = K_{22} = K_{33} = K$ gives a good approximation and is often used [54]. For $Er >> 1$, the director is determined by the flow, and for $Er << 1$, the flow-alignment effects are negligible.

A relevant example use-case is considering the flow-alignment of a LC droplet spreading on-top of a substrate. Once the droplet impacts the substrate it will spread on top of it at a velocity v. Using appropriate values for the LC E7: $\gamma_1 = 40mPa.s$, $L = 40\mu$m (typical droplet radius produced via inkjet printing), $K = 10^{-11}$N (single elastic constant approximation), suggests that flow-alignment occurs for flows exceeding $v >\approx 625\mu ms^{-1}$ (for $Er = 100$).

2.4.2 Viscosity and Temperature

As the temperature of a LC sample is increased the viscosity decreases rapidly. Figure 2.14 shows how two Miezowicz viscosity coefficients vary as the temperature is increased [71]. As the LC is heated to the isotropic phase, it exhibits a single isotropic viscosity.

Much of the literature is concerned with the rotational viscosity γ_1 due to its significance in determining LC display response times [42]. There have been several attempts to rigorously describe the physical origin of LC viscosity [68, 71, 215]. However, theoretical results are not fully satisfactory and a general

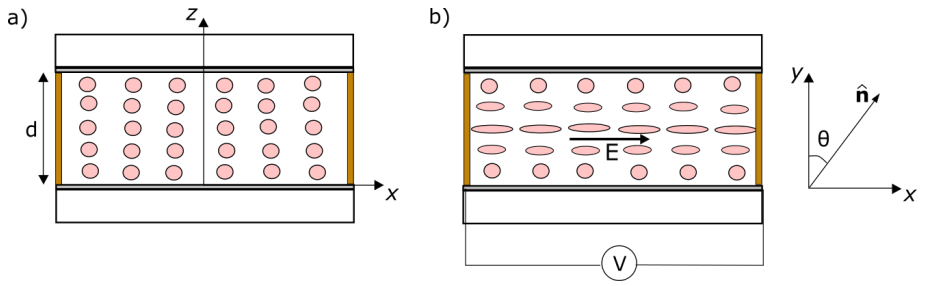

FIGURE 2.15: a) Uniformly aligned planar cell. b) Twist deformation produced by an electric field $\boldsymbol{E}$ and an illustration of the director $\hat{\boldsymbol{n}}$ in the x-y plane.

temperature-dependent viscosity is often used:

$$\gamma_1 bS \cdot e^{E/kT} , \tag{2.22}$$

where γ_1 is the rotational viscosity[2], b is a 'proportionality constant' which incorporates molecular parameters such as moment of inertia, shape and size, S is the order parameter, E is the activation energy of molecular rotation, k is Boltzmann's constant and T is the temperature.

2.4.3 Freedericksz Transition

As discussed in Section 2.2, LCs reorient when subject to an external electric field due to their anisotropic dielectric properties. This is referred to as the Freedericks Transition [214].

Figure 2.15 shows a twist deformation induced by an electric field $\boldsymbol{E}$. The director $\hat{\boldsymbol{n}}$ is defined as: $\hat{\boldsymbol{n}} = (cos\theta, sin\theta, 0)$. The elastic free energy due to deformation (Equation 2.11) is given by:

$$f_d = \frac{K_{22}}{2}\left(\frac{\partial\theta}{\partial z}\right)^2 . \tag{2.23}$$

From Equation 2.6, the electric energy is approximated by:

$$f_{electric} = -\frac{\Delta\varepsilon}{2}(\hat{\boldsymbol{n}} \cdot \boldsymbol{E})^2 = -\frac{\Delta\varepsilon}{2}\boldsymbol{E}^2 sin^2\theta . \tag{2.24}$$

[2]Other viscosity coefficients can be used in place of the rotational viscosity. However, most of the literature considers the rotational viscosity only and thus b and E, which is specific to a viscosity coefficient, are better characterised.

The free energy density is:

$$f = \frac{K_{22}}{2}\left(\frac{\partial\theta}{\partial z}\right)^2 - \frac{\Delta\varepsilon}{2}\boldsymbol{E}^2 sin^2\theta\,. \tag{2.25}$$

An approximation of the threshold electric field of switching (E_c) can be found by using the Euler-Lagrange method to minimise Equation 2.25 (see DeGennes [214]). Using small θ approximations and boundary conditions assuming infinitely strong anchoring at the substrate, the threshold field is approximated by:

$$E_c = \frac{\pi}{d}\sqrt{\frac{K_{22}}{\Delta\varepsilon}}\,. \tag{2.26}$$

The rotation of the LC director is governed by the elastic and electric torques, balanced by the rotational viscous torque:

$$\gamma_1\frac{\partial\theta}{\partial t} = -\frac{\partial f}{\partial\theta}\,, \tag{2.27}$$

$$\gamma_1\frac{\partial\theta}{\partial t} = K_{22}\frac{\partial^2 f}{\partial z^2} + \Delta\varepsilon\boldsymbol{E}^2 sin\theta cos\theta\,. \tag{2.28}$$

The first mode solution to this equation takes the form:

$$\theta(t) = Asin\left(\frac{\pi z}{d}\right)e^{-t/\tau}\,, \tag{2.29}$$

where τ is the relaxation time, given by:

$$\tau = \frac{\gamma_1 d^2}{\pi^2 K_{22}}\,. \tag{2.30}$$

The relaxation time approximates the time taken for the cell to relax back to an unperturbed state (state (b) to (a) in Figure 2.15). Although mathematically defined for a planar cell in twist deformation, Equation 2.30 gives a good approximation of the relaxation time of nematic droplets where d is defined as the droplet diameter, rather than the cell thickness and K_{22} [72].

2.5 Conclusions

This chapter has covered some of the fundamental theory of LCs which form a basis of the studies to come. The significance of the order parameter and its relationship to temperature and the refractive index of a LC has been discussed. The basics of the elastic continuum model, elastic free energy and the effect of LC alignment has been introduced. There has been a particular emphasis on nematic droplets, presenting common LC director configurations and their characteristic polarised optical microscopy signatures. This is used to qualitatively determine the LC director in sessile and dispersed nematic droplets presented in the following Chapters and facilitates models of the LC director in nematic droplets printed onto different aligning surfaces to be constructed. The basics of nematohydrodynamics has been presented, which is critical for understanding the mutual coupling between the LC director and fluid flow observed in flow-aligning LCs. Finally, the Freedericks transition has been discussed which demonstrates the alignment of LCs in an electric field which can be used to estimate the switching voltage and response times in LC cells and droplets.

Chapter 3

Experimental

A significant objective of this thesis was the design and build of an inkjet printing system capable of depositing complex fluids such as LCs and polymer solutions. This chapter details the design and build of a bespoke inkjet printing system to deposit arrays of functional inks and visualise the printing process. The system presented is highly versatile and customisable, making it ideal for investigating the printing of a range of different fluids. The development of each component of the printing rig is described in detail sufficient to aid the development of a similar system. The chapter then goes on to detail common experimental methods used throughout the thesis. This includes polarised optical microscopy, pendant drop measurements and image analysis conducted using MATLAB.

3.1 Design and Build of Experimental Inkjet Printing System

Commercial experimental inkjet systems are both expensive (Full microfab® systems are in excess of £60,000) and lack the ability to deposit unconventional inks, such as polymer solutions, without risk of damage. The design and build of a custom bespoke printing rig allowed maximum flexibility with respect to the choice of inks, substrate and printing conditions. Furthermore, a custom set-up facilitates components such as a polarised microscope and UV-curing light source to be integrated into the system. The printing rig was designed as a research, proof-of-concept and prototyping system. For this reason, practicality, ease-of-use and

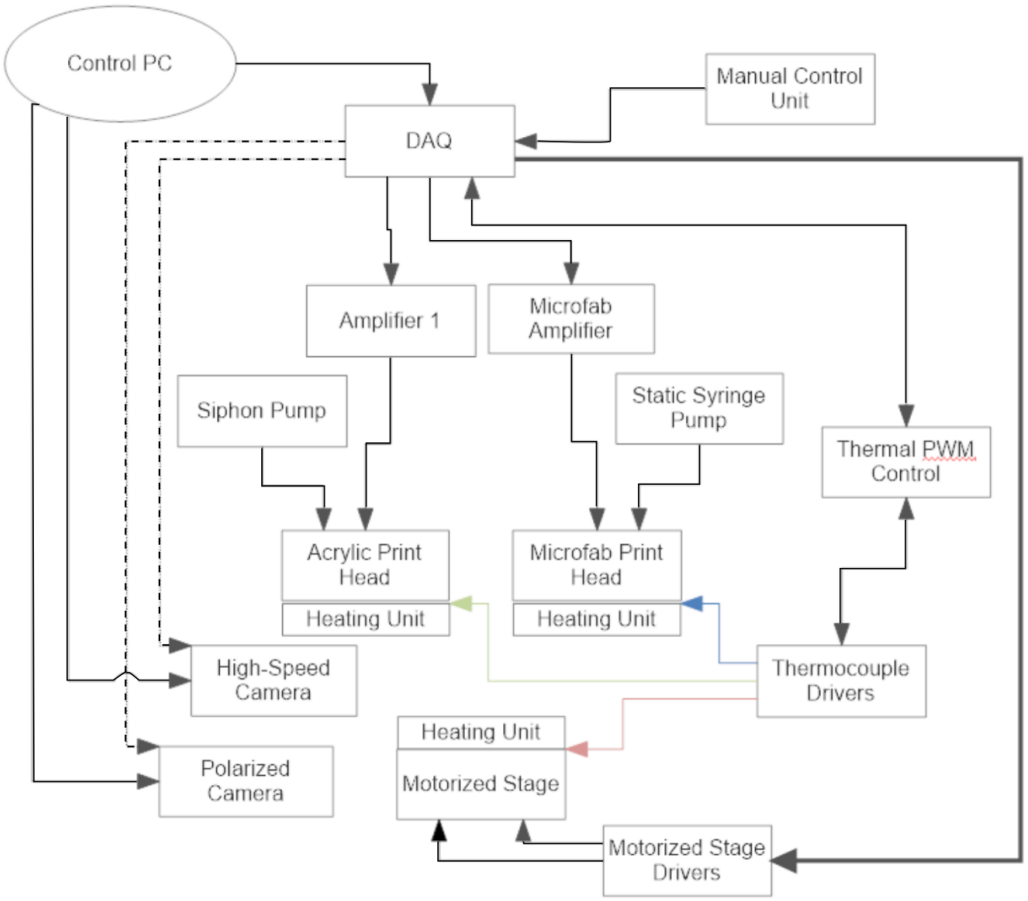

FIGURE 3.1: Schematic overview of the printing system. The arrows indicate the flow of data and/or signals between the components. The coloured arrows represent different thermocouples and the dotted lines are triggering signals.

flexibility were favoured over the ability to produce high-resolution printed designs, which require expensive and slow-moving substrates.

The printing rig was developed incrementally throughout the duration of the thesis as additional requirements arose. Figure 3.1 shows the high-level schematic of the full printing system. It is noted that the system was designed to use up to three printheads simultaneously with full timing synchronisation. This functionality was only exploited in one study described in Appendix §A.1. The figure shows the inclusion of an 'acrylic printhead' - a custom printhead made for the aforementioned study.

Central to the printing rig is a data and acquisition card (DAQ card, NI-6452, National Instruments). Positioning of the motorised stage, actuation waveform

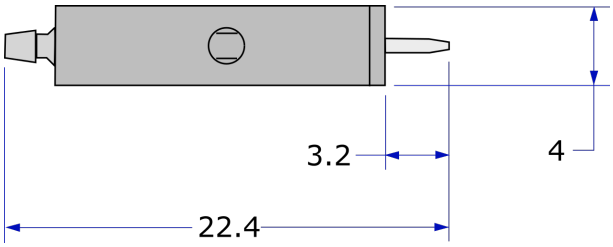

FIGURE 3.2: Technical drawing of the MJ-AB microfab nozzle showing the dimensions in millimetres.

generation, thermal control and timing was achieved using the DAQ and a multi-level LabVIEW program described in section 3.1.6.

3.1.1 Printheads

Depending on the fluid to be printed, two types of piezoelectric printheads can be used. This section details the commercially available microfab MJ-AB nozzles (Microfab), used to deposit LCs and prepolymer formulations described in the main body of the thesis. The design and build of the custom-made 'acrylic' printhead, used to deposit polyvinyl alcohol solutions, is described in §A.1.1.

Figure 3.2 shows a technical illustration of the MJ-AB series of microfab nozzle used. Fluid is delivered to the device via a barb fitting and using PTFE microbore tubing to carry the ink. The nozzle is made from a drawn glass capillary tube (right side of figure) which is bonded to an annular piezoelectric actuator in the body of the device. The MJ-AB nozzles have a quoted operating temperature range of 20-50°C. It is noted that the printing temperatures in this thesis often exceed this quoted temperature range. The device was found to tolerate temperatures up to 70°C for short periods of time.

The nozzle is driven by an amplifier supplied with the package, labelled 'Microfab Amplifier' in Figure 3.1. The voltage waveform supplied to the amplifier is defined using associated the 'JetDriver' software loaded onto the control PC. Assuming an appropriate choice of waveform, a droplet will be produced each time the amplified waveform is supplied to the printhead (see §4.3.1 for details of droplet generation). The software allows for a continuous, or finite, number of drops to be produced at a designated drop frequency. Finite mode operation can

be triggered by a TTL wave supplied to the microfab amplifier. Once triggered, the microfab will then deposit the defined number of droplets at the specified drop frequency. This mode of operation was chosen for synchronising droplet generation to the translation of the printing substrate.

The microfab nozzles were mounted using the heating sheaths machined from a single block of aluminium. The sheaths were designed to accommodate the full body of the nozzle, with just the tip protruding to image droplet generation at the nozzle. Thermal paste was applied to a heating element (DBK HPOS-1/04/-24-20W) bolted to the side of the heating sheath. A hole was drilled through the heating sheath, allowing a thermocouple to be inserted such that it made contact with the printhead chamber. The tip of the thermocouple was coated in thermal paste to ensure good contact with the printhead body. The sheath was fastened to an x-y-z manual translation stage via a laser-cut acrylic bracket. The manual stage was used for fine control of the nozzle over the substrate and for aligning the printhead and high-speed camera.

Fluid Inlet and Ink Reservoir

The ink was supplied to the nozzle using PTFE microbore tubing which was connected the a syringe used as the ink reservoir. Commercial inkjet systems use vacuum controlled reservoirs to control the back-pressure of the printhead (see §4.6.3). However, such set-ups typically require >10mL of fluid to operate efficiently. Due to the high-cost of the fluids used, disposable or glass syringes (volume 1-5 mL) were instead used. Such ink reservoirs could operate efficiently with just 0.1mL of fluid and could be interchanged and stored without contamination for long periods of time. A syringe holder was 3D-printed to secure the syringes in place. A mechanical translation stage screw was re-purposed and bolted to the holder such that the pin was aligned with the syringe plunger. Turning the translation stage screw allowed delicate mechanical pressure to be applied to the syringe plunger.

3.1.2 Preparing and Cleaning the Nozzles

It is important to clean the nozzles prior and after use. The following procedure was used to ensure the nozzles remained clean and debris free:

- A clean foam swab or tissue is used to wipe the exterior surface of the dispensing device and the glass tip using isopropyl alcohol.
- A designated cleaning syringe filled with isopropyl alcohol, using a 5μm filter attachment and PTFE tubing, was used to manually flush the nozzle.
- The device can then be back-flushed by dipping the tip of the nozzle into isopropyl alcohol and pulling back on the syringe plunger ($\approx$1-2mL).
- The process of flushing and back-flushing is repeated several times. However, the fluid sucked into the syringe during the back-flush should be disposed of by disconnecting the nozzle and dispensing the fluid directly from the syringe.
- If the fluid jet during flushing of the tip is straight and uniform, it indicates that the nozzle is clean.
- Filtered air is then used to dry the exterior of the nozzle prior to use.

Once cleaned, the nozzle is inserted into the heating sheath. The temperature of the nozzle is increased to around 60°C for a period of 30 minutes to ensure the solvent has evaporated off. The ink reservoir can then be connected to the nozzle. The filling of the nozzle is best done whilst imaging the nozzle tip using the high-speed microscope camera described in Section 3.1.5. The nozzle is filled such that an excess of fluid is ejected from the tip and no air bubbles are visible at the outlet. Once the excess fluid is carefully wiped off using optical tissue, the nozzle is primed for printing.

If, during printing, droplets appear to deviate from their expected flight path or are not generated at all, it is most often due to clogging of the nozzle or the presence of air bubbles. Air bubbles can be removed in-situ by flushing an excess of ink through the nozzle. For debris clogging the nozzle, the cleaning process above can be repeated. During this process, it is often useful to observe the tip

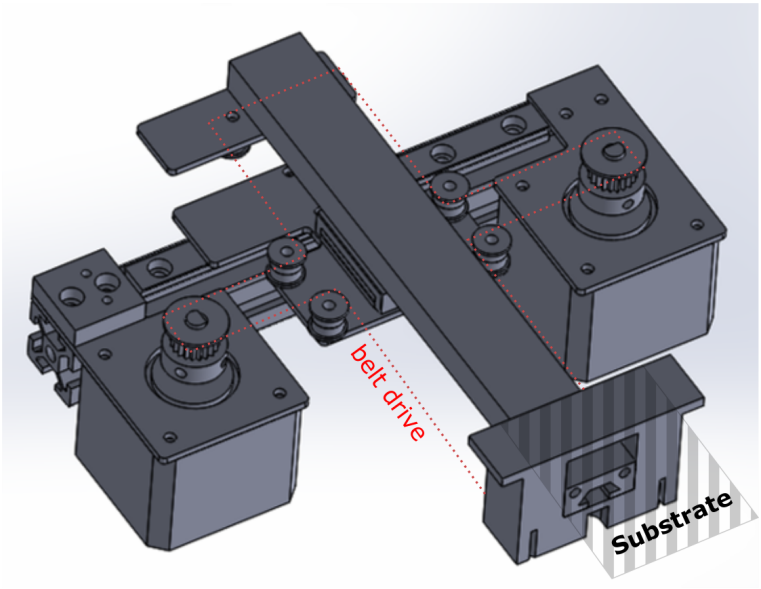

FIGURE 3.3: CAD drawing of the motorised stage.

of the nozzle under a microscope to determine whether any clogging particles are present. Stubborn particles can be removed by soaking the orifice for several hours in isopropyl alcohol, sonicating the tip for up to 4 minutes and finally performing a series of back-flushes.

3.1.3 Motorized Stage

Automated droplet positioning was achieved by translating the printing substrate, rather than the printhead, in order to reduce any residual vibrations that may effect droplet generation. A custom-built motorised stage was developed to automate droplet positioning.

Two stepper motors (4118M-01-RO, Lin Engineering inc) and two linear motion guides with rails (1180mm LMG, THK) were used to provide 2D translation. The linear guides were bolted to two 160mm-long, 20x20mm, aluminium struts (RS Pro) and fastened perpendicular to each other using a machined aluminium plate. The stepper motors were secured to each end of the bottom alloy strut, allowing the top rail to travel freely in x/y directions. A single-toothed rubber belt was used in a cross-configuration to transmit rotational motion of the stepper motors to linear motion of the stage. The substrate was secured to one end

FIGURE 3.4: Table correlating the translation directions of the automated stage to the rotation direction of the two stepper motors, labelled S1 and S2.

	S1	S2
+y	↻	↺
-y	↺	↻
+x	↻	↻
-x	↺	↺

	S1	S2
x/y	0	↺
-x/-y	0	↻
y/-x	↻	0
x/-y	↺	0

TABLE 3.1: Table of stepper driver inputs.

Input	Function
EN	Enable motor (high)
CW	Clockwise (high), anti-clockwise (low)
CLK	Low-to-high transition advanced motor one increment

of the top rail via a 3D-printed bracket. Figure 3.3 shows a CAD drawing of the assembly showing the belt drive and substrate positions.

The rotation of the stepper motors and the corresponding substrate translation is shown in Figure 3.4. Note, that in order to achieve translation purely in x or y, the steppers must rotate synchronously with the same angular velocity. A single step corresponds to a 1.8°rotation.

Stepper Motor Drivers

Each bipolar stepper was driven using a single-axis stepper motor driver (TB6560), which powers each of the coils in the motor. The drivers take three differential digital inputs: EN, CW and CLK (see Table 3.1), and are both powered using a 24V DC power supply. A single counter output, defined in the LabVIEW program, was supplied to both drivers simultaneously to synchronise rotations. The drivers were run in 1/8 step increments (0.225°rotation) which corresponded to a 25μm translation in x or y. Translation speeds in excess of 200mms^{-1} were attainable and with a resolution of 25μm, assuming no there were no missed steps.

Manual Control Unit

A portable unit was made for convenient control of the substrate position. The unit consisted of 5 button switches (4 directions and a start button) and a potentiometer for controlling the translation speed of the stage. The unit connected to the main relay board via a VGA connector and read as digital inputs to the DAQ card.

3.1.4 Thermal Control

Two heating elements (DBK HPOS-1/04/-24-20W) were used to independently control the printhead and substrate temperatures. The temperature of the elements is proportional to the electrical power supplied to them. Power was supplied to each element either by using a multi-channel power supply, or for full-automation, using a software controlled Pulse-Width-Modulation (PWM) set-up.

The temperature was measured using K-type thermocouples (Labfacility XE-3505-001) that were attached to the printhead sheath and printing substrate. The output of each thermocouple was amplified using an Analog Output K-Type Thermocouple Amplifier (AD8495, Adafruit) with built-in cold-junction reference. This amplified the output signal to $1mV$ per degree, well within the input specification of the DAQ. The expected voltage input range, which is supplied by the user, further increased the DAQ's sensitivity as the expected voltage is evenly split by the 16-bit ADC. For normal operating conditions of 15°C to 90°C, this corresponds to a sensitivity of:

$$\frac{0.9V - 0.15V}{2^{16}} = 11.4\mu V\,,$$

PWM offers a robust and effective means of automating the power delivered to high-powered components such as heaters. PWM was implemented using a Proportional-Integral-Derivative (PID) control loop in LabVIEW. The analogue voltages of the thermocouples were inputs to the PID loop, which would then modulate the duty cycle of two pulse trains. A simple control circuit was designed to switch power on and off to each heating element according to the voltage level of the pulse trains. A temperature of ± 1°C of accuracy was achieved

using a hot-plate with $\pm 0.5°$as reference.

3.1.5 Visualisation

Two different optical arrangements were used for visualisation, one to image droplet generation and impact with the substrate, the other to visualise the droplet from underneath the substrate after printing.

High-Speed Shadowgraphy

High-speed shadowgraphy imaging was used to visualise droplet formation, drop flight and impact [7]. The high-resolution technique images the droplet's silhouette, requiring a back-light to function effectively. A phantom V12.1 high-speed camera with 12x zoom microscope lens attachment with a 150W high-powered halogen light source (OLS2, Thorlabs) was used. The light source was coupled to an optical fibre with a collimating lens attachment and was positioned behind the nozzle orifice in back-light configuration. The high-speed camera is capable of frame-rates in excess of 200,000fps. However, higher frame-rates result in reduced image resolution and require very short exposure times. Frame-rates in the range of 14,000 to 20,0000fps were generally found to give good image quality (important at high droplet velocities) without the need for excessively high-powered back-lighting. The high-speed camera can be triggered by a timing waveform generated by the DAQ, or by defining an image-based area/brightness threshold trigger.

Polarized Camera

For some studies, a colour CCD camera (DFK 23U618, The Imaging Source) was used to visualise a deposited droplet from below. In this configuration, a dual output optical fibre was connected to the halogen light-source, with the second fibre being used as top-down illumination of the sample. Figure 3.5 shows the optical arrangement used to view the droplet from underneath the substrate. A 9x microscope lens was attached to the CCD camera, which was positioned in a 30mm optical cage below the printing substrate. A 10x objective lens was then

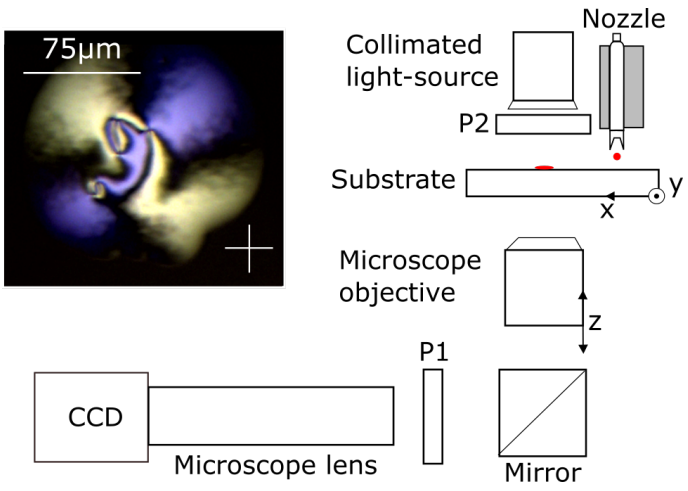

FIGURE 3.5: Optical arrangement for viewing a polarised microscopy image of a droplet shortly after printing. The components P1 and P2 are linear polarisers in the crossed axes configuration. The inset shows a polarised microscopy image of a single nematic LC droplet deposited onto a glass substrate 200ms after printing and viewed between crossed polarisers.

positioned 10mm below the substrate. Polarisers were placed either side of the droplet with their axes of polarisation crossed so that the birefringence of the samples printed could be examined. Due to the positioning of the nozzle, direct deposition of the droplet could not be imaged. Instead, the microscope objective was placed at a distance of 15mm away from the nozzle (x direction in Figure 3.5). Droplets could be visualised shortly after printing as the substrate moved in the $+x$ direction. Using this arrangement, droplets could be viewed 150-300ms after deposition.

3.1.6 LabVIEW Program

The main steps of the printing program is shown in Figure 3.6. During stage 1, the user inputs key parameters for the printing process such as substrate speed, number of drops and the array pattern. The user can define a substrate moving pattern by inputting a series of coordinates. The substrate will then move sequentially to each coordinate at the speed selected by the user. There are two possible patterning modes. The first is an 'Arbitrary Pattern', whereby the user manually inputs all the coordinates defining the array to be printed. The second is a 'Repeated Pattern', where the user inputs a finite number of coordinates - defining a

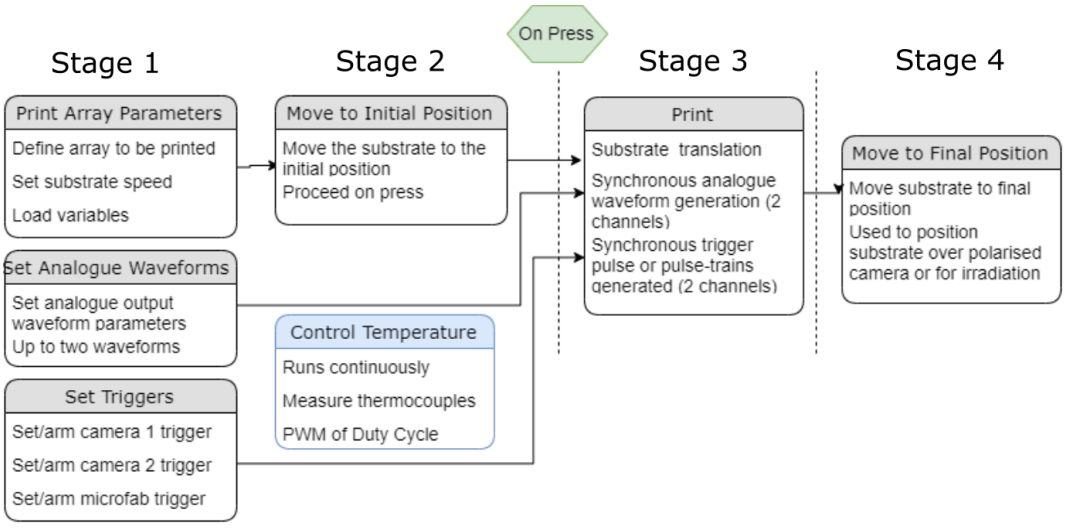

FIGURE 3.6: Schematic diagram of the different stages in the LabVIEW printing program.

particular series of translations, and the number of times this pattern will be repeated. The repeated pattern mode was particularly useful for producing larger, regularly repeating, arrays. After uploading the printing pattern, a line plot is generated for the user to verify before initiating the printing process. During stage 1, the user also defines (if used) the analogue output waveform characteristics and the timing of the trigger waveforms. The user panel for this process is shown in Figure 3.7.

During stage 2, the user moves the substrate to the initial position using the control unit. On depressing the 'start' button on the controller, stage 3 is initiated. The DAQ synchronously generates all the necessary outputs (see Table 3.2) and the print begins. Once the print has finished, stage 4 is initiated and the user has the option of manually moving the substrate to a final position. This function was particularly useful for the studies carried out in Chapter 7, where the substrate could be positioned underneath a UV light source.

Table 3.2 shows a list of the various digital and analogue inputs and outputs used in the printing rig. Careful design of the program was required in order to utilise the full functionality of the DAQ hardware which has a single digital to analogue converter. LabVIEW is not designed for software implementation such as the printing program presented, unless it is combined with supported hardware such as motion controllers and automated translation stages. However,

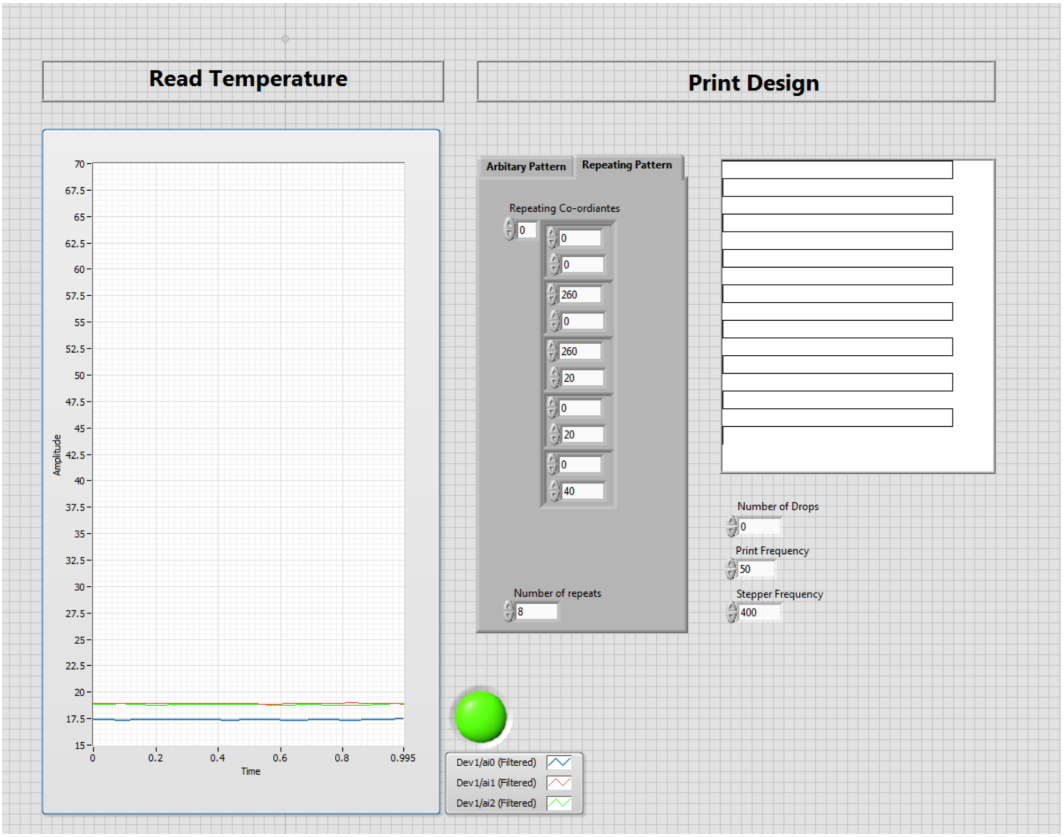

FIGURE 3.7: User interface for the controlling the printhead and substrate temperature(s) and defining the array pattern to be printed.

TABLE 3.2: Table of I/O to the DAQ.

No	I/O	Description	No	I/O	Description
1 (DO)	+5V	Supply line	13 (AI)	T1	Thermocouple 1 +
2 (DO)	CW1	Stepper 1 direction	14 (AI)	T1	Thermocouple 1 -
3 (DO)	CW3	Stepper e direction	15 (AI)	T2	Thermocouple 1 +
4 (DO)	EN1	Stepper 1 enable	16 (AI)	T2	Thermocouple 1 -
5 (DO)	EN2	Stepper 2 enable	17 (AI)	T3	Thermocouple 1 +
6 (DO)	CLK	Increment steppers	18 (AI)	T3	Thermocouple 1 -
7 (DI)	Lx	Limit switch x	19 (AO)	A1	Analogue waveform 1
8 (DI)	Ly	Limit switch y	20 (AO)	A2	Analogue waveform 2
9 (DI)	GO	Read start button	21 (DI)	+x	Direction button
10 (DO)	GO	Start signal	22 (DI)	-x	Direction button
11 (DO)	T1	Trigger 1	23 (DI)	+y	Direction button
12 (DO)	T2	Trigger 2	24 (DI)	-y	Direction button

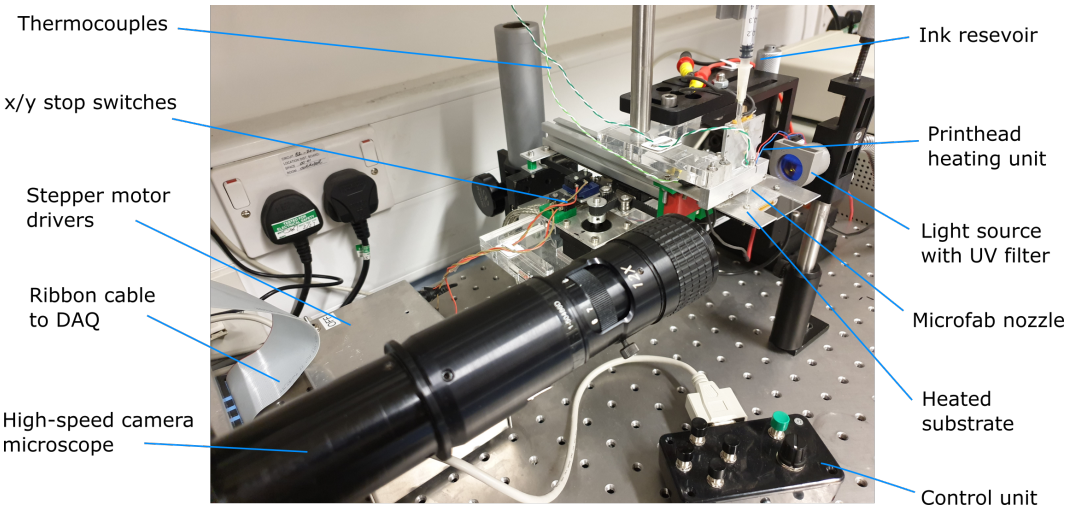

FIGURE 3.8: Photo showing the printing rig using the microfab nozzle.

TABLE 3.3: Composition of E7 [73].

Chemical Substance	Abbreviation	Ratio (%)
4-cyano-4'-n-puntyl-biphenyl	5CB	51
4-cyano-4'-n-heptyl-biphenyl	7CB	25
4-cyano-4'-n-oxyoctyl-biphenyl	80CB	16
4-cyano-4''-n-pentyl-p-terphenyl	5CT	8

due to the evolving nature of the project and the reliance on National Instrument hardware (DAQ), the decision was made to stick with LabVIEW. An image of the printing system with a single printhead in place is shown in Figure 3.8.

3.2 Materials

Two different commercially used nematic LCs developed by Merck have been used in this thesis: E7 and BL006. Both are examples of LC blends and consist of multiple constituent LCs of varying chain lengths. Combining these into a single blend results in improved stability of the nematic phase over an increased temperature range. Table 3.3 shows the chemical composition of E7. The exact composition of BL006 is unknown and is not disclosed by Merck. However, it consists of cyano-biphenyls and cyano-terphenyls LC components. Table 3.4 lists the relevant fluid properties for both LCs.

TABLE 3.4: Fluid parameters for the two LCs used in this thesis. Temperature is reported in °C. Surface tension measurements were made using the pendant drop method (see Section 3.3.2). Fluid parameters over a range of wavelengths and temperatures can be found in Appendix §A.4.1.

Parameter	T_{20}	T_{40}	T_{60}
E7			
ρ (g.cm^{-3})	1.03	1.02	1.00
σ (mN.m^{-1})	30.4	27.6	26
γ_1 (mPa.s)	252	73	20
n_o (λ = 589.3 nm)	1.522	1.524	1.543
n_e (λ = 589.3 nm)	1.747	1.712	1.651
BL006			
ρ (g.cm^{-3})	1.05	1.02	1.00
σ (mN.m^{-1})	36.4	36	34.2
γ_1 (mPa.s)	426	142	50
n_o (λ = 589.3 nm)	1.529	1.526	1.524
n_e (λ = 589.3 nm)	1.814	1.794	1.776

UV-curable optical adhesives were frequently used in this thesis to form LC/polymer composites. The main adhesives used were the thiolene-based polymers NOA65 and NOA68, supplied by Norland. Both adhesives undergo a step-growth polymerization process when irradiated with UV light in the range of 350 - 380 nm (see Appendix §A.4.1). Table 3.5 lists important parameters for these materials.

3.3 Experimental Methods

3.3.1 Polarized Optical Microscopy

A polarized optical microscope (Olympus BX51-P) was used to take microscopy and polarised microscopy images. The microscope can be used in transmission or reflection mode. Unless specified, all microscopy images presented have been taken in transmission mode. In this mode, a halogen filament bulb provides illumination via a condenser and a removable and rotatable linear polariser before reaching the sample. A second rotatable polariser is positioned after the objective lens and before the eye-piece. The term 'crossed polarisers' describes the condition when the axis of each polariser are orthogonal to one another. This is the common configuration used to analyse LCs as only birefringent samples can

TABLE 3.5: Fluid parameters for the two optical adhesives used in this chapter. Surface tension measurements were made using the pendant drop method (see Section 3.3.2). Fluid parameters over a range of wavelengths and temperatures can be found in Appendix §A.4.1.

Parameter	**NOA65**	**NOA68**
$\gamma_{1\,T=20}$ (mPa.s)	1200	≈5000
$\gamma_{1\,T=40}$ (mPa.s)	400	1670
$\gamma_{1\,T=60}$ (mPa.s)	240	1000
$\sigma_{1\,T=20}$ (mN.m^{-1})	37.5	29-33
$\sigma_{1\,T=40}$ (mN.m^{-1})	33	29-33
$\sigma_{1\,T=60}$ (mN.m^{-1})	30.9	29-33
$\rho_{1\,T=20}$ (g.cm^{-3})	1.037	1.288
Refractive Index(589.3nm, 20°C)	1.524	1.54

be viewed through the objective lens. The direction of the polarization axes for each polariser is indicated in the figures presented by white arrows in the bottom corner of the image.

3.3.2 Pendant Drop Measurements

Surface tension and interfacial tension measurements were carried out using a FTA200 device from First Ten Angstroms. The device uses the pendant drop method which analyses the droplet shape based on the Young-Laplace equation:

$$\Delta P = (P_{int} - P_{ext}) = \gamma \left(\frac{1}{R_1} + \frac{1}{R_2} \right) , \tag{3.1}$$

where γ is the interfacial tension and R_1 and R_2 are the radii of curvature about orthogonal axes (see Figure 3.9). A microscope camera is used to image the shape of a droplet which is suspended from the tip of a thin needle, as shown in Figure 3.9a. This mode is used when the density of the fluid droplet is much larger than the density of the surrounding fluid, in this case air. The method assumes the droplet shape is determined by surface tension and gravity only, such that the pressure difference ΔP is given by:

$$\Delta P(z) = \Delta P_0 \pm \Delta \rho g z \, , \tag{3.2}$$

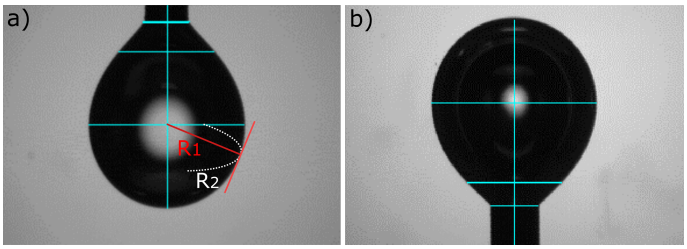

FIGURE 3.9: Images of a pendant drop of fluid using a normal (a) and inverted needle (b). The lines superimposed on the image are generated by the pendant drop software and are used to determine the radii of curvature.

where P_0 is the ambient pressure and z is the vertical distance from the dispensing tip. The shape of the droplet is fitted using the device's software. Equations 3.1 and 3.2 are used to determine the interfacial tension, requiring only the fluid density as an input. An inverted needle can be used to measure the interfacial tension between two fluids when the density of the fluid droplet is much less than the density of the surrounding fluid, as shown in Figure 3.9b.

It has been noted when the surface tension values quoted in this thesis have been measured using this device. It proved useful for measuring the surface tension for several of the fluids used in air. However, the method was not capable of measuring the interfacial tension between two liquids, for example a LC and prepolymer. From Equation 3.2, the change in density between the two fluids must be sufficient to cause a detectable change in curvature. In practise this was found to be $\approx$10% and thus the technique could not be used to measure the interfacial tension between liquids used in this thesis.

Contact Angle Measurements

The FTA200 device was also used to measure the contact angle of certain fluids. This is done by depositing a droplet of fluid onto a substrate and imaging the droplet profile. The software then measures the contact angle by fitting a spherical shape to the droplet profile. Although this device was used to measure the contact angle for some fluid/substrate combinations, the device was not situated in the same building as the printing rig. Fitting a spherical curve (using ImageJ software) to the microscope images taken using the high-speed camera produced

contact angles in good agreement and proved to be a more efficient in-situ contact angle measurement method.

3.4 Image Analysis Using Matlab

Several Matlab scripts were developed to automate the analysis of droplet generation and deposition. The scripts were used to determine key parameters such as droplet velocity, volume and deposited droplet diameter. The main functions and important steps of the commonly used scripts are described in the following sections.

3.4.1 Get Velocity, Get Volume

Key droplet parameters such as velocity and volume are used to assess the printability of a fluid. Maximum droplet velocity and volumes are observed when printing conditions such as printhead temperature, driving voltage and actuation waveform shape are optimised. Further, it is critical to determine the reproducibility of droplet volumes and flight-path, particularly in applications requiring uniform arrays of droplets to be deposited.

Inputs

The script analyses high-speed image files of the printing process. All images for a particular 'run' are captured using the same camera settings, camera position and identical back-lighting. In general, a run would consist of varying a single variable such as temperature, or looking at the distribution of droplet properties under constant conditions. To aid the analysis, image files are stored in a folder-tree structure. The parent folder will represent a single run and contains subfolders, each containing a sequence of high-speed images captured at a particular condition. The image files in each subfolder are stored sequentially in time and may contain many thousands of images.

In addition to the image files, the script requires the frame rate, pixel length and expected droplet diameter. The pixel length is determined by taking a calibration image for the particular camera arrangement of a 200μm scale-bar positioned at the nozzle. Under normal operating conditions, the droplet diameter is $\pm$10% of the nozzle orifice size (see §4.6), thus the nozzle orifice size is used as the expected droplet diameter.

Image Analysis Steps

Image analysis is carried out on each image in the subfolder. The steps are as follows:

1. Use the first image in the sequence as a base image. The first image shows the printhead before a droplet emerges from the nozzle. This is subtracted from all images in that subfolder.

2. The current image is converted to a binary image using a threshold value which is calibrated to the lighting conditions and camera settings of that particular run.

3. Remove null objects. Non-zero elements that are adjacent to one another are summed into objects. Any objects with an area much smaller, or greater than, the expected droplet diameter are removed.

4. Remaining objects are 'filled-in' using a standard MATLAB function.

5. The centroid, area, minor, and major axes length for the image are stored.

Figure 3.10 shows the above image analysis applied to a typical image of a droplet in-flight. If there are no objects present then a 'drop state' variable is set to zero, indicating there is no drop present. When a sequence of images shows the presence of an object in three sequential images, the 'drop count' variable is incremented by one. This allows the script to determine whether a droplet is present and count the number of droplets produced in an images sequence.

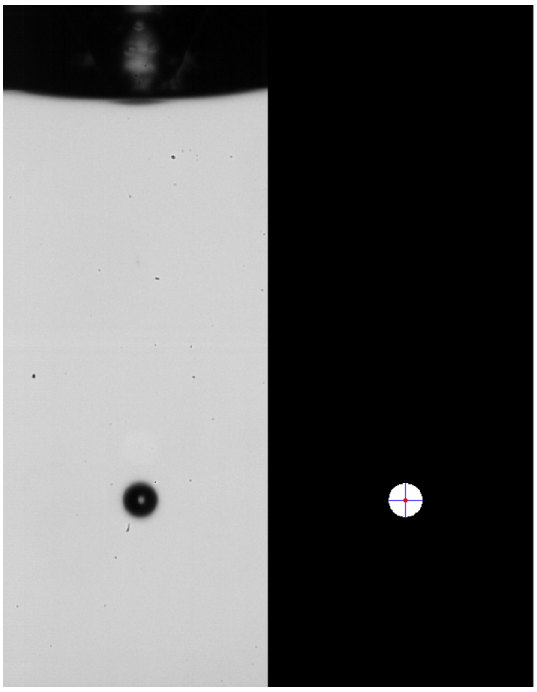

FIGURE 3.10: Images of the original high-speed image of a droplet being printed, with the corresponding processed image showing the centroid, minor and major axis.

Outputs

The script is run on the parent folder, storing the centroid, area, minor and major axis length in separate tables for each subfolder.

The output of the program is an $n \times 5$ table, with n equal to the number of subfolders. The columns are: Drop Volume, Drop Velocity, Jet Straightness and Drop Diameter. These are calculated using the object properties stored for each 'drop' in the image sequence for a subfolder. When there are multiple droplets detected in a subfolder, the columns represent average values.

The droplet velocity is taken in the y-direction only, i.e. vertical velocity and is calculated by tracking the centroid position over several frames. The jet straightness is taken as the horizontal difference between the center of the nozzle and the last horizontal position of a detected drop. It is noted that the program disregards the first three frames when an object is detected in a droplet sequence, as well as the last frame. The reason being, that the object properties may be distorted by the presence of a fluid tail, or by a portion of the droplet leaving the frame of the image.

Uncertainty and Error in Measurement

The program was tested against the microfab 'test jetting parameters' supplied with nozzle with almost perfect agreement[1]. The main source of error is resolution uncertainty. At high frame-rates, above 15,000fps, the camera operates at reduced resolution with typical images being 304x800 pixels. At high magnification, this gives a pixel length of 2μm. To reduce uncertainty, determination of the pixel length was done using a long calibration length of 200μm. With careful calibration an uncertainty of $\pm 1\mu$m, giving a relative uncertainty in the pixel length of 1%. The other source of uncertainty is in the conversion to a binary image. A typical droplet will occupy 40 pixels and one can assume an uncertainty of $\approx \pm 1$ pixel. This approximation can be validated by comparing the pixel values at the edge of the droplet to the binary image, in which there is a clear transition occurring over a single pixel. This gives a total relative uncertainty in droplet diameter (and velocity) of 3.5%, and an uncertainty in droplet volume of 10.7%.

3.4.2 Get Diameter of Sessile Droplets

A Matlab script was produced to assess the repeatability of the droplet wetting process, discussed in detail in Chapter 5. It's function is to determine the quality of the printed droplets and compare them to different printing substrates.

Inputs

The script reads in microscope images of the printed droplets once they have reached an equilibrium configuration. In addition, the script requires the pixel length and expected diameter. The pixel length is determined using a calibration image of a scale bar.

Image Analysis Steps

1. The microscope image is converted to greyscale.

[1] Microfab quoted a droplet diameter of 80μm using this fluid and jetting parameters, average over 100 droplets was found to be 80.8μm

2. Median-filtering of the greyscale image is carried out to reduce noise (see Figure 3.11a).

3. The image is converted to a binary using a threshold value which is calibrated to the individual image.

4. Canny edge detection is applied.

5. Remove null objects. Non-zero elements that are adjacent to one anotherare summed into objects. Any objects with an area much smaller, or greater, than the expected droplet diameter are removed.

6. Remaining objects are 'filled-in' using a standard MATLAB function.

7. The centroid, area, minor, and major axes length for the image are stored.

It is noted that additional image processing steps were used in this script as analyses a small number of images with a higher resolution.

Outputs

The script outputs an $nx4$ table with the following columns: Area, Centroid, Major Axis and Minor Axis length. Each row corresponds to a detected droplet. The average droplet diameter, standard deviation, average 'roundness' and 'roundness' standard deviation is recorded. The 'roundness' is taken as the percent difference between the major and minor axis lengths and can be used to approximate how circular the drops are.

Uncertainty and Error in Measurement

The microscope images are high-resolution - 1040x1392 pixels. One can assume a relative uncertainty of 1% due to calibration. An estimate of the uncertainty due to the binary image conversion and edge detection is again dependent on the magnification and size of droplet. However, by comparing the original pixel values to the binary pixel values of a typical droplet boundary, the uncertainty is approximated as ± 2 pixels at each edge. This gives a total uncertainty of $\approx 5\%$, which is indicated by the error bars in the Figures produced using this script.

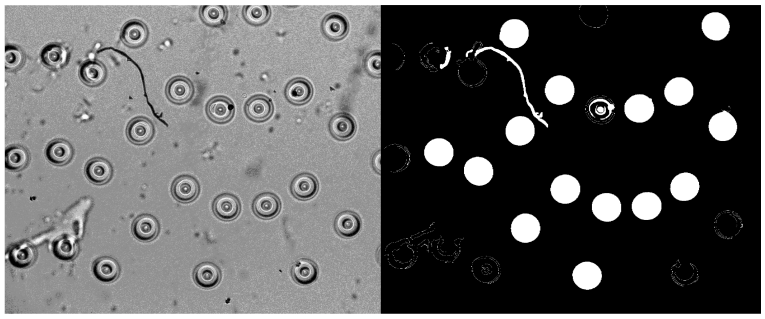

FIGURE 3.11: Images of the original gray-scale microscopy image of a printed droplet, with the corresponding processed image. This particular image was chosen as it represents a 'messy' image, with no single well-defined droplet boundary.

3.5 Conclusions

The design and build of the printing system was a key outcome of this project. The system developed proved a versatile and rugged tool for the inkjet printing of functional fluids. The system could accommodate precision engineered commercial nozzles, used for depositing precise amounts of LC or compatible polymers, or custom-made printheads for use with fast-drying solutions such as PVA. Small reservoir volumes of fluid and control of the nozzle pressure is achieved using mounted syringes. Multiple and arbitrary waveforms can be generated, giving full control over the actuation waveform. Combined with thermal control, visualisation of the printing nozzle and a high degree of timing accuracy, allows for fine tuning of the printing conditions, critical for reliably printing viscous and non-Newtonian fluids such as LCs and optical adhesives. Additional components such as a polarised camera and UV-curing light source can be integrated into the system. Although not fully exploited in this project, the printing system can accommodate synchronous use of multiple nozzles, making it a valuable tool for future researchers in this field. Common experimental methods such as polarised optical microscopy and the pendant drop method has been described. The main image analysis programs used to extract key droplet parameters from images taken both during the printing process, and after drop deposition, has been described in detail.

Chapter 4

Inkjet Printing of Nematic Liquid Crystals

This chapter presents an analysis of droplet generation from a piezoelectric DoD inkjet nozzle using a nematic LC ink. The relationship between the actuation waveform and the resulting acoustic pressure wave is described. The process of thinning, pinch-off and break-up of the resulting fluid ligament is then examined. Critical dimensionless parameters used throughout the studies described in this thesis are discussed, and a dimensionless operating space defined for the inkjet printing of LC inks. The procedure for determining the optimal printing conditions, such as printhead temperature and determining the appropriate actuation waveform, is detailed. The chapter considers a case study using the nematic LC E7, which is used extensively throughout this thesis. The same procedures described for optimising printing conditions in this Chapter were applied whenever confronted with printing a new LC or polymer formulation. Finally, critical droplet properties such as volume, velocity and accuracy of placement in relation to the printing parameters are measured for E7.

The main goal of this chapter is to lay an experimental framework and understanding that facilitates the successful inkjet printing of a range of different LC-based inks used throughout this thesis, and which may also be of benefit when considering the inkjet printing of other viscous and non-Newtonian fluids.

4.1 Introduction

The first example of inkjet printing a LC that is documented in the literature was for the rapid production of tertiary libraries of LC formulations [74]. Most LCs used in displays consist of multiple components and the exact composition of the LC is tailored to the specific display. Inkjet printing was used to deposit precise volumes of a particular LC component to speed the rate of LC formulation creation and testing, whilst using minimal amounts of LC. Another example utilising the precise volumes produced by inkjet printing, was a report by Alino et al. who demonstrated the fabrication of nematic LC dispersions with homogeneous droplet diameters by inkjet printing [26]. A nematic LC was inkjet printed onto a pretreated substrate before then rinsing the substrate with a Polyethylenimine solution, thereby releasing the droplets into a dispersion.

A well-aligned chiral nematic LC has a photonic band-gap which, when doped with an appropriate fluorescent dye, can produce band-edge lasing [75]. This has been exploited to form optically-pumped thin film lasers by inkjet printing a dye-doped chiral nematic LC onto prepared substrates [29]. Chiral nematic LCs has also been used for printable optical time-temperature sensors which, when combined with embossing at high temperatures, undergo an irreversible reflected colour-shift [28]. In a similar manner, a polyermisable H-bonded chiral nematic LC formulation has been printed to produce thin-film humidity sensors [28].

A LC elastomer is a slightly cross-linked LC polymer network which can act as electrical or light-responsive micro-actuator [76]. The inkjet printing of elastomer LC materials containing photoisomerizable azobenzenes has been used to develop light sensitive artificial cilia [30]. Since then, the 3D and 4D printing (a term used to describe the printing of stimuli-responsive materials) of elastomers has been demonstrated, although this uses extrusion printing rather than inkjet printing due to the high viscosity of the elastomer materials [77, 78].

A fundamental, and often over-looked, requirement in the studies referenced above, is reliably generating uniform droplets of LC. Difficulty in generating well-defined droplets by printing is often alluded to in the studies. However, the

processes taken to successfully and accurately print LCs is not discussed. Researchers looking to utilise inkjet printing are required to re-navigate the challenges of inkjet printing LCs, which are often highly viscous and non-Newtonian. This lack of understanding can lead to a belief that a fluid is incompatible with inkjet printing, when a more rigorous investigation of the printing conditions may in fact lead to reliable droplet generation.

4.2 Experimental

The inkjet printing system described in Chapter 3 was used to carry out the studies presented in this Chapter. The experimental configuration used is shown in Figure 4.1. The MJ-ABP-01-80 dispenser (Microfab ®) with an 80 μm nozzle diameter was used to generate LC droplets. The nematic LC chosen for this study was the nematogen mixture, E7 (Synthon Chemicals GmbH & Co.KG). This nematic LC was chosen as its macroscopic physical properties, such as the refractive indices, elastic and viscosity coefficients, are well-documented. E7 is also liquid crystalline at room temperature and, importantly for assessing the effect of printing conditions, the isotropic phase ($T_c = 58$°C) is readily accessible with the heating element fitted to our printhead (see Section 3.1.1). Furthermore, E7 was the LC used in the majority of the work presented in this thesis.

4.3 Drop Actuation

In DoD inkjet printing, a droplet of fluid is ejected via a pressure impulse in the printhead chamber. A schematic of the printhead used is shown in Figure 4.2. The pressure impulse is induced via piezoelectric deformation of an annular piezoelectric element bonded to a glass tube. The annular piezoelectric element consists of an outer and inner electrode which is used to generate an electric field across the piezoelectric material. When this electric field is applied, it causes the piezoelectric element to expand or contract radially. The rated operating conditions and recommended range of viscosity and surface tension values for printable fluids using the microfab nozzles is shown in Table 4.1.

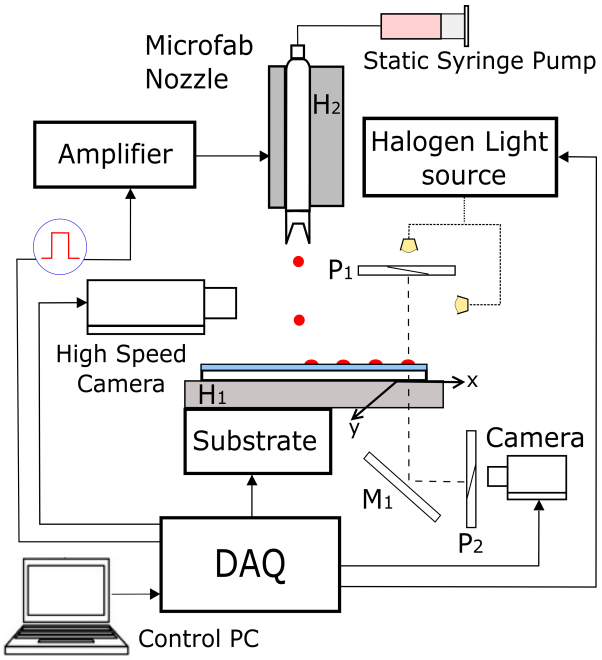

FIGURE 4.1: A schematic showing the experimental apparatus used to print the nematic LC onto a range of different substrates. P_1 and P_2 are linear polarisers, M_1 is a mirror and H_1 and H_2 are the substrate and nozzle heating elements, respectively.

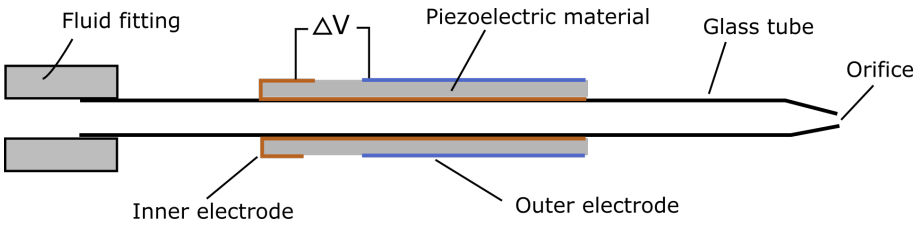

FIGURE 4.2: Schematic of a microfab dispensing device where ΔV is the voltage applied across the piezoelectric electrodes.

TABLE 4.1: Specification table for the MJ-AB microfab dispenser.

Property	Operating Range
Orifice diameter	80 μm
Max Operating Temperature	65°C
Droplet volume (avg)	270 pL
Fluid viscosity	3-20 cPs
Fluid surface tension	20-70 dynes/cm
Fluid pH	2-11

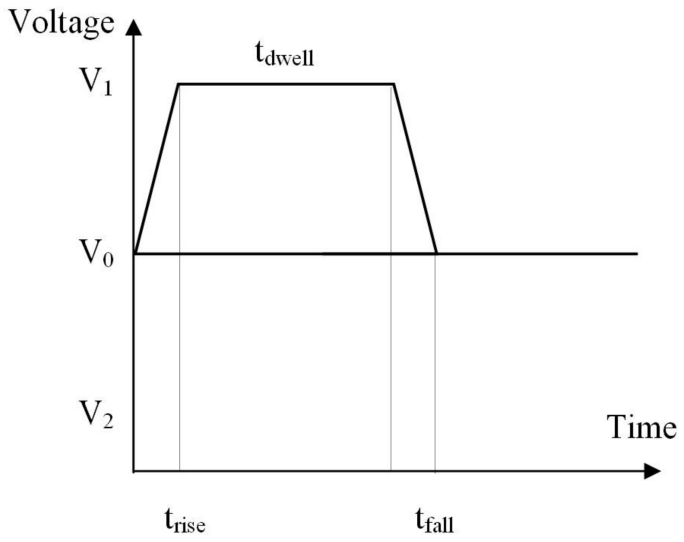

FIGURE 4.3: A simple trapezoid waveform used to actuate drop formation showing the actuation voltages V_1, the rise time t_{rise}, dwell time t_{dwell} and the fall time t_{fall}.

4.3.1 Actuation Waveform

The simplest drop actuation waveform is a trapezoid shown in Figure 4.3. One of the electrodes is grounded ($V_0 = 0$), whilst the other is connected to an amplifier supplying the waveform. The time taken to increase the voltage from V_0 to V_1 is called the rise time, t_{rise}. The dwell time, t_{dwell}, is the time the voltage is held at V_1. Finally, the fall time, t_{fall}, is the time taken for the voltage to return back to V_0. Depending on the polarity of the electrodes/waveform, the piezoelectric actuator can undergo either radial contraction or radial expansion, which happens during ΔV - the rise and fall times. Thus the ink is accelerated during the rise/fall times of the driving waveform.

For simplicity, no frequency dispersion or losses in the pressure wave will be assumed in the following discussion. To separate the effects of contraction and expansion of the printhead chamber, a waveform with a long t_{dwell} is supplied to the printhead, as shown in Figure 4.4a. A positive ΔV results in fast radial expansion of the printhead chamber during t_{rise}. This produces a negative pressure impulse at the point of the perturbation, shown in diagrammatically in Figure 4.4b. This creates two negative pressure waves which propagate in opposite directions

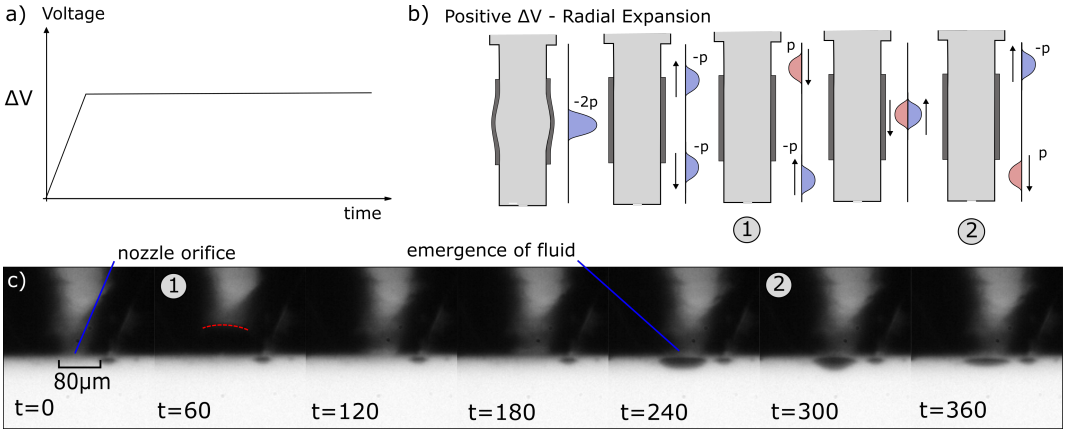

FIGURE 4.4: a) Driving waveform with used to induce radial expansion of the printhead chamber. b) Schematic representation of the pressure wave propagation inside the printhead chamber, where $2p$ is the amplitude of the pressure wave resulting from the initial piezoelectric deformation. c) Resulting high-speed images (16,831 fps, 8 μs exposure) captured using E7 LC. The driving waveform used had an amplitude of 53 V with t_{rise}=3 μs and t_{dwell}=1 s. The printhead temperature was 60°C. The numbers at the bottom of the frames indicate the time in μs since the arrival of the driving waveform.

in the printhead chamber and with half the amplitude of the initial pressure impulse. The arrival of the negative pressure wave can be seen in the high-speed image, labelled 1 in Figure 4.4c. The fluid meniscus at the orifice is seen to rise, indicating a negative pressure at the nozzle. This is also referred to as pull-action or pre-fill, as the negative pressure pulls fluid from the ink reservoir to fill the nozzle [79].

There are two boundary conditions to consider as the waves propagates inside the printhead chamber, one at the ink supply end and the other at the nozzle orifice. An open-ended boundary condition can be assumed between the ink supply and fluid chamber due to the significant enlargement of the diameter [80]. The negative pressure wave encountering this boundary will be reflected and experience a π-phase shift, resulting in a positive wave of the same amplitude and speed travelling towards the nozzle orifice. The arrival of this pressure wave is indiscernible in the high-speed images in Figure 4.4c. However, a pressure wave is seen to arrive at t$\approx$300 μs. This positive pressure wave is due to the decharging of the piezoelectric element and the resulting relaxation of the printhead chamber.

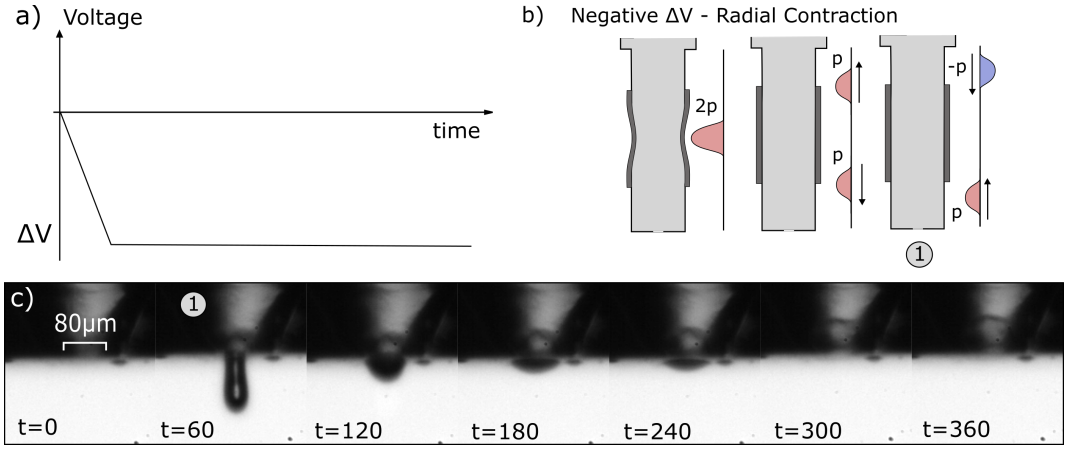

FIGURE 4.5: Driving waveform used to induce radial contraction of the printhead chamber. b) Schematic representation of the pressure wave propagation inside the printhead chamber where $2p$ is the amplitude of the pressure wave resulting from the initial piezoelectric deformation. c) Resulting high-speed images (16,831 fps, 8 μs exposure) captured using E7 LC. The driving waveform used (a) had an amplitude of -53 V, t_{rise}=3 μs andt_{dwell}=1 s. The printhead temperature was 60°C. The numbers at the bottom of the frames indicate the time in μs since the arrival of the driving waveform.

The nozzle orifice can be modelled as a closed boundary due to the significant reduction in diameter between the fluid chamber and the orifice. The wave encountering this boundary will be reflected without a phase shift, resulting in a negative pressure wave of the same amplitude and speed travelling toward the ink supply end. This happens during t_{dwell}, in which there is no further displacement of the piezoelectric actuator (assuming there are no residual oscillations resulting form the initial displacement, or de-charging of the piezoelectric element).

Radial contraction of the printhead chamber can be induced using a waveform of equal amplitude but opposite polarity, as seen in Figure 4.5a. This produces a positive pressure wave which reaches the nozzle orifice, indicated by number 1 in Figure 4.5b. The pressure produced during the radial contraction produces a fluid ligament to emerge from the nozzle orifice, as seen in the high-speed images shown in Figure 4.5c. If the positive pressure p is sufficient in amplitude then then a droplet will be generated (see Section 4.4). However, this positive pressure wave will be followed by a second pressure wave resulting from the second reflection caused by the fluid inlet. This may result in secondary drop formation or reduce the maximum print frequency attainable.

4.3.2 Optimum Trapezoid Waveform

There exists an optimum time, t_{dwell}, which is tuned to the acoustics of the printhead and fluid used [80]. Figure 4.6a shows a schematic illustration of such a waveform and the associated pressure wave propagation inside the printhead chamber. If the radial contraction of the printhead chamber (stage 4 on the figure) coincides with the arrival of the reflected pressure wave produced by the initial radial expansion, then a large positive pressure wave of amplitude 2p is produced which travels towards the nozzle orifice. Simultaneously, the residual negative pressure wave travelling towards the fluid inlet is effectively cancelled out by the positive pressure wave produced during the radial contraction. This results in a large positive pressure wave which travels toward the nozzle orifice, whilst the secondary pressure perturbations are cancelled out. In practise, this kind of waveform optimisation is often used to produce larger droplet velocities and volumes for a given waveform amplitude and remove the possibility of secondary droplets being produced. The experimental procedure for determining the optimum dwell time is described in section 4.6.2.

Figure 4.6b shows high-speed images of E7 being printed using a 18 μs dwell time. The high-speed images show the arrival of the 'pre-fill' negative pressure wave (number 3) and the large positive pressure wave producing the fluid jet (number 6). In addition, after the actuation pressure wave which produced the fluid jet is reflected and π-shifted at the fluid inlet, it arrives as a negative pressure wave at the nozzle ($t \approx 180$ μs) and serves to pull a portion of the fluid back into the nozzle. This has the effect of decreasing the length of the fluid jet produced and reduces the likelihood of satellite droplet formation (see Section 4.4.2).

The analysis assumes that no energy dissipation in the fluid, and perfect acoustic reflections. In practise, there will be energy losses due to viscous damping, non-ideal reflections and dissipation of the acoustic wave. Despite this, the analysis gives a good insight into the physical mechanisms involved in drop formation and the importance of the actuation waveform.

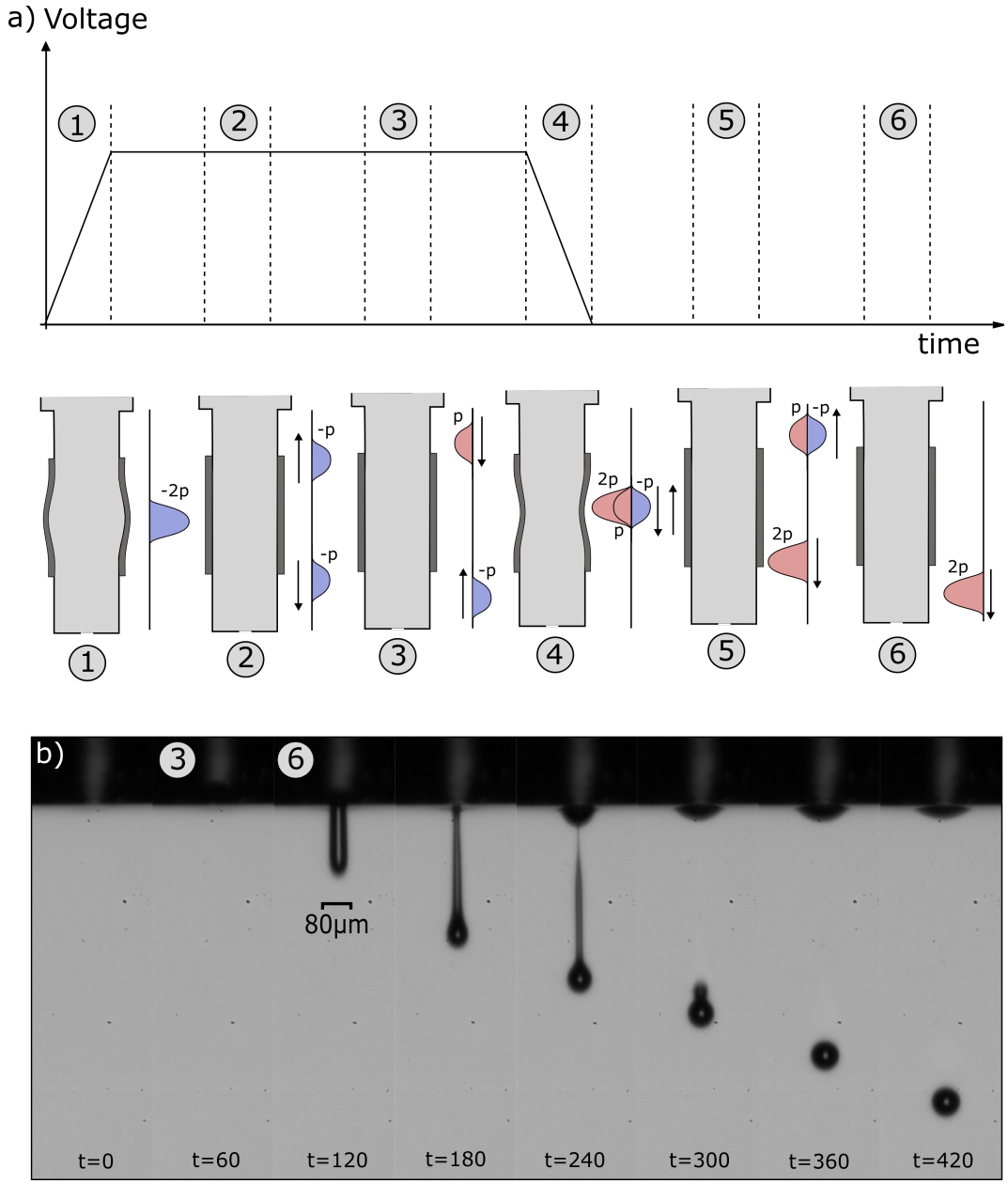

FIGURE 4.6: a) A diagram showing an optimum actuation waveform and the associated expansion and contraction of the printhead chamber. The numbers correlate the points in the driving waveform with the pressure waves inside the printhead and the high-speed images of drop formation. The waveform is timed such that a positive pressure wave of amplitude 2p arrives at the nozzle orifice shown by number 6 in the figure. b) High-speed images of the printing of E7 using the 80 μm microfab nozzle, heated to 60°C and using waveform W1.

4.4 Drop Formation

In order for a droplet to be produced in DoD printing, a fluid jet of sufficient length and velocity must be produced at the nozzle orifice. The jet is generated by a positive pressure wave arriving at the nozzle orifice. This column of fluid then undergoes thinning and pinch-off, driven by surface tension forces, producing single or multiple droplets.

4.4.1 Nozzle Pressure

A simple analysis can be done to estimate the pressure required to produce a column of fluid at a given velocity and of the same dimensions as the nozzle diameter [80]. It is reasonable to assume that the meniscus velocity at the nozzle boundary gives an approximate velocity of the droplet ejected. In reality, viscoelastic, anisotropic flow profiles and surface tension forces will also influence the velocity, but in relation to the contributing forces, this approximation is valid. The pressure at the nozzle has to overcome viscous, inertial and surface tension forces. Applying Bernoulli's Principle at the nozzle exit and assuming steady flow, we can estimate the steady pressure required to balance inertial forces of the fluid:

$$p_b = \frac{1}{2}\rho u^2 \,, \tag{4.1}$$

where u is the meniscus/drop velocity and ρ is the fluid density. However, an initial force must be applied to the fluid to accelerate it to this velocity. This can be approximated by applying Newton's 2nd Law to give the unsteady contribution of pressure:

$$p_i A_n = m\frac{du}{dt} \,,$$

where A_n is the cross-sectional area of the nozzle orifice. Estimating the volume of the fluid column to be: $A_n N_d$, where N_d is the nozzle diameter (the length of the fluid column must be at least as long as the drop diameter), this can be rearranged to give:

$$p_i = \rho N_d \frac{du}{dt} \,, \tag{4.2}$$

In this equation the acceleration of the drop, $\frac{du}{dt}$, can be approximated to occur during the rise time (3μs) of the driving waveform. There will also be a pressure induced at the nozzle exit due to interfacial forces within the fluid, known as the capillary pressure. This pressure difference can be expressed by balancing surface tension using the Young-Laplace equation:

$$p_c = \frac{2\sigma cos\theta}{r}\,, \tag{4.3}$$

where σ is the surface tension of the fluid and r is the radius of the capillary tube. Applying this to the nozzle orifice, the capillary pressure becomes:

$$p_c = 4\frac{\sigma cos\theta}{N_d}\,, \tag{4.4}$$

where the contact angle θ is the angle between the nozzle orifice and the free surface of the fluid. Note that $cos\theta$ will be approximately 1 as the nozzle can be assumed to be completely wetted during operation. Finally, the pressure contribution of viscous forces can be calculated by assuming a Poiseulle flow through the nozzle:

$$p_v = \frac{8\pi v N_D \eta}{A_n}\,, \tag{4.5}$$

where η is the dynamic viscosity of the fluid. The total nozzle pressure required to generate a droplet at a given velocity is then:

$$p_t = p_b + p_i + p_c + p_v\,. \tag{4.6}$$

To produce a droplet of E7 travelling at 3 ms^{-1} and using the values listed in Table 3.4, on page 48, for E7 LC at 20°C, the pressure contributions are as follows: $p_b \approx$ 0.05 bar, $p_i \approx 0.8$ bar, $p_c \approx 0.015$ bar and $p_v \approx 3$ bar. This gives a total pressure requirement of approximately 3.8bar. Almost 80% of the pressure requirements is attributed to the viscous pressure, indicating that viscous resistance will be the greatest hindrance to droplet generation. Repeating the calculation for E7 at 60°C, the total pressure drops to 1.8 bar, of which half is attributed to viscous pressure.

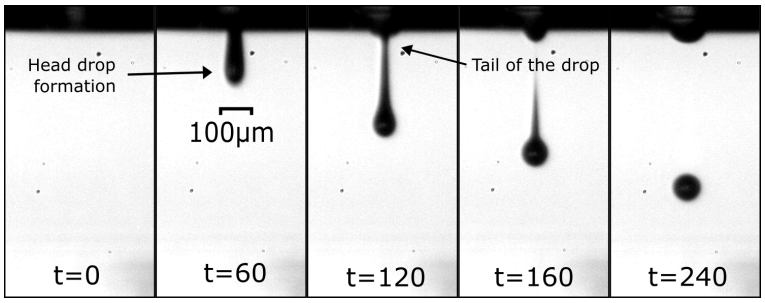

FIGURE 4.7: Sequence of high-speed images showing jet formation and pinch-off for E7 LC where t is the time in μs since the arrival of the actuation waveform. The jet pinches off at a single point indicated in the figure and results in a single well-defined droplet. The driving waveform used was W1 (see Table 4.3) and the printhead temperature was 60°C.

4.4.2 Jet Formation and Pinch-off

Figure 4.8 shows high-speed images of the break-up of a fluid jet, forming a single well-defined droplet of fluid. The waveform used was the optimised waveform 'W1', the details of which are shown in Table 4.3. The initial fluid pushed out of the nozzle forms a round leading edge. As the pressure decreases at the nozzle orifice, so does the liquid flow rate and velocity. The difference in this velocity is what causes the fluid jet to elongate as the head of the droplet separates from its tail. This fluid jet then undergoes thinning and break-up to form an individual droplet. The driving force behind thinning of the fluid ligament is the capillary pressure.

For droplet generation, the speed at which the jet thins must be fast enough compared to the fluid velocity to induce pinch-off whilst the jet still has sufficient momentum. The speed at which the jet of fluid thins is defined as the capillary velocity U:

$$U = -\frac{dR}{dt}, \tag{4.7}$$

where R is the radius of the fluid jet. The capillary pressure (Equation 4.3) is dependent on the surface tension and the radius of curvature $(1/R)$. As regions of the fluid jet undergo thinning, additional curvature is induced which further increase the local capillary pressure. Thus, pinch-off will occur first at the point of highest curvature of the fluid jet. For the high-speed images shown in Figure 4.8, this is seen to occur just before t=160 μs.

The thinning of the fluid jet is opposed by the viscous, inertial and elastic forces. Most often, there is a dominant force opposing the thinning velocity resulting in either viscous, inertial or elasticity controlled thinning. The magnitude of these forces is dependent on the fluid properties and the dimensions of the jet. A jet of fluid may experience inertial, viscous and elasticity controlled thinning throughout its evolution.

Satellite Drop Formation

For most applications, including those discussed in this thesis, it is critical that only a single drop is generated. Additional droplets can be generated if there are multiple pinch-off points on the droplet tail. These are called satellite droplets and can be seen in Figure 4.8. The first and largest satellite drops are produced by the tail of the jet labelled tail drop formation in the figure. This type of satellite droplet is common due to the high radius of curvature at the point where the tail meets the droplet head. Smaller satellites can also be produced when spontaneous capillary instabilities occur in the tail of the droplet, seen at t=360 μs in the Figure 4.8.

Satellite drop formation can be suppressed by reducing the length of fluid jet, using high viscosity fluids or decreasing the surface tension of the fluid via the use of surfactants [80]. Often the fluid parameters of the ink are fixed. In which case, the best solution is to reduce the driving voltage, reducing the droplet velocity and resulting tail length. Another solution is to use an optimum waveform which acts to pull a portion of the droplet tail back into the nozzle.

4.5 Dimensionless Analysis

Dimensionless analysis offers valuable practical insight into the thinning mechanisms driving pinch-off and eventual droplet generation. The set of dimensionless numbers below can be used to characterise the behaviour of liquid jets and drops:

$$Re = \frac{\rho U L}{\eta}, \tag{4.8}$$

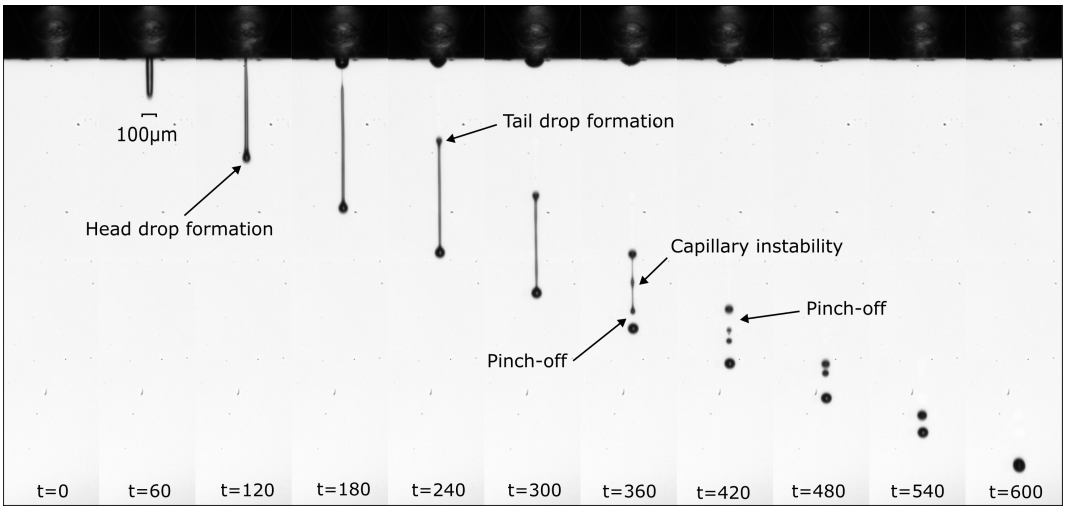

FIGURE 4.8: Sequence of high-speed images showing jet formation and multiple pinch-off points for E7 LC. The jet pinches off at six different points along the fluid ligament resulting in multiple droplets that eventually coalesce to form a single drop at t = 600 μs. The printhead temperature was 60°C and the driving waveform used was W1, but with an increased amplitude of 64 V.

$$We = \frac{\rho U^2 L}{\sigma}, \tag{4.9}$$

$$Oh = \frac{\eta}{\sqrt{\sigma \rho L}} = \frac{\sqrt{We}}{Re}, \tag{4.10}$$

where ρ is the density of fluid, U is the velocity, σ is the surface tension, η is the dynamic viscosity and L is the characteristic length scale. Unless otherwise stated, the velocity U is the fluid velocity of the jet, whilst the characteristic length scale, L, is the diameter of the jet. The Reynolds Number (Re) gives a balance of the inertial and viscous forces. The Weber number (We) gives the balance of inertial to surface tension forces.

The Ohnesorge Number, Oh (Equation 4.10), gives the balance of viscous to surface tension forces and is independent of the fluid velocity. Wolfgang von Ohnesorge, whom the number is named after, developed it to identify distinct regimes of jet break-up [81]. An alternative interpretation of the number is that of a ratio between interfacial and viscosity controlled thinning velocities. Large Ohnesorge numbers ($Oh >\approx 1$) indicate systems dominated by viscous forces,

TABLE 4.2: Table showing the dimensionless values encountered during the IJP of E7 using the 80 μm nozzle.

	Re	*We*	*Oh*	*Z*
Max	22.4	54	0.56	3
Min	2.3	2	0.33	1.8

whilst low Ohnesorge numbers ($Oh <\approx 0.1$) indicate systems dominated by surface tension. In an overly viscous dominated system, the thinning of a fluid ligament is impeded to such a degree that a drop is not generated, or that viscous dissipation inside the nozzle is so large that a fluid jet does not emerge in the first place [82]. In this case, the thinning of the jet is not fast enough for pinch-off to occur whilst the jet has sufficient momentum. The jet lacks either, or both, the inertial and surface tension energy to produce a droplet. In a system dominated by surface tension forces, the thinning velocity is sufficient for the jet to break up into multiple satellite droplets during the life-time of the fluid jet.

Over the evolution of the drop formation process, the velocity and characteristic length scale will change, particularly during pinch-off and drop impact. If the values used represent the initial characteristics of the jet, the dimensionless numbers are 'global values'. There term 'local values' is given to dimensionless numbers that represent a discrete point in time. Although global values represent the initial configuration only, they are the most practical values to measure and a good prediction of the behaviour of the jet and the regimes likely to be encountered. Global minimum and maximum values that resulted in droplet generation using E7 and the 80μm nozzle are shown in Table 4.2:

4.5.1 Printing Regime

Fromm was the first to use the Ohnesorge Number, *Oh*, to characterise regimes specific to IJP [216]. The parameter $Z = 1/Oh$ was introduced to characterise either a no drop scenario (small Z values) or multiple satellite droplets being formed (large Z values). A number of different values for Z which result in drop generation have been proposed, via simulation or experimentally, for a range of

fluids from ethanol, dilute polymers and particulate suspensions [83, 84, 85]. Albeit with some discrepancies, a range of $10 > Z > 1$ is agreeable for many different inks [85]. However, Z takes into account only the geometry, density, surface tension, viscosity of a fluid and is independent to the velocity of a fluid. Although highly transferable for Newtonian inks, this makes the printing regimes proposed quite specific to the inks used. Given the non-Newtonian, visco-elastic and anisotropic properties of LCs, it is likely that the range of Z values for LCs will be somewhat different. Nevertheless, it gives a good initial indicator as to the operating space likely to be encountered given the printing conditions selected. Figure 4.9 shows the printing range where the horizontal black lines represent the bounds quoted above.

The Ohnesorge number can be used to assess the printability of a fluid. However, it does not take into account the fluid inertia required to overcome the nozzle pressure (see Equation 4.6). Duineveld proposed a mimium Weber number of $We > 4$ required to overcome specifically the capillary and Laplace pressures [86]. This corresponds to a diagonal line indicating insufficient energy for droplet formation in Figure 4.9. Another bound to the printing regime can be found by considering drop impact and the critical threshold above which splashing occurs. The work by Stowe and Hadfield proposed that splashing occurs when $We^{1/2}Re^{1/4} > 50$ [221] (see §5.2.1 for a more in-depth discussion of drop impact). Together these boundaries can be used to define a general printability regime shown in Figure 4.9 [82].

The dotted lines superimposed onto Figure 4.9 represent the limiting dimensionless values shown in Table 4.2. The red lines represent Oh and Re numbers which resulted in a no drop scenario, whereas the dotted blue lines represents the maximum Oh and Re value achievable given the maximum operating temperature of the printhead and the maximum droplet velocity observed before satellite droplet formation ($v \approx 6$ ms^{-1}). Satellite droplets were only observed at elevated driving voltages (V > 63V), which corresponds to the bottom right corner of the printable region (coloured green in the figure). The printing regime presented is a good indicator of the expected behaviour of other LC-based inks used in this thesis such as BL006. For example, the nodes (indicated by the green circles on

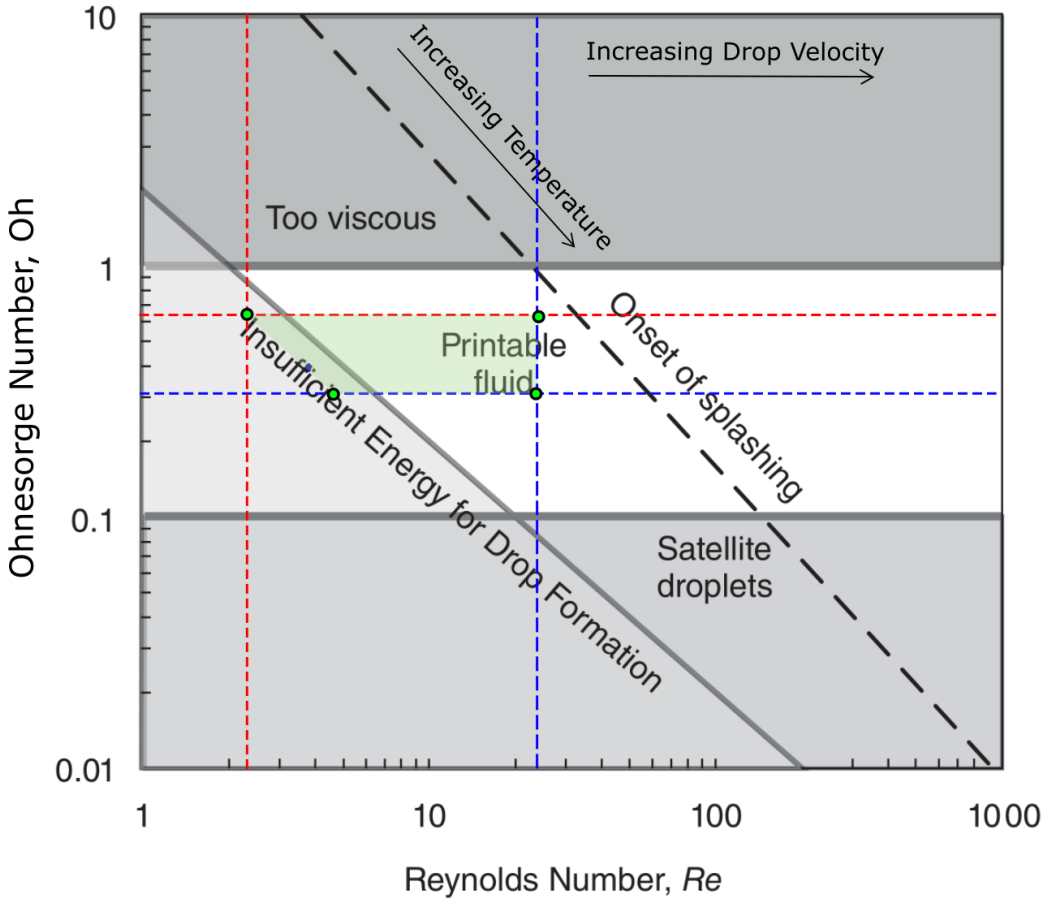

FIGURE 4.9: Inkjet printing parameter space using the Ohnesorge and Reynolds numbers. The green coloured area shown in the figure is the printable regime defined for E7 LC using an 80μm microfab nozzle. Figure is adapted from Derby, 2011 [85].

Figure 4.9) are shifted in the negative x and positive y direction due to the increased viscosity of BL006, indicating that sufficient kinetic energy will be the most difficult barrier to printing.

4.5.2 Effect of Temperature

Changing the printhead temperature enables some control over the surface tension and viscosity of the LC ink. The surface tension of a LC is dependent on the director profile at the air interface. The LCs used in this thesis form a homeotropic boundary with air. The surface tension measured using the pendent drop method (see §3.3.2) was also measured in air and indicated a reduction of only 4.6 mNm^{-1} for E7 at 20 and 60°C (15% reduction). As described in §2.4, the viscosity of a nematic LC is coupled to the direction of flow and dependent on the director profile. This makes a complete analysis of the effect of viscosity on the IJP of LCs exceedingly complex. However, broadly speaking the components of viscosity for a LC follow a typical Arrhenius relationship (see §2.4.1). Thus, increasing the temperature will bring about large reductions in viscosity compared to surface tension. Increasing the temperature decreases the Ohnesorge number, whilst increasing the Reynolds number, equivalent to travelling in a diagonal downward direction in Figure 4.9.

Figure 4.10 shows high-speed images of droplet formation for a printing temperature (T) of 50, 60 and 70°C. The Ohnesorge numbers are indicated on the figure. Figure 4.10a corresponds to the limiting cases where the fluid is too viscous to print (top bound on Figure 4.9). On the other hand, Figure 4.10c corresponds to a limiting case where satellite droplet started to form (bottom bound on Figure 4.9). It is noted that the temperature could not be increased past 70°C due to the maximum operating temperature of the printhead.

4.6 Printing Parameters and Droplet Properties

Once a fluid is deemed printable, droplet properties such as volume, velocity, jet straightness, and repeatability are critical in IJP applications. These parameters

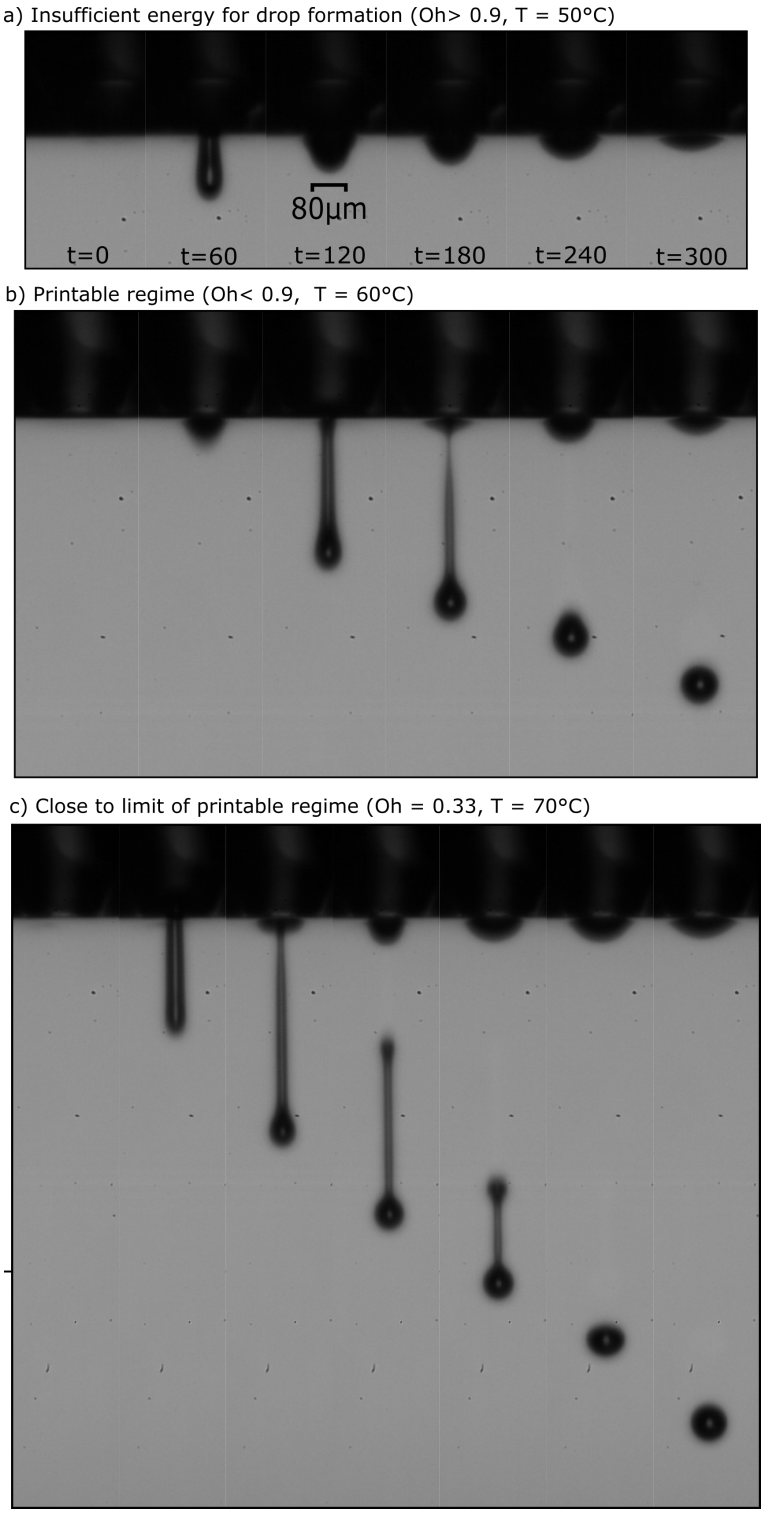

FIGURE 4.10: High-speed images (16,831 fps, 8 μs exposure) of drop formation of E7 LC, using the 80 μm microfab nozzle. a), b) and c) were all produced using waveform W1 but with different printing temperatures indicated on the figure, t is the time in μs since the arrival of the actuation waveform.

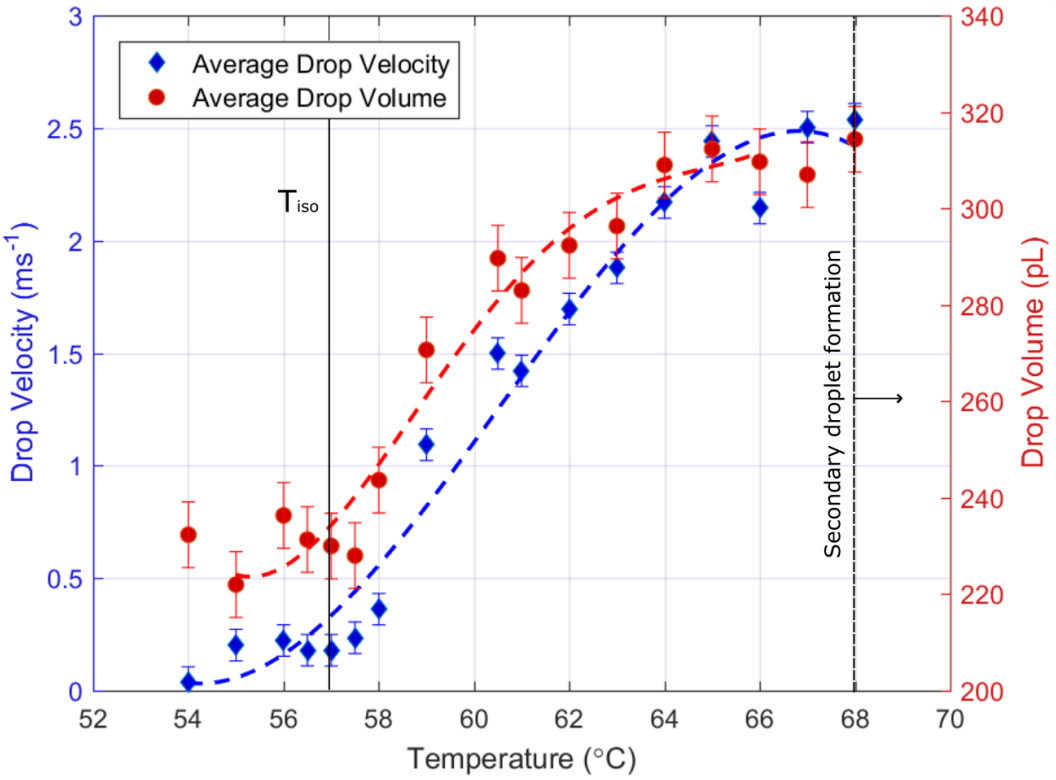

FIGURE 4.11: Graph showing drop volumes and velocities over a temperature range for E7. The waveform W1 was supplied to an 80 μm nozzle. The isotropic temperature and the temperature above which satellite droplets formed is indicated on the figure.

are also used to determine optimum waveform characteristics and printing conditions. The main printing variables affecting droplet properties are the printhead temperature, driving voltage amplitude and the dwell time [80]. The aim of this section is to discuss the effect these parameters have on the droplet properties. The findings form a basis for inkjet printing other LC and polymer formulations presented in the chapters to follow.

4.6.1 Printhead Temperature

As discussed, the printhead temperature is the most significant variable effecting the printability of a LC. Figure 4.11 shows a graph of the effect of printhead temperature on droplet velocity and volume using waveform W1 and E7 LC. At each temperature, the average velocity and volume of 10 consecutive drops, printed at a frequency of 50 Hz, was extracted using the MATLAB program described in §3.4. The diameters and velocities of the 10 drops printed at each temperature

were highly mono-disperse, with a standard deviation in velocity and volume of 0.03 ms^{-1} and 3pL, respectively (see Section 4.6.3 for a more detailed discussion on consistency of drop volume and velocity). After incrementing the temperature, the printhead was left for 5 minutes before printing another 10 drops. This procedure was carried out over a temperature range of 54-66°C. This cycle was repeated on four separate occasions, the data points in Figure 4.11 are an average over these cycles.

The solid line in Figure 4.11 indicates the nematic-isotropic temperature (T_{iso}). Upon reaching the isotropic temperature, the viscosity dependency on director orientation and flow direction effectively disappears, and is accompanied by a reduction in the apparent viscosity (see Section 2.4.2). This results in a sharp increase in the drop volume and velocity. Droplets printed below 58°C (for Δ V = 53 V), had very low droplet velocities that are impractical for many inkjet printing applications. Drops travelling at such low velocity are easily deflected from a linear flight path by non-static air or slight rotation of the droplet, and require more careful synchronisation with a moving substrate.

The dashed line in Figure 4.11 represents the temperature at which the formation of secondary and satellite droplets were observed. Due to the length of the fluid ligament produced at temperatures above 68°C, secondary droplets began forming at the droplet tail (such as that shown in Figure 4.10c). The momentum transfer as the secondary droplet is pulled towards, and coalesces with, larger droplet can cause the droplet to deviate from its flight path, effecting drop placement. Also, the length of the droplet tail made image analysis of the droplet volume and velocity more difficult for droplets to the right of the dotted line in Figure 4.11.

4.6.2 Optimizing the Driving Waveform

Dwell Time

Section 4.3.1 described how using an optimum waveform results in an increased pressure wave arriving at the nozzle by exploiting the resonance of the printhead coupled with the fluid being used [87, 88]. In order to determine this resonance,

TABLE 4.3: Optimum waveform W1, calculated using E7 LC ink and a 80 μm microfab nozzle held at 60°C.

t_{rise}	t_{dwell}	t_{fall}	V_1
3μs	15μs	3μs	53V

the velocity and drop volume can be analysed over a range of different dwell times (t_{dwell}). As the dwell time approaches the optimum dwell time, a maximum droplet velocity is observed due to a maximum pressure being produced at the nozzle.

Figure 4.12a shows droplet velocities and volumes as the dwell time is varied for the 80μm nozzle and E7. A printing temperature of 60°C such that the LC was in the isotropic phase and the viscosity is low enough to print without the need to use a large driving voltage. Each data point in the figure represents the average of 10 consecutively printed droplets deposited at 50Hz. The rise time, t_{rise}, and fall time, t_{fall}, were held at 3μs. Shorter rise and fall times leads to higher droplet velocities as it determines the rate at which the piezoelectric element deflects [80]. However, the microfab amplifier is unable to produce more than 30 Vμs^{-1} and has previously been damaged when amplifying signals generated around this rate. The decision was therefore made to limit the rise and fall times to 3 μs to reduce the risk of damage.

The fundamental period of the printhead and fluid can be defined as $T_f = 1/F_1$, where F_1 is the fundamental resonance frequency. For an optimal polar waveform (Figure 4.6), $T_f/2 = t_{rise} + t_{dwell} + t_{fall}$. From Figure 4.12a, the optimum dwell time is between 13-17 μs. Thus, the fundamental resonance frequency of the printhead is 2400kHz. The droplet properties would vary greatly if the printing frequency were to approach this value due to residual pressure fluctuations in the printhead. However, the microfab nozzle is rated at 1kHz and the applications presented in this thesis rarely exceed 400Hz. This analysis produced the parameters for a standard waveform, W1, which is used extensively in this chapter and detailed in Table 4.3.

In addition to increasing the efficiency of energy delivered to the droplet, an optimum waveform also reduces the length of the droplet tail. After producing

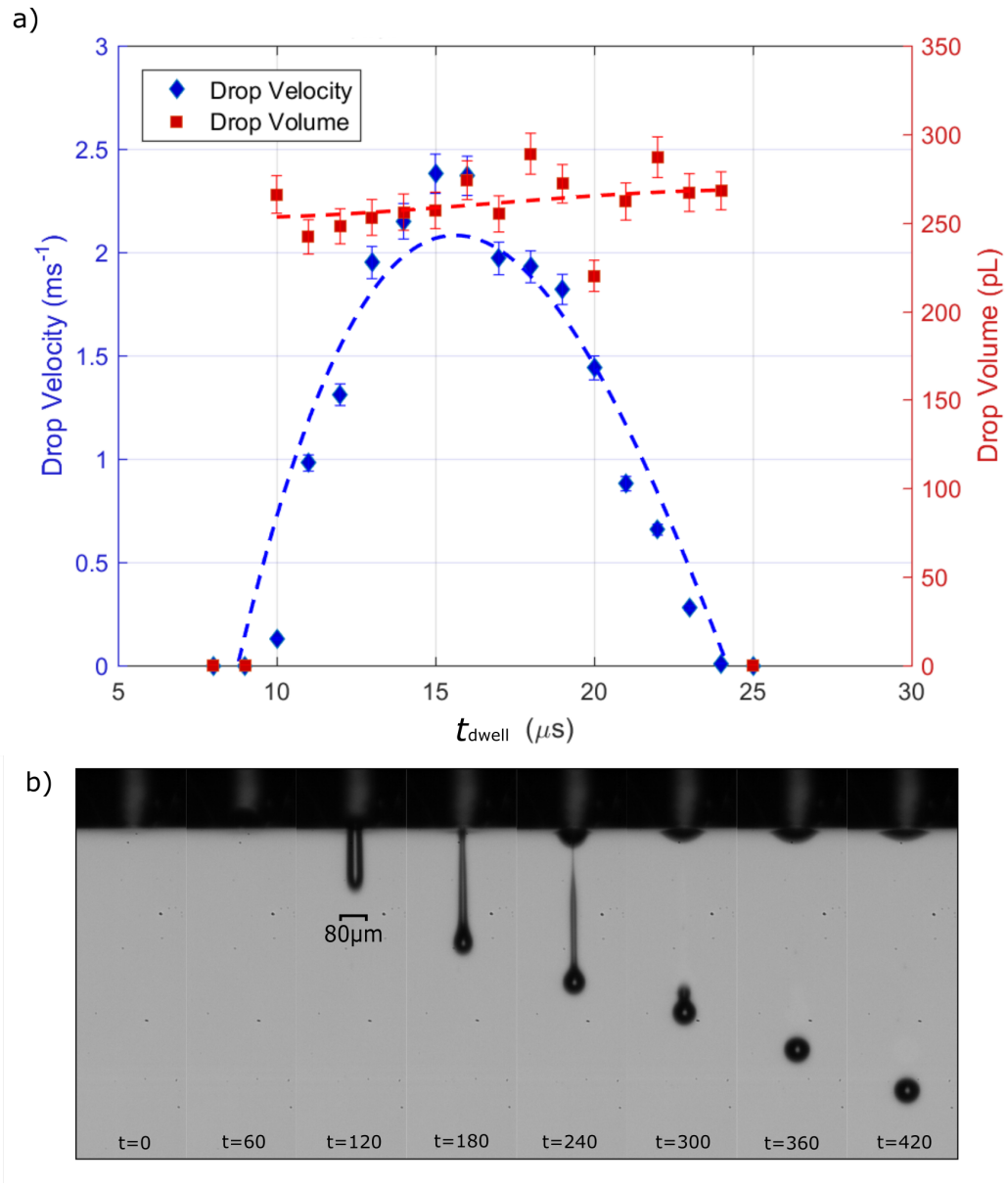

FIGURE 4.12: a) Graph showing the effect of t_{dwell} on droplet velocity and volume for E7. The waveform W1 was supplied to an 80μm nozzle, however t_{dwell} was varied. A 80 μm nozzle and printing temperature of 60°C. b) High-speed images of a droplet of E7 formed using an optimum dwell time of 15 μs.

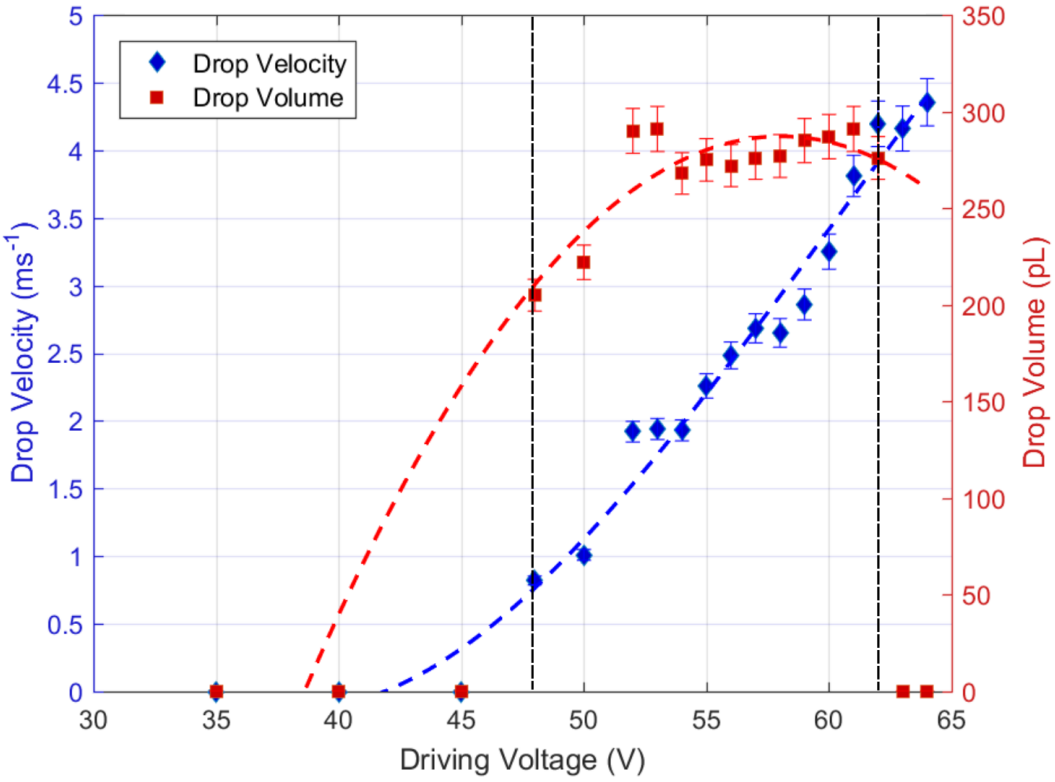

FIGURE 4.13: Graph showing drop velocity and volume as the driving voltage is increased. The waveform W1 was supplied to an 80 μm nozzle, however the driving voltage (V_{pk-pk}) was varied. An 80 μm nozzle was used and held at a temperature of 60°C. The dotted lines indicate the voltages at which droplets were not formed and the onset of satellite droplets.

the fluid jet, the amplified positive pressure wave is reflected and π-shifted at the fluid inlet. This negative pressure wave acts to pull some of the droplet tail back into the nozzle orifice. This is seen to happen during frames t = 120 and t = 180 in the high-speed images in Figure 4.12b.

Driving voltage

Simply increasing the driving voltage increases the volume of the droplet as more fluid is delivered to the nozzle orifice. The effect of increasing the driving voltage is shown in Figure 4.13. The dotted lines indicate voltages which were insufficient for drop formation or resulted in satellite droplet formation. Voltages above 64 V resulted in satellite droplets, effectively limiting the droplet volume to 275pL and droplet velocity to 4.5ms $^{-1}$.

Increasing the driving waveform (whilst keeping the rise and fall times constant) will also increase the droplet velocity as it increases the rate of deformation of the piezoelectric element. Typical droplet velocities for Piezoelectric inkjet printers range from 2 - 10 ms^{-1} [80]. Due to the high viscosity of the fluids used in this thesis, droplet velocities did not exceed 4.5 ms^{-1}. In industrial applications the droplet velocity is important as it facilitates higher printing throughput and leads to more accurate deposition droplet placement. In this thesis, droplet velocity is commonly varied to assess its effect on drop impact and spreading. This was achieved by increasing the driving voltage from 53 V. From Figure 4.13, voltages above 53 V lead to sharp increases in droplet velocity with minimal changes to the droplet volume.

4.6.3 Droplet Consistency

Consistency in droplet volume, straightness and velocity is of up-most importance in high-fidelity IJP printing applications, such as those discussed in this thesis. Due to the highly non-Newtonian properties of LCs, it is particularly important to investigate the repeatability of printing when using a LC ink. Figure 4.14 shows the spread of individual droplet sizes and volumes over 580 droplets printed using the 80 μm nozzle and E7. The waveform W1 was used with a printhead temperature of 60C and a droplet frequency of 1000Hz.

Over 580 droplets, the standard deviation in velocity and volume was 0.16 ms^{-1} and 14.6 pL respectively. However, considering 100 consecutive drops, the standard deviation of velocity drops to 0.025 ms^{-1}, which is 1.2% of the mean velocity. The standard deviation in volume drops to 2.6pL, which is 1.1% of the mean volume. This indicates homogeneity in droplet properties for droplets printed in a single run.

Effect of Back-Pressure on Drop Velocity and Volume

The apparent linear decrease in droplet velocity and volume observed in Figure 4.14 is due to fluid depletion in the printhead as droplets are ejected. Back-pressure is the term given to the pressure applied to the fluid inlet. The ideal back-pressure is such that the fluid is constantly flush with the nozzle orifice,

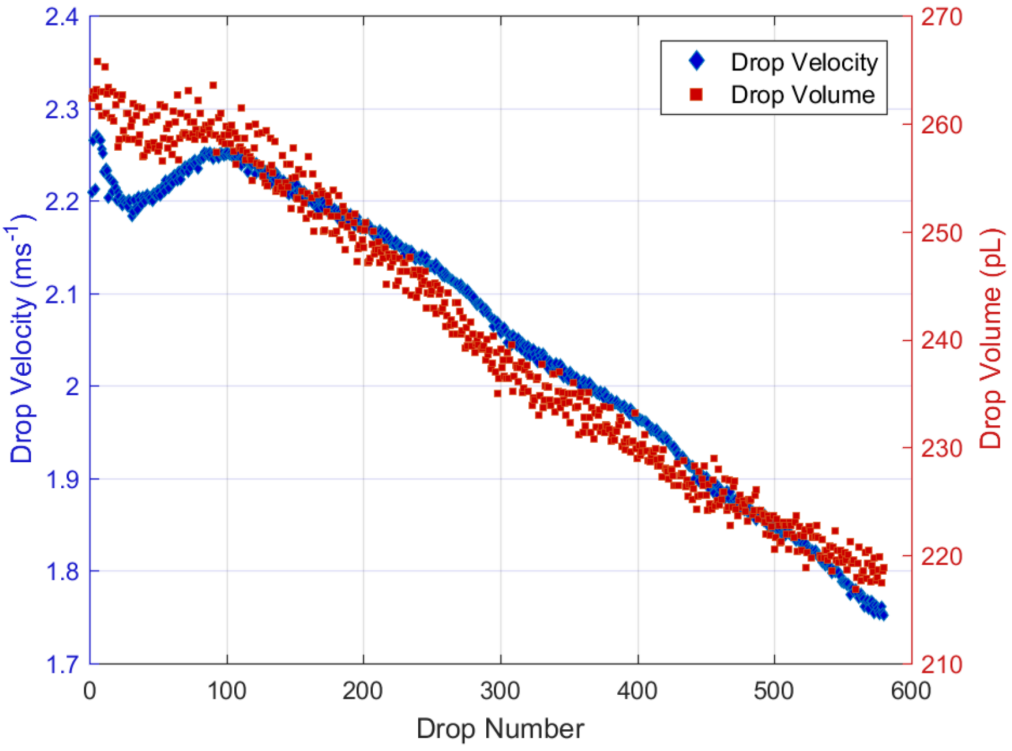

FIGURE 4.14: Graph showing drop velocity and volume measured for individual droplets of E7 printed in a single run using the 80 μm microfab nozzle. The driving waveform W1 was used with a print frequency of 1000Hz, the printhead was held at 60°C.

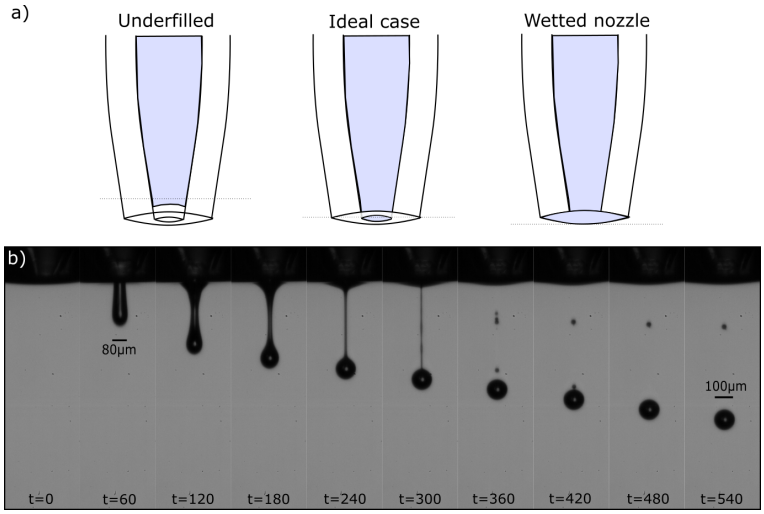

FIGURE 4.15: a) Schematic illustration of the fluid level in an under-filled, ideally wet, and overly wet nozzle. b) High-speed images (16,831fps, 8 μs exposure) of a droplet of E7 being generated in an overly-wet 80 μm nozzle, using waveform W1 and a printhead temperature of 64°C.

shown diagrammatically in Figure 4.15a. As the ink reservoir is placed above the nozzle orifice (the case in the majority of inkjet systems including this one), a negative pressure is usually required to maintain this. In commercial inkjet systems, a vacuum regulator is often used. However, as discussed in Section 3.1.1, the back-pressure in this inkjet system is applied using a syringe. This static pressure hinders the refilling of the printhead as fluid is ejected. Over 580 drops, the drop volume is reduced by 48 pL (18%) and the velocity drops by 0.5 ms^{-1} (22%). This is an important consideration in applications requiring highly homogeneous droplet diameters over hundreds of droplets.

Nozzle Wetness

A thin-layer of fluid can build up on the outside of the nozzle, which can significantly affect drop formation. In overly wet nozzle, illustrated by Figure 4.15a, there is additional viscous dissipation, leading to reduced droplet velocities and in some cases no drop formation. Figure 4.15b shows high-speed images of an exceptionally large droplet, with satellites, being generated due to an overly wet nozzle.

Figure 4.14 highlights another observation associated to nozzle wetness. The

dip observed between 0-85 droplets is due to de-wetting of the nozzle orifice and is commonly observed when the nozzle is very slightly over-wet. In this case, normal printing conditions was sufficient to fully de-wet the nozzle after $\approx$ 100 drops. The most effective method of removing excess fluid is to carefully wipe the nozzle with optical tissue and, if necessary, gently increase the back pressure. Note, that if the high-speed images indicate a degree of wetting of the nozzle, a 100 drop purge is often carried out before continuing with the experiment.

Jet Straightness

The straightness of the jet was defined as the horizontal difference between the center of the nozzle and the centroid of the droplet as the droplet leaves the bottom of the frame in the image sequence. There was a standard deviation of 0.64 μm over the 580 drops shown in Figure 4.14. This represents an average deviation of less than a pixel in the high-speed camera images, indicating an extremely high level of accuracy in drop placement. Large deviations in jet straightness are only observed at low droplet velocities ($\approx$<1 ms^{-1}) and when the nozzle became clogged.

4.6.4 Depositing New Fluids

The insights and procedures determined for E7 can be used to define some generalised guidelines that are useful when faced with depositing a new fluid. It is first beneficial to determine the approximate position in the dimensionless printing regime. This gives an initial marker as to the feasibility of droplet generation and the main factors expected to affect printability. The waveform W1, optimised for E7, serves as an initial guide. Using this waveform, a printhead temperature of 60°C and a driving voltage of 50V, one observes the high-speed images of the fluid ligament at the nozzle. If there is insufficient kinetic energy, the fluid ligament will be short and not extend far from the nozzle. In this scenario, the temperature and/or driving voltage can be increased. On the other hand, if the jet produced is overly long, the temperature and/or driving waveform can be decreased.

By carefully observing the fluid meniscus at the nozzle during drop generation, the dwell time of the actuation waveform can be varied to produce a waveform of optimal length (see Section 4.3.2). If a droplet is still not generated, then a bipolar waveform can be used. Such a waveform operates in the same way an optimised pulsed waveform (dwell time is the same for a bipolar waveform). However, the piezoelectric element undergoes greater deflection during the fall time and a greater nozzle pressure can be achieved. The different waveforms used in this thesis is shown in §A.4.

4.6.5 Sources of Inconsistency in Droplet Properties

The main factors contributing to variation in droplet properties are: 1. Wetting of the nozzle, 2. Back-pressure, 3. Low droplet velocities, and 4. Nozzle clogging or air bubble entrapment. However, as discussed in Section 4.6.3, wetting of the nozzle and back pressure have a negligible effect on droplets printed in the same run, unless several hundred drops are being printed. More significant variation in droplet properties, primarily jet straightness, is observed at low droplet velocities, which were limited to >0.8ms^{-1} in the studies presented. Debris in the nozzle or the presence of air bubbles would result in no drop formation or distorted jets forming. The common source of debris was due to removing excess fluid from the nozzle. Although the manufacturers of the nozzle suggest fine cotton buds to achieve this, gently pressing optical tissue (MC-5, Thorlabs) onto the nozzle was found to minimise the chance of nozzle clogging. The procedure for removing debris or air bubbles is described in §3.1.2.

4.7 Conclusion

An understanding of the physical processes contributing to droplet generation in a piezoelectric printhead is critical when depositing functional and viscous fluids. Piezoelectric deformation induced by the actuation waveform, and propagation of the resulting pressure wave in the printhead, is used to generate a column of fluid at the nozzle orifice. Driven by capillary pressure, the jet of fluid will undergo spontaneous thinning and break-up, ideally with pinch-off occurring just

at the tail of the droplet. Longer jets are more likely to have multiple pinch-off points, forming unwanted satellite droplets. Viscous resistance is the largest force to overcome in producing a jet of fluid sufficient for drop formation, accounting for ≈80% of the total pressure at room temperature and using E7 ink. Dimensionless analysis can be used to define a generalised printing regime for different inks and printing conditions and is useful for assessing how different parameters affect printing outcomes such as droplet generation, splashing and satellite droplets. Increasing the printhead temperature is the most convenient means of reducing viscosity and increasing the printability of the fluid. However, given the thermal restrictions of the printhead, it is critical to optimise the printing parameters.

Increasing the printhead temperature above the isotropic point is associated with marked increases in droplet volume and velocity for E7. Optimising the dwell time of the actuation waveform generates a maximum pressure and is used to increase the inertial energy of the fluid, as well as suppressing satellite droplet and secondary pressure wave formation. Increasing the amplitude of the driving waveform is used to increase the droplet velocity and volume but can lead to lead to satellite droplet formation. Using appropriate printing conditions, consecutive droplets show excellent homogeneity in drop volume and velocity, with a deviation of ≈1% over 100 droplets. However, the static back pressure of the syringe reservoir restricts the refilling of the nozzle and over hundreds of drops results in large reductions in drop volume, which should be accounted for when depositing large numbers of drops in a single run. This chapter has considered the inkjet printing of E7 as it is the most frequently used ink in the studies presented. However, the knowledge and procedures discussed is used to print different LC and prepolymer formulations presented in Chapters 6 and 7.

Chapter 5

Printing Substrates and Applications

In this chapter, the mechanisms of droplet impact with a printing substrate, spreading and the final droplet equilibrium configuration are examined. Uniquely to LC inks, the LC director must be considered, which could be affected by the printing process, droplet shape and anchoring conditions. The following sections discuss the printing of a nematic LC onto a variety of substrates including homeotropic and planar aligned surfaces. The formation of radially aligned LC droplets will then be considered in detail. The findings from the studies presented in this chapter inform the choice of printing substrates in the formation of LC microlenses in chapter 6 and patterned polymer-dispersed LC films in Chapter 7.

5.1 Introduction

A conventional LC device consists of a thin layer of LC ($< 10\mu$m) sandwiched between two glass substrates that have been specially treated with an alignment layer. This ensures that the director aligns with a preferential orientation and/or tilt. The deposition of the alignment layer typically involves a number of steps such as the baking of a thin polyimide layer (100 nm) that is subsequently rubbed in order to promote a macroscopic and uniform alignment of the LC molecules parallel to the rubbing direction [42]. Other techniques that have been adopted to obtain a macroscopic and pre-defined alignment of the LC include the use of

photoalignment layers, monolayers of surfactants, such as silane and lecithin, controlled evaporation of SiO films and flow induced alignment [212, 89, 90].

Inkjet printing of the LC requires consideration of droplet impact and wetting, as well as alignment of the LC at the substrate and air interface. The report by Alino et al. deposited a nematic LC onto clean untreated glass [26]. The substrate was then rinsed with a solution of Polyethylenimine (PEI) to release the nematic droplets, producing mono-disperse LC droplets. However, as the goal of the study was producing LC droplets dispersed in an aqueous solution, the effect of drop impact, wetting and LC alignment after deposition on the substrate was not considered in detail.

Gardiner et al. reported the inkjet printing of a dye-doped chiral nematic LC onto a planar aligned rubbed polyimide and Poly(vinyl alcohol) (PVA) substrates with the aim of producing chiral nematic LC droplets which can act as optically-pumped lasers [29]. It was noted that printing directly on to glass substrates that had been treated with rubbed and baked polyimide layers resulted in considerable wetting of the surface, which made them unsuitable for the purposes of printed laser sources. In order to achieve the standing helix configuration of the chiral nematic phase, the authors found that such an alignment could be obtained by printing onto a PVA layer that was coated onto the glass substrate prior to printing. The mechanism by which this alignment was achieved was not investigated further.

Evidently, the choice of printing substrate is critical in determining the final droplet shape and the alignment of the LC director. However, there is little consideration of droplet impact and spreading of LCs reported in the literature. This chapter considers the use of several conventional and non-conventional printing substrates to investigate the effect of droplet impact and spreading on the droplet shape and LC director. The formation of radially aligned nematic LC droplets is then presented, which takes advantage of the inherent fluid flow generated from the spreading of the droplet. The findings from this chapter are used to inform substrate/droplet interactions and material selection in the studies presented in Chapters 6 and 7.

5.2 Drop Impact, Wetting and Spreading

5.2.1 Drop Impact

Drop impact can be broken down into two separate processes; mechanical impact and subsequent wetting. Similarly to droplet generation, dimensionless analysis is used to identify dominant mechanisms affecting the final droplet configuration. The drop impact and wetting processes can be driven by inertial, capillary and gravitational forces, described by the Reynold and Weber numbers introduced in Chapter 4:

$$Re = \frac{\rho U L}{\eta}\,, \tag{5.1}$$

$$We = \frac{\rho U^2 L}{\sigma}\,, \tag{5.2}$$

where ρ is the fluid density, U is the fluid velocity, η is the LC viscosity (γ_1), and L is the characteristic length-scale. When considering drop impact, U is the velocity of the printed droplet and L is the droplet diameter. When considering wetting and spreading, U can be taken as the wetting velocity (i.e. the rate at which the droplet spreads) and L is the wetted droplet height.

During the impact process it is important to ensure that there is no splashing and that the droplet boundary and droplet shape are maintained. The splashing parameter, mentioned in Section 4.5.1, is defined as:

$$K = We^{1/2} Re^{1/4} > 50\,. \tag{5.3}$$

Using fluid properties for E7 and the measured droplet velocities, the spreading parameter was found to be $K \approx 4$, which is well below the critical splashing threshold of $K > 50$ [91]. Therefore, splashing on impact with the surface was not expected to occur, or indeed was observed, for any of the experimental situations presented in this chapter.

Figure 5.1 shows high-speed images of an E7 droplet impacting a cleaned glass microscope slide. As expected, there is no splashing observed and there is minimal distortion to the droplet shape on impact. When using low-viscosity

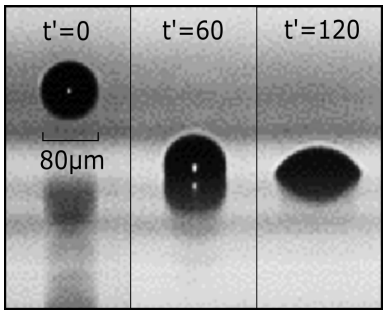

FIGURE 5.1: High-speed images (16,831 fps, 5 μs exposure) showing impact between an E7 droplet on a solid untreated glass substrate, t' is the time in μs since drop impact.

fluids, the formation of crowns and secondary droplets are often observed [92, 92]. However, due to the high viscosity of LC, these effects are subdued.

Effect of Drop Impact on the LC Director

The time-scale of droplet impact can be approximated by: $\frac{d}{u}$, where d is the droplet diameter (before impact with the surface) and u is the droplet velocity. During this period, an instantaneous radial shear force and fluid flow are generated in the LC droplet. Using droplet diameters of 80 μm and droplet velocities of 1.5 ms^{-1}, this gives an impact time-scale of 50 μs. The relaxation time (Equation 2.30 in §2.4.3) is an estimation of the time taken for the director to relax back to its unperturbed state. For a LC droplet, it is given by:

$$t_{relax} = \frac{\gamma_1 d^2}{\pi^2 K}, \tag{5.4}$$

where γ_1 is the rotational viscosity, d is the droplet radius and K is the single elastic constant. Using the values for an E7 droplet at room temperature (γ_1=250 mPa, d=40 μm and K=10^{-11} Nm), results in a decay time of $\approx$ 4 s. This is orders of magnitude larger than the time-scale of mechanical impact. Thus, it is expected that the resultant forces and flow generated during transient droplet impact do not contribute significantly towards the alignment of the LC director.

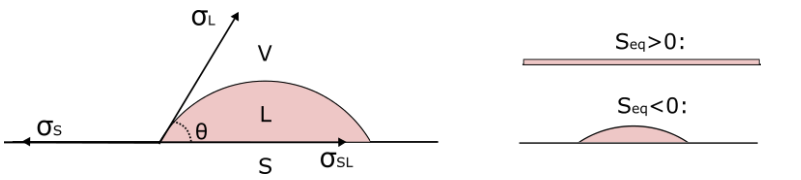

FIGURE 5.2: Schematic of the interfacial force balance of a droplet in contact with a solid substrate and the potential equilibrium configurations, as defined by the spreading coefficient S_{eq}.

5.2.2 Droplet Wetting

There are two potential equilibrium droplet configurations for a three-phase system consisting of a fluid, solid surface and air, shown in Figure 5.2. The contact angle, defined by θ in the figure, is the angle between the substrate and the tangent to the droplet at the contact point between the three phases. By balancing the surface tension at the contact point, one comes to the Young equation [93]:

$$\sigma_S - \sigma_{SL} - \sigma_L \, cos\theta_{eq} = 0 \,, \tag{5.5}$$

where the subscripts denote the liquid (L) and solid (S) phases, and θ_{eq} is the equilibrium contact angle. The surface tension between the solid and liquid phase (σ_{SL}) is sometimes referred to as the interfacial tension (denoted by γ_{SL}). The equation above uses the symbol for surface tension (σ_{SL}) for simplicity and continuity.

For a system dominated by surface tension and in the absence of external forces or specially engineered surfaces, Equation 5.5 can be used to predict the thermodynamic equilibrium configuration and contact angle, θ_{eq}. The equilibrium spreading coefficient S_{eq} is used to characterise full or partial-wetting systems and is defined as:

$$S_{eq} = \sigma_S - (\sigma_{SL} + \sigma_L) \,. \tag{5.6}$$

For $S_{eq} > 0$, there is a thermodynamic drive for the droplet to indefinitely wet the substrate, forming a thin-film with θ_{eq} tending toward zero. On the other hand, $S_{eq} < 0$ indicates a partial-wetting system whereby an equilibrium non-zero contact angle is reached. Both cases are shown diagrammatically in Figure 5.2. In general, the drop will have an initial contact angle, θ_i , which is far from its

equilibrium configuration, θ_{eq}. As the drop wets, its volume is preserved. This, along with factors such as non-perfect surfaces, contamination and contact angle pinning, often results in the observed contact angle not reaching the equilibrium contact angle, even when left over very long time-scales [94, 91].

Contact Angle Hysteresis

In practise the contact angle is dynamic and real surfaces are not truly homogeneous due to debris, roughness and chemical heterogeneity. This results in a range of possible contact angle values that change over time and, to a degree, position on the substrate. The maximum observed contact angle is referred to as the advancing contact angle (θ_A), whereas the minimum observed contact angle is referred to as the receding contact angle (θ_R). The contact angle hysteresis is defined as $\theta_A - \theta_R$. For analytical study and in-depth modelling of wetting phenomena, it is important to characterise these angles, which can be done using force tensiometry. However, the spreading of the LC observed in the studies appeared to occur quickly and contact angle hysteresis was not observed using any of the surfaces detailed in this chapter.

Droplet Shape

The effect of gravity on the equilibrium droplet shape is characterised by the dimensionless Bond number, Bo:

$$Bo = \frac{\rho g L^2}{\sigma}, \tag{5.7}$$

where g is the acceleration due to gravity and L is the droplet diameter. For $Bo << 1$, the effect of gravity is negligible. Using the parameters for E7, this corresponds to droplet diameters less than $\approx$ 1mm. Thus, the wetting process is driven by inertial and capillary forces with negligible contribution of gravity.

For isotropic fluids, Equation 5.7 suggests the equilibrium shape of the droplet is defined by the reduction of free surface energy. Thus, a sessile drop will assume the shape of a spherical cap. The drop volume, V_{drop}, can be equated to that of a

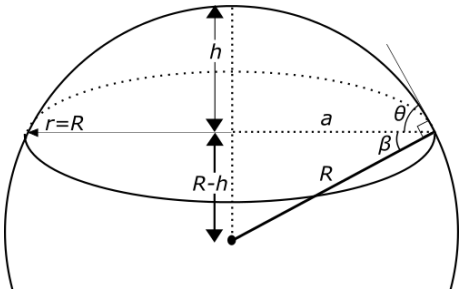

FIGURE 5.3: Diagram of a spherical cap.

spherical cap:

$$V_{drop} = V_{cap} = \frac{\pi h}{6}(3a^2 + h^2)\,, \tag{5.8}$$

where the values are defined by the diagram in Figure 5.3. This cubic expression can be solved for the drop height h in the following form $Ah^3 + Bh^2 + Ch + D = 0$. Where $A = \pi/6$, $B = 0$, $C = \pi a^2/2$, $D = -V_{drop}$. For thin drops ($h/R << 1$)), the term A vanishes and the thickness of the droplet can be approximated as:

$$h(r) = \frac{2V_{drop}}{\pi a^2}\left[1 - \left(\frac{r}{a}\right)^2\right]\,, \tag{5.9}$$

where r is the the distance from the centre of the droplet. The contact angle θ is given by:

$$\theta = \frac{\pi}{2} - sin^{-1}\left(\frac{R-h}{R}\right)\,. \tag{5.10}$$

Using pythagoras, the radius of curvature R is:

$$R = \frac{a^2}{2h} + \frac{h}{2}\,. \tag{5.11}$$

For a thin droplet ($tan\theta \approx \theta$) the contact angle can be approximated by:

$$\theta = \frac{4V_{drop}}{\pi a^3}\,. \tag{5.12}$$

Which is dependent only on the drop volume and radius of the wetted droplet. As these are measured during the printing using the high-speed images and after deposition using optical microscopy images, Equation 5.12 gives a convenient means of approximating the contact angle. It is also evident that the dynamic

contact angle, $\theta(t)$ scales with $1/a(t)^3$.

Measurements of the contact angle were also taken using the device described in §3.3.2. However, as the spherical cap reliably describes the shape of the droplets encountered in this thesis, the above equations were used to give approximations of the contact angle, drop height and radius of curvature, using the measured values of the drop volume and equilibrium droplet diameter.

Effect of the Liquid Crystal Director on Droplet Shape

The Bond number and microscope images of sessile droplets indicate that the LC droplet assumes the shape of a spherical cap. However, there may be elastic distortion of LC director within the droplet. The effect of any LC director distortion on the equilibrium shape of the droplet can be approximated by considering the dimensionless ratio (D) of surface tension over the elastic constant:

$$D = \frac{\sigma L}{K}, \tag{5.13}$$

where σ is the surface tension of the LC, L is the characteristic length scale and K is the relevant LC elastic coefficient associated with the LC director distortion (single-constant approximation). Using the diameter of the LC droplet, the surface tension for E7 at room temperature and a single elastic coefficient of 10pN [95], D is in excess of 200,000. This indicates that the shape of the droplets free surface is determined by the reduction in free surface energy and that any distortion of the LC director has a negligible effect on the shape of the droplet's free surface. It is expected that the shape of the droplet (in air) will only deviate from a spherical shape for droplets less than 1 μm in diameter, which is in agreement with literature describing the prolateness of nematic LC droplets as a function of diameter [96].

5.3 Modelling the Liquid Crystal Director

The following sections experimentally examine the LC director and droplet shape for homeotropic, planar and degenerate planar printing substrates. Modelling the

LC director alignment in droplets printed onto substrates with different aligning properties allows for a better physical understanding of the expected droplet configurations. This section describes the method used to model the LC director in various droplet configurations.

Modelling was carried out using COMSOL Multiphysics, a versatile simulation software package based on MATLAB. In COMSOL, the underlying physics and geometry of the problem is defined by the user in terms of partial differential equations (PDEs). These PDEs are then solved using discretization methods. COMSOL uses the finite element method (FEM) to find approximations to the real solution to the PDEs. For example a function u can be approximated by a function u_h using a linear combination of basis functions, ψ_i, such that:

$$u_h = \sum_i u_{ij}\,\psi_i\,. \tag{5.14}$$

The benefit of using the FEM method is that the discretization may be selected in terms of geometric space and the linear basis functions ψ_i. The reader is directed to the following reference for a detailed description of how COMSOL implements the FEM method [97].

A drawback of COMSOL is that the PDEs must conform to a predefined equation. Most often this approach allows the user to quickly generate simulations by selecting the appropriate governing physical equations. However, COMSOL does not directly support LC director modelling. The 'coefficient form PDE', gives the user the most flexibility in terms of the physics to be described and takes the following form:

$$\boldsymbol{e_a}\frac{\partial^2 \boldsymbol{u}}{\partial t^2} + \boldsymbol{d_a}\frac{\partial \boldsymbol{u}}{\partial t} + \nabla\cdot(-c\nabla\boldsymbol{u} - \alpha\boldsymbol{u} + \gamma) + \beta\cdot\nabla\boldsymbol{u} + a\boldsymbol{u} = f\,, \tag{5.15}$$

where $\boldsymbol{u}$ is variable to be solved which may be a vector, $\boldsymbol{e_a}$, $\boldsymbol{d_a}$, c, α, γ, β and a are coefficients which can take the form of tensors and f is the source term vector. The equation above uses partial derivatives where the operator ∇ is $\left[\frac{\partial}{\partial x}, \frac{\partial}{\partial y}, \frac{\partial}{\partial z}\right]$. The notation $\nabla\boldsymbol{u}$ is equivalent to taking the tensor product: $\nabla \otimes \boldsymbol{u}$, and as convention $\nabla\cdot\boldsymbol{u}$ denotes the inner product. The challenge is thus producing PDEs of this

form which minimize the free energy of the LC systems to be modelled.

The equilibrium director configuration is achieved by minimising the total free energy of the system (see §2.3). The single elastic constant approximation is often used to describe the free energy due to elastic deformation in simulations of nematic droplets [98, 99]. As the models presented in this chapter are used to support the POM images and allow for a higher degree in confidence in assessing the droplet configurations, the single elastic constant approximation is sufficient:

$$F = \frac{1}{2}K\left[(\boldsymbol{\nabla}\cdot\hat{\boldsymbol{n}})^2 + (\boldsymbol{\nabla}\times\hat{\boldsymbol{n}})^2\right] . \tag{5.16}$$

The director is defined as $\hat{\boldsymbol{n}} = (n_x, n_y, n_z)$, where n_x, n_y and n_z are the components of director in cartesian coordinates. Equation 5.16 can be minimized using the Euler-Lagrange equation to give 3 equations for each component of $\hat{\boldsymbol{n}}$. Minimizing for the x component gives:

$$0 = \frac{\partial F}{\partial n_x} - \frac{\partial}{\partial x}\left(\frac{\partial F}{\partial\left(\frac{\partial n_x}{\partial x}\right)}\right) - \frac{\partial}{\partial y}\left(\frac{\partial F}{\partial\left(\frac{\partial n_x}{\partial y}\right)}\right) - \frac{\partial}{\partial z}\left(\frac{\partial F}{\partial\left(\frac{\partial n_x}{\partial z}\right)}\right) . \tag{5.17}$$

Substituting in Equation 5.17 with the expansion of Equation 5.16, where $\hat{\boldsymbol{n}} = (n_x, n_y, n_z)$, and equating to viscous dissipation gives the following PDE for the x component of the director $\hat{\boldsymbol{n}}$:

$$-\gamma\frac{\partial n_x}{\partial t} = K\left(-\frac{\partial n_x^2}{\partial x^2} - \frac{\partial n_x^2}{\partial y^2} - \frac{\partial n_x^2}{\partial z^2}\right) , \tag{5.18}$$

where γ is the rotational viscosity of the LC. Similar PDEs can be constructed for the y and z components. By inspection, Equation 5.18, and the equivalent equations in y and z, can be represented by the coefficient form PDE in Equation 5.17 by setting the coefficients $\boldsymbol{e_a} = \alpha = \gamma = \beta = f = 0$. The coefficients c, d_a and a are all 3x3 matrices with non-zero diagonal elements, with all other elements equal to zero. The diagonal elements of c is the one constant elastic coefficient K and d_a is the rotational viscosity γ.

In the absence of an applied electric field, the coefficient form PDE for the LC director becomes:

$$-\gamma \frac{\partial \hat{\boldsymbol{n}}}{\partial t} + \nabla \cdot (-\boldsymbol{K} \nabla \hat{\boldsymbol{n}}) + a\hat{\boldsymbol{n}} = 0 \,. \tag{5.19}$$

It is noted that the source term f in Equation 5.15 can be used to model the free energy associated with an applied electric field. An electric field term can be added to Equation 5.16 in the form:

$$f_e = \frac{\Delta\varepsilon}{2} (\hat{\boldsymbol{n}} \cdot \boldsymbol{E})^2 \,. \tag{5.20}$$

Such that when applying the Euler-Lagrange minimization, the first term in Equation 5.17 will be non-zero if there is a component of the applied field in this direction. This can be represented by the appropriate x, y, z components of the source term f in Equation 5.15.

5.3.1 Boundary Conditions

Two types of boundary conditions were used in the modelling: A Dirichlet boundary and a Rapini-Papoular anchoring condition. A Dirichlet boundary condition defines the values the analytical solution must have at the boundary and represents an infinitely strong anchoring. This is an appropriate choice when modelling interfaces with high anchoring energies and which do not have any degrees of freedom. For example, when modelling the director configuration of a droplet with strong homeotropic anchoring energies of similar magnitudes at the top air interface and bottom substrate.

The second type of boundary specified is a Rapini-Papoular anchoring condition, described in §2.3.1. A surface energy term can be added to Equation 5.16 which represents the energetic penalty associated with any misalignment of the local director $\hat{\boldsymbol{n}}_r$ to the easy axis of the substrate or air interface:

$$f_s = \frac{1}{2} W_{ij} n_i n_j \,, \tag{5.21}$$

where W_{ij} is the symmetric anchoring tensor. COMSOL allows for a surface flux term to be added to a geometry surface and takes the form:

$$-\boldsymbol{n}_{\perp} \cdot (-\boldsymbol{K}\nabla \boldsymbol{u}) = g - q\boldsymbol{u}\,, \tag{5.22}$$

where $-\boldsymbol{n}_{\perp}$ is the unit vector normal to the boundary condition surface, q is a tensor form coefficient and g is a vector form coefficient.

The geometry of the droplets in the model is defined by the droplet diameter and contact angle measured for each of the printing substrates. The single elastic constant K was taken as 10 pN, the rotational viscosity γ as 250 mPas, which are appropriate values for E7 at room temperature[1]. The anchoring strength W was selected as necessary depending on the printing substrate and is described in the relevant sections.

5.4 Different Printing Substrates

The following sections describe the printing of E7 onto a variety of different substrates. Parameters such as droplet diameter, contact angle and LC director configurations are measured. In addition, the distribution of sessile droplet diameters is used to assess the quality of the printing substrates for applications requiring homogeneous droplet diameters.

5.4.1 Experimental

The experimental set-up used in this chapter is shown in Figure 4.1, on page 60. The preparation of each of the substrates, as well as any additional preparation procedures are presented in the relevant sections. The 80 μm microfab nozzle was used to deposit droplets of E7. The printing temperature was 60 °C and the optimised waveform W1 was used (see page 78). As described in §8.2, an initial purge of the nozzle was carried out before assessing the distribution of wetted droplet diameters.

[1] This is appropriate as an 80 μm droplet will cool to ambient temperature in less than a second

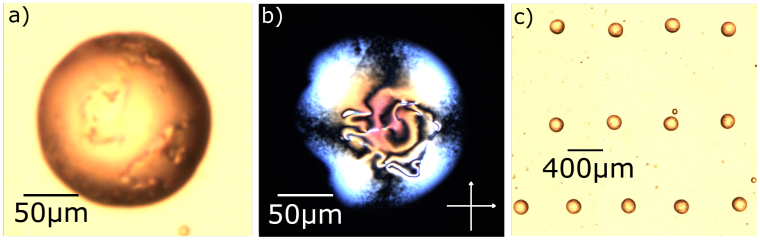

FIGURE 5.4: a) Microscopy image of a droplet of E7 printed onto a bare glass substrate. b) Polarised microscopy of a single droplet through crossed polarisers. c) Array of droplets printed onto the same substrate.

5.4.2 Bare Amorphous Glass

As an initial reference substrate, bare amorphous glass in the form of cleaned microscope slides were studied. Microscope glass slides (Super Premium Microscope Slides, VWR) were first cleaned by immersing the slide in a solution of 5wt% Decon-90 in deionized water for a period of 2 hours, followed by sonication in deionized water for 15 minutes. It was critical for the slides to be cleaned thoroughly as manufacturers often polish the slides which can significantly affect the contact angle and LC alignment.

Untreated amorphous glass induces degenerate planar anchoring, whereby the LC molecules align parallel to the glass surface but with no preferential macroscopic orientation [100]. Figure 5.4a shows a microscopy image of the droplet boundary of the droplet once it had reached an equilibrium state. The wetted diameter is approximately 180 μm, with a contact angle of 21°.

The polarised microscopy image in Figure 5.4b indicates poor uniformity of the LC director, which is expected due to the random degenerate planar anchoring conditions at the glass substrate. However, there is a degree of either radial, or concentric alignment, indicated by the presence of dark brushes which follow the axis of polarisation.

The LC E7 is flow-aligning, meaning the director tends to align parallel to the direction of flow (See Section 2.4). The Ericksen number (Equation 2.21) is used to determine whether a flow will align the LC direction and is repeated below:

$$E_r = \frac{\eta \gamma_1 v L}{K},$$

where γ_1 is the rotational viscosity, v is the flow velocity, L is the characteristic length scale and K the elastic coefficient. For Er numbers greater than unity, the flow is sufficient to affect the direction of the LC director. Using values for E7 and a characteristic length of 10μm, In our case, this corresponds to flows exceeding $\approx 4\ \mu\text{ms}^{-1}$. Post-impact, the time taken for the droplet to reach its final equilibrium configuration is approximately 200 ms, corresponding to a fluid flow of $\approx 250\ \text{s}^{-1}$. Combined with the degenerate planar anchoring conditions of the glass substrate, which can accommodate many planar orientations of the LC director, it is therefore possible that the wetting process can induce a preferential radial orientation. This, in part, can explain the apparent radial alignment observed in the polarised microscopy images. However, multiple defects in the droplet are clearly visible, which implies that the flow-driven alignment of the wetting process is insufficient to radially reorient the bulk of the LC director. Additionally, it is likely that radial flow at the substrate interface will only occur in a region outside the area of the droplet that is in contact with the substrate during impact.

Figure 5.4c shows a microscope image of an array of printed E7 droplets. The droplets show consistency in droplet shape with some variation in the quality of the droplet boundary and diameter. The distribution of the wetted droplet diameter can give an indication of the quality of the substrate for printing purposes. An array of 100 E7 droplets were printed and multiple microscopy images were taken of the resulting droplets. The diameter distribution was analysed using the 'Get Diameter of Sessile Droplets' MATLAB script described in Section 3.4. Figure 5.5 shows the resulting distribution of droplet diameters. It is noted that 10 droplets were discarded in the analysis due to contamination of the substrate surface due to debris. The average droplet diameter was found to be 178 μm with a standard deviation of 1.7 μm.

When determining the role of the printing substrate on the distribution of droplet diameters, the variation in droplet volume due printing must also be considered. The variation in the measured droplet volume over multiple droplets is discussed in §4.6.3. After an initial purge of 50 droplets, the variation in droplet volume over 90 droplets was found to be 1.1% (see Figure 4.14 on page 82). From

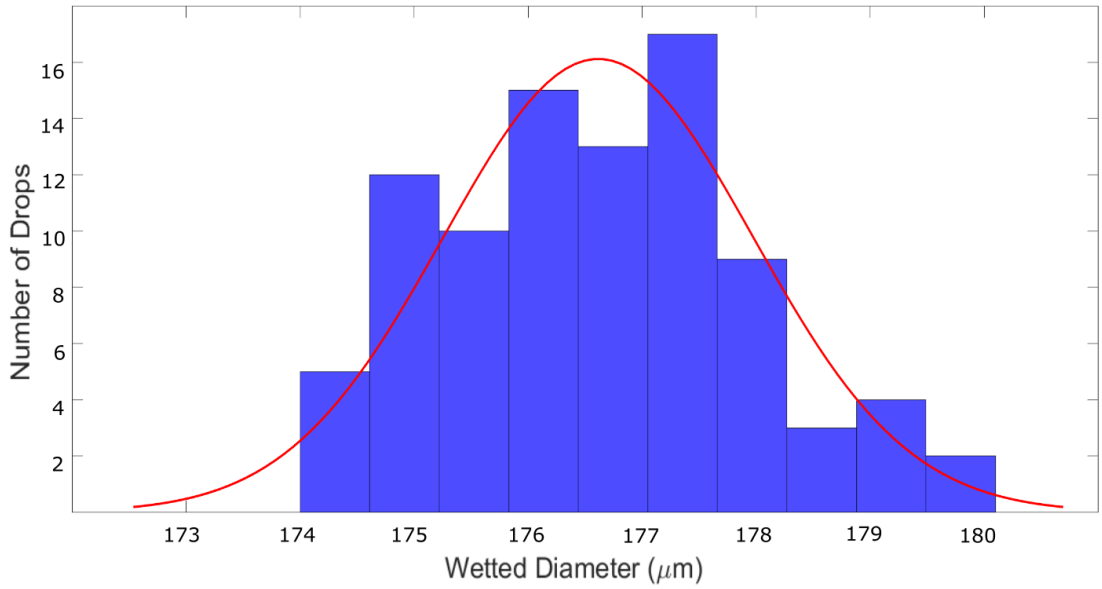

FIGURE 5.5: Histogram plot showing the variation of the measured wetted droplet diameter of 90 E7 droplets printed onto an untreated bare glass substrate. The red curve is the normal distribution fit of the experimental data.

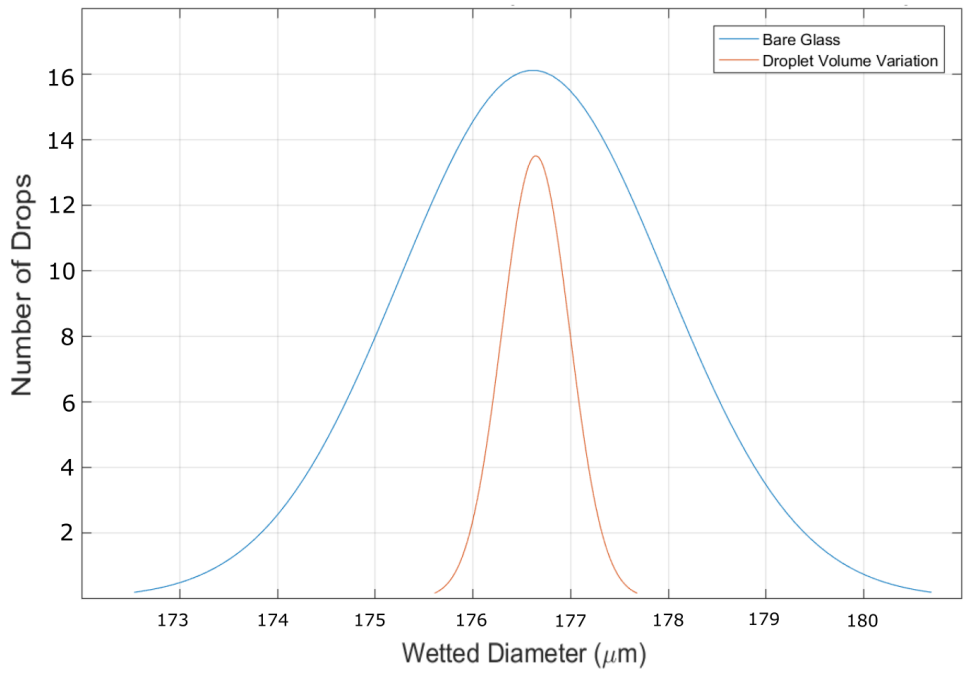

FIGURE 5.6: Plot showing the normal distribution of the measured wetted diameter of E7 droplets printed onto untreated bare-glass, compared to the normal distribution of the wetted diameter expected due to the variation in droplet volumes resulting from the droplet formation.

Equation 5.8, the drop volume is proportional to the square of the wetted diameter. Thus, one can expect a variation in the wetted diameter of ≈1.2%. Note that this does not include any uncertainty due to measurement discussed in Section 3.4.

Figure 5.6 shows the normal distribution of measured droplet diameters on bare glass, compared to the normal distribution expected due to variation in the droplet volume during printing. In practise, there is significant broadening of the diameter distribution attributed to the effect of the printing substrate. The orientation of the LC at the contact line will affect the equilibrium contact angle. As the anchoring of LC at the printing substrate is poorly defined, some variation in the droplet diameter is expected.

5.4.3 Homeotropic Alignment

Homeotropic alignment is usually achieved using surfactants, detergents and some specially engineered polymers [212]. Two alignment materials were used to induce homeotropic alignment: Lecithin and 'Nissan' (SE4811) polymer. The lecithin substrate was prepared by drop-casting a small volume of lecithin onto a cleaned glass substrate and spin-coating at 1,000 rpm for 30s, before baking the substrate for 60 seconds at 70°C. These conditions were found optimal for inducing homeotropic alignment in droplets of E7 and BL006 and was based on work carried out by a colleague. The NISSAN coated substrate was similarly prepared via the spin-coating method, however, the samples were pre-prepared and the exact preparation parameters are unknown.

The E7/air interface imposes strong homeotropic anchoring in the order of 10^{-4} Jm^{-2}[54]. A LC droplet with strong homeotropic boundary conditions often assumes an axial configuration, shown schematically in Figure 5.7a. A sessile droplet printed onto a homeotropic aligned surface has similar boundary conditions to a hemispherical slice through an axial droplet, shown by Figure 5.7b. An axial droplet with strong anchoring ($\approx> 10^{-4}$ Jm^{-2}) has a hemispherical defect line indicated by the blue dots on Figure 5.7a. Both Nissan and lecithin coatings are considered to be strongly anchoring, with polar anchoring strengths in the order of 10^{-3} Jm^{-2} (Nissan) and 5×10^{-4} Jm^{-2} (Lecithin) [101, 89]. However, the

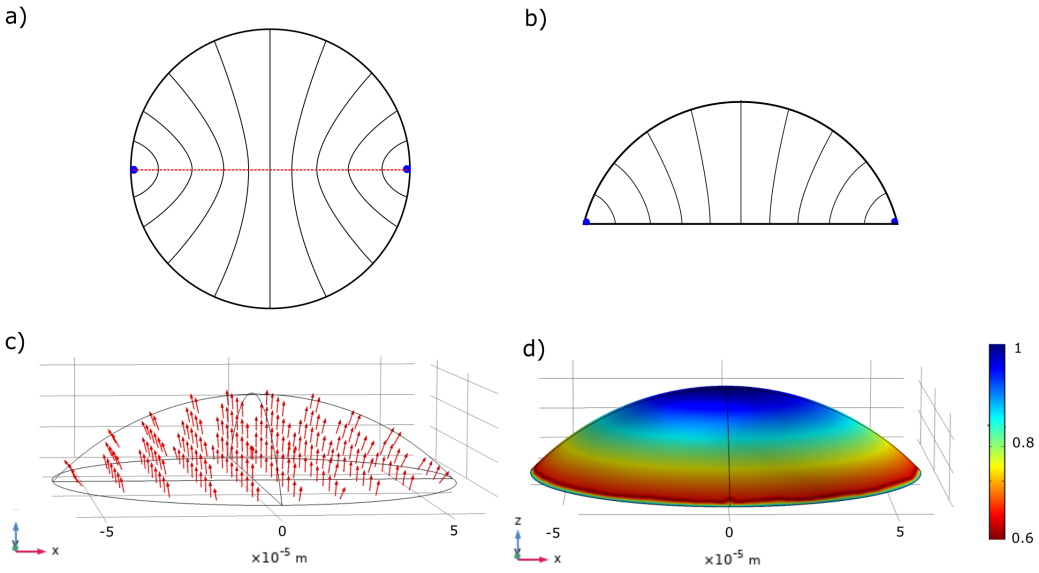

FIGURE 5.7: a) Schematic illustration of the director profile in an axial LC droplet, the blue dots indicate an equatorial defect line. b) Schematic illustration of the director profile of a hemispherical LC droplet with homeotropic boundary conditions. c) 3D simulation of the director profile within a droplet printed onto a homeotropic aligned surface. d) Surface plot of the z-component of the local LC director.

elastic distortion at the contact line in a sessile droplet will depend on the contact angle and be less pronounced than in a spherical droplet, thus a defect line may not be present.

A model of the LC director within the droplet was constructed as discussed in Section 5.3 and using the droplet geometries for an E7 droplet on a NISSAN coated substrate. Homeotropic, Dirichlet, boundary conditions were applied to the surfaces to model the strong anchoring imposed at the substrate and air interfaces. Figure 5.7c shows the director profile within the droplet, with the arrows indicating pointing in the direction of $\hat{\boldsymbol{n}}$ ($\hat{\boldsymbol{n}} = -\hat{\boldsymbol{n}}$). Figure 5.7d shows a surface plot of the z-component n_z of the director $\hat{\boldsymbol{n}}$. A possibly advantageous property of homeotropically aligned droplets is that due to symmetry in the LC director, they will possess largely polarisation independent optical properties for collimated incident light.

Figure 5.8a shows a microscope image of an E7 droplet printed onto a Lecithin coated substrate. The droplet has uniform circularly boundary with a wetted diameter of 140 μm. The surface is more hydrophobic than glass with a contact

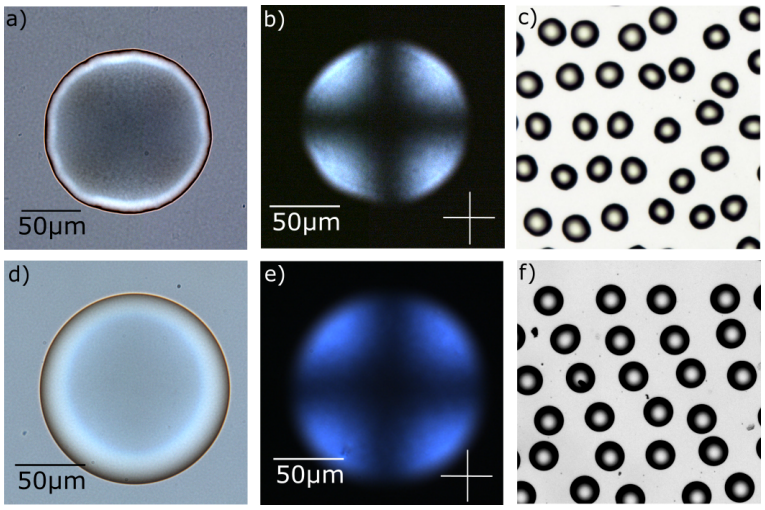

FIGURE 5.8: a) Microscopy image of an E7 droplet boundary printed onto a Lecithin prepared substrate. b) Polarised microscopy image of single E7 droplet through crossed polarisers. c) Microscope images of an array of E7 droplets printed onto a Lecithin prepared substrate. d), e) and f) are the corresponding images for an E7 droplet printed onto a NISSAN-coated substrate.

angle of 32°. Figure 5.8d shows the microscopy image of an E7 droplet deposited onto a NISSAN coated substrate. The droplet shows an almost perfect circular boundary with an average diameter of 144 μm and a contact angle of 29°.

In accordance to the COMSOL model, the POM images in Figures 5.8b and e indicate largely homeotropic alignment throughout the volume of the droplet. There is a degree of birefringence indicated by the blue quadrants in the POM images, which is due to the slight tilt of the LC director at the droplet/air interface.

The diameter of the wetted droplets were measured over 90 samples for both the lecithin and Nissan treated surfaces. Figures 5.9 and 5.10 show the distribution of droplet diameters for the lecithin and NISSAN treated substrates, respectively. Given ideal, perfectly homogeneous surfaces with null contaminants, one would expect a normal distribution of wetted droplet diameters. However, the histograms in both Figures 5.9 and 5.10 are not well correlated to a normal distribution and are skewed in the positive and negative x direction respectively. The average droplet diameter was 138 μm for lecithin and 144.5 μm for the Nissan coated substrates. The Nissan surface has a more mono-disperse distribution of wetted diameters, with a standard deviation of just 0.63 μm, compared to 3.4 μm for lecithin. The variation in both the diameter and quality of the droplet shape

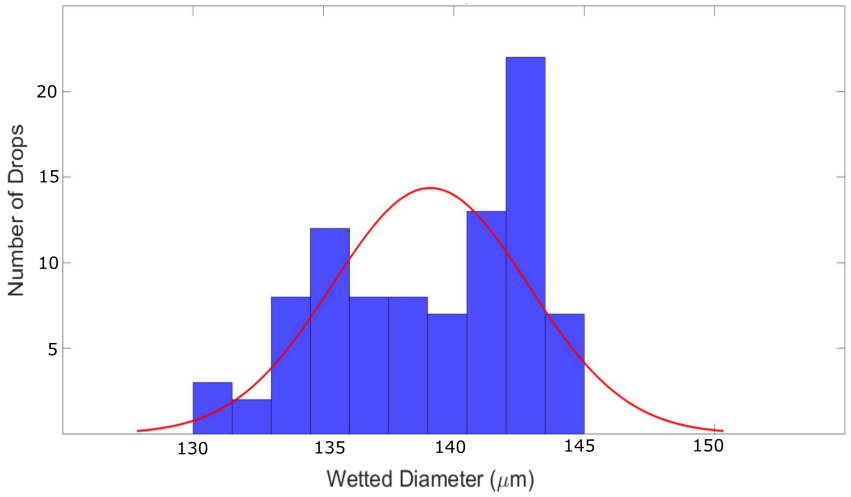

FIGURE 5.9: Histogram plot showing the variation of the measured wetted droplet diameter of 90 E7 droplets printed onto a lecithin coated substrate. The red curve is a normal distribution with an average and standard deviation of wetted droplet diameters equivalent to those measured experimentally.

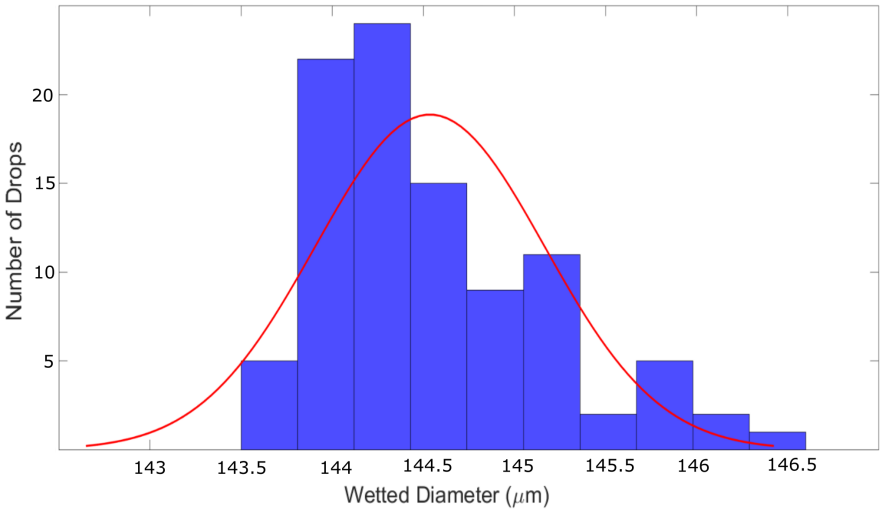

FIGURE 5.10: Histogram plot showing the variation of the measured wetted droplet diameter of 90 E7 droplets printed onto NISSAN coated substrate. The red curve is a normal distribution with an average and standard deviation of wetted droplet diameters equivalent to those measured experimentally.

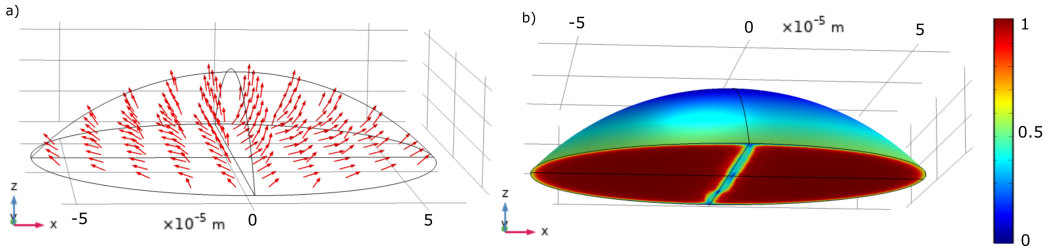

FIGURE 5.11: a) 3D simulation of the director profile within a droplet printed onto a planar aligned surface. b) Surface plot of the x-y component of the LC director, with the easy axis aligned with the x-axis.

can also be clearly seen comparing the microscope images of droplet arrays for each substrate in Figures 5.8c and f. The NISSAN substrate shows excellent homogeneity of droplet diameters with a range in droplet diameters equivalent to that expected due to the variation in droplet volumes produced by the nozzle (1.2%).

5.4.4 Planar Alignment

A rubbed planar alignment surface promotes uniaxial orientation of the LC director at the substrate interface. Rubbed polyimide is a common alignment surface used in LC devices as it promotes strong uniform planar anchoring parallel to the rubbing direction. Rubbed polyimide surfaces typically have an azimuthal (in-plane) anchoring energy on the order of 10^{-3} Jm^{-2} and a polar (out of plane) anchoring energy in the order of 1.4×10^{-5} Jm^{-2} [102, 103, 42]. An empty glass LC cell with rubbed polyimide alignment layers and a pre-tilt of 1-3°(LC2, Instec) was carefully split open and one of the glass substrates was used as the printing substrate. Another rubbed polyimide planar substrate with a pre-tilt of 4-6°was prepared in a similar manner using a Samsung OCBIX-*-000 cell. Filtered air was used in an attempt to remove some of the spacer beads. Washing and wiping of the substrate using solvents was not undertaken as previous results had indicated the process affects the alignment of the LC. It is noted that there were still spacer beads present on the substrates during printing. The droplet was exhumed from analysis if the bead was deemed to significantly affect the droplet shape.

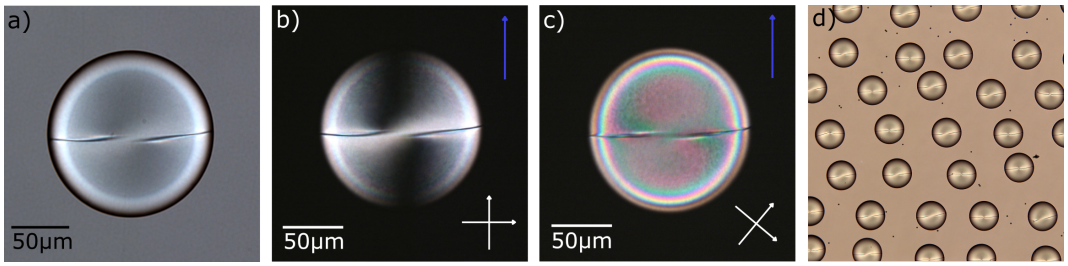

FIGURE 5.12: a) Microscopy image of an E7 droplet boundary printed onto a planar aligned surface. b) Polarised microscopy image of a droplet, with the rubbing direction indicated by the blue arrow. c) Polarised microscopy images of the same droplet but with the polarisation axis rotated by 45°. d) Microscope images of an array of E7 droplets printed onto a rubbed polyimide planar surface.

A model of the LC director configuration for droplets deposited on the INSTEC substrate was constructed using the droplet geometries found during printing. Strong homeotropic anchoring at the air interface was modelled using Dirichlet boundary conditions. Planar anchoring at the bottom substrate was modelled by applying a flux/source boundary condition with $a_{22} = W_\theta = 1.4 \times 10^{-5}$ Jm^{-2} and $a_{33} = W_\phi = 10^{-3}$ Jm^{-2}. Thus, at the bottom substrate, an energy penalty is incurred when the director deviates from parallel to the substrate (a_{33}) and parallel/anti-parallel to the x-axis (a_{22}), which corresponds to the rubbing direction. Figure 5.11a shows the director configuration in the droplet, in which two oppositely oriented splay configurations is clearly seen. Figure 5.11b shows the magnitude of the x-y components of the LC director: $n_x^2 + n_y^2$. At the substrate, the LC director aligns parallel to the easy axis, with a disinclination line clearly visible running through the centre of the droplet and perpendicular to the rubbing direction.

Figure 5.12a shows a microscope image of a typical droplet printed onto an Instec rubbed polyimide coated substrate. The equilibrium diameter of the droplet was 141 μm with a contact angle of 31°. As indicated by the model, a horizontal line perpendicular to the rubbing direction is observed in all the droplets deposited onto this substrate. Figures 5.12b and c show the polarised microscopy images of a single droplet with crossed polarisers oriented at 0°and 45°. The upper air/LC interface imposes homeotropic anchoring conditions, whereas the

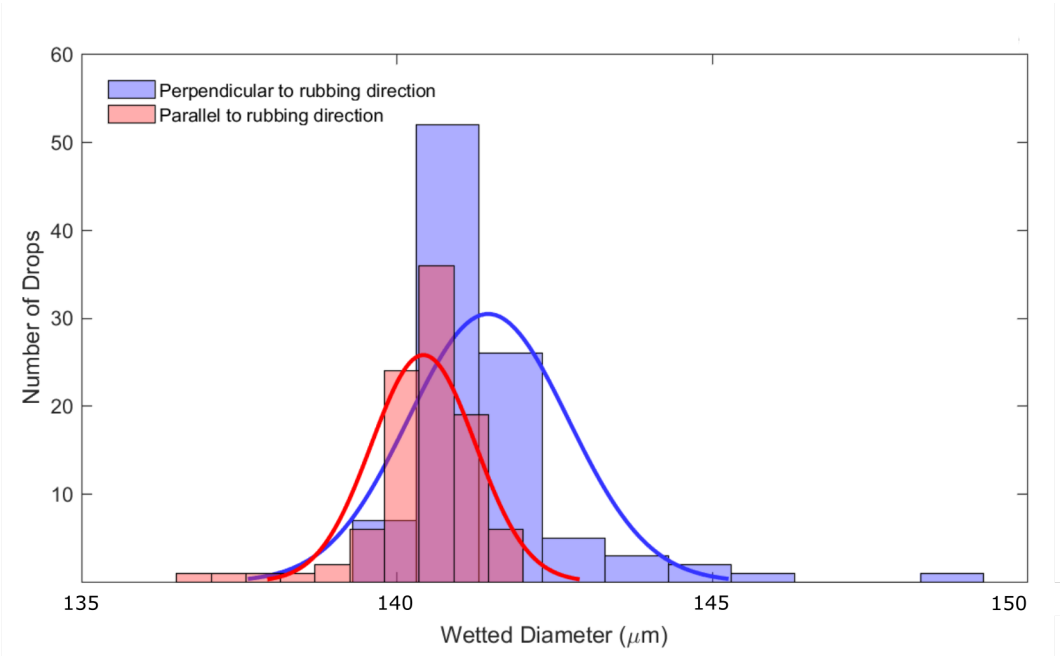

FIGURE 5.13: Plot showing the distribution of droplet diameters parallel and perpendicular to the rubbing direction for 97 E7 drops, printed using the 80 μm nozzle onto an INSTEC rubbed polyimide substrate. The red and blue curves represent a normal distribution with an average and standard deviation of wetted droplet diameters equivalent to the experimentally observed data.

rubbed polyimide layer induces planar anchoring with the easy axis parallel to the rubbing direction, which is indicated by the blue arrow in Figure 5.12b and c. The alignment imposed by the top curved air interface results in oppositely oriented splay director profiles. The horizontal line visible in the images is a disinclination resulting from the topologically impossible interface between the two oppositely oriented splay distortions.

The extent to which a droplet spreads depends on the balance of surface tension at the contact point between the three phases. Due to the anisotropic alignment of the LC at the substrate, it is possible that the droplet will accordingly wet to different extents parallel and perpendicular to the rubbing direction. To examine this, the diameters of 97 droplets were measured perpendicular and parallel to the rubbing direction. Figure 5.13 shows the distributions of diameters. A marginal difference of 1.1 μm was found between the semi-major and semi-minor axes. This difference may be a result of either/or the anisotropy of the surface properties and orientation of the LC director at the contact line. However, there

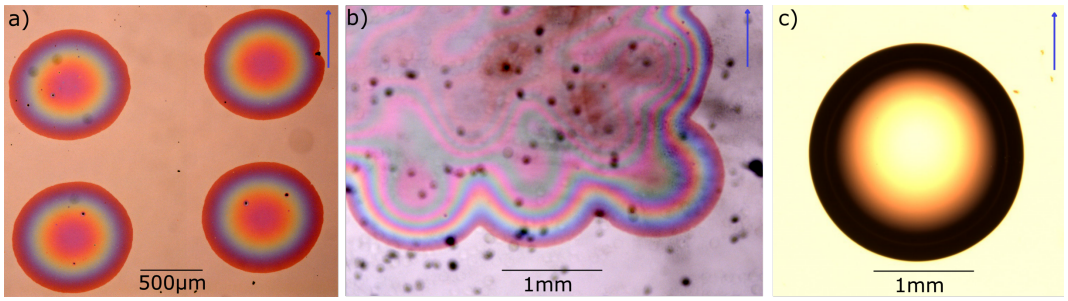

FIGURE 5.14
a) Microscopy image of four E7 droplets deposited onto the Samsung substrate, taken five minutes after deposition. b) Microscopy image of the corner of an array of E7 droplets printed onto the Samsung substrate 15 minutes after deposition. Note that the black dots are contaminants present on the imaging system. c) Microscopy image of a droplet of deionized water on the Samsung substrate 6 minutes after deposition. The blue arrow in the figures indicates the easy axis of the cell.

are many overlapping diameters observed in the histogram bins in Figure 5.13 and the difference is not significant in accordance with the microscope images.

Samsung Substrate

Figure 5.14a and b show microscope images 5 and 15 minutes after deposition. At five minutes the droplets were 965 μm in diameter. The droplets continued to spread for a further 24 hours, at which point their diameter was indistinguishable. This substrate is an example of the complete wetting configuration discussed in Section 5.2.2. The colourful rings present in Figures 5.14a and b are due to interference between light reflected from the top and bottom boundaries of the thin-film. An approximation of the film thickness (t) can be made by considering the optical path length required for constructive interference of light: $2t = (m + 1/2)\lambda$. Here, λ is the wavelength of the light undergoing constructive interference and $m = 0, 1, 2, 3, ...$ We can take $\lambda = 636$ nm as the reflected colour in the center of the droplet appears red. As the outer part of the droplet, where the thickness is at a minimum, is also red one can assume $m = 1$, i.e. the light has undergone double internal reflection. This gives an approximate droplet thickness after 5 minutes of 480nm, which is in accordance with the expected volume of the sessile droplet. It is noted that POM images are not included as birefringence was not detected due to the film thickness.

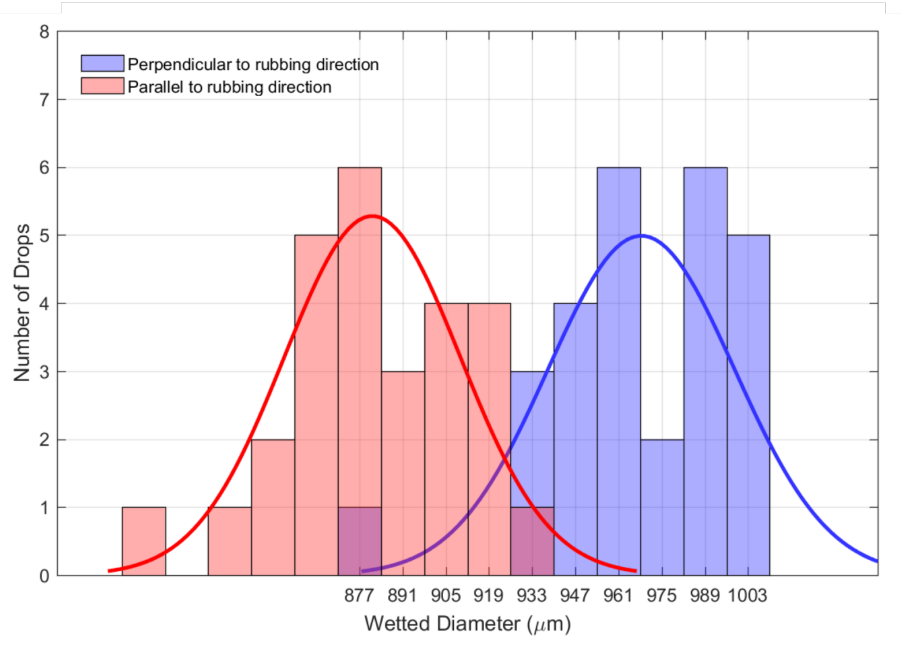

FIGURE 5.15: Plot showing the distribution of droplet diameters parallel and perpendicular to the rubbing direction for 27 drops, printed with the 80 μm nozzle, on a Samsung substrate. The red and blue curves are normal distributions with an average and standard deviation of wetted droplet diameters equivalent to the experimentally observed data.

As seen in the Figure 5.14a, it is apparent that the droplets spread further perpendicular to the easy axis. Due to the extent of wetting, 27 E7 droplets could be analysed before droplets began to coalesce. Figure 5.15 shows a histogram plot of the printed droplet diameters after 5 minutes. It is noted that in this case, the poor fit to a normal distribution may be a result of the small sample size of 27 droplets. The average parallel diameter was 880 μm, as opposed to 968 μm perpendicular to the rubbing direction. Clearly, the rubbing direction has a significant effect on the extent to which the droplet spreads.

To test whether the difference in droplet diameter is due to surface anisotropy imparted during the treatment process, or a difference in surface tension due to the alignment of the LC, an isotropic fluid was deposited onto the substrate. Several droplets of deionised water were deposited using a pipette. Figure 5.14c shows the microscopy image of single droplet of water. There was no significant difference in parallel or perpendicular droplet diameters observed using the isotropic fluid. This interesting finding suggests the significant variation in wetted parallel and perpendicular diameters is due to the alignment of the LC director. The reasons as to why the Samsung cell yielded complete and anisotropic wetting when the INSTEC cell did not, is a topic for future work, described in §8.3.

5.5 Radially Aligned Droplets

Radial alignment for printed droplets is inherently difficult to achieve via methods such as rubbing as each droplet must be locally aligned about its center. Such alignment can be produced using lithography techniques, however, this would still require near perfect positioning of the droplet during printing which in practise would be impractical to achieve. As discussed in Section 5.2.1, there is a radial force and flow generated during impact and wetting, which could be used to align the LC director at the printing substrate. Such a configuration would require a planar aligned surface that can accommodate many different orientations.

Untreated Poly(vinyl alcohol) (PVA) was chosen as the alignment layer as it

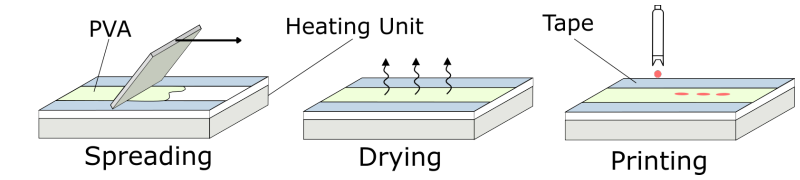

FIGURE 5.16: a) Illustration of the procedure used to prepare the PVA-treated substrate.

imposes degenerate planar anchoring, with a polar anchoring strength in the order of 10^{-5} Jm^2 [54]. Additionally, PVA was used as the substrate layer in previous work detailing the alignment of chiral nematic LC droplets [29]. In this work, a wet PVA layer was used to impose planar alignment at the bottom of the droplet such that the helical axis was oriented perpendicular to the substrate. However, the study did not go into any detail about the alignment process or the substrate conditions required. This section considers three separate conditions for the PVA substrate: fully-dry, fully-wet, and partially-wet.

5.5.1 Preparation of Polymer Substrate

Figure 5.16 illustrates the procedure for preparing the substrates. Solutions of 10wt% and 2wt% PVA (80% hydrolysed, 9,000-10,000 MW, Sigma Aldrich) were prepared in deionized water. Other PVA formulations using different molecular weights and degree of hydrolysis were also tested, however, this solution was selected due its transparent optical properties and low viscosity, allowing it to be easily deposited onto glass microscope slides using simple doctor blade-coating processes. The solutions of PVA in deionized water were heated to a temperature of 45°C and agitated for 72 hrs to ensure full mixing. Tape was first applied to the microscope slides to form 70 μm-thick 'walls' at the edges of the substrates and the PVA solution was then drop cast onto the channel that had been formed by the tape and then coated using doctor blading. This thickness was selected as the drying time was approximately 90 minutes, giving a good window of time to print in fully-wet, partially wet and dry films. Additionally, a film of this thickness would allow an 80 μm droplet to penetrate the film (in the case of a fully-wet substrate). Films of different thicknesses were tested, however, the only noticeable difference was the drying time.

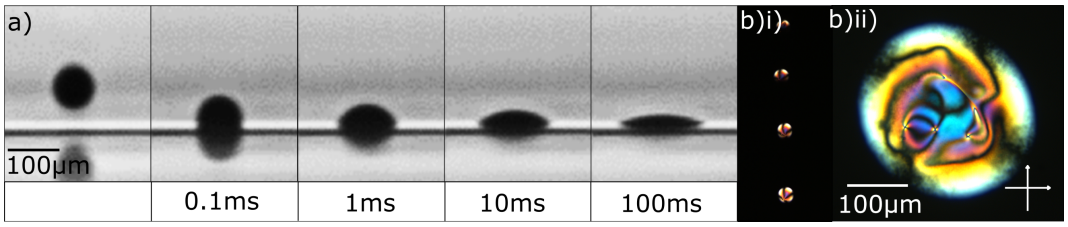

FIGURE 5.17: a) Shadowgraphy images captured using the high-speed camera (15,000 fps, 8 μs exposure) showing the impact of the nematic LC, E7, onto a fully-dry PVA layer over a time-scale of 100 ms. b)i) Polarising optical microscopy image of an array of 4 droplets. b)ii) Enlarged polarising optical microscopy image of the droplet array showing the boundary between neighboring droplets. The white arrows in the crossed configuration represent the orientations of the transmission axes of the polarisers.

5.5.2 Printing onto a Dry Polymer Layer

A 70 μm-thick sample of 10% wt PVA was prepared and left to dry under ambient conditions for 6 hours at a temperature of 22°C. The drying of the PVA was accompanied by a reduction in volume of approximately 1/3. Figure 5.17 shows shadowgraphy images of droplet deposition onto the fully-dry PVA layer that was held at a constant temperature of $T = 22$°C. From the images presented in Figure 5.17, the wetting process observed was similar to that seen for cleaned, untreated glass substrates with the final droplet configuration being reached in approximately 100 ms with an equilibrium droplet diameter of 170 μm and contact angle of 26°. The corresponding optical polarizing microscopy images reveal the presence of multiple defects and poor macroscopic uniformity of the LC director. However, the LC droplet boundary was found to be spherical in shape and was consistent across successively-printed droplets.

5.5.3 Printing onto a Wet Polymer Layer

For the wet PVA layer, which comprises mostly deionized water, microscope glass slides were again prepared following the process shown in Figure 5.16. However, there was no drying stage and the LC was deposited soon after spreading of the wet PVA layer. Figure 5.18 shows the captured shadowgraphy images of the deposition process onto a fully-wet 70 μm-thick PVA layer that was held

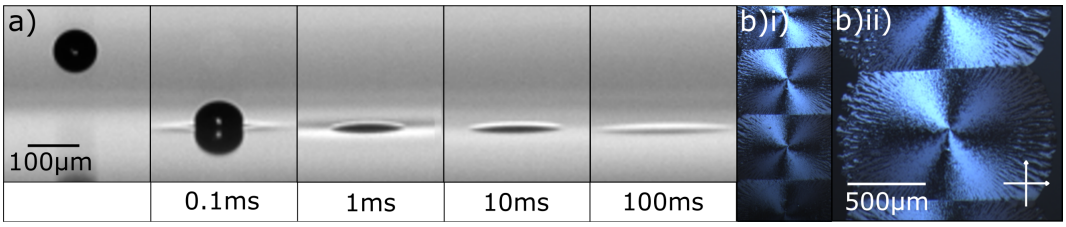

FIGURE 5.18: a) Shadowgraphy images captured using the high-speed camera (15,000 fps, 8 μs exposure) showing the impact of the nematic LC, E7, onto a fully-wet PVA layer over a time-scale of 100 ms. b)i) Polarised optical microscopy image of an array of droplets between crossed polarisers. b)ii) Polarised optical microscopy image of a single droplet. The white arrows in the crossed configuration represent the orientations of the transmission axes of the polarisers.

at a constant temperature of $T = 22°C$. During impact, the droplet was seen to penetrate the PVA layer, which was also noted by Gardiner et al. [29].

The droplet velocity in Figures 5.17 and 5.18 was held constant at 2 ms^{-1}. To assess the effect of droplet velocity on impact, the droplet velocity was increased to 3.5 ms^{-1}. However, there was no observable difference seen when printing at increased droplet velocities. As seen in the images, the LC settles above the PVA layer due to the thermodynamic requirement to wet the PVA surface. Comparing Figures 5.17 and 5.18, after 100 ms, the LC has spread out substantially upon the wet PVA bed. Due to the extent of spreading, after 200 ms it was almost impossible to distinguish between the LC and the PVA solution in the high-speed images.

The polarized microscopy images in Figure 5.18 show the resultant LC droplets 5 minutes after deposition. Radial planar anchoring within the droplet is evident, indicated by the dark brushes that align with the transmission axes of the polarisers. Although some uniformity in the director alignment is achieved, after 5 minutes the spreading of the droplet had reached diameters of 600 μm and the LC continued to wet the PVA surface. These findings represent the complete wetting case (see Figure 5.2).

It was found that printing into a fully wet PVA layer results in substantial wetting of the PVA and does not lead to the desired droplet configuration. However, depositing the LC onto a wet PVA solution rather than a dry polymer bed did

result in a marked improvement in the uniformity of the LC director. A full description of the exact mechanisms responsible for the improvement in the director alignment is outside the scope of this thesis, however, the following remarks can be made. Firstly, the impact of the LC droplet on the PVA bed is cushioned, thus the process imparts less of an impulse force on the LC in the bulk, which could cause less disruption to the alignment of the LC. Additionally, it is evident that the high composition of water during the wetting process contributed significantly to the quality of the planar orientation. During the drying of polymer solutions, water molecules diffuse to the free surface before evaporating, forming a thin layer of water at the air interface. It is entirely feasible that the interaction between the LC and the printing substrate is akin to that of pure water, allowing the LC molecules to reorient under a flow, even if they have already been adsorbed at the anchoring surface.

Spreading Instabilities

The formation of dendritic structures were observed when printing onto a fully wet PVA layer. These are shown in Figure 5.19, which compares printed arrays 5 minutes after deposition when the PVA was fully dry (a) to droplets printed onto a wet PVA layer held at 22°C (b) and 45 °C (c). As seen in the figure, the dendritic structures are more prominent at elevated temperatures.

The dendritic structures observed are very similar to those resulting from Marangoni instabilities during the drying of thin-films [104, 105]. The evaporation of water from the top surface of the film increases the concentration of water at the interface. This leads to local variations in the interfacial tension, which is concentration dependent, between the LC and the PVA film around the droplet perimeter. The variations in interfacial tension drives droplet spreading differently around the perimeter of the droplet and has been shown to cause the formation of dendritic or 'flower/snowflake' patterns. As the temperature of the substrate is increased, the rate of evaporation increases, leading to more pronounced instabilities forming which is in accordance to the observations presented in Figure 5.19c. To minimize such effects, the temperature of the substrate was thus kept at room temperature.

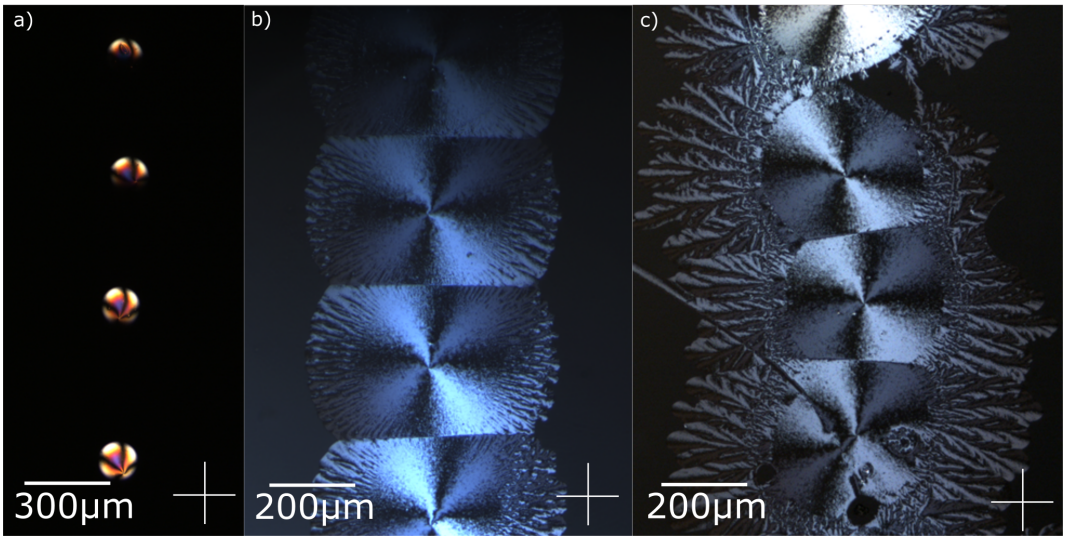

FIGURE 5.19: Polarized microscopy images of E7 droplets taken 5 minutes after deposition on: a) A fully dry PVA layer. b) A wet PVA layer held at 22°C. c) A wet PVA layer held at 45°C.

A Note on the Addition of Solvents

The addition of organic solvents has been shown to improve the surface quality of PVA films. In particular, Dimethyl Sulfoxide (DMSO) has been used extensively with PVA formulations [106, 107]. The addition of DMSO to a PVA mixture decreases the viscosity whilst increasing the gelation and drying time of the films. It was found that the addition of DMSO significantly affected the interaction between the wet PVA and LC in unpredictable ways and even at low concentrations of DMSO (<10%wt). The formation of instabilities during wetting, as well as potential mixing between the PVA and LC was observed. Thus, DMSO was not used for the films produced in this section.

5.5.4 Printing onto a Partially Dry Substrate

To combine the favourable droplet boundary seen when printing onto a dry PVA substrate with the uniformity of the LC director apparent when printing onto a wet PVA substrate, a partially-dry PVA layer was used as the printing substrate. The layer was prepared as illustrated in Figure 5.16, with the thickness of the PVA layer being 70 μm when wet and the temperature held constant at 22°C. The time between spreading and the printing of the LC was used to quantify the

'dryness' of the substrate. It was found that there was a critical dryness of the PVA that promoted both a defined droplet boundary and uniformity of the LC director. This occurred at approximately 75-95% of the time taken to for the PVA bed to fully dry, corresponding to approximately 60 minutes of drying in an air environment and at room temperature ($T = 22°C$) and a relative humidity of 40% RH.

Figure 5.20 shows the high-speed images captured during the deposition process. The droplet was found to reach equilibrium in less than 100 ms with an almost identical degree of wetting to that observed with the fully-dry PVA substrate, reaching a final diameter of 160 μm. However, in contrast to the dry PVA substrate, there is a uniform radial alignment of the LC director, as can be seen in the microscope images in Figure 5.20 b) and c). Even though the wetting process is almost identical to the dry polymer and the droplet boundary formed is stable, the alignment is significantly better. This suggests that there is an increased ability of the LC director to reorient at the substrate surface, which may be due to the presence of a thin layer of water at the free surface of the PVA film.

A model of the LC director configuration for droplets deposited onto a partially dry PVA substrate was constructed using the geometry of the sessile droplets produced. Strong homeotropic anchoring at the air interface was imposed using Dirichlet boundary conditions. Degenerate planar anchoring at the bottom substrate was modelled by applying a flux/source boundary condition with $a_{33} = W_\theta = 10^{-5}$ Jm^{-2}. Thus, at the bottom substrate, an energy penalty is only incurred when the director deviates from parallel to the substrate, allowing the director to orient freely in the substrate plane. Figure 5.21a shows the director configuration in the droplet. The radial alignment at the bottom substrate is caused by the orientation imposed by the top interface only. The model indicates that the curvature of the top interface is sufficient to reorient the molecules at the substrate interface when they are able to reorient in-plane. Figure 5.21b shows the magnitude of the x-y components of the LC director: $n_x^2 + n_y^2$, for the bottom substrate. The central defect point can be seen by the central discontinuity in the figure.

The radial alignment observed in droplets printed on to a partially dry PVA

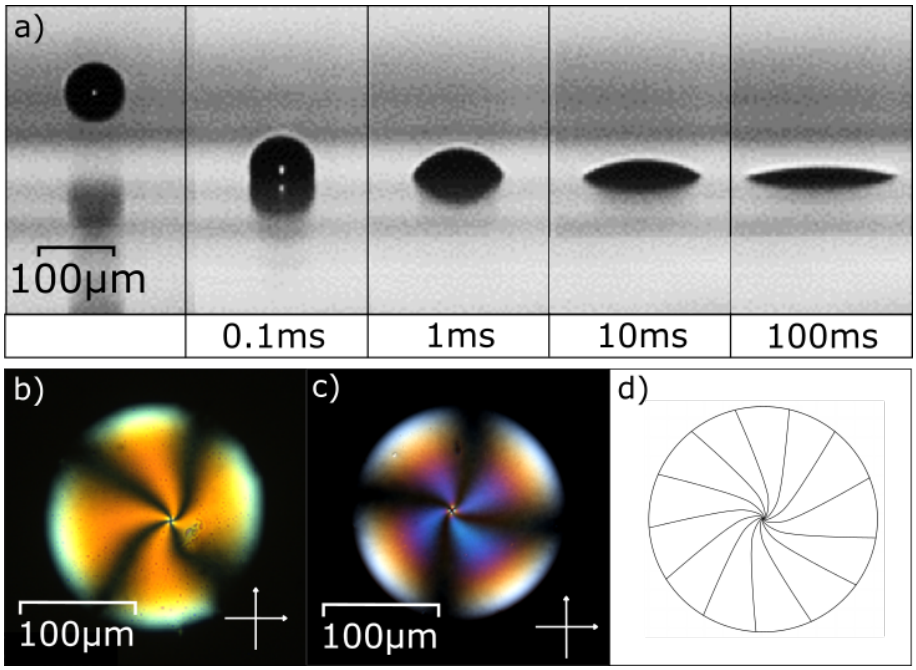

FIGURE 5.20: a) Shadowgraphy images captured with the high-speed camera (15,000 fps) of the deposition of the nematic LC onto a partially-dry PVA substrate. b) and c) Polarized microscopy images of a nematic LC droplet printed onto a substrate at 75% and 90% dryness, respectively (corresponding to 56 and 63 minutes after spreading). d) An illustration of the resultant radial alignment of the nematic LC director.

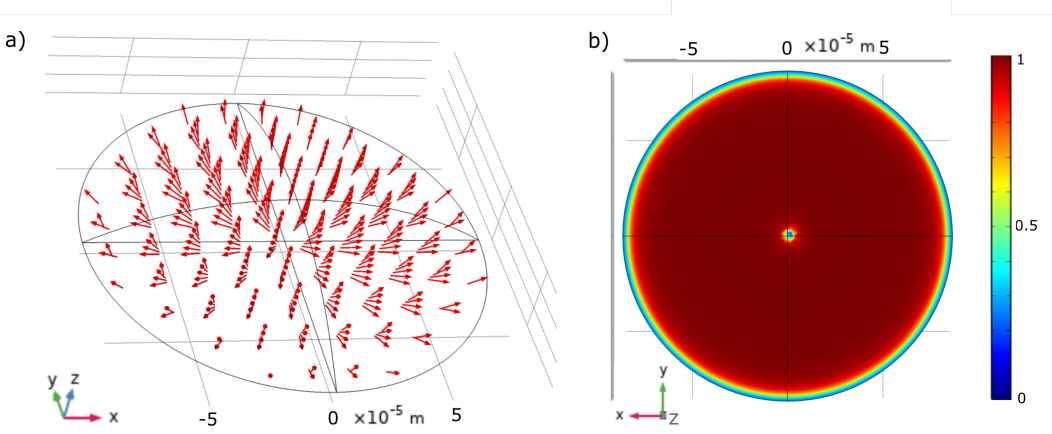

FIGURE 5.21: a) 3D simulation of the director profile within a droplet printed onto a partially dry PVA substrate. b) Surface plot of the normalized x and y components of the local LC director in the radial direction.

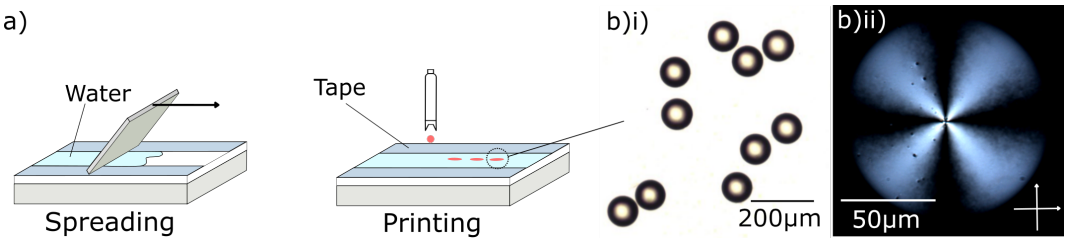

FIGURE 5.22: a) Illustration showing the preparation of a thin-film of water and the deposition of E7 droplets. b)i) Microscopy image of what was originally a line array of droplets 3 minutes after printing. b)ii) Polarised microscopy image of a droplet deposited onto a film of de-ionised water.

layer is attributed to the ability of the LC director to reorient at the substrate surface, presumably due to the increased concentration of water. The LC director is encouraged to align radially because of the curved top surface, as indicated by the Figure 5.21. Additionally, the radial flow of LC during the wetting phase is of sufficient velocity to align the LC director in a direction parallel to the flow.

5.5.5 Pre-wetting of Polymer Substrate

A major problem using the partially dry PVA substrate was the non-uniform drying of the PVA film. This is a natural phenomena of evaporating films and difficult to control. This results in relatively large variations in the droplet diameter and uniformity of the LC director between droplets printed in a single sample, particularly in large area films. As it is hypothesised that favourable radial alignment is due to the presence of a thin layer of water at the surface, such radial alignment may also be achieved by pre-wetting a dry PVA film before printing.

Printing into a Thick-Film of Water

As an initial test, a film of deionized water was coated on top of a microscope slide by the process shown in Figure 5.22a. Due to the high surface tension of water and the relatively hydrophobic nature of the glass slide, the resulting film was thicker than the 35 μm tape applied to the slide, approximately 100 μm-thick in the central part of the slide.

After deposition, the LC droplets were free to move on top of the water film and were seen to flow quite readily. However, the droplets were seen to retain a

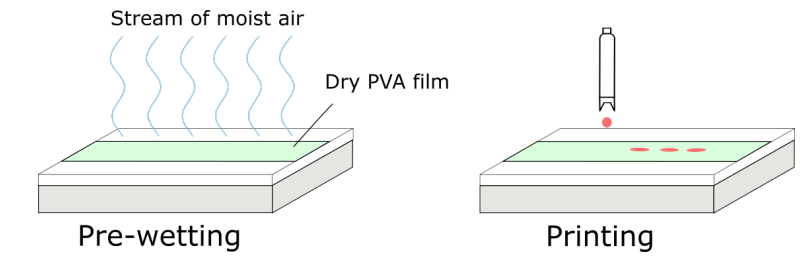

FIGURE 5.23: Process used to 'pre-wet' the dry PVA films.

circular droplet boundary. A partial wetting configuration was expected and observed due to high surface tension of water (Equation 5.6). Figure 5.22b)i) shows a microscopy image of the droplets 5 minutes after deposition onto the film of water. The position of the droplets had completely changed, however, the droplets retained a homogeneous droplet boundary approximately 100 μm in diameter. As hypothesised during the printing onto a wet PVA layer, the droplets show excellent radial alignment, indicated by the POM image in Figure 5.22b)ii).

Printing in High Humidity

Rather than printing onto a thick-film of water which results in an unpredictable final droplet location, it would be desirable to pre-wet the PVA film whilst having minimal impact on the printing process and final drop location. To achieve this, the LC was deposited onto a dry PVA layer in a high humidity environment. Humidity was increased by using a humidifier (Humidifier Digital Hygro+), which was placed next to the printing substrate. Dry PVA films were prepared using the process described in Section 5.5.1 and left to dry in ambient conditions for 4 hours.

Figure 5.24a shows POM images taken with the humidifier placed in the vicinity of the printing substrate. The images are indistinguishable from POM images of droplets printed onto a dry PVA substrate (Figure 5.17). To further increase the moisture level of the dry PVA films, the substrates were placed directly under the stream of moist air generated by the humidifier, as illustrated in Figure 5.23. In practise, this was achieved by moving the substrate directly underneath the humidifier for a set amount of time in the pre-print sequence.

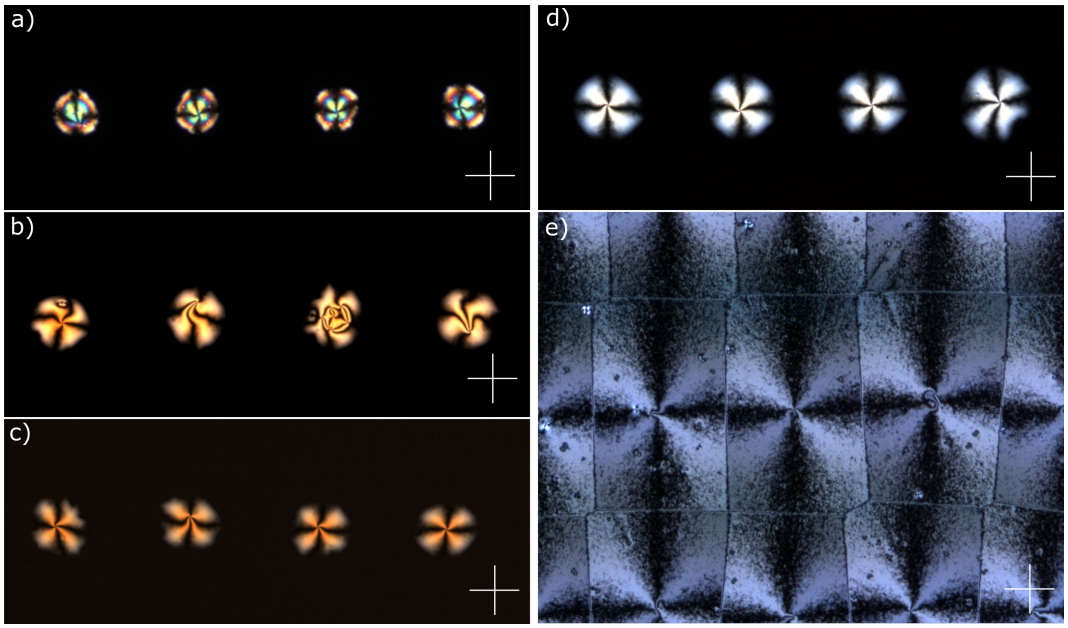

FIGURE 5.24: Polarised optical microscopy images of E7 droplets deposited onto a dry 80 μ-thick PVA film that had been: a) Printed in ambient humidity. b) Subject to 1s under the humidifier prior to printing. c) 2s under the humidifier prior to printing. d) 3s under humidifier before printing. d) 4s under humidifier prior to printing.

Figures 5.24b-e show POM images of droplets printed onto substrates exposed to the moisture stream for increasing amounts of time. It appears that longer exposure to the moist air results in more uniform radial alignment, with less evidence of defects. Increased moisture levels also leads to larger droplet diameter. Figure 5.24e suggests there is a transition from partial to complete wetting at approximately 4s exposure and the images closely resembles those of droplets printed onto a fully wet PVA substrate (Figure 5.18). The box-like structures in the figure indicate where the perimeters of adjacent droplets have come into contact. Printing onto a pre-wetted PVA substrate appears to yield similar results to printing onto a partially dry PVA film with exposure times between 2-3s (Figures 5.24c and d).

5.6 Conclusions

For the inkjet printing of LCs, the choice of printing substrate is of critical importance. In addition to conventional inkjet printing processes such as drop impact

and wetting, the alignment of the LC director must also be considered. Splashing during drop impact is suppressed due to the high viscosity of the LC and is not observed at any droplet velocities accessible by the printhead. Further, the time-scale of drop impact is much less than LC relaxation time, indicating that impact mechanics does not significantly affect the director configuration. The extent the LC wets the substrate is governed primarily by the balance of surface tension and droplets assume the shape of a spherical cap.

Several different conventional and non-conventional LC substrates were investigated. The Nissan SE4811 coated substrate produced droplets with excellent homogeneity of the droplet boundary and uniform homeotropic alignment. The outcome of droplets deposited on planar-aligned surfaces was strongly dependent on the pretilt of the substrate. Some surfaces produced uniform droplet boundaries with a dislocation line running perpendicular to the rubbing direction. On the other hand, some surfaces induced what appears to be full and anisotropic wetting for a LC drop, and uniform partial wetting of an isotropic fluid such as water.

By printing onto a semi-dry (partially-wet) PVA layer it was found that both a circular droplet boundary and uniformity of the LC director could be achieved simultaneously. It is supposed that the wetness of the PVA film allows for the LC molecules to reorient at the substrate surface. Radial alignment is encouraged by the flow generated during the spreading of the droplet and by the curvature of the LC/air interface, which is supported by modelling the LC director in hemispherical droplets with degenerate radial alignment. Radially aligned drops can also be achieved by pre-wetting a dry PVA which may prove a more efficient method of aligning printed droplets.

Chapter 6

Inkjet Printing of Microlens Arrays

In this chapter, the inkjet printing of a thermally tunable nematic LC microlens with polarisation independent focussing properties is shown. The printing conditions and choice of substrate discussed in Chapters 4 and 5 are tailored to produce highly reproducible and uniform LC lenses. It is demonstrated how inkjet printing can be used to quickly fabricate bespoke arrays of lenses on demand. The thermal tuning of the focal length is then demonstrated. Finally, the chapter considers an encapsulated LC lens and goes on to demonstrate the inkjet printing of a LC/prepolymer formulation that could be used to fabricate encapsulated polymer-dispersed LC lenses.

6.1 Introduction

Microlens arrays are fundamental micro-optical components used in a wide variety of imaging, sensing and optical communications applications [108]. Due to their small geometric profile and optical properties, microlenses are perfectly suited to light collection applications where space is limited; for example, they are commonly found in CCD cameras, photovoltaic cells and fibre optic bundles [109, 110, 111]. Historically, microlens arrays have been manufactured using multi-step processes such as photolithography, resit-melting and hot-embossing [112, 113, 114]. Although highly scalable, these techniques are limiting with respect to the range of compatible materials and possible substrate geometries. Moreover, these

techniques often require a master lens array template which can increase the cost and complexity in the ad-hoc fabrication of bespoke microlens arrays [115].

A variable focus microlens adds extra functionality as it has the ability to change the focal distance without the use of multiple lens systems or mechanical displacement. This has the effect of reducing the number of components required during manufacturing and allows smaller and more compact devices to be produced. Applications using variable focus microlenses include optical communications, sensing [116], lab-on-a-chip [117], image processing and switchable 2D/3D displays [118]. Current methods for achieving compact tunable microlenses include liquid-filled elastic lenses [119, 120], electro-wetting lenses [121], responsive hydrogels and LC lenses[122, 123]. Liquid-filled microlenses achieve variable focussing by using microfluidic networks to control the volume of an isotropic liquid encased in an elastic membrane, thus changing the radius of curvature of the microlenses. In electro-wetting microlenses, an electric potential is generated between a liquid droplet and the substrate, which is coated with an insulating layer. The field is varied to change the curvature of the droplet and the extent to which it spreads on the substrate. Hydrogel-based microlenses use a responsive hydrogel as the lens material which swells in response to change in stimuli such as temperature, humidity or pH. Liquid-filled, electro-wetting and hydrogel microlenses all achieve adaptive focussing by changing the shape of the lens.

6.1.1 Liquid Crystal Microlenses

Adaptive LC lenses have gained much attention due to their low power consumption, voltage actuation and small footprint [124]. The ability of the LC director to reorientate in the presence of externally applied stimuli allows for control of the refractive index and consequent focussing properties without any mechanical deformation of the lens profile, or the need for complex microfluidic control [42]. Current LC lenses rely upon a gradient refractive index distribution (GRIN) across the LC cell. This is achieved by creating a change in the LC director profile across the cell.

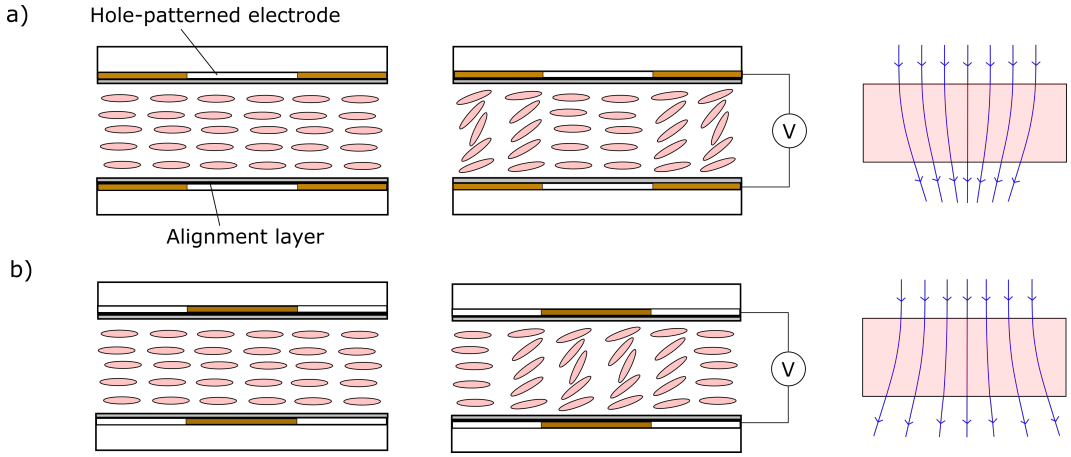

FIGURE 6.1: Schematic of a LC GRIN lens using a hole-patterned electrode to achieve a non-uniform switching field. The voltage on and off states are shown, as well as the resulting optical ray path through the LC medium for: a) Converging, or positive lens. b) Diverging, or negative lens.

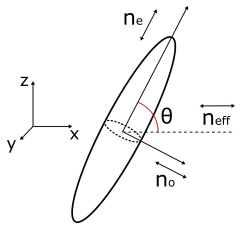

FIGURE 6.2: Diagram of a LC molecule oriented at an angle (θ), showing the ordinary (n_o), extraordinary (n_e) and effective (n_{eff}) refractive indices with respect to incident light, polarised in the direction of n_{eff}.

In the formation of a GRIN LC lens, two common approaches are used to produce the required LC director profile. The first is the application of an inhomogeneous electric field to a homogeneously aligned nematic LC device, often produced using curved or hole-patterned electrodes [122, 125, 126, 127]. Figure 6.1 illustrates how a hole-patterned electrode can be used to create an equivalent convex (a) and concave (b) lens in the voltage on state. The other method relies on an inhomogeneous LC morphology induced either via specially treated alignment layers [128, 129], or by using the polymer-scaffold method to fix the orientation of a portion of the LC cell [125, 130, 131]. Figure 6.1 is an example of an inhomogeneous electric field being applied to a homogeneously aligned planar cell.

6.1.2 Operation Principle of a LC GRIN Lens

Figure 6.2 shows a thermotropic LC molecule oriented at an arbitrary angle θ. The effective refractive index (n_{eff}) for incident light that is linearly polarised in the direction of x can be determined by considering the contributions of the ordinary and extraordinary refractive indices:

$$n_{eff} = \frac{n_e n_o}{\sqrt{(n_e sin\theta)^2 + (n_o cos\theta)^2}}\,, \tag{6.1}$$

The optical path difference (OPD) is used to determine the phase difference of incident light after passing through the LC cell. The maximum possible OPD for a nematic cell can be determined by comparing the optical path of linearly polarised light passing through a uniform planar and uniform homeotropic nematic LC cell. Considering a planar aligned cell (as shown in Figure 6.1), if the light enters the cell normal to the glass substrate and is polarised in the direction of the easy axis, the optical path lengths are: $L_1 = dn_e$ and $L_2 = dn_o$ for the planar and homeotropic cell respectively, where d is the cell thickness.

For light of wavelength λ (in a vacuum), the OPD results in a phase difference of:

$$\Delta\phi = \frac{2\pi}{\lambda} d(n_e - n_o)\,. \tag{6.2}$$

However, taking the LC tilt angle (θ) into consideration and using Equation 6.1, the phase difference becomes:

$$\Delta\phi = \int_0^d \frac{2\pi}{\lambda} \left(n_{eff} - n_o\right) dz\,. \tag{6.3}$$

The effect on the phase is equivalent to that imposed by an isotropic material of varying thickness. Figure 6.3 shows the optical ray path and focussing of a GRIN lens. The focal length, or optical power, can be found by considering the OPL for a ray travelling through the center of the GRIN lens: $OPL_{(r=0)} = nd + f$. According to Fermat's principle of least time, this will be equal to the OPL through the edge of the GRIN lens: $OPL_{(r)} = n(r)d + \sqrt{r^2 + f^2}$, where f is the focal length, n and $n(r)$ is the refractive index at the center and edge of the lens respectively.

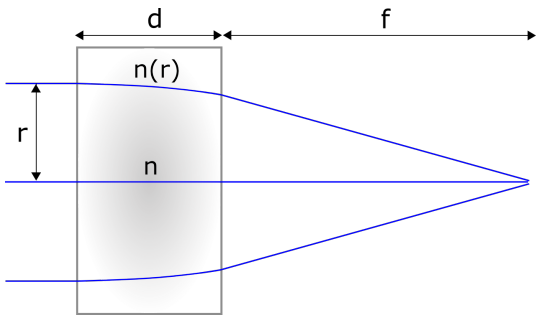

FIGURE 6.3: Illustration showing the optical ray path through a material with a gradient index (GRIN), where d is the sample thickness and f is the focal length.

Applying Fermat's principle in the paraxial approximation [132]:

$$nd + f \approx n(r)d + \sqrt{r^2 + f^2}\,. \tag{6.4}$$

Taking $\delta n = n - n(r)$ and using :

$$\delta n d + f \approx \sqrt{r^2 + f^2} \approx f\left(1 + \frac{r^2}{2f^2}\right)\,, \tag{6.5}$$

$$f \approx \frac{r^2}{2\delta n d}\,, \tag{6.6}$$

where f is the focal length, r is the radius of the lens, d is the thickness of the LC layer and δn is the refractive index difference between the centre and perimeter of the lens, which cannot exceed the birefringence of the LC Δn.

From Equation 6.6, for a given lens radius the focal length is dependent on the birefringence of the LC and the thickness of the cell. The typical diameters of LC GRIN microlenses range from 20 to 1000 μm, with focal lengths in the range of 200 μm to ∞ [124]. GRIN lenses often have large focal lengths unless the cell is very thick. For example, for a lens radius of 5 mm and a focal length of 22 mm (average values for the lens in the human eye) and using E7 as the LC material, the LC GRIN lens would need to be at least 2.8 mm thick (compared to a 22 μm thick human lens). A cell of this thickness would have very slow switching speeds, be very difficult to achieve uniform alignment through the bulk of the cell and have low optical transmission. Highly birefringent LCs can be used to decrease the

focal length. However, such LCs are highly viscous which increases the response time (see Equation 6.11 on page 145).

In addition to large focal lengths, LC lenses fabricated in this manner have polarisation dependent focussing properties due to the uniaxial alignment imposed by alignment layers. It is possible to design LC lenses that are not polarisation dependent via the use of isotropic materials such as blue phase LCs [133, 134], residual phase modulations [135] and photoalignment [136]. Due to the complex fabrication procedures required to form such lenses and the relative instability of blue-phase LCs, they are not readily compatible with low-cost, highly scalable manufacturing processes such as printing.

6.2 Printed Nematic LC Lens

The precision jetting of UV-curable optical polymers to form in-situ fixed-focus microlenses has been widely demonstrated in recent years and it has since become a key technology in the production of cost-effective microlens arrays [137]. The deposition of UV-curable, low-viscosity polymers was first demonstrated by MacFarlane et al. [138]. The spherical cap formed by the microlenses was exploited to form plano-convex microlenes with diameters between 50 and 150 μm with focal lengths ranging from 50-150 μm. Since then, the inkjet printing of a range of different isotropic photo-curable polymers has been demonstrated to form fixed-focus microlenses [139, 140]. By depositing a curable polymer onto a pre-patterned substrate, produced via photolithography to form hydrophilic and hydrophobic regions, the packing density of the lenses can be increased as well as more control over radius of curvature [141].

Despite the success of DoD inkjet printing in the fabrication of efficient, low-cost, fixed-focus microlenses, the technique has yet to be applied to the fabrication of variable focus microlenses. This section demonstrates a printed LC microlens by forming a sessile nematic LC droplet on impact with a treated glass substrate. In addition to leveraging the numerous positives of DoD inkjet printing, lenses produced in this manner have intrinsically short focal lengths due to the curved

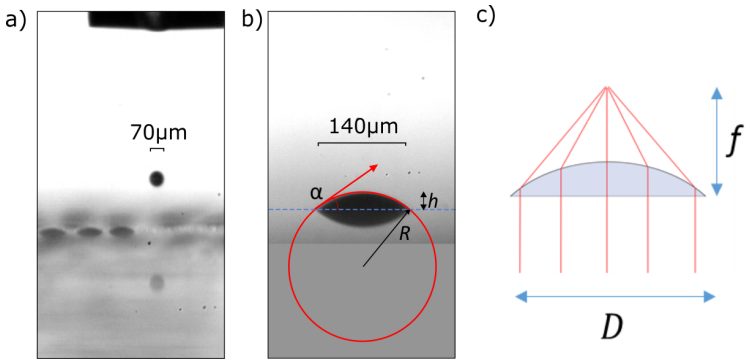

FIGURE 6.4: High-speed images (15,000 fps, 8 μs exposure time) taken during the printing process. a) An array of homogeneous LC microlenses being printed. b) Example of a single sessile drop with a plano-convex profile (reflection of the glass substrate can also be seen). The radius of curvature is defined as R, contact angle as α and droplet height as h. c) Schematic illustrating a sessile droplet acting as a plano-convex spherical lens.

LC/air interface and, depending on the alignment of the substrate, polarisation independent focussing properties.

6.2.1 Experimental

Droplets of the nematic LC E7 (Merck KGaA) were printed and visualised using the experimental set-up shown in Figure 4.1 on page 60[1]. This LC was chosen as it is well characterised, has good birefringence and a clearing temperature which is accessible using the selected printhead. The printhead used was a MJ-ABP-01-80 dispenser (Microfab Technologies inc) with a 80μm nozzle diameter. A printing temperature of 60°C was chosen in order to raise the LC above the clearing temperature. At this temperature, the rotational viscosity of the fluid is reduced from 252mPa.s to approximately 20 mPa.s, sufficient to reliably deposit the LC using inkjet printing. Additionally, at this temperature, the anisotropic components of the viscosity disappear, leading to increased homogeneity in the droplet properties (See §4.5.2 for details). Glass microscope slides coated with the Nissan (SE4811) polymer (as described in §5.4.3) were chosen as the printing substrate due to the excellent homogeneity of the droplet boundary and the strong homeotropic alignment imposed.

[1]Unless explicitly stated, the experimental conditions were as described in §4.6.2 and Table 4.3 on page 78.

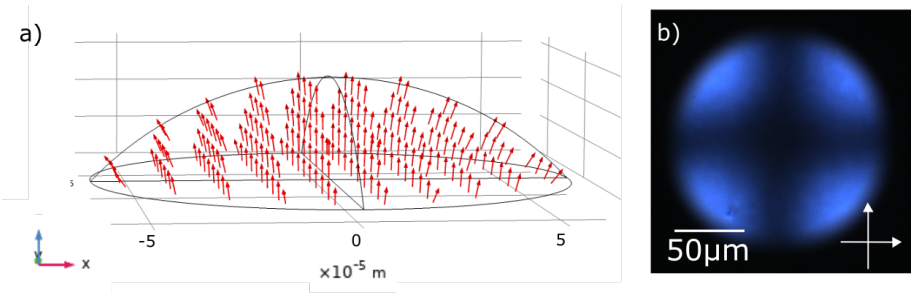

FIGURE 6.5: a) Model of the LC director profile within the droplet. b) Polarised microscopy image of a single nematic microlens between crossed polarisers.

6.3 Results and Discussion

The criteria for successful LC lens formation is a stable droplet boundary, uniform alignment of the LC director and repeatability of the printed volume. Figure 6.4a shows high-speed images of a LC droplet being deposited as part of an array. The impact velocity of the droplet was 1.5 ms^{-1} which, as discussed in §5.2.1 ,is well below the point at which splashing may occur. After impact with the printing surface, equilibrium of the LC droplet diameter and contact angle $\alpha = 28.5°$is reached in under 10 ms, with no observable hysteresis of the contact angle.

The final droplet diameter using a single droplet was 144 μm with a standard deviation of 0.6 μm (equivalent to the analysis presented in §5.4.3). As discussed in §5.2.2, the effects of gravity on the printing process and droplet shape are negligible. Due to the reduction of the surface free energy, the droplet assumes the shape of a spherical cap of radius R, displayed in Figure 6.4b.

The focal length f of a lens is given by the lens maker equation for a thick lens:

$$\frac{1}{f} = (n-1)\left(\frac{1}{R_1} - \frac{1}{R_2} + \frac{(n-1)\,d}{nR_1R_2}\right), \tag{6.7}$$

where n is the refractive index of the material and R_1 and R_2 are the radii of curvature describing the shape of the lens and d is the lens thickness. For a plano-convex lens, whereby $R_2 \to \infty$, this reduces to:

$$f = \frac{R}{n-1}. \tag{6.8}$$

Evidently, the focal length f can be selected by changing either the radius of curvature R or the refractive index n of the lens material. Comparing Equations 6.6 and 6.8, the focal length for a nematic droplet lens (in air) is intrinsically shorter due to the curved LC/air interface. As the lens aperture (equivalent to the droplet diameter) is very small, any incident light can be assumed to be collimated, shown schematically in Figure 6.4c.

Equation 6.8 assumes a homogeneous refractive index. This would only be true if the droplet had perfect homeotropic alignment such that incident light only interacts with the ordinary component of the refractive index. Figure 6.5a illustrates the director alignment in the lens. The largely homeotropic alignment is confirmed by the polarised optical microscopy (POM) image in Figure 6.5b. The characteristic dark cross, which follows the polarisation axes, implies homeotropic alignment throughout the depth of the lens. However, the blue quadrants in the image indicate a degree of birefringence resulting from the slight tilt of the LC director induced by the upper curved interface. The tilt of the director is present only at the edges of the lens and at the top interface, with a maximum deviation from homeotropic alignment being equal to the contact angle, α. The effect of this tilt on the focussing properties of the microlens was found to be indiscernible and is discussed further in the next section.

6.3.1 Determining the Focal Length

Using collimated light from the microscope, a quick inspection of the focal plane can be done by observing the point at which light diffracted by the microlens is most tightly focussed. In a similar manner, an object can be imaged by the microlens and viewed using a microscope. Figure 6.6a shows an illustration of this process, using a 25 μm grid etched onto a glass microscope slide as the object. Figure 6.6b shows microscope images taken using a 350 μm diameter LC lens with the microscope focused at the planes object, lens and image planes.

An interferometric set-up such as a Twyman-Green or Mach-Zehnder interferometer has been used to measure the profile of solid, isotropic microlenses [142, 143]. However, due to the anisotropic refractive index of the LC lenses, coupled with their spherical profile and small profile makes such methods difficult to use

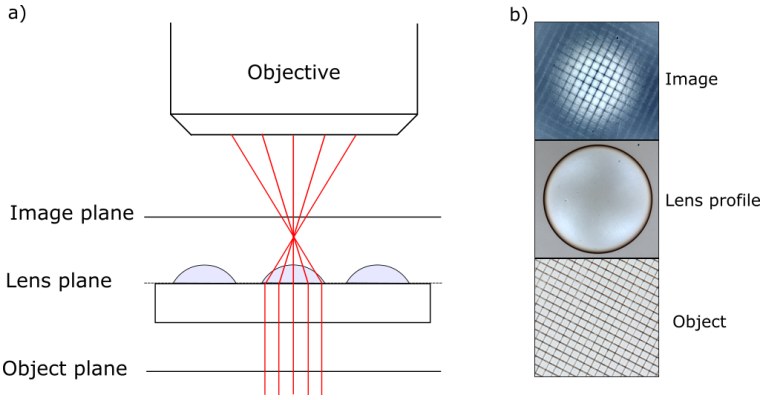

FIGURE 6.6: Illustration of using a microscope to visually inspect the image plane of the LC microlenses. The images on the right are microscope images taken of the indicated planes. The object is a regular 25 μm grid etched onto a glass microscope slide.

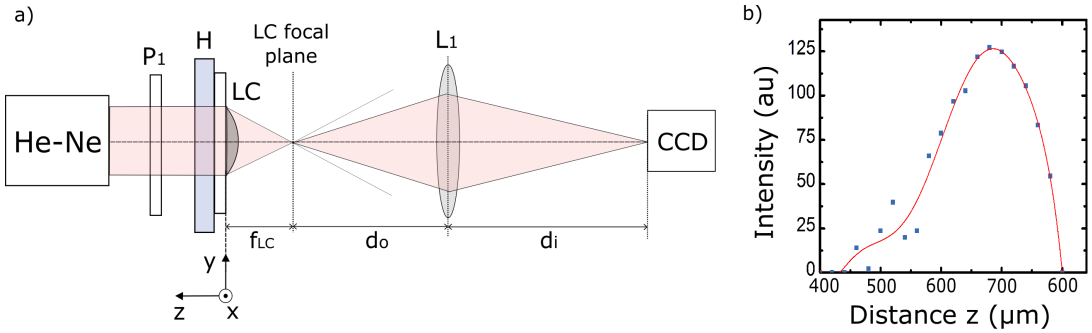

FIGURE 6.7: a) The optical set-up for determining the focal length of the microlens arrays, where L_1 is a biconvex lens with a fixed focal length of 25 mm, P_1 is a linear polariser, H is a heating element and LC is the liquid crystal microlens array. b) Shows the variation in the light intensity measured at the CCD of a 350 μm diameter lens as the array is moved in the positive z-direction. The peak in the intensity curve corresponds to the focal length of the microlens.

for liquid microlenses. The majority of literature characterising the focal length of variable-focus liquid microlenses uses focal spot analysis similar to that described below [144, 145, 146].

An evaluation of the focal length was undertaken using the optical arrangement shown in Figure 6.7a. A continuous wave He-Ne laser (λ =632.8 nm) was used to illuminate the sample. This light source was chosen to remove chromatic aberration and ensure incident light is highly collimated. Initially, the lens L_1 and CCD were positioned such that an in-focus image of the LC lens substrate surface was formed at the CCD ($z = 0$). A series of images were then taken as the LC

microlens array was translated in the positive z-direction in 25μm intervals using a mechanical translations stage. The focal length of L_1 was chosen to be 25 mm such that the distances d_o and d_i were 30 mm and 150 mm respectively[2]. This configuration gave a clear image of the LC Lens plane and utilised the majority of the CCD sensor. Additionally, laser light that was not focussed by the LC microlens was sufficiently refracted by L_1 so that it did not fall on the CCD sensor and saturate the pixels.

A drawback of using such an approach to determine the focal length of the LC microlenses was quantitatively determining the focal length from pixel intensities measured by the CCD. The paraxial approximation in Equation 6.8 is valid for small angles of refraction θ, so that $sin\theta = \theta$. For a spherical lens, such as those formed by a sessile droplet, light is refracted more towards its outer edge. This is particularly prominent for lenses with small radii of curvature and has the effect of elongating the apparent focal plane. Figure 6.8a models the ray tracing of collimated light ($\lambda = 632.8$ nm) through a LC lens with a diameter of 144 μm and a single refractive index equivalent to the ordinary refractive index of E7 ($n = 1.52$). The model, produced in COMSOL, uses a more exact approximation of $sin\theta$:

$$sin\theta = \theta - \frac{\theta^3}{3!} + \frac{\theta^5}{5!}... \tag{6.9}$$

Although the model does not take into account any variance of the refractive index of the lens due to the tilt of the LC director, it clearly illustrates the significance of monochromatic spherical aberration in micro-spherical lenses. The 'circle of least confusion' is defined as the point with the minimal vertical distance between rays refracted by the lens and is indicated on Figure 6.8. As shown in the figure, there is approximately a 50 μm distance between the circle of least confusion and the paraxial focal length.

The images in Figure 6.8b were taken at the planes indicated using the optical arrangement shown in Figure 6.7a for a 144 μm LC diameter lens. The difficulty in assessing the focal length is evident as there is not only spherical aberration, but also constructive and destructive interference of the coherent laser light. This

[2]Note that distances d_o and d_i were varied when determining the focal length of larger lenses to ensure as much of the CCD sensor was being used as possible.

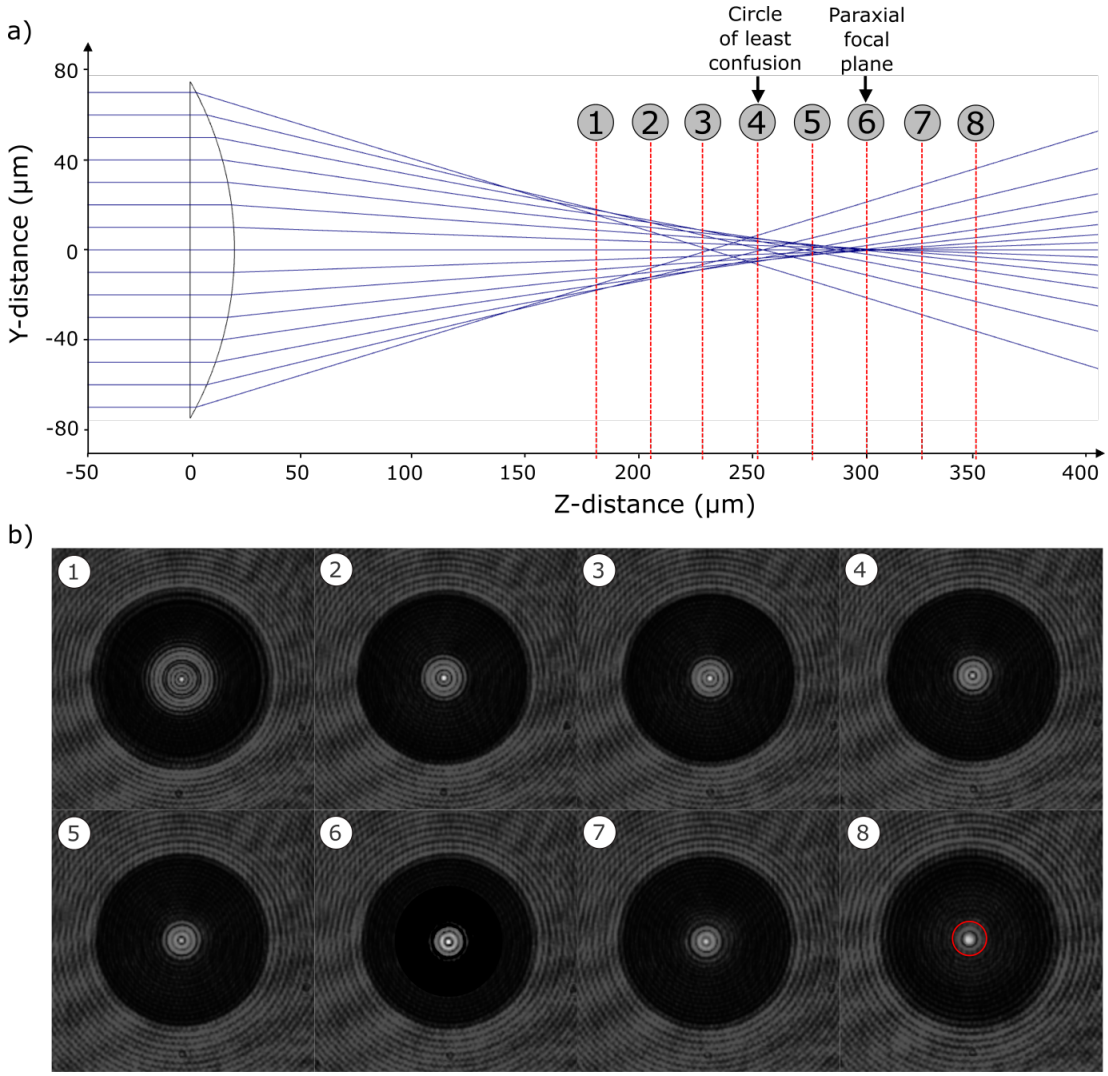

FIGURE 6.8: a) Model of light rays being focussed by a plano-convex lens of the same dimensions as a LC lens (144 μm) and a single refractive index equal to the ordinary refractive index of E7 ($n = 1.52$). Spherical aberration is evident with the light rays converging at different points along the z-axis. The paraxial focal length and the circle of least confusion are indicated on the figure. b) CCD images take at the planes indicated using the optical set-up shown in Figure 6.7a for a 144 μm diameter LC lens.

made determination of the focal length using just maximum pixel intensities difficult. Close to maximum pixel intensities were detected in the images labelled 2-7, such that fitting a parametric curve did not yield a reliable focal length.

To circumnavigate this problem, a MATLAB script was written to integrate the pixel intensities around a circular central region of interest. Evidently, the choice of diameter of the central region is critical. Edge detection with a mean-value threshold was applied to a far-field image of the lens plane to determine the area of this region of interest. Such a region is indicated on image 8 in Figure 6.8b. The average pixel value of this region was then plotted against horizontal displacement z and a curve fitted to determine the focal plane of the lens. Figure 6.7b shows such a plot for a larger LC lens.

Such approach offers a standardised means of determining the focal length of lenses with different diameters and focal lengths. The method was tested using a manufactured lens of known focal length with good agreement. The measured focal lengths were also cross-checked using a microscope and in-focus object/image formation (shown in Figure 6.6), again to good agreement. The estimated error in the mechanical translation stage is ± 5 μm, whilst the estimated error in determining the focal length using the MATLAB program was deemed to be ± 15 μm. This error was estimated by considering the uncertainty in determining the peak intensity against substrate position shown in Figure 6.7b. This gives a total error of ± 20 μm. This may seem like a large error, however, it represents $< 15\%$ of the shortest focal length measured. Moreover, the method was suitable for assessing the validity of the inkjet printing technique and the tunability of the lenses.

Figure 6.9a shows an example of the variation in intensity along the x-direction of a 140 μm diameter lens at the focal plane. The lenses demonstrates good focussing properties indicated by the narrow spike in pixel intensity measured at the focal length. An optical power meter (PM100D, Thorlabs) was used to determine an optical transmission of 74% for a 144 μm lens, which is comparable to other LC microlenses. However, as most LC lenses require an additional polarising film, the transmission of most LC GRIN lenses are $< 50\%$ [124].

A property of lenses fabricated in this manner is the polarisation independent focussing properties. Collimated incident light will interact predominantly with

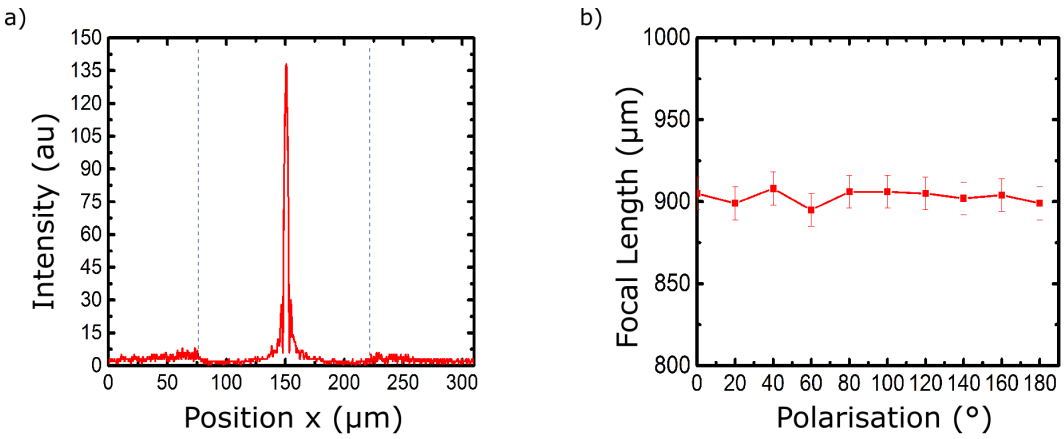

FIGURE 6.9: a) The intensity cross-section at the focal plane of a 140!μm diameter lens, the dotted lines indicate the corresponding position of the lens perimeter. b) The focal length of a single 450!μm diameter microlens as a function of the orientation of incident linearly polarised light.

the ordinary component of the refractive index n_o. Due to symmetry of the director profile, the focussing properties of the microlens will be constant for light that is normal to the lens plane, regardless of its polarisation state. This is exemplified in Figure 6.9b, which shows the focal length of a single 450 μm diameter lens as a function of the orientation of linearly polarised incident light.

6.3.2 Pre-selecting the Focal Length

The focal length can be selected by changing the radius of curvature of the lens or the refractive index. The radius of curvature can be varied by changing either the contact angle or the lens volume. The contact angle is given by Young's equation: $\sigma_S - \sigma_{SL} - \sigma_L \, cos\alpha = 0$, and is fixed for a given fluid and substrate. On the other hand, the relationship between the lens volume, radius of curvature and contact angle is given by the equations of a spherical cap discussed in §5.2.2.

Increasing the contact angle will result in a smaller radius of curvature and correspondingly shorter focal length. A hydrophobic coating EGC-1700 (3M Novec) which consists of a single component fluorinated polymer (2%wt) diluted in a hydrofluoroether solvent was used to decrease the surface tension between the LC and substrate. As recommended by the suppliers, the coating was applied by dip-coating a clean glass substrate into the solution and leaving it to dry for 10

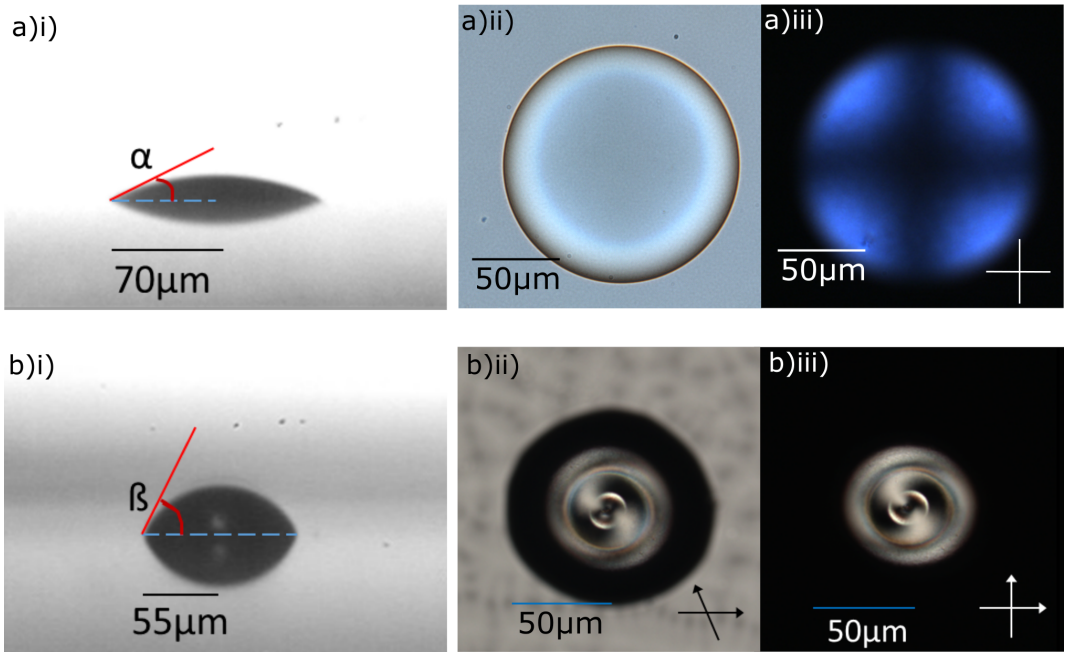

FIGURE 6.10: a)i) High-speed images of the equilibrium droplet profile of E7 printed onto a Nissan-coated glass substrate with a contact angle $\alpha = 28.5°$. a)ii) Microscopy image of a single droplet. a)iii) Polarised microscopy image of the same droplet with the polarisers crossed. b)i) High-speed images of the equilibrium droplet profile of E7 printed onto a hydrophobic-coated glass substrate with a contact angle $\beta = 65°$. b)ii) Polarised optical microscopy image of the same droplet with the polarisers uncrossed. b)iii) Polarised microscopy image of the same droplet with the polarisers crossed.

minutes under ambient conditions. Once the solvent has evaporated off, a thin approximately 200 nm thick layer of polymer remains, henceforth referred to as the 'hydrophobic' surface.

Figure 6.10a)i) and b)i) compares the contact angles of a single droplet of E7 deposited onto the Nissan-coated and hydrophobic substrates. The contact angle, labelled β on the figure, was measured to be 65°. Although effective at changing the contact angle, such coatings will completely change the alignment at the LC interface. This is evident when comparing the POM images in Figures 6.10a)iii) and b)iii). There is a birefringent spiral structure observed in the centre of Figure 6.10b)iii), which persists despite the orientation of the polariser, suggesting that the LC director is non-uniform. It is noted that the dark outer rim observed in b)ii) and b)iii) are not a result of the LC alignment, rather it is the microscope objective lens being unable to collect the highly divergent light focused by the droplet. The reasoning of such alignment is unclear. However, it is likely due to a combination of the coating being weakly homeotropic with some degeneracy and increased curvature of the top interface (R is approaching that of the radius of the lens). Nevertheless, the non-uniform LC director in droplets deposited onto the hydrophobic surface resulted in them acting as poor lenses, with no identifiable focal spot or object/image formation.

Changing the interfacial chemistry of the substrates was found to be unsuitable for selecting the focal length of the lenses due to effect on the LC alignment. The hydrophobic droplets produced poor images when inspecting the focal plane using a microscope. The other means of selecting the focal length is by changing the lens volume. Using inkjet printing, it is possible to make small changes to the droplet volume, and subsequent lens diameter and focal length, by changing the duration of the driving waveform. However, as described in §4.4.2, this can lead to jet instabilities and the formation of satellite droplets. Instead, large changes in the lens diameter were achieved by printing multiple droplets onto the same position. Figure 6.11a shows a high-speed image of 10 droplets being printed onto the same location at 5,000 drops per second. Figure 6.11b compares the equilibrium droplet shape of two lenses with different diameters but the same contact angle, α.

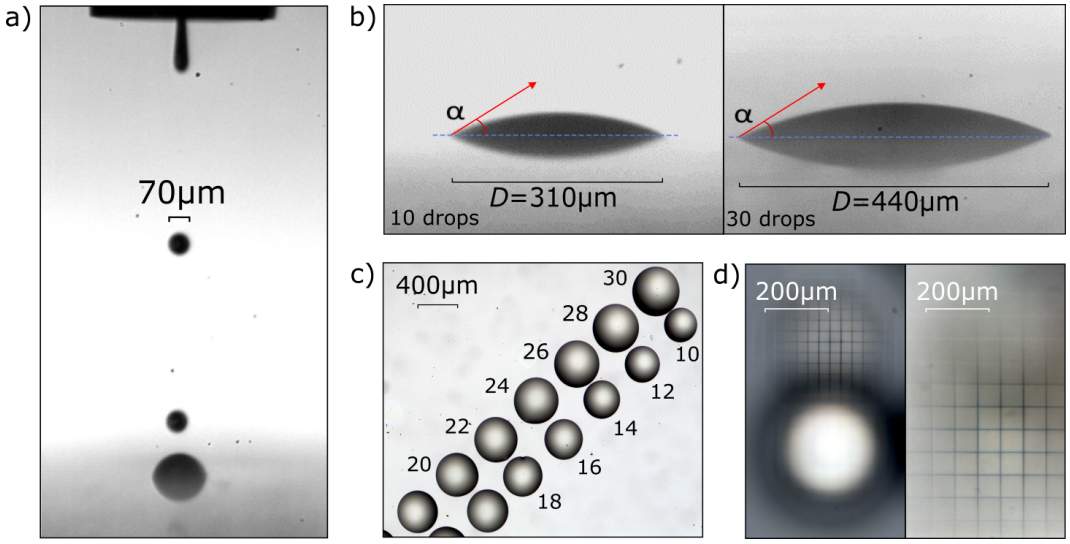

FIGURE 6.11: a) High-speed camera images (15,000 fps, 5 μs exposure time of: a) Multiple droplets being printed at the same location to form a larger lens (5,000 drops per second), and b) Two spherical plano-convex lenses with different droplet diameters D, but the same contact angle, α. c) Microscope image of a microlens array with different diameters. The numbers indicate the number of individual droplets printed in each microlens. d) Optical polarising microscopy images showing the real image formed of a 25 μm spacing grid placed under two lenses of different diameters. The left image is focussed at the image plane for the smaller lens with a focal length of 610 μm, whereas the right image is focussed at the larger lens image plane with a focal length of 880 μm.

The f-number ($N = \frac{f}{D}$) is a dimensionless parameter which characterises the ability of a lens to collect light, with lower f-numbers corresponding to more efficient light collection. As the contact angle of a spherical cap is proportional to its radius of curvature and corresponding focal length, the f-number of lenses printed on the same substrate with the same fluid will be constant, regardless of lens diameter. In our configuration this resulted in a relatively low f-number of $N = 2$. This is comparable to that of glass and plastic microlenses produced using techniques such as photolithography and resist melting, making them suitable for optical communication and imaging applications [147].

A printed array of microlenses of different diameters, produced in a single sequence, is shown in Figure 6.11c, the numbers accompanying each lens correspond to the number of constituent droplets printed to form each lens. The difference in focal length is emphasised in Figure 6.11d, which shows microscope images of the real image formed of an underlying 25 μm grid, placed 2 mm below the lens plane. The smaller lens in the figure was formed by printing 10 droplets onto the same position at a print frequency of 3.5 kHz resulting in a focal length of 610$\pm$15 μm. The right hand image of Figure 6.11d shows the in-focus image of the object given by the larger lens which was produced in the same manner, but using 30 droplets, with a larger focal length of 880$\pm$15 μm. The in-focus image is formed at a greater distance from the lens plane and with two times higher magnification.

To investigate the degree of correlation between droplet volume and focal length, the measured focal length (using the method outlined in Figure 6.7a) was compared to the focal length calculated for a perfectly spherical plano-convex lens with the same physical dimensions and a single uniform refractive index that is equivalent to the ordinary refractive index for the nematic LC, E7 determined at 632.8nm ($n_o = 1.52$). As shown in Figure 6.12, the experimental data are in strong agreement with the modelled focal length. This suggests that the radius of curvature of the lens is indeed governed by the droplet volume and is consistent with what we would expect for a spherical cap. Additionally, the strong agreement confirms that the small tilt imposed on the LC director (Figure 6.5b) does not noticeably affect the focussing properties of the lenses.

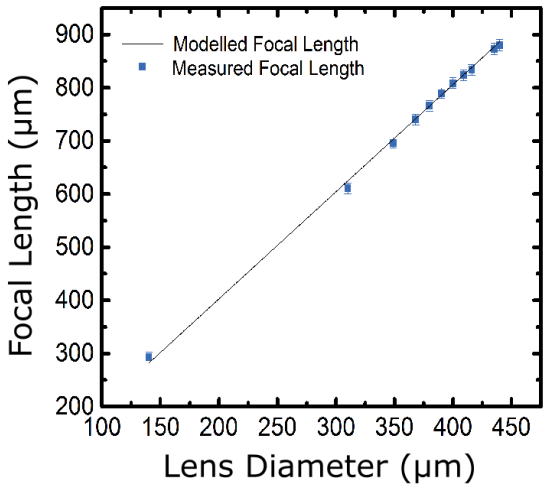

FIGURE 6.12: Focal length as a function of the diameter of a microlens. The solid line represents the results for a perfectly spherical plano-convex lens with a constant refractive index.

6.3.3 Thermal Tuning

To assess the tunability of the microlenses, the focal length was measured over a range of temperatures. The experimental data for a single lens were compared to a model of the focal length of a lens with a uniform refractive index equal to n_o of E7, taking into account the temperature dependency (see Appendix §A.4.1), and constant dimensions equal to that of the printed LC microlens. As seen in Figure 6.13, the experimentally determined focal length decreases as a function of temperature and closely follows the modelled data, which take into account the increase of the refractive index n_o caused by the temperature dependency of the order parameter of the LC. The droplet boundary was also measured as the temperature was changed to assess whether any change in the contact angle and droplet boundary was observed. No observable change in droplet boundary or profile was noted, indicating the decrease in focal length was due to the decrease in the order parameter of the LC as it approached the isotropic phase. It can be seen that for a change in temperature of 40°C, the focal length changes by 60 μm, however, the majority of this change happens within 15°C of the clearing temperature.

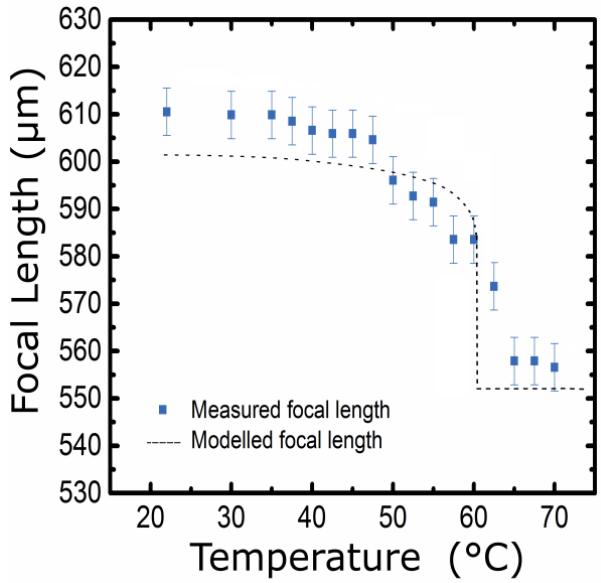

FIGURE 6.13: The focal length of a single microlens as a function of temperature. The modelled focal length was calculated using a uniform refractive index equal to that of E7 over a range of temperatures and using lens dimensions consistent with the printed lens being compared.

6.4 Encapsulated LC Microlenses

A problem with these microlenses is the unprotected free surface of the LC fluid. Without adequate protection, the lenses are easily damaged. Encapsulation of most conventional LC devices is achieved by in-filling the LC into a designated space, often between transparent substrates [42]. The most familiar example being the filling of the glass substrates of an LCD. In a similar manner, the LC lenses could be encapsulated by attaching a top substrate after the LC lenses are deposited and using spacer beads to ensure the droplets are not flattened. The final step would be to fill the air gap with a immiscible polymer such as an optical adhesive. The refractive index of the polymer (n_p) would determine the focussing characteristics of the lens, for example matching $n_p = n_o$ would result in a non-focussing passive state.

The main draw-backs of using such an encapsulation procedure are the additional processing steps required which also render the technique incompatible with the use of curved, or flexible substrates. Moreover, the in-filling of the polymer will change the interfacial chemistry at the LC interface, possibility affecting

both the droplet shape and alignment of the LC.

6.4.1 Polymer-Dispersed LC Microlenses

Ideally, the encapsulation process should not impede the lenses variable focussing properties, or negate the advantages of inkjet printing, such as the ability to produce arbitrary array patterns on a range of different substrates and surface geometries. An alternative method of producing encapsulated IJP LC lenses is now proposed using polymer-dispersed LCs (PDLCs). The following section presents proof-of-concept work on the inkjet printing of a LC/polymer formulation to form (nano)-PDLC lenses.

The LC domains in a PDLC are encapsulated within a polymer matrix. PDLCs are used extensively in optical applications requiring thin, potentially flexible and robust films [148, 149]. There are several methods of producing a PDLC film which are described in greater detail in §7.1. Photo-polymerisation induced phase-separation is used in this study, which produces LC domains that are mostly spherical in shape, with typical diameters ranging between 1-25 μm [150]. Due to the size of the LC droplets and the refractive index mismatch between the LC droplets and the polymer matrix, they will scatter visible light, making them unsuitable for lensing applications. However, if the LC domains formed are smaller than the wavelength of light to be focussed, the scattering becomes negligible.

6.4.2 Operation Principle

Nano-PDLCs have been successfully employed as variable focus microlenses [151]. For example, Ren et al. filled a pre-fabricated concave lens template with a LC and prepolymer formulation and then fastened a top glass substrate. The device was then photopolymerised using conditions sufficient to form nano-PDLC domains. If the LC and prepolymer formulation could be deposited directly then this would leverage the numerous advantages of inkjet printing, significantly improve the efficiency and flexibility of the fabrication process.

Figure 6.14 shows a schematic of a nano-PDLC microlens. As described in §2.3.4, the director in small nematic droplets (diameter$<$1 μm) is free from elastic

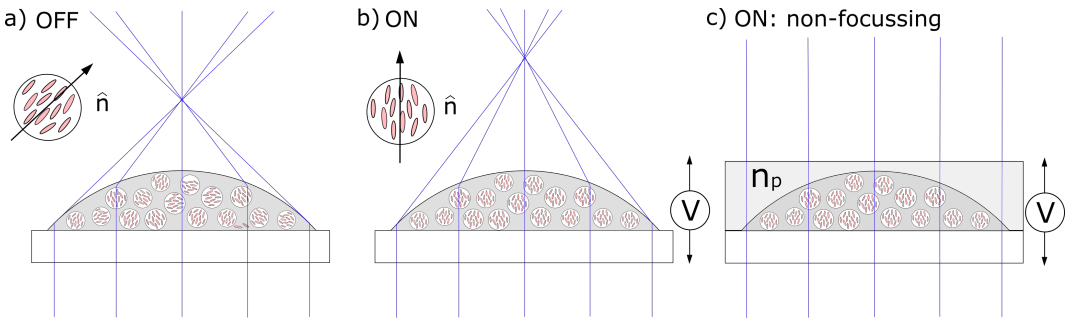

FIGURE 6.14: Side-profile schematic of the operation principle of a nano-PDLC microlens showing electronic switching in the: a) Off, and b) On states. c) Shows how a LC lens with an infinite focal length could be achieved by encasing the lens in a material with a refractive index (n_p) matched to the ordinary refractive index of the LC (n_o).

strain and is uniformly aligned. In the absence of an orienting electric field, the LC director in each droplet points in an arbitrary direction and the droplet has an anisotropic refractive index. The effective refractive index of the lens (n_{eff}) is an average of the refractive index of the polymer (n_p) and the LC droplets ($n_{LC} = (n_e + 2n_o)/3$).

On application of an electric field of sufficient magnitude, the LC director in the droplets will orient in the direction of the applied field. This correspondingly reduces n_{eff} as the refractive index of the LC domains approaches the ordinary refractive index: $n_{LC} = n_o$. As $n_p \approx n_o$, for very strong electric fields, $n_{eff} \approx n_p$.

The voltage-on state of the lens could easily be made to be non-focussing by filling the encapsulated nano-PDLC lens with an optically-matched material, as shown in Figure 6.14c. In this configuration, the focal length of the lens in the OFF state is equivalent to that of a LC GRIN lens (see page 127):

$$f = \frac{r^2}{2d\delta n}, \tag{6.10}$$

where in δn is the difference in refractive index between the center of the lens and the lens border, r is the radius of the lens and d is the thickness.

After photo-polymerisation, the microlenses would be fully encapsulated. Like the lenses presented earlier, the nano-PDLC lenses will also be polarisation independent. As the LC domains are surrounded by a polymer matrix, the alignment

of the LC is independent of the substrate and there is no need for alignment layers. The only consideration of the substrate is contact angle of the droplets formed (or a conductive coating for switching). Additionally, the fabrication technique is fully compatible with flexible and curved substrates.

The response times of the lenses would be fast, making them viable for use in display and beam-steering applications [124]. The response times are the time it takes for the LC director to align with the applied electric field (rise time) and the time taken to relax back to its passive state (decay time). The decay time can be estimated using the relaxation time discussed in §2.4.3:

$$\tau_{decay} = \frac{\gamma_1 d^2}{\pi^2 K_{22}}, \tag{6.11}$$

where γ is the rotational viscosity, K_{22} is the twist elastic constant and d is the droplet diameter. The rise time is given by [152]:

$$\tau_{rise} = \left(\frac{V^2}{V_{th}^2} - 1 \right)^{-1} \cdot \tau_{decay}, \tag{6.12}$$

where V is the applied voltage and V_{th} is the threshold voltage. Note that these values are approximations only, factors such as the droplet shape and proportion of prepolymer still present in the LC domains after photopolymerisation affect the response times [153]. The rise time can be reduced by over-driving the voltage. However, the decay time is fixed by the material parameters, most importantly the LC viscosity.

6.4.3 Experimental

Mixtures of the optical adhesive NOA65 (Norland) and the nematic LC E7 were mixed in a ratio of 65:35%wt. This photo-polymerisable polymer was selected as the refractive index ($n_p = 1.524$) is well matched to the ordinary refractive index of E7 ($n_o = 1.523$), the materials are commonly used together in PDLC applications [154]. Additionally, Ren et al. used this the prepolymer NOA65 and in this ratio to form nano-PDLC lenses [151].

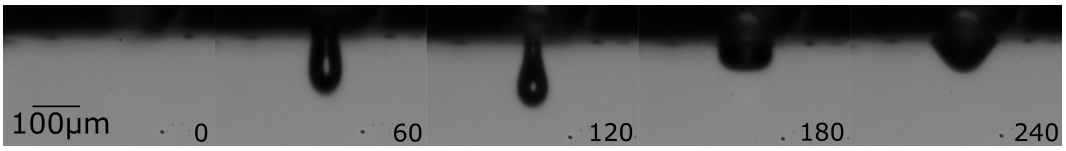

FIGURE 6.15: High-speed images (15,000 fps, 8 μs exposure) of a fluid ligament of E7 and NOA65 (35:65%wt) emerging from the 80 μm nozzle but failing to form a droplet. The numbers indicate the time in μs from the initial piezoelectric deformation.

In order to deposit via inkjet printing, the prepolymer and LC must be miscible at the selected printing temperature. Ideally, the LC must form a single homogeneous phase with the prepolymer so that printed droplets have the same composition of components and phase separation occurs upon photopolymerisation. E7 is highly miscible with NOA65 and a homogeneous mixture of the two components forms even at room temperature (see page 165 for a phase diagram of E7 and NOA65). It is noted that even though a homogeneous mixture of the components is formed at low temperatures, the mixture still needs to be agitated or thermally cycled before printing to ensure thorough mixing. This was achieved by heating the mixture to 60°C for 5 minutes. The reader is directed to §7.2.2 for a more detailed description of mixing between a LC and polymer.

The addition of the prepolymer significantly increased the viscosity of the LC/polymer formulation, making droplet generation difficult. The optimised waveform (see page 78), using a maximum driving voltage of 60 V was found to be inadequate for producing droplets of E7/NOA65. Figure 6.15a shows high-speed images of the fluid ligament using this waveform, which clearly show a lack of sufficient kinetic energy for drop formation. Using pure LC inks, simply increasing the temperature is a convenient means to sufficiently reduce the viscosity. However, the Norland series of optical adhesives are known to undergo a degree of thermal curing at elevated temperatures and the manufacturers do not recommend exceeding temperatures of 60°C for extended periods. Partial curing of the polymer inside of the printhead could potentially damage the nozzle beyond repair. It was thus decided to use a maximum printing temperature of 60°C.

Using the printing regime shown in §4.5.1 on page 71, reducing the droplet

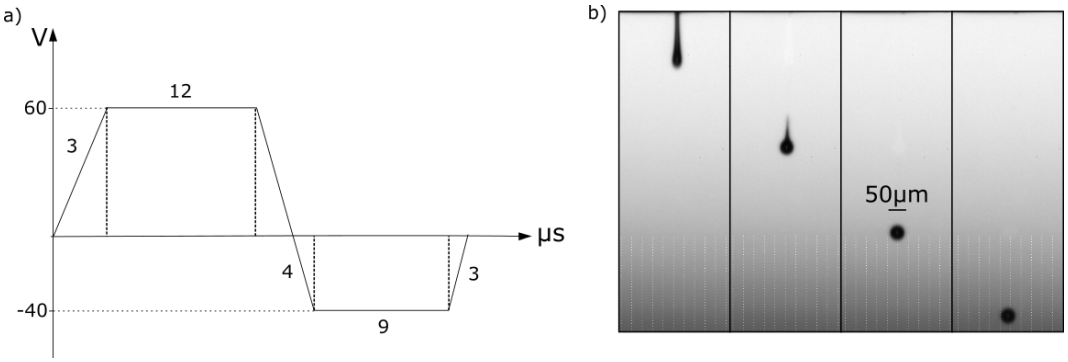

FIGURE 6.16: a) Waveform used to generate droplets of E7/NOA65 using the 50 μm nozzle. b) High-speed images of the resulting droplets (15,000 fps, 8 μs exposure, 60 μ s between frames).

size would increase *Re* and decrease *Oh*, moving away from the low inertial energy regime. The 80 μm nozzle was replaced with a 50 μm nozzle of the same model. An appropriate waveform was determined using the protocol discussed in §4.6.4. Reliable droplet generation was achieved using the bipolar waveform shown in Figure 6.16a. Figure 6.16b shows high-speed images of the resulting droplets, which were found to be $\approx$ 50 μm in diameter.

6.4.4 Results and Discussion

When using a PDLC formulation, the substrate does not need to be treated with an alignment layer, thus to facilitate electrical switching, indium-tin-oxide (ITO) coated glass (SPI supplies) was used as the printing substrate. After impact, droplets quickly spread to a diameter of 111 μm with a contact angle of 28°. Figure 6.17a)i) and ii) show microscope images of droplets prior to photo-polymerisation, exhibiting excellent spherical droplet boundaries and mono-disperse sessile droplet diameters.

A high-powered UV LED (Thorlabs, CS2010 UV high power UV curing LED system) was used to photo-polymerise the samples which were placed on a heat stage to control the curing temperature. Increasing the UV-intensity, curing temperatures and concentrations of prepolymer is known to decrease the LC domain size in PDLCs [155, 156]. As the concentration of prepolymer is fixed by printing, various UV intensities and curing temperatures were experimented with to

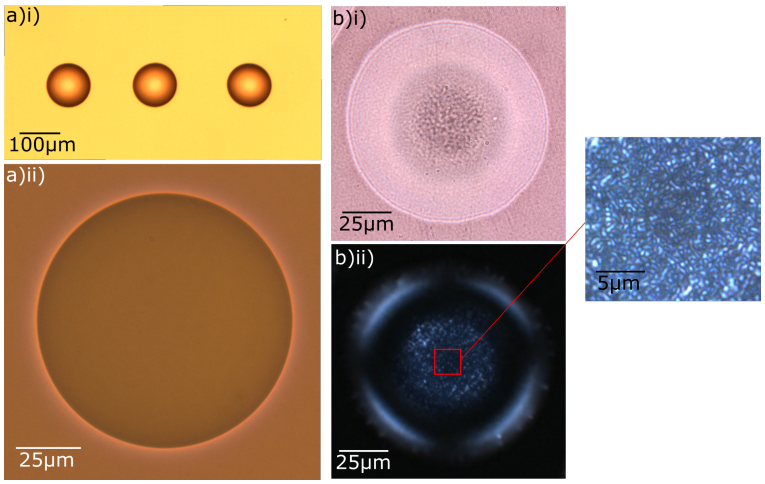

FIGURE 6.17: a)i) Microscopy images of three E7/NOA65 droplets prior to photopolymerisation deposited using inkjet printing on to an ITO-coated glass substrate. a)ii) Close up image of single E7/NOA65 droplet. b)i) Microscopy image of a single droplet of E7/NOA65 after irradiation with UV-light at an intensity of 173 mW/cm^2 for 30 minutes at a temperature of 56°C. b)ii) Polarised optical microscopy of the same droplet between crossed polarisers.

form nano-PDLC domains. Figure 6.17b)i) shows POM images of E7/NOA65 droplets after irradiation with UV-light at an intensity of 173 mW/cm^2 for 30 minutes whilst the sample was held at 56°C. The LC domains are visible in Figure 6.17b)i), as is a degree of scattering, indicating the LC domains are larger than the wavelength of visible light. This is confirmed by the POM image in Figure 6.17b)ii) which show LC domains in the order of 1 μm.

The optimum curing intensity for PDLC formation was achieved by placing the sample as close as possible to the UV source ($\approx$ 1 mm gap). This was the maximum UV intensity achievable using the curing system, corresponding to 190 mW/cm^2. The optimum curing temperature was found to be 60°C, as measured by the hotplates the samples were cured on top of. Curing temperatures >60°C were found to negatively effect the PDLC morphology, with larger LC domains appearing to form at the droplet surface after photopolymerisation. Figure 6.18a shows such a droplet, cured using the maximum UV intensity of 190 mW/cm^2 and a curing temperature of 70°C. The POM images in Figure 6.18b

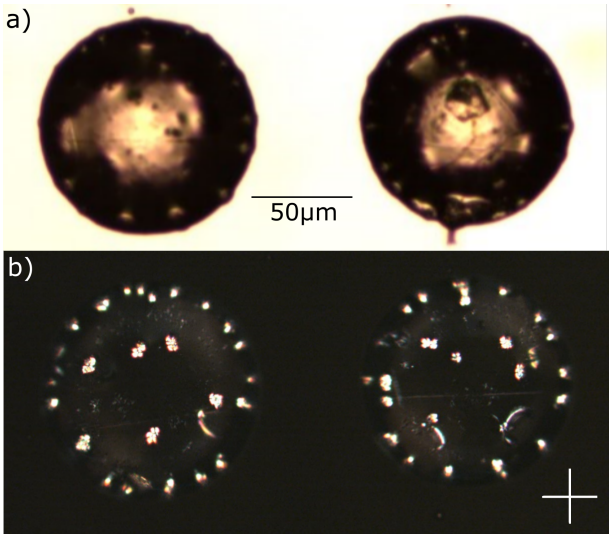

FIGURE 6.18: a) Microscopy image of a droplet after photopolymerisation using a UV intensity of 170 mW/cm^2 and a curing temperature of 70°C. b) Polarised optical microscopy image of the same droplets.

indicate these pimpled regimes may be due to larger phase-separated LC domains. It is likely that this effect is due to a degree of thermally induced polymerisation of NOA65 as the suppliers indicate this can happen when subject to sustained temperatures above 65°C. Additionally, it may be due to curing photopolymerisation occurring above the clearing temperature of the LC. As nano-PDLC domains could be formed at lower temperatures, the curing temperature was limited to 60°C and the phenomena was not investigated further.

Figures 6.19a and b show microscopy images of successful nano-PDLC lenses that were formed using a UV intensity of 190 mW/cm^2 and a curing temperature of 58°C. Figures 6.20a)i) and b)i) show microscopy images of the cured lens profile, showing good spherical droplet boundaries. There does not appear to be any visible indication of LC domains, or any scattering in the body of the lens, suggesting the LC domains are smaller than the wavelength of visible light. Figures 6.19a)ii) and b)ii) show microscopy images where the microscope has been focussed at the focal plane of the lenses, which show obvious focussing properties. Figures 6.19a)iii) and b)iii) show POM images of the lenses with the polarisers crossed. The images closely resemble the POM image of a nano-PDLC lens produced by Ren et al. shown in Figure 6.19c. To create PDLC domains, the authors

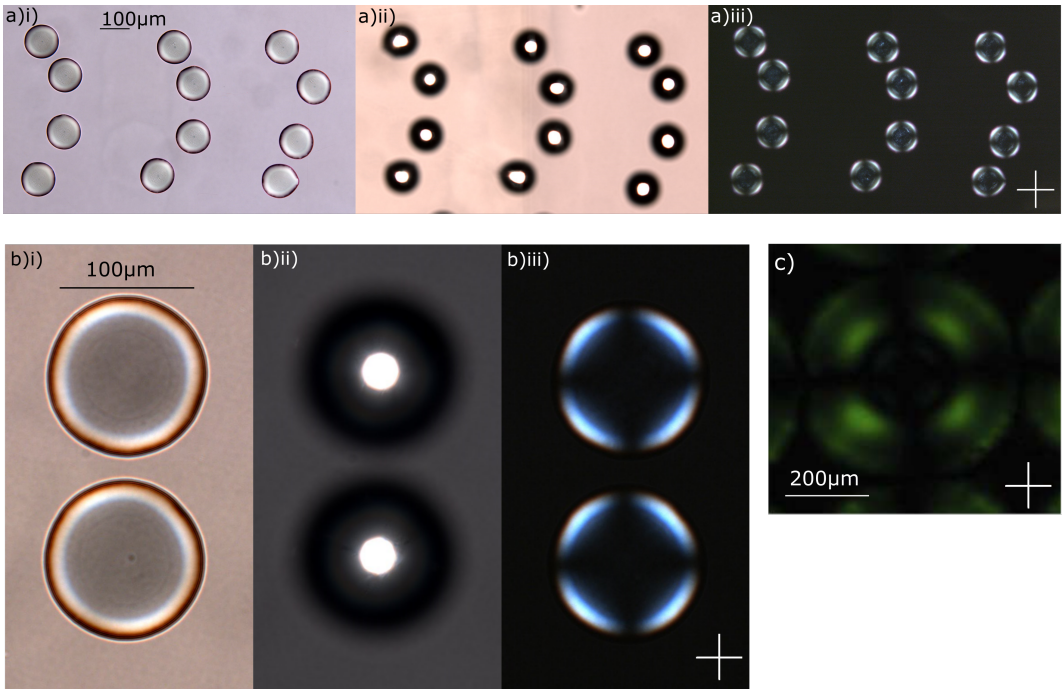

FIGURE 6.19: a) and b) Microscopy images of inkjet printed PDLC microlenses taken at: i) lens plane, ii) focal plane, iii) polarised optical microscopy image at lens plane with crossed polarisers. c) Polarised optical microscopy image of a 450 μm diameter nano-PDLC lens produced by Ren et al. Reproduced with permission [151].

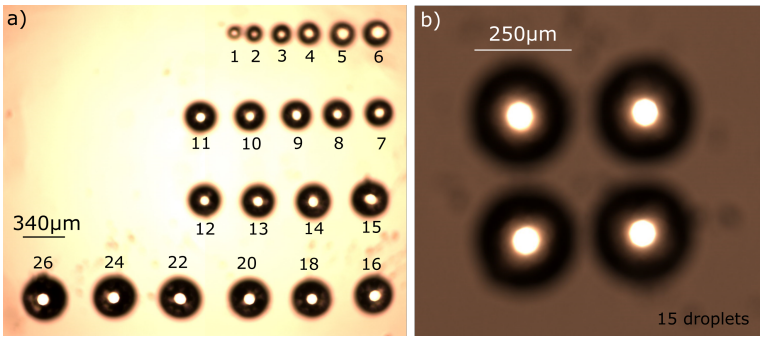

FIGURE 6.20: Microscopy images of arrays of PDLC microlenses of varying diameter taken at the focal plane. The numbers in the figure indicates the number of 50 μm droplets deposited to make the lens.

photopolymerised a 45 μm-thick formulation of E48:NOA65 (35:65%wt) using a UV intensity of 15 mWcm^{-2}, a curing temperature of 50°C and curing duration of 30 minutes.

Similarly to the nematic LC lenses, inkjet printing allows for lenses of different diameters to be easily produced via the deposition of multiple droplets at the same location. Figures 6.20a and b show microscopy images taken at the focal plane of lens arrays produced by consecutively depositing 50 μm droplets at the same location. The numbers in the figure correspond to the number of droplets forming a single lens. Further details about this study are found in Appendix §A.3.

6.5 Conclusion

Variable focus microlenses are an important optical component used in sensing, imaging, lab-on-a-chip and display applications. The excellent droplet profile and uniform homeotropic alignment observed in Chapter 5 was exploited in the formation of drop-on-demand inkjet printed nematic LC microlenses. A printed sessile nematic droplet can be considered a plano-convex microlenses that can be readily deposited into bespoke, pre-programmable arrays. Hydrophobic substrates can be used to form microlenses with a shorter focal length, however, the effect on the alignment of the LC directory must be considered. The diameter and focal length of the microlenses can be controlled for by depositing multiple

droplets at the same position. The microlenses presented have diameters ranging from 140 to 880 μm and f-numbers of 2. The focal length of these LC microlenses can be thermally tuned, which would be of importance for applications requiring passive focussing elements.

The chapter goes on to present a proof-of-concept fully encapsulated lens via the inkjet printing of a LC/prepolymer formulation. By using a smaller nozzle diameter and tailored bipolar waveform, a formulation of E7:NOA65 (35:65%wt) could be deposited without the need to excessively heat the printhead. Using the maximum accessible UV-intensity, sub-micron sized LC domains were formed. The cured droplets showed no indication of scattering of visible light and show polarised microscopy images indicative of nano-PDLC droplets. Similarly to a nematic microlens, multiple droplets can be deposited onto the same location to quickly produce different array patterns. The idea of encapsulated LC dispersions and the LC ability to deposit PDLC formulations using inkjet printed is now applied in the inkjet printing of PDLC films.

Chapter 7

Inkjet Printing of Polymer-Dispersed Liquid Crystal Films

In Chapter 6, the inkjet printing of a polymer-dispersed liquid crystal formulation was successfully demonstrated. The ability to deposit such formulations gives rise to the possibility of producing inkjet printed polymer-dispersed liquid crystal films - an optical component with a variety of applications including switchable windows, holographic films, light shutters and biosensors. This chapter presents two novel methods of utilising inkjet printing to produce patterned, single-layer, polymer-dispersed liquid crystal films. The The feasibility of each method is thoroughly investigated before presenting an inkjet printed, patterned polymer-dispersed liquid crystal film.

7.1 Introduction

Polymer dispersed liquid crystals (PDLCs) are an important class of optical material that have found wide-ranging commercial applications in devices such as smart windows, light shutters, holographic gratings and light valves [157, 158, 159, 160, 149, 161, 12]. The use of PDLCs for microlens applications, as well as some of the underlying physical principles, has already been discussed in §6.4.1. The novel methods of fabricating PDLC films discussed in this chapter allows for localised PDLC regimes to be formed in a single layer. The techniques have

the potential to generate patterned PDLC films, potentially consisting of different LC/polymer formulations, that are fast, efficient and simple to manufacture. In the discussion, pertinent physical processes such as impact with a fluid substrate, spreading and mixing of partially miscible fluids and photo-induced phase separation are covered.

A PDLC film consists of droplets of LC that are suspended in a polymer matrix. Typically, films are composed of 40-60% LC dispersed in a flexible polymer film [150]. As the LC domains are only in contact with the polymer binder, there is no need for rigid substrates or alignment layers [153]. Many of the electro-optical properties of a PDLC film are determined by the size and alignment of the LC domains which are typically spherical or prolate in shape [149].

Types of PDLCs

A PDLC can be formed either from a heterogeneous or homogeneous mixture. A heterogeneous mixture consists of an emulsion in which there exists two or more distinct phases. On the other hand, the components in a homogeneous mixture form a single phase and are mixed at an atomic or molecular scale. In order to form a PDLC, a homogeneous mixture must undergo a phase separation process. The mechanism of phase separation further categorises PDLCs formed from a homogeneous mixture into: Solvent-Induced Phase Separation (SIPS), Thermally-Induced Phase Separation (TIPS) and Polymerization-Induced Phase Separation (PIPS).

The first PDLC films were formed using a heterogeneous mixture of a nematic LC and a water-based solution of polyvinylalcohol by James Fergason, a major contributor to the development of twisted nematic LC displays [162]. A LC/polymer emulsion is initially formed and often agitated to improve droplet size dispersion. The mixture is then deposited as a thin-film using techniques such as spin coating and bar-to-bar processing. As the water evaporates away, the LC domains become encapsulated in a polymer matrix. There is a large reduction in volume during the evaporation process, with dry films often shrinking to a third of the thickness of the wet films. The change in volume often leads to

the LC droplets assuming an oblate shape, resulting in the LC director of each drop tending to orient parallel to the substrate [153].

Most modern PDLC films are made via phase separation of an initially homogeneous mixture. It is a popular method for producing PDLCs as it allows for an additional degree of control over droplet size and shape compared to emulsification techniques [163, 164, 150]. Phase separation by solvent evaporation (SIPS) requires the LC and polymer to be dissolved into a common solvent. The solvent is then evaporated off to leave phase separated LC droplets enclosed in a polymer matrix. This method is useful when the chosen polymer component has a high melting point [165].

In thermally induced phase separation (TIPS), a homogeneous mixture of LC, polymer and any other components is first formed at an elevated temperature and deposited as a film. As the film is cooled, the LC and polymer phase separates. The method requires the polymer to be solid at the operating temperature and the LC to be miscible at the mixing temperature. The LC droplet size is determined by the rate of cooling, component concentrations and material parameters such as viscosity, chemical potential and molecular weight [166]. Materials commonly used in TIPS PDLCs are polymethyl-methacrylate (PMMA) and poly-vinylformal (PVF) along with cyanobiphenyl LCs. It is important for the polymer to be readily soluble with the LC, with a cured refractive index that is reasonably matched to the ordinary or extraordinary refractive index.

Phase separation by polymerisation (PIPS) requires a homogeneous mixture of a prepolymer (consisting of monomers and/or oligomers), LC and any other components. Polymerisation is achieved via thermally-induced polymerisation or photo-polymerisation, during which the LC phase-separates as it becomes insoluble with the polymer [167, 12, 168, 164]. The LC domain size, shape and homogeneity are determined by the viscosity, molecular weight, chemical potential and also the conditions of the phase separation process [156]. Photopolymerisation-induced phase separation allows for greater control over the droplet size and

distribution as both the curing temperature and rate of polymerisation (determined by the UV curing intensity) can be varied independently. Using photopolymerisation, sub-micron and nano-sized LC domains can be formed, a property that is difficult to achieve via other techniques. Irradiation with coherent light allows the use of holographic masks, which enables a patterned light-intensity to be applied to the sample. Furthermore, if the LC host is doped with an azobenzene dyes, which undergo cis-trans photopolymerisation, the use of a linearly polarized light source during photopolymerisation can cause the LC director to adopt a preferential orientation due to steric interactions with the azobenzene molecules [169].

PDLC Film Morphology

The LC director configuration in each droplet depends on its size and shape, as well as the anchoring imposed at the LC/polymer interface (see §2.3.4). For nematic droplets in a polymer binder imposing planar anchoring (such as the thiolene based adhesives used in this chapter), LC droplets assume a bipolar configuration for a wide range of droplet diameters $\approx$ 1-15 μm [58]. The operating principle of a basic PDLC film is shown in Figure 7.1. As each LC domain is independent, the LC director in each droplet ($\hat{\boldsymbol{n}}_d$) is arbitrarily oriented and there lacks any preferential macroscopic orientation between LC domains. Using a polymer binder with a refractive index (n_p) that is matched to the ordinary refractive index of the LC (n_o), results in a scattering passive state shown in Figure 7.1a. The scattering results form the refractive index mismatch between the polymer matrix and the LC droplet, shown in Figure 7.1a.

The orientation of the LC director in the droplets can be switched by an electric field [170, 42]. Upon application of an electric field, the LC director in the droplets align parallel to the field. For collimated incident light, the refractive index of the droplets tends towards n_o as the voltage increases and a transparent state is achieved, as shown in Figure 7.1b.

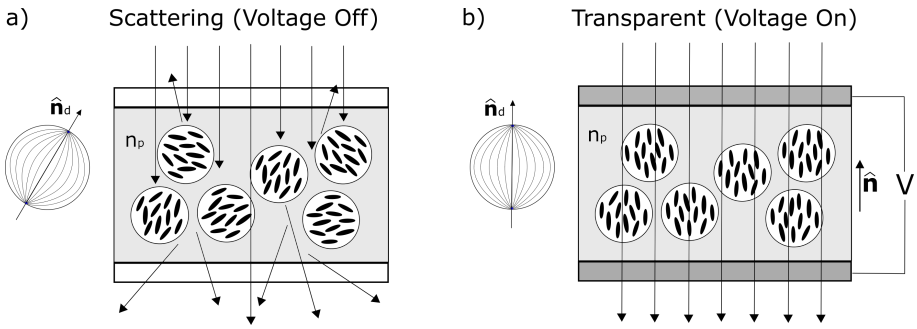

FIGURE 7.1: A schematic showing a PDLC film where the LC droplets are suspended in a polymer matrix with a refractive index $n_p = n_o$. The LC droplets are bipolar with a local LC director in each droplet labelled $\hat{\boldsymbol{n}}_d$. a) In the scattering state, $\hat{\boldsymbol{n}}_d$ is arbitrary oriented. b) In the transparent state, $\hat{\boldsymbol{n}}_d$ aligns parallel to the applied electric field.

7.1.1 Smart Windows

Smart Windows, or smart glass, are panels or adhesive films through which the the transmission of light can be electronically, photonically, or thermally controlled [171]. Smart glass has found industrial use as privacy glass, where they offer a digitally controlled aesthetic alternative to conventional blinds or curtains. In the automotive industry, as brightness control and as heads-up displays [172]. A future prerogative for smart windows is their potential for energy saving by controlling the wavelength of light transmitted into buildings, thereby offering an opportunity to dynamically heat large buildings such as offices. The worldwide market for smart windows is estimated to be around $2.6 billion in 2016 and expected to exceed $8 billion by 2022 [171]. The main underlying technologies are PDLC, suspended particle devices, electrochromic (EC), thermochromic, photochromic, thermotropic and nanocrystal devices [173, 174, 175].

In 2016, PDLC smart windows accounted for around 14% of the market share, equating to $360 million in annual revenues [171]. Although some variations exist in terms of the manufacturer and materials used (for example azo-dyes used for tinting), the vast majority of commercially available PDLC windows are based on the light scattering principle introduced earlier using films produced by photopolymerisation. The benefits of PDLCs are that they are low-cost and relatively simple to manufacture. The films produced can be flexible and applied as adhesive films to existing glass. In addition, they have fast switching times when

compared to other technologies.

7.1.2 IJP PDLC Films

The benefits of using PDLC films include the ability to operate without polarisers, and the possibility of doping with a range of materials such as dyes, chiral dopant and nano-particles to increase functionality [161, 28, 176]. Another key advantage of PDLCs is their suitability for the manufacturing of large-area films. The pre-polymerisation (or emulsified) mixtures are compatible with wet-processing techniques such as bar coating, roll-to-roll coating, spin-coating and even painting. However, a drawback of such wet-processing techniques is the inherent homogeneity resulting from the mixing and coating process. Additionally, using such techniques makes it difficult to produce patterned PDLC films which possess spatially varying concentrations of LC domains. Such films have many potential applications in communications, photonics and sensors [155, 177, 178].

A current method of achieving a patterned PDLC film utilises holographic photopolymerisation. Two laser beams are used to generate an interference pattern within a homogeneous LC/prepolymer formulation leading to the formation of polymer-rich and LC-rich domains [155, 179, 180]. Other methods of producing a patterned PDLC film include the use of high-power LEDs, photomasks, chemically patterned substrates and using mechanical stamping processes [166, 181, 182]. Such methods require multiple additional processing steps, the use of templates or photo-masks and restricts a PDLC film to be composed of a single LC/prepolymer formulation.

There is a potential to utilize the numerous advantages and versatility of DoD inkjet printing in the manufacture of PDLC films. Figure 7.2a illustrates the printing of the LC component independently from the UV-curable prepolymer, which is already deposited as a thin-film. If the LC was to form a sufficiently homogeneous mixture upon deposition, high concentration LC domains could be formed around the position of drop impact. Figure 7.2b shows an alternative method, where a homogeneous mixture LC and prepolymer are deposited onto a substrate and then photo-polymerised. In both methods, there is the potential to use multiple printheads containing different coloured dyes, LCs, or surfactants, to

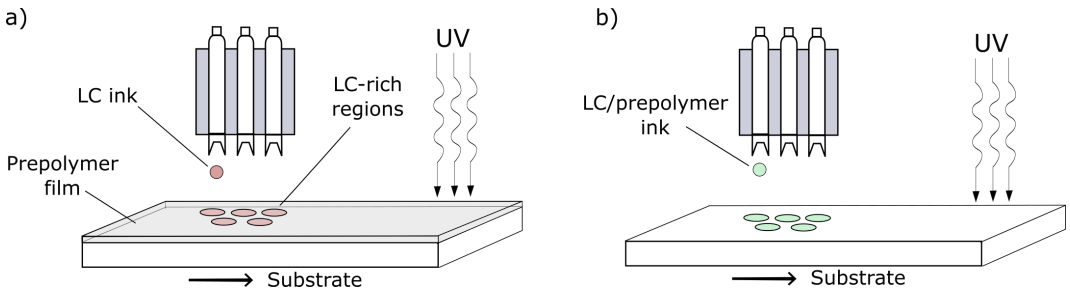

FIGURE 7.2: Illustration of two concepts using inkjet printing to form polymer dispersed liquid crystal films. a) Printing the liquid crystal component into a prepolymer film that has been deposited on top of the substrate. b) Printing a liquid crystal and prepolymer formulation directly onto the substrate. In both cases, the samples are then photo-polymerised using UV light.

produce films that can switch into coloured images, patterns or logos. Further, the suitability of IJP for large-scale manufacturing has the potential to make cost-effective, large-area films that could, for example, be suitable for office exterior or advertising.

7.1.3 Objectives and Requirements

The objective of this chapter is to produce a patterned PDLC film via inkjet printing. This chapter is not intended as an analytic study of the underlying physical principles. Rather, it serves to identify the necessary conditions and key parameters required to produce an IJP PDLC film. The PDLC domains formed should be localised and be electrically switched from scattering to a transparent state. To achieve and an IJP PDLC, the main requirements are as follows:

1. The LC must be sufficiently miscible with, or dispersed into, the prepolymer film such that phase separation occurs upon UV irradiation.

2. On phase separation, the LC domains must be sufficiently localised within the polymer film such that a single film can be patterned (with or without the use of different LC inks) to form 'pixels' which contain a significantly higher density of LC droplets. This requires the LC to not diffuse too readily into the prepolymer layer.

3. The PDLC domains must effectively scatter visible light, requiring the LC domains to be larger than the wavelength of visible light and present in sufficient quantity.

4. The LC should be fully encapsulated by the polymer film, whose surface should ideally be flat and homogeneous.

5. The PDLC film must be electronically switchable. The LC domains should not be too small, or the film too thick, such that an excessively large electric field is required.

7.2 Method 1 - Printing of a LC Droplet into a Prepolymer Film

Inkjet printing has been shown to be a useful substrate patterning tool for polymer and inorganic films [183]. The patterning of lead zirconate titanate (PZT) films on a silicon substrate via the deposition of alkanethiolate-based droplets has been demonstrated [184]. In bio-engineering, inkjet printing of different proteins and stem cells has been used to engineer cell microenvironments in the study of growth factors and disease on living tissue [185, 186]. So far, the effect of the substrate on deposited properties has been investigated in detail. However, in these applications, droplet deposition is instead used to achieve the desired effect on the substrate. The first method of producing PDLC films via inkjet printing, shown schematically in Figure 7.2a, uses a similar concept.

7.2.1 Experimental

Printing Set-up

The experimental set-up used in this study is shown in Figure 7.3. Two printheads were used; a MJ-ABP-01-120 and MJ-ABP-01-80 dispenser with 120 and 80 μm nozzle diameters, respectively (Microfab Technologies Inc.). The 120 μm printhead was used to investigate the effect of larger LC droplets and to more easily facilitate the printing of larger PDLC patterns.

The samples were photo-cured in-situ using a high-powered UV LED (Thorlabs, CS2010 UV high power UV curing LED system) fixed at a variable distance above the sample and adjacent to the printhead. The distance between the point of droplet impact and the region of the film exposed to the UV light was 4 mm, and is indicated in Figure 7.3. When the substrate is moving in the y-direction with a typical speed of 0.2 ms^{-1}, a minimum UV delay of 20 ms is achievable. A longer UV-cure delay could be selected via an automated switch. The UV curing duration, power, temperature and time delay after printing were altered to investigate the effects on the resulting PDLC film. Unless otherwise stated, the substrate temperature was held constant throughout the duration the sample was photo-polymerised.

To reliably deposit the LC, the temperature of the printhead was maintained at 65°C and the optimised waveform W1 (see page 78) was used to generate single well-defined droplets. The amplitude of this waveform was varied to produce droplets with velocities between 0.9 $\pm$ and 2.5 ms^{-1}, depending on the printhead and LC used. Drop formation at the nozzle as well as the subsequent impact onto the substrate was captured using a combination of a high-speed camera (Phantom V12.1) and a halogen high-intensity white light source (OSL2 3200K, Thorlabs), which was directed through a UV filter and arranged in a shadowgraphy configuration.

Materials Used

Two commercial nematic LC mixtures were chosen for this study; BL006 and E7 (Merck KGaA). The thiolene-based optical adhesives NOA65 and NOA68 (Norland Products inc.) were selected as the UV-curable prepolymer binders [187] (see §3.2 for more details). For continuity, NOA65 and NOA68 are referred to as 'prepolymer' before they are cured and 'polymer' once they have undergone polymerisation. These nematic LCs and UV-curable polymers were chosen as the ordinary refractive index (n_o) of the LCs are matched to the refractive index of the polymer binder (n_p). Additionally, both prepolymers are at least partially miscible with the LCs used (discussed in Section 7.2.2) and have been used in PDLC

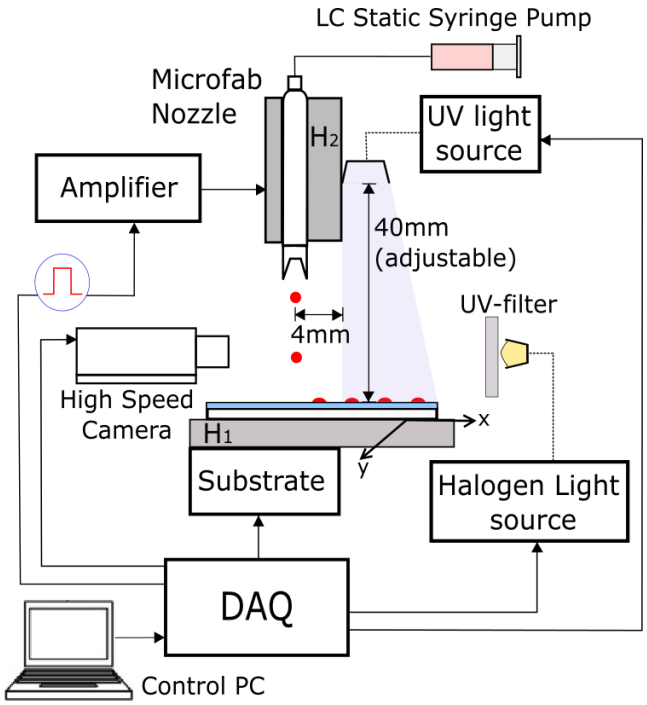

FIGURE 7.3: A schematic of the experimental apparatus used to print the patterned nematic PDLC films with in-situ UV-curing. H_1 and H_2 are the substrate and nozzle heating elements, respectively.

applications [188, 189, 161]. The relevant parameters for the materials used in this chapter are repeated in Table 7.1.

Film Preparation

Films were prepared following the three step process presented in Figure 7.4. Microscope slides (Super Premium Microscope Slides, VWR) were first cleaned and wiped using acetone and optical tissue and dried using filtered air. Boundaries were formed using various adhesive tapes which was used to define the thickness of the sample with thicknesses of 35, 40, 70 and 80 μm ± 3 μm could be attained depending on the adhesive tape used, the thickness was verified using an optical microscope. The prepolymer was drop-cast into the channel formed and then doctor-bladed to form a thin film, with a depth approximately equal to the thickness of the tape. Different types, or multiple layers, of tape were used to vary the film thickness.

TABLE 7.1: Fluid parameters for the two LCs and optical adhesives used in this chapter. Surface tension measurements were made using the pendant drop method (see Section 3.3.2). Fluid parameters over a range of wavelengths and temperatures can be found in Appendix §A.4.1.

Parameter	**E7**	**BL006**	**NOA65**	**NOA68**
$\gamma_{1\,T=20}$ (mPa.s)	252	426	1200	≈5000
$\gamma_{1\,T=40}$ (mPa.s)	73	142	400	1670
$\gamma_{1\,T=60}$ (mPa.s)	20	50	240	1000
$\sigma_{1\,T=20}$ (mN.m^{-1})	30.4	36.4	37.5	29-33
$\sigma_{1\,T=40}$ (mN.m^{-1})	27.6	36	33	29-33
$\sigma_{1\,T=60}$ (mN.m^{-1})	26	34.2	30.9	29-33
$\rho_{1\,T=20}$ (g.cm^{-3})	1.024	unknown	1.037	1.288
Refractive Index$_{1\,T=20}$ (589.3nm)	n_o=1.522 n_e=1.7472	n_o=1.529 n_e=1.814	n=1.524	n=1.54

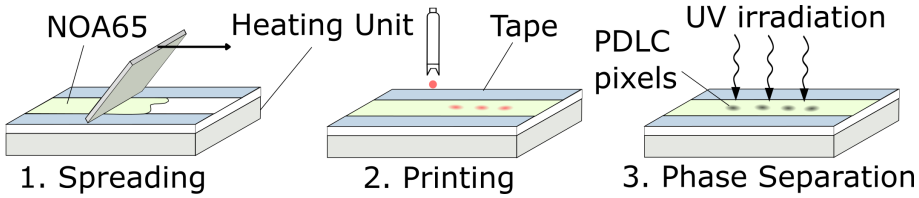

FIGURE 7.4: Diagram of the spreading, printing and phase separation steps involved in forming the printed and patterned PDLC films.

7.2.2 Mixing of the LC and Prepolymer Film

In order to produce a PDLC film via the printing of a LC into a prepolymer layer, it is critical for a homogeneous mixture of LC and prepolymer to form. For an IJP PDLC film, adequate mixing of the LC and prepolymer must take place after droplet deposition and before the film is photo-polymerised.

Whether a homogeneous mixture is formed depends on the mixing free energy. Considering the simple case of a binary mixture with two components, the mixing free energy is given by:

$$F_m = U_m - TS_m \,, \tag{7.1}$$

where U_m is the mixing interaction energy, S_m is the mixing enthalpy and T is the temperature. For $F_m < 0$, the system is in a single-phase homogeneous state, and for $F_m > 0$, a heterogeneous two-phase system forms. The mixing entropy (S_m) is always negative and favours mixing. The mixing interaction energy is the difference between the interaction energy of the homogeneous mixture and interaction energy of the phase-separated heterogeneous mixture: $U_m = U_{homo} - U_{hetero}$. If $U_{hetero} > U_{homo}$, the free energy of mixing is negative and the system will be homogeneously mixed. If the mixing interaction is positive, then the relative contributions of U_m and TS_m will determine whether a homogeneous mixture is formed. A more detailed explanation can be found in [190, 163].

The free energy of mixing is dependent on the concentration of the components and the temperature. By definition, two fluids are fully miscible if they exist in a single phase at any given concentration. A fluid system is considered partially miscible if there exists a two phase system over a set of concentrations. This is a common situation and often the case when mixing fluids with varying degrees of polarity. A typical phase diagram for a binary fluid system is shown in Figure 7.5a. The Upper Critical Solution Temperature (UCST, labelled T_{UCST} in the figure) is the temperature above which the two fluids exist in a single phase at all concentrations [191]. The binodal decomposition region indicates the parameter space where two phases may coexist. On the other hand, the spinodal decomposition region indicates the rapid unmixing of the fluid components.

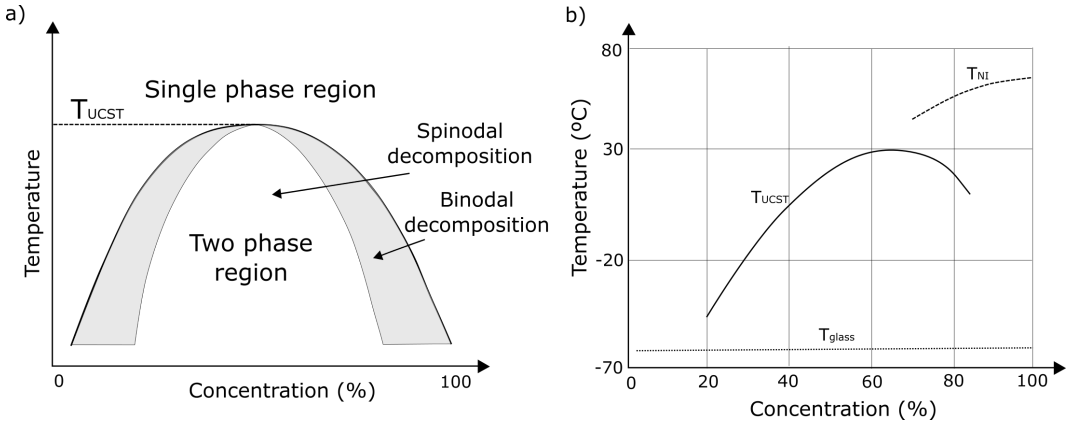

FIGURE 7.5: a) Phase diagram for a partially miscible fluid system over a range of concentrations and temperatures. The critical temperature above which the fluids are miscible at all concentrations is denoted by T_{UCST}. b) Phase diagram for a mixture of E7 and NOA65 with varying concentrations of E7 and over a range of temperatures. The glass transition and nematic-isotropic temperatures for the mixture is indicated by the curves labelled T_{glass} and T_{NI} respectively. The temperature above which the mixture exists as a single phase is indicated by the curve labelled T_{UCST}. The figure has been adapted from Smith [188].

Figure 7.5b shows the phase diagram for a mixture of E7 and the prepolymer NOA65 before photopolymerisation. The authors of the study determined the values for T_{UCST} by using differential scanning calorimetry and fitting to constants found using Flory-Huggins theory, which considers the enthalpy of mixing [192, 217, 188]. The T_{NI} curve indicates that a nematic phase only existed for LC concentrations above 70%. It is noted that below the curve T_{UCST}, the system is not completely phase-separated.

In the case of a LC droplet being deposited onto a prepolymer film, the concentration of LC will be dependent on factors such as the LC droplet diameter, thickness of the polymer film, and also the mechanism in which the droplet impacts and diffuses into the prepolymer film. This makes homogeneous mixing by controlling the LC concentration difficult. However, varying temperature is a convenient means of increasing the miscibility of the LC and prepolymer. As the concentration of LC and prepolymer is highly localised at the position of droplet deposition and will vary dynamically over time, the substrate temperature should ideally be above the UCST to ensure a single homogeneous phase is formed.

TABLE 7.2: Estimated mixing temperatures for different binary mixtures containing 1:1%wt of LC and prepolymer. Unless specified, the temperatures were defined using the procedure described in §7.2.2.

	NOA65	**NOA68**
E7	30°C	50°C
BL006	65°C	90°C

Mixing Temperature

In this study, two different nematic LCs (E7 and BL006) were deposited onto two photo-curable optical adhesive films (NOA65 and NOA68). It would be beneficial to estimate the UCST temperature for each combination of fluids to inform the choice of substrate temperature. The phase diagrams for E7 in NOA68, or BL006 in either of the optical glues could not be found in the literature. However, when the LC/prepolymer exists as a homogeneous single-phase, the mixture is isotropic. One can observe the temperature at which a mixture of LC/prepolymer becomes clear. This is similar to observing the clearing point of a nematic LC, indicating the nematic-isotropic phase transition of the sample.

An estimation of the mixing temperature (T_{mix}) for solutions of LC/polymer was conducted by observing the clearing temperature of the mixture. Four clear glass vials containing 1:1%wt LC/polymer mixtures were made. This concentration was selected as it gives a good intermediary value to estimate the mixing temperature. The samples were placed in an aluminium sleeve and heated slowly on a hot plate whilst being agitated by a small magnetic stirrer. The temperature at which the mixture became clear was noted. The mixtures were cooled and the process repeated to estimate T_{mix}, shown in Table 7.2.

7.2.3 Drop Impact, Spreading and Dissolution

Mixing between the LC and prepolymer in the context of a single LC droplet, itself a multi-component mixture, impacting a partially miscible fluid substrate is a non-trivial system. There is the initial droplet impact, followed by the wetting and spreading of the unmixed LC on the partially miscible prepolymer film. Simultaneous to this hydrodynamic flow, the LC dissolves into the prepolymer

TABLE 7.3: Table of parameters relating to the LC drop and prepolymer film before photopolymerisation.

LC		Prepolymer		Notes
Drop density	ρ_{drop}	Film density	ρ_{film}	Negligible variance over accessible temperature range.
Drop viscosity	μ_{drop}	Film viscosity	μ_{film}	Large variance achievable via substrate temperature (see Table 7.1).
Drop surface tension	σ_{drop}	Film surface tension	σ_{film}	Small variance achievable via substrate temperature (see Table 7.1).
Drop diameter	d	Film thickness	h	Drop diameter fixed by choice of nozzle (80, 120μm). Film thickness varied incrementally using spacer tape ($\approx$30-80 μm).
Drop temperature	T_{drop}	Film temperature	T_{film}	Drop temperature fixed over a narrow range due to printing parameters (50-75°C). Film temperature can be varied between 18 - 70°C.
Drop velocity	v			Drop velocities in the range of $\approx 1 - 2.5\ ms^{-1}$ accessable due to printing parameters.

across its contact area via diffusion and or advection/convection. The outcome of this dynamical system is dependent on an interplay between inertial, viscous, capillary forces, as well as being dependent on thermal and solutal effects occurring as the fluids mix.

There are many critical variables and parameters making complete theoretical analysis exceedingly complex. Important variables relating to the LC drop and prepolymer film are presented in Table 7.3. The following sections combine theory and experimental observation to determine the underlying physical processes involved. The aim before the photopolymerisation stage is to understand the conditions required to achieve the following goals:

1. A localised area of LC, sufficiently mixed or dispersed with the prepolymer, at a concentration suitable for forming light-scattering PDLC domains upon photopolymerisation.

2. The LC should be fully encapsulated by the polymer binder, ideally with a free surface that is flat and homogeneous.

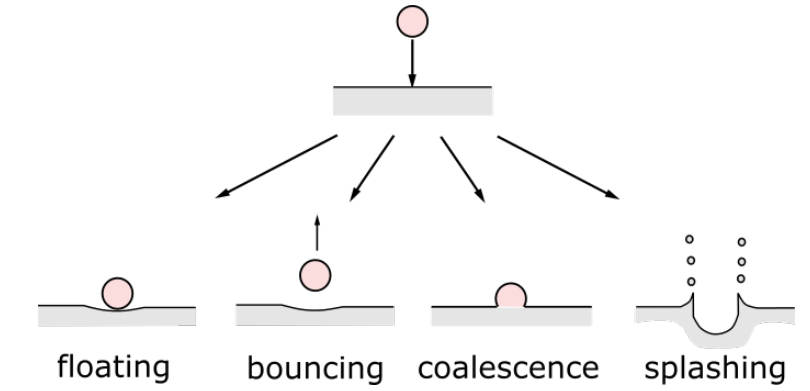

FIGURE 7.6: Schematic showing the different possible regimes resulting from drop impact.

Drop Impact

Drop impact on a solid substrate has already been discussed in §5.2.1. When a drop impacts a liquid film, partial-encapsulation, encapsulation, splashing, bouncing and dissolution may occur, shown schematically in Figure 7.6. There have been numerous studies dedicated to the transition between bouncing/coalescence and deposition/splashing, as well as impact crater formation [193, 194, 92, 195]. However, many of these studies deal with low-viscous miscible fluids, where the drop is often the same fluid as the substrate and there is little consideration of the more complex mass-transfer phenomena encountered using a two-component, partially miscible, complex fluid system such as a LC and prepolymer.

In particular, any splashing or bouncing of the droplet should be avoided, as well as establishing whether wetting, full, or partial-encapsulation will occur. Dimensionless analysis is used to reduce the initial complexity of the system and reveal the governing mechanisms involved. The relevant dimensionless parameters are shown in Table 7.4. As the fluid substrate will dissipate much of the droplet's momentum, the splashing parameter for a solid substrate ($K = We^{1/2}Re^{1/4}$, $K > 50$ for splashing) can be used to give a limit for impact with a fluid substrate. In all scenarios encountered, it was found that $K < 30$, thus splashing was not expected or observed. Cossali et al. determined a threshold between deposition and splashing for a wetted fluid substrate in terms of an amended splashing constant, $K = Oh^{-0.4}We$ [196]. However, this was defined for Oh numbers much lower than those seen in this study and was not considered.

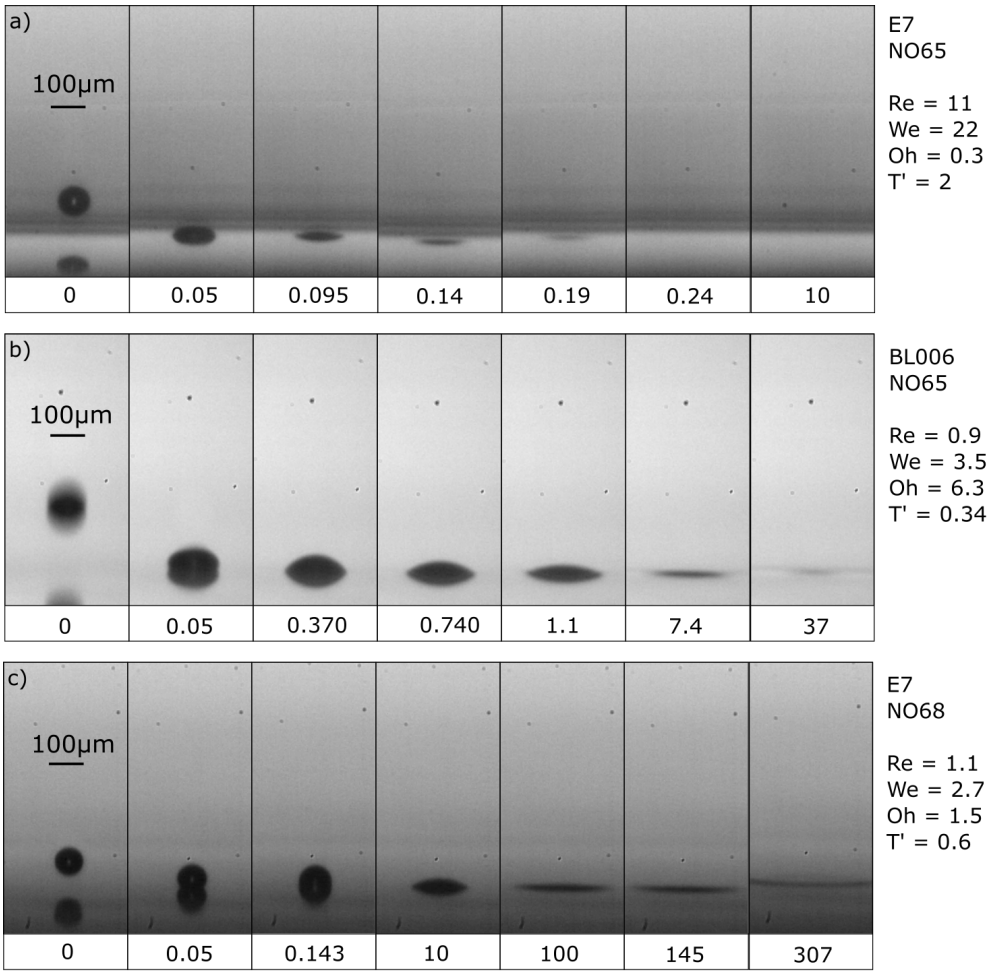

FIGURE 7.7: Figure comparing droplet impact in the most inertially dominated system and the most viscous dominated systems (b and c). High-speed images and the corresponding dimensionless parameters for: a) 80 μm droplet of E7 impacting a film of NOA65 held at 60°C. b) 120 μm droplet of BL006 impacting a substrate of NOA65 held at 20°C. c) 80 μm droplet of E7 impacting a substrate of NOA68 held at 36°C. In each case, the prepolymer film was 70 μm-thick. The numbers below each image indicate the time since droplet impact in ms.

TABLE 7.4: Table of dimensionless parameters relating to the LC drop and prepolymer film. The maximum and minimum dimensionless parameters encountered in this chapter were calculated using the values corresponding to the drop impact state of the system.

Dimensionless Parameter	**Definition**	**Min**	**Max**
Reynolds number	$Re = \frac{\rho_{drop} v d}{\mu_{drop}}$	0.9	11
Weber number	$We = \frac{\rho_{drop} v^2 d}{\sigma_{drop}}$	2.7	22
Ohnesorge number	$Oh = \frac{\mu_{drop}}{\sqrt{\rho_{drop} \sigma_{drop} d}}$	0.3	6.3
Thickness ratio	$h' = \frac{h}{d}$	0.3	0.9
Viscosity ratio	$\mu' = \frac{\mu_{film}}{\mu_{drop}}$	2.8	16
Surface tension ratio	$\sigma' = \frac{\sigma_{film}}{\sigma_{drop}}$	0.9	1.2
Density ratio	$\rho' = \frac{\rho_{film}}{\rho_{drop}}$	1.01	1.26
Temperature ratio	$T' = \frac{T_{film}}{T_{mix}}$	0.34	2

The dimensionless parameters suggest viscous and surface tension dominate the system behaviour. Figure 7.7 shows a selection of high-speed images of different printing and substrate conditions. The initial impact time can be estimated by $t_{impact} = h/v$ and ranges from 0.0175-0.12 ms. During this time, any deformation or fluid flow results from inertial effects of droplet impact. Figure 7.7a. shows an image sequence of a droplet of E7 impacting impacting a 70 μm thick film of NOA65 at 60°C. This represents the most inertially-dominated case encountered, with maximum Re and We numbers. As seen in the high-speed images, the droplet flattens on impact, with no observable deformation to the prepolymer surface. In less than 0.24 ms, the drop cannot be distinguished from the film. As $T_{film} > T_{mix}$ $(T' > 1)$, this is is likely due to the droplet mixing quickly with prepolymer film in this time.

Figure 7.7b and c. show the opposite side of the spectrum, with low Re and We numbers. Figure 7.7b depicts a larger droplet of BL006 impacting a 70 μm thick NOA65 film held at 22°C. The image sequence resembles Figure 7.7a, however,

the time taken for the drop to disappear into the film is much longer. This is expected, as $T_{film} < T_{mix}$ ($T' < 1$) and the LC will not mix as readily with the prepolymer. Additionally, the hydrodynamic flow in the droplet from wetting and/or encapsulation is strongly opposed by viscous forces, indicated by the high Oh number. Figure 7.7c shows high-speed images of an E7 droplet impacting a 70 μm thick film of NOA68 held at 22°C. The images strongly resemble that of a droplet impacting a solid substrate, with the LC droplet spreading and forming a sessile drop on top of the film. It is noted that the formation of surface waves begins to form in the final frames of the image sequences in Figures 7.7b and c, which will be discussed in the following section.

It has been proposed that the film thickness (h) has a significant effect on the impact mechanics [197, 198]. The effect of varying the film-thickness, as well as droplet velocity (v), on the impact process was studied. However, the impact mechanics were not observed to be affected as h and v were varied. This is attributed to significant viscous damping both in the LC droplet and in the prepolymer film. This is not surprising as the kinematic viscosities of the fluids used in the literature reporting the significance of the film-thickness are (at least) an order of magnitude less than that of the fluids used in this study.

The literature proposes six possible mechanisms for the mixing of a droplet impacting a miscible, or partially miscible, fluid film: 1. Mixing at the crater due to turbulence and oscillatory fluid motion resulting from impact inertia. 2. Formation of a 'crown wall' and the resulting fluid flow. 3. Fingering instability. 4. Formation of secondary droplets. 5. Diffusion of the two miscible fluids at the interface. 6. Surface waves propagating on the surface of the film [197, 198, 193, 199]. Figure 7.8 shows schematics of the mixing mechanisms, along with the corresponding top-down images, taken using de-ionized water and dye [198]. Of these, mechanisms 1 - 4 are suppressed in our case due to viscous dissipation. This is confirmed by contrasting the high-speed images in Figure 7.7 to the mechanisms in Figure 7.8. Thus, mixing during the impact phase is attributed to diffusion at the fluid-fluid interface and via the production of surface waves - which typically operate over longer time-scales than t_{impact}. If the time taken for the volume of LC to diffuse into the prepolymer film (t_{mix}) is smaller than the impact

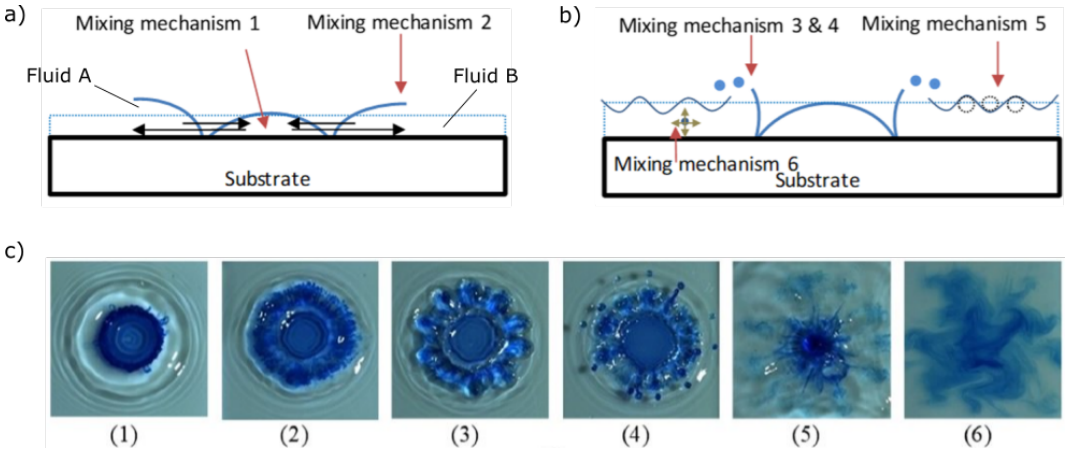

FIGURE 7.8: Six possible mixing mechanisms of a droplet (fluid A) impacting a miscible liquid film (fluid B). a) and b) show schematics of the mixing and c) shows the corresponding images where a dye has been added to the droplet (fluid A). The mixing mechanisms are: 1) Expansion and compression waves and induced turbulence. 2) Crown formation and spreading on top of the fluid film. 3) crown fingering. 4) Secondary droplet formation. 5) Surface Waves. 6) Diffusion. The figure has been reproduced with permission from AIP Physics of Fluids [198].

time (t_{impact}), then droplet spreading and/or engulfing must be considered.

Droplet Spreading

The spreading factor for a droplet on a solid surface is described in §5.2.2. The case of a droplet in contact with a fluid substrate is shown in Figure 7.9a. The angles θ and β are taken about the triple point (the point which is in contact with all three phases simultaneously). Figure 7.9b shows Neumann's triangle, relating the surface tension forces and contact angles. The tension $\sigma_{LC/P}$ is the interfacial tension between the LC and prepolymer. Assuming mechanical equilibrium, resolving forces in the directions of σ_{LC} and σ_P gives:

$$\sigma_{LC} + \sigma_{LC/P}cos\theta + \sigma_P cos(\theta + \beta) = 0\,, \tag{7.2}$$

$$\sigma_P + \sigma_{LC/P}cos\beta + \sigma_{LC}cos(\theta + \beta) = 0\,. \tag{7.3}$$

There are multiple solutions to Equations 7.2 and 7.3, which depend on the interfacial tensions. Complete engulfing will occur if $\sigma_{LC} > \sigma_P + \sigma_{LC/P}$ (LC engulfed

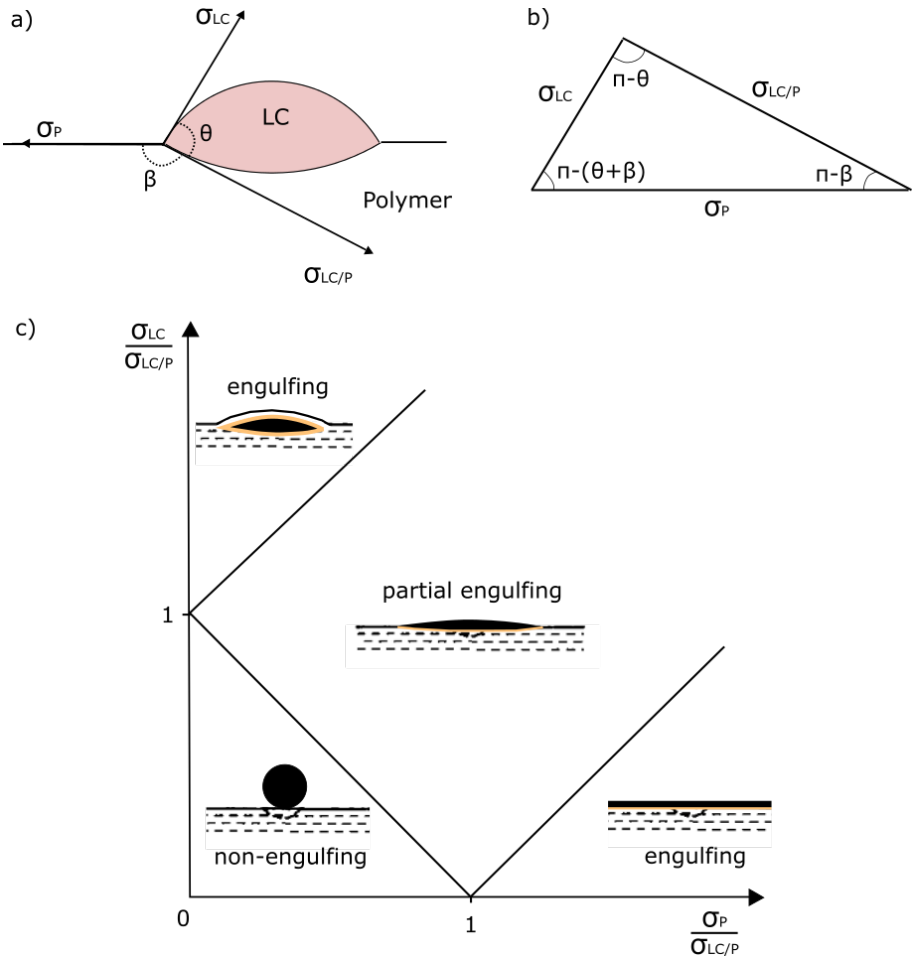

FIGURE 7.9: a) Three-phase diagram showing a LC droplet in contact with a prepolymer substrate in air. b) The resulting Neumann's triangle. c) Parameter space defining the possible engulfing mechanisms in terms of the ratios $\sigma_{LC}/\sigma_{LC/P}$ and $\sigma_P/\sigma_{LC/P}$.

by prepolymer), or $\sigma_P > \sigma_{LC} + \sigma_{LC/P}$ (prepolymer engulfed by LC - complete wetting). No engulfing will occur if $\sigma_{LC/P} > \sigma_P + \sigma_{LC}$. For all other possibilities, partial engulfing occurs. The types of solutions in terms of a normalised surface tension: $\sigma_i/\sigma_{LC/P}$, are plotted in Figure 7.9c.

The surface tensions of the different individual fluids and mixtures used is shown in Table 7.1, on page 163. The interfacial tension between the LC and the prepolymer ($\sigma_{LC/P}$) could not be evaluated via the pendent drop method due the similarity in density of the two phases (see §3.3.2 for details). Although systems containing E7 and NOA65 are well-studied, values for the interfacial tension ($\sigma_{LC/P}$) could not be found in the literature. However, due to the similarity between σ_P and σ_{LC} for all fluid combinations and temperature ranges, it is likely

that partial engulfing occurs (the central region of Figure7.9c). This is particularly evident in samples where $T' < 1$ (i.e. the substrate temperature is less than the mixing temperature) and the droplet has time to exhibit spreading behaviour before it diffuses into the prepolymer film.

Even for fully miscible fluids, there still exists an interface and interfacial tension between the two phases which diminishes over time as the fluids mix [200]. Depending on the degree of mixing and the time-scale over which it occurs, the spreading behaviour of the drop may significantly affect the resulting LC/prepolymer film as it determines the area over which the LC has to diffuse into the prepolymer film.

Adequate Mixing

Figure 7.10a shows high-speed images of a droplet of the nematic LC, BL006, printed onto a NOA65 prepolymer film held at 22°C. As seen in the sequence of high-speed images, the LC droplet is still visible after 37 ms, suggesting that the LC had not dissolved into the polymer. The sample was left for 10 seconds before phase-separation took place in-situ, triggered by irradiating the sample with UV light for 4 minutes at an intensity of 40 mW/cm^2. Figure 7.10b shows the subsequent polarized microscopy image of the photo-cured polymer-LC sample captured after deposition and the photopolymerisation process.

The center of the image in Figure 7.10b shows a pure LC region with a horizontal width of 220 μm. The area of this domain is comparatively large with respect to the printed droplet and, in addition to the high-speed images, indicates that a portion of the LC may have spread on top of the polymer film without dissolving fully into the UV polymer prior to photo-polymerization. This was confirmed experimentally, since upon gentle agitation of this central region with a cotton bud, the LC domain was easily disturbed. After the polarized microscopy images were taken, the sample was thermally cured for 4 hours at 70°C and then re-examined using polarized microscopy. There was no identifiable difference between the images taken before and after thermal curing, indicating the sample had undergone near complete photo-polymerization.

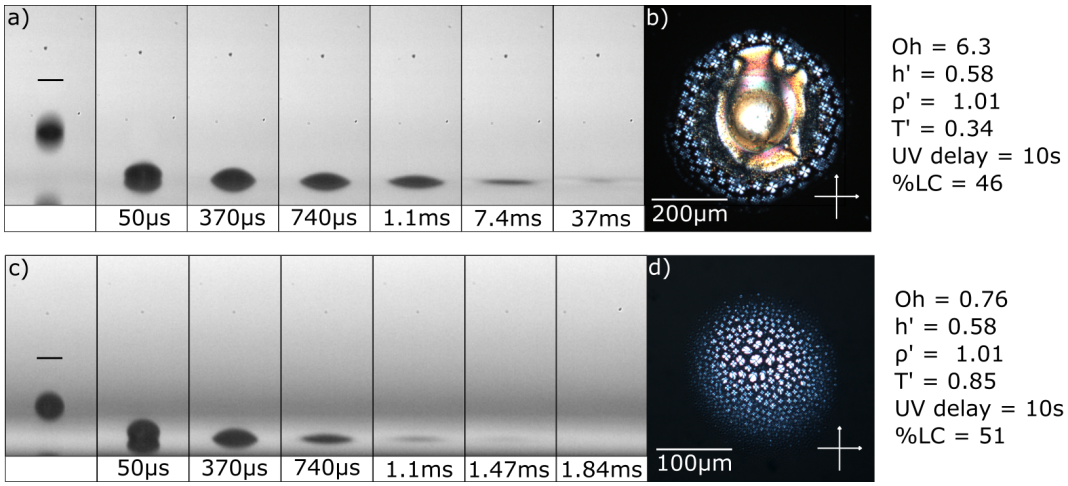

FIGURE 7.10: a) Shadowgraphy images captured using the high-speed camera (13,500 fps) showing the impact of the nematic LC (BL006) droplet onto a 70 μm thick wet, uncured layer of polymer (NOA65), held at a temperature of 22°C. b) Optical polarized microcopy image of the sample after having been irradiated with UV light (intensity of 40 mWcm^{-2}, 365 nm) for 4 minutes and then thermally cured for 2 hours at 70°C. c) Shadowgraphy images captured using the high-speed camera (13,500 fps) showing the impact of a droplet of nematic LC, BL006, onto a wet, uncured 70 μm-thick layer of NOA65, held at a temperature of 55°C. d) Polarized microcopy images of the sample after having been exposed to UV light for 4 minutes and then thermally cured for 2 hours at 70°C. The white arrows in the crossed configuration in c) and d) represent the orientations of the transmission axes of the polarisers.

To encourage further initial mixing on impact of the LC droplet with the uncured polymer binder layer, the temperature of the substrate was increased. As expected, higher temperatures resulted in a higher degree of mixing between the two components. Figure 7.10c shows the impact between a LC droplet, printed at 65°C, with a photo-curable layer held at 55°C. After 1.84 ms, the LC droplet is indiscernible from the prepolymer layer in the high-speed images (last pane in Figure 7.10c), suggesting that the LC has diffused into the prepolymer film. After a delay of 10s, the sample was then photo-cured using identical UV conditions to the sample presented in Figure 7.10a. The polarized microscopy image of the resulting droplet is shown in Figure 7.10d and confirms the increased miscibility between the LC and polymer phase. After photo-polymerisation, there is a higher-density region of PDLC droplets that occupy a circular region, or 'pixel', of approximately 170 μm in diameter. It is evident that the LC droplets within this region are polydisperse, with diameters ranging from $\approx$1 to 8 μm. The full encapsulation of the LC domains was confirmed as agitating its surface did not in any way affect the LC droplets. Despite the formation of PDLC 'pixels', the size of the LC droplets in the region are too large, and the density of the domains too low, to efficiently scatter visible light.

7.2.4 Formation of Surface Waves

Figure 7.11 shows high-speed images from three different samples of a LC being deposited into a prepolymer film, and the resulting microscopy images of a single 'pixel' after it has been photo-polymerised. In each sample, a constant UV-intensity of 60 mWcm^{-2} was applied for 20 minutes whilst it was held at the substrate printing temperature. The fluids used, dimensionless parameters, UV-delay and substrate temperature are indicated in the Figures.

The formation of surface waves can be clearly seen in the high-speed images in each of the samples shown in Figure 7.11. After impact, the LC droplet spreads and there is a thermodynamic drive to become partially engulfed by the prepolymer film. Fluid is pulled from the bulk of the film in order to encapsulate the LC droplet, which simultaneously spreads, forming a lens-like shape. The depletion of fluid around the perimeter of the droplet causes the free-surface of the

FIGURE 7.11: High-speed images with the corresponding microscopy/polarised microscopy images and dimensionless parameters for a 80 μm droplet of E7 impacting a 35 μm thick film of NOA68. The substrate temperature, T_{films}, was: a) 20°C b) 35°C. c) 65°C. The red circle in the polarised optical microscopy images shows the position and diameter of the printed LC droplet for reference.

film to curve. This curvature creates a pressure described by the Young-Laplace equation:

$$\Delta P = \sigma_P \left(\frac{1}{R_1} + \frac{1}{R_2} \right) , \tag{7.4}$$

where R_1 and R_2 describe the curvatures of an arbitrary curved area and σ_P is the surface tension of the prepolymer. This pressure creates a capillary waves which is seen to propagate at low velocities and over long time-scales. Visible surface waves were observed for over 5 minutes, after which point they become difficult to discern in the high-speed images. The characteristic structures observed in Figure 7.11c)ii) is also noted in the deposition of a drop onto an immiscible viscous film [201].

It is noted that the presence of obvious and significant surface waves are only visible in systems where $T' <\approx 0.6$. For systems where $T' >\approx 0.6$, the phenomena is not observed, at least using the side-profile microscopy images taken during printing. It is hypothesised that this is due to the LC sufficiently mixing with the prepolymer, before such waves are formed. The microscopy images in Figure 7.11 show indication of the surface waves and the outer ridges formed. This is particularly evident in Figure 7.11c)ii) where a deliberately short UV-delay of $\approx$1 second was able to capture the ridged structure. It is particularly pronounced in this sample due to low substrate temperature and using NOA68, which does not mix as readily with the LC and is also more viscous.

A Note on Marangoni Forces

The Marangoni effect should be considered whenever there is a gradient in the surface tension between two phases. A surface tension gradient can arise from variations in temperature, solute concentration, or surfactant concentration. In systems dominated by surface tension, the tangential stress created by the surface tension gradient can produce convective motion and significantly affect mass-transport [199, 104, 105].

Due to the pico-litre volumes and small temperature differentials between the droplet and the prepolymer film encountered in this system, temperature-driven surface tension gradients have been disregarded. However, there will be a solutal

concentration gradient across the boundary of the LC and prepolymer. This in turn creates a surface tension gradient with a magnitude that is dependent on the extent of mixing and therefore T'. This is known as the solutal Marangoni effect and can cause large surface distortions, instabilities and other mass-transfer phenomena [202, 104].

Due the similarity in surface tension between the prepolymer, LC and the LC/prepolymer mixtures and the high viscosities of the prepolymer (see Table 7.1), significant marangoni effects are not expected. Indeed, the fact that no surface waves visible for higher T' (when mixing does occur and a surface tension gradients exists) supports the hypothesis that the large surface waves observed are caused principally by capillary action due to the fluids not mixing.

Varying the film thickness, h, is expected to impact the type and propagation of surface waves observed. However, as this study is concerned with creating a flat, homogeneous film, this is outside the scope of this chapter and further analytical study of surface wave phenomena was not undertaken.

Interestingly, there was no indication of birefringence in the POM images of the UV-cured samples presented in Figures 7.11a)ii), b)ii) and c)iv). As $T_{film} < T_{mix}$, it is not expected that the LC fully mixed with the prepolymer film and so dispersed LC domains were unlikely to be seen. However, the polymer imposes planar anchoring conditions, thus the presence of any unmixed LC should be visible in the POM images as a thin birefringent film. It is suspected that that the LC has spread to such a degree that either the effective LC concentration is sufficiently low for mixing to occur[1]. As a minimum LC concentration of ≈20% is required for PDLC formation [167], this may be a reason why no birefringence was observed.

Figure 7.11c)iii) shows a POM images of a sample of E7 and NOA68 after photo-polymerisation. Some birefringence is observed despite $T_{film} < T_{mix}$. The birefringence observed in Figure 7.11c)iii) is not typical of a PDLC domain which are certainly not droplet shaped. As $T' = 0.33$, it is suspected that the LC did not mix with the prepolymer prior to photo-polymerisation and that the ridges in the

[1]The literature reports that up to 14%wt of E7 stays in solution with NO65 after photopolymerisation [189]. Although, NOA68 will differ to NOA65, due to their chemical similarity, it is reasonable to expect a similar proportion of E7 may stay in solution.

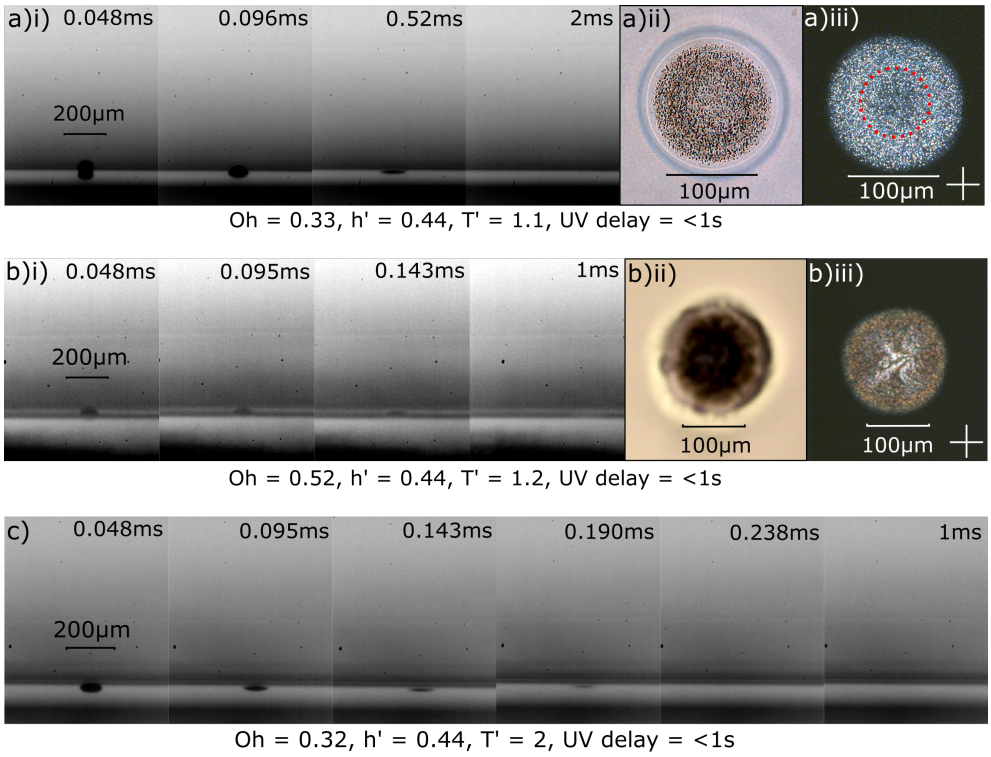

FIGURE 7.12: High-speed images with the corresponding microscopy/polarised microscopy images and dimensionless parameters for a 80 μm droplet of E7 impacting a 35 μm-thick film of NOA65. The substrate temperature, T_{films}, was: a) 20°C b) 35°C. c) 65°C.

surface effectively pooled the LC sufficiently so that mixing did not occur. This was in part confirmed, as gentle agitation of the surface by blowing filtered air over the film surface was seen to disturb the LC surface under inspection with POM.

7.2.5 Diffusion of LC Droplet

To avoid surface wave formation and to ensure the LC mixes with the prepolymer, $T' \approx> 0.6$. Figure 7.12 shows three samples with elevated substrate temperature. The presence of surface waves cannot be observed in the high-speed images and the drop is seen to disappear quickly in to the prepolymer. The corresponding POM images in Figures 7.12a and b, taken after photo-polymerisation, show clear indication of PDLC domains. These domains are highly localised around the area of drop impact, which is indicated on the POM images by a

red circle. Although promising PDLC domains are observed, samples printed at higher temperatures $T' \approx> 1.2$ were highly sensitive to the UV delay.

Using NOA65 and a substrate temperature of 60°C, multiple attempts were made at curing the sample using the minimum achievable delay of 20 ms (see §7.2.1). However, in all scenarios, there was no indication of any LC domains, or indeed any evidence of droplet deposition at all. It is highly likely that this is due to the rapid dissolution of the droplet into the prepolymer film. After 0.238 ms, the LC droplet cannot be discerned in the high-speed images in Figure 7.12c, supporting this hypothesis.

The concentration of LC dissolved into the prepolymer prior to photopolymerisation is a critical factor in determining whether a PDLC is formed, as well as the resulting size and shape of the LC domains. Estimating the LC concentration is complex as it requires knowledge of the extent of droplet has spread and diffused into the prepolymer film. Despite these difficulties, it is informative to make an approximation of the LC concentration in order to speculate as to why LC domains are observed in some samples and not others.

Assuming that the entire LC droplet volume has mixed with the prepolymer layer, an average volume fraction of LC can be estimated by considering the ratio of LC drop volume, over a cylindrical volume of the prepolymer film that the LC has diffused into:

$$R_{LC} = \frac{2d^3}{3d_p^2 h}, \tag{7.5}$$

where d is the LC drop diameter, h is the thickness of the film and d_p is the estimated diameter of the region the LC has diffused into. It is worth emphasising that Equation 7.5 is used to give a rough estimate of the average LC volume fraction only. It is expected that the LC concentration varies significantly throughout the depth and width of the prepolymer film. Additionally, it is very difficult to assess the extent of in-plane diffusion from the POM images, as it relies upon detectable LC domains to be formed upon photo-polymerisation.

Figure 7.13 shows microscopy and POM images of five different samples after photo-polymerisation. The concentration of LC present in the samples has been estimated using Equation 7.5, where d_p is taken as the diameter of the LC regions

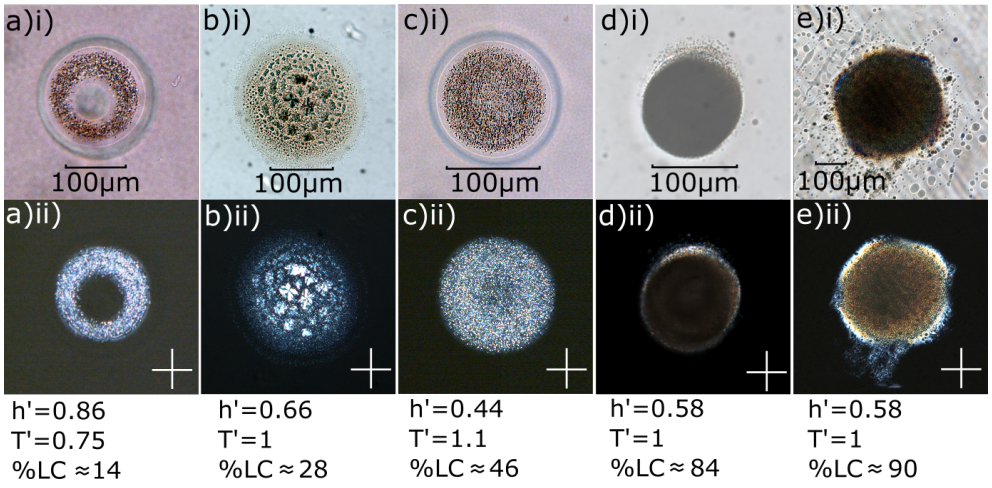

FIGURE 7.13: i) Microscopy and (ii) polarised optical microscopy images taken after photo-polymerisation comparing the approximate percent of LC (%LC) in the PDLC regions for various samples. a) 80μm droplet of E7 printed into a 80μm-thick film of NOA68, held at 45°C and cured with a UV-intensity of 40mW/cm^2. b) 120μm droplet of BL006 printed into a 80μm-thick film of NOA65, held at 40°C and cured with a UV-intensity of 40mW/cm^2. c) 80μm droplet of E7 printed into a 35μm-thick film of NOA68, held at 35°C and cured with a UV-intensity of 50mW/cm^2. d) 120μm droplet of BL006 printed into a 70μm-thick film of NOA65, held at 60°C and cured with a UV-intensity of 70mW/cm^2. e) 20 80μm droplets of E7 printed onto the same location into a 70μm-thick film of NOA65, held at 30°C and cured with a UV-intensity of 40mW/cm^2.

visible in the POM images. There are PDLC domains visible in all the samples presented. It can be seen that samples with an apparently higher proportion of LC form denser LC domains which appear to scatter light more efficiently. Figure 7.13e was formed by printing 20 droplets at the same location into a 70μm-thick film of NOA65. Although a dense region of PDLC is formed, it appears some of the LC has bled out of the film, indicated by the blotches seen in Figure 7.13e)i).

Across the board, formation of PDLCs was only ever observed in samples with $\%LC > \approx 0.25(\mathrm{v/v}\ \%)$, which agrees with reported LC concentrations necessary for PDLC formation. It is very difficult to accurately control the LC concentration as it is dependent on the area the droplet spreads, the extent and rate the drop mixes with the prepolymer layer, the film-thickness and the extent the LC diffuses into the prepolymer film. In addition, the UV delay is critical as it effectively captures the state of the system at the time of photopolymerisation and so is an additional critical parameter.

7.2.6 Material Selection

Although successful PDLC regions were formed using NOA68, on many occasions the mixing of the LC led to the formation of detrimental surface waves, or there was evidence that the LC was not fully encapsulated after photopolymerisation. Ultimately, it was difficult to reproduce results using this prepolymer. Out of the possible combinations of LC and prepolymer, BL006 and NOA65 were found to form the most replicable and light-scattering PDLC regions. It was thus decided to henceforth focus on these materials only and determine the optimal curing conditions and UV-delay.

7.2.7 Photo-polymerisation

For optimum light scattering, the LC domain size should be slightly larger than the wavelength of light [203, 204]. For visible light scattering applications, this corresponds to a droplet size distribution $\approx$ between 0.5 to 1.5μm in diameter. The size of the LC domains in a PDLC film are primarily determined by the UV

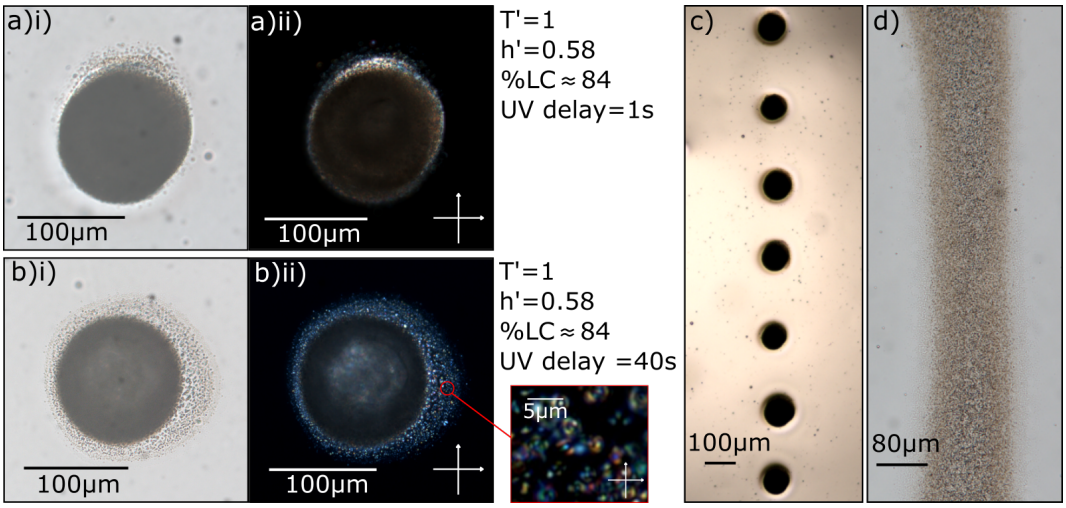

FIGURE 7.14: a)i) and ii) Optical microscope and polarized microscope images, respectively, of a single nematic LC droplet printed onto a 70μm-thick layer of wet, uncured polymer (NOA65), held at a temperature of 65°C. The sample was irradiated with UV light for 4 minutes with an intensity of 70mW/m^2, after a delay time between printing and UV (365 nm) irradiation of 1 second. b)i) and ii) Optical microscope and polarized microscope images, respectively, of a single nematic LC droplet printed onto a 70μm-thick layer of wet, uncured polymer (NOA65), held at a temperature of 65°C. The sample was irradiated with identical illumination conditions to the sample presented in Figure 7.14a), but with a delay time between printing and UV-irradiation of 40 seconds. c) Microscopy images of a single line array of printed PDLC pixels. The dark regions are due to the high degree of scattering caused by the combination of small LC droplets (dimensions) and polymer binder. d) Optical microscopy image of a printed PDLC line. Samples in c) and d) were photo-cured under identical conditions as the sample presented in Figure 7.14a).

curing intensity, curing temperature, LC concentration, and the physical properties of the LC and polymer phases - such as the elastic coefficients, interfacial tension and viscosity [153].

In this system, there is an additional parameter, which is the delay between the deposition of the droplet and photo-polymerization process. Increasing the UV curing intensity and/or curing temperature increases the rate at which polymerization occurs, resulting in smaller LC domains. The film temperature is limited by to the approximate range of $0.6 < T' < 1.2$ ($T' = \frac{T_{film}}{T_{mix}}$), making the UV intensity the most practical variable for controlling the PDLC droplet diameter.

Over many samples, it was found that a UV intensity of 70 mW/cm^2 produced PDLC droplets that were highly scattering. Figures 7.14a)i) and a)ii) show

the resulting microscopy and polarized microscopy images of a printed PDLC pixel, which was formed by printing a 120 μm droplet of BL006 into a 70 μm thick NOA65 film. The initial delay between printing and curing was 1 second. As can be seen in the microscopy image, there is a darker central area that is approximately 120 μm in diameter, indicating that the domain is highly light scattering. There is a thin region around the perimeter of the droplet which has a lower density of LC domains, which is particularly visible in the polarized microscopy image in Figure 7.14a)ii). By inspection of the microscopy image, it can be seen that the higher photo-curing intensity resulted in LC domains that were between 0.5 to 1 μm in diameter and the resulting PDLC 'pixel' has vastly improved light scattering properties. The LC domains are confined to a localised area around the point of drop impact.

7.2.8 UV Delay

To examine the effect of the delay time between droplet deposition and photopolymerisation, a sample was prepared under identical conditions to that presented in Figure 7.14a), but with a delay time of 40 seconds. Figures 7.14b)i) and b)ii) show the resulting microscopy and polarized microscopy images for the longer delay time process. The low-density regime of the LC droplets around the perimeter of the pixel is larger than that observed for the sample photo-cured 1 second after printing, which is particularly evident from the image in Figure 7.14b)ii). Nevertheless, the area of the high-density central regime is of a comparable size to that of the previous sample, with a diameter of 120 μm.

It was expected that for an increase in the delay time there would be a more substantial increase in the effective PDLC pixel diameter, as there is more time for the LC to diffuse within the prepolymer layer. However, the results suggest that the majority of the LC is effectively pinned to an area close to that of the maximum area of the droplet as it initially spreads on top of the prepolymer (NOA65) layer during droplet impact. It is suspected that the mobility of the LC molecules is severely hindered due to the large, high molecular weight, polymer chains of the prepolymer.

In addition to the formation of individual PDLC pixels, inkjet printing makes it possible to form arrays of pixels as seen in 7.14d. The line array was printed with the wet prepolymer layer held at a temperature of 65°C. After a 10 second delay, the sample was then cured at 65°C using a UV-light source with a power density of 55!mWm^2 at the exit of the source, which was held at a distance of 2 cm from the sample. The printed line seen in Figure 7.14d) was deposited by supplying the printhead with a step-input voltage pulse. This results in an extended fluid ligament, which combined with translation of the printing substrate, results in the ability to print lines. Additionally, line geometries could also be produced by printing LC droplets close to each other, akin to how conventional graphical inkjet printers function. Although this study is concerned with droplet diameters of the order of 100 μm, tests have been carried out using smaller nozzles, with preliminary results indicating that with further optimization, feature sizes as small as 15 μm could be produced.

7.2.9 Optical Properties

After determining the suitable conditions required to produce IJP PDLC domains, the same procedure was applied using ITO-coated substrates, so that the switching could be observed. However, it was observed that prepolymer films deposited onto the ITO-coated glass behaved somewhat differently. The prepolymer films had a tendency to pool as the film was left and also during curing. This often resulted in films with varying thicknesses, significantly effecting the formation of PDLC regions.

As the PDLC fims are fully encapsulated, the films deposited onto the glass microscope slides were carefully peeled away from the substrate using a scalpel and sandwiched between ITO-coated glass. To ensure a constant cell gap of 70 μm, spacer tape was used around the perimeter of the cell and optical glue was then used to bind the substrates together.

Figures 7.15a)ii) and b)ii) shows optical microscopy images of a single 'PDLC pixel' in the Off/dark state and ON/transparent state, respectively. To characterize, qualitatively, the change in the light scattering of the printed PDLC pixels with electric field, a He-Ne laser (633 nm, continuous wave) was focused onto

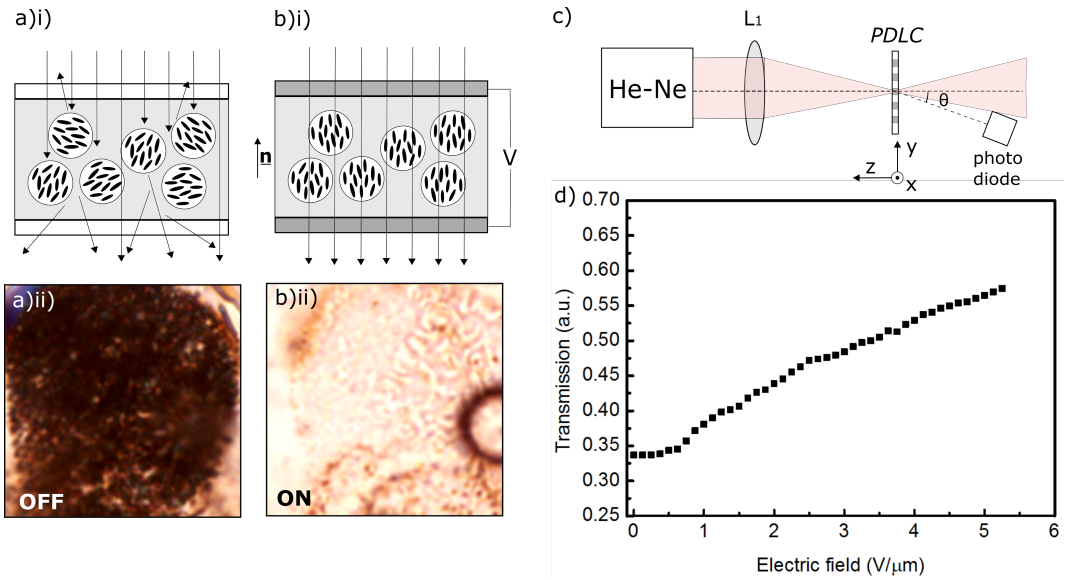

FIGURE 7.15: a)i) and b)i) Schematic representation of a printed 'PDLC pixel' in the OFF (scattering) and ON (transparent) state under the application of an electric field where the unit vector $\hat{\boldsymbol{n}}$ depicts the macroscopic alignment of the nematic director. a)ii) Optical microscope image of a single printed 'PDLC pixel' in the passive scattering state. b)ii) Microscope image of a single printed 'PDLC pixel' under the application of an external electric field. c) Optical set-up used to characterize the light scattering of the printed PDLC pixels, L1 is the lens used to focus the He-Ne laser onto an individual 'PDLC pixel'. d) Plot showing the effective transmission of laser light through a single PDLC pixel as a function of the applied electric field amplitude. The sample is initially in a scattering state in the absence of an applied electric field.

an individual PDLC pixel using a focusing lens (f = 250 mm). A photo-diode (PDA36A-EC, Thorlabs) was then positioned at an angle of 8°from the laser beam propagation direction so as to measure the forward off-axis scattered light. A schematic of the set-up is shown in Figure 7.15c). The intensity of light reaching the photodiode was recorded as the voltage across the PDLC film was increased. Figure 7.15d) shows the effective transmission of the PDLC pixel as the voltage is increased. The PDLC pixel is seen to change from a dark to transparent state. However, the cells were easily damaged at high voltages, above 5 V. This was attributed to the presence of air gaps in the cell, produced as films were transferred onto ITO-coated glass.

7.2.10 Method 1 - Conclusions

It has been shown how drop-on-demand inkjet printing can be used to selectively position PDLC regimes within a single film. By ensuring adequate mixing of the LC and photopolymer during droplet impact, a PDLC pixel consisting of a high density of LC droplets is formed upon irradiation of the sample with UV light. Over a narrow range, photopolymerisation conditions can produce PDLC regimes efficiently scatter visible light. BL006 and NOA65 proved the most effective formulation to use. The resulting printed 'PDLC pixel' using this formulation is surprisingly robust to the delay time between the printing and photo-curing steps.

However, despite a relatively comprehensive analysis of the physical processes and important parameters, the reliable formation of patterned PDLC films using this meothd was very difficult to achieve. In addition to the LC and prepolymer selected, the number of key and interrelated variables such as substrate temperature, mixing temperature, film-thickness, drop diameter, UV-intensity and UV-delay made the determining the optimal conditions exceedingly difficult.

7.3 Method 2 - Direct Printing of a PDLC Formulation

The direct inkjet printing of a LC/prepolymer formulation was demonstrated in §6.4.1. The second method of forming IJP PDLC films builds upon this result and

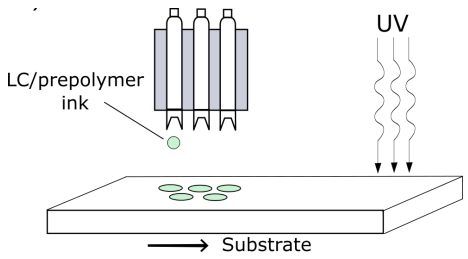

FIGURE 7.16: Illustration of the second method of forming patterned polymer-dispersed LC films via the inkjet printing of a LC/prepolymer formulation.

is shown schematically in Figure 7.16. Inkjet printing of individual components of the PDLC formulation (Method 1) potentially allows for more control over the composition of the PDLC films, for example the concentration of LC prior to photopolymerisation. However, directly printing the PDLC formulation overcomes many of the problems encountered in method 1. In particular, the complex mixing and diffusion processes between the LC and prepolymer are avoided entirely. Furthermore, there is no requirement for a pre-prepared thin-film of prepolymer to be deposited prior to printing, potentially reducing the number of processing steps required to fabricate a PDLC film.

As previously stated, inkjet printing is a valuable tool in the fabrication of small and large-area thin-films [205, 206]. Films, rather than individual droplets can be fabricated by depositing droplets close enough such that they coalesce.to coalesce. This section reports the direct inkjet printing of patterned PDLC films that has, to date, been unreported in the literature.

7.3.1 Experimental

A formulation of E7 and NOA65 was selected as the LC and prepolymer components for this method. These materials were selected as they were found to produce light scattering PDLC regimes in Method 1. Additionally, a formulation of these components was shown to be printable in Chapter 6. A concentration of 40:60%wt LC:prepolymer was chosen as this ratio is known to form films with good light scattering properties [156]. Furthermore, preliminary results indicated that using higher concentrations often resulted in LC becoming phase separated at the free surface of the droplet after photopolymerisation.

The same printing set-up used in method 1 (see page 162) was again used. However, it was found that in-situ UV-curing at the printing substrate was unnecessary. After droplet deposition, the samples could be left at room temperature and even stored for periods of time (some samples were left for 12 hours) with no observable effect to the PDLC morphology after photopolymerisation. It is supposed that this is due to the high miscibility of E7 and NOA65, the phase diagram in Figure 7.5b, on page 7.5, indicates that a single homogeneous phase is formed for temperatures above 5°C at this concentration. The samples were instead transported to a designated UV-curing station consisting of a high-powered UV LED (Thorlabs, CS2010 UV high power UV curing LED system) and hot-plate.

As discussed in §6.4.3, the addition of the prepolymer makes the printing of the formulation difficult. In that study, a 50 μm nozzle was used to deposit a 35:65%wt formulation of E7/NOA65. However, as this study uses a higher proportion of LC which is less viscous than the prepolymer, droplets could be reliably deposited using the 80 μm nozzle. The larger nozzle was selected as it better facilitated the formation PDLC regimes that were visible to the naked eye. Figure 7.17a shows the bipolar waveform used to generate droplets in this study. It is noted that the maximum rated $\pm V$ of the nozzle is 120 V. The printing temperature was held at 60°C to minimise the possibility of thermal curing of the prepolymer.

The printing substrate used in this study was ITO-coated glass (SPI supplies), used in §6.4.4. The printing substrate was held at a constant temperature of 20°C in all the samples presented in this section. Figure 7.17b shows high-speed images of a droplet of E7/NOA65 generated using this waveform. The droplets were approximately 78$\pm$1 μm in diameter. Figure 7.17c shows the equilibrium shape of a single droplet before photopolymerisation. Upon impact with an ITO-coated glass cell, the droplets assumed a spherical shape with a diameter of 160 μm and a contact angle of 27°.

7.3.2 Results and Discussion

Once the PDLC formulation was deposited the challenge was to form LC domains that efficiently scatter visible light. As a baseline, the UV-intensity found

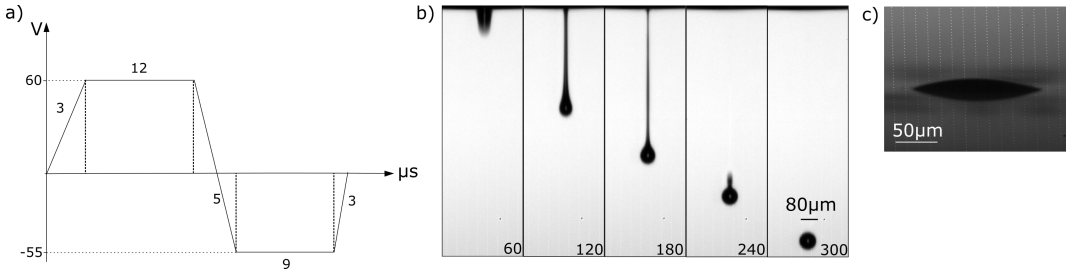

FIGURE 7.17: a) The bipolar waveform used to produce droplets of E7 and NOA65 (40:60%wt) using the 80 μm microfab printhead. b) High-speed images of the resulting droplets (16,000 fps, 8 μs exposure). The numbers in each frame correspond to the approximate time in μs since the arrival of the driving waveform at the nozzle. c) An image of the equilibrium profile of a single droplet prior to photopolymerisation and deposited onto an ITO-coated glass cell.

to achieve appropriate scattering from Method 1, namely 28 mW/cm^2 for E7 and NOA65 was used. Figure 7.18a shows microscopy and POM images of a single droplet that was polymerised using this UV intensity for 30 minutes, whilst held at a temperature of 20°C. As is evident from the images, the LC domains formed were too large to efficiently scatter visible light, with droplet diameters ranging from 1-7 μm in diameter. The POM image show optical signatures characteristic of concentric droplet configurations in the larger droplets, and bipolar configurations in smaller droplets, $<\approx 2\mu$m in diameter (see §2.3.4). The PDLC were agitated using a cotton bud and cloth with no observable effect on the sample, indicating the LC domains are fully encapsulated.

To create more scattering from the PDLC droplets, the UV-curing intensity was increased to 29 mW/cm^2. In addition, the amount of LC deposited was increased by printing 10 consecutive droplets at the same location. Figure 7.18b shows microscopy and POM images of an arbitrary array of PDLC dots and hashes after the sample had been irradiated at this UV-intensity for 30 minutes. A slightly mundane but nevertheless important observation is the poor uniformity of the droplet boundary due to the 'oily streaks' visible in Figure 7.18b. It was discovered that shaking the duster cannister (CA4, Thorlabs) prior to use caused some of the gas propellent to be deposited onto the surface, significantly effecting the droplet boundary. However, the droplet boundary is not as significant in the fabrication of light scattering PDLC domains, the sample is still presented.

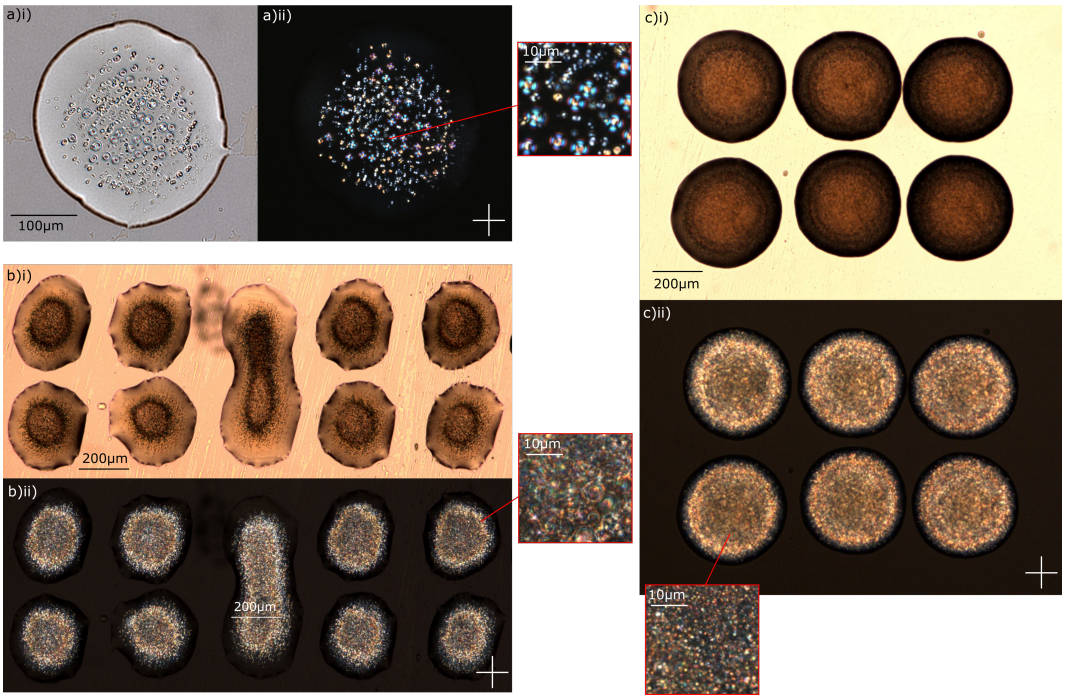

FIGURE 7.18: Microscopy (i) and polarised microscopy (ii) images of droplets and arrays of printed PDLCs after irradiation with different UV intensities for 30 minutes. a) A single droplet deposited onto ITO-coated glass and cured using 28 mW/cm^2. b) Array where each droplet consists of 10 droplets deposited at the same location. Cured using 30 mW/cm^2. c) Array where each droplet consists of 20 droplets deposited at the same location. Cured using 34 mW/cm^2. All the samples were photopolymerised at a temperature of 20°C.

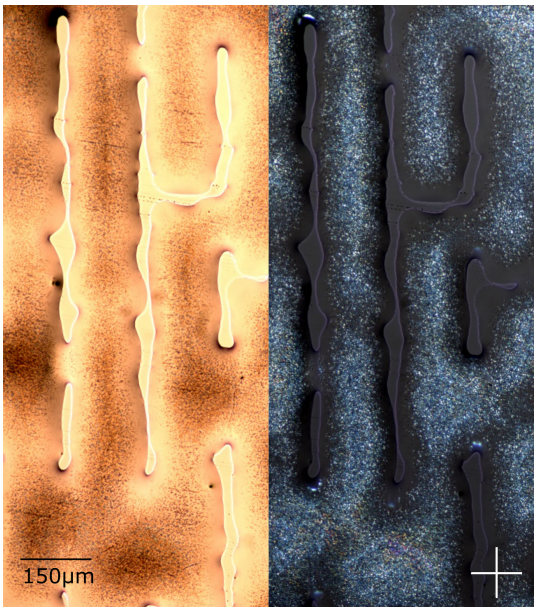

FIGURE 7.19: Microscopy and polarised microscopy images of lines of PDLC domains. The sample was cured for 30 minutes using 185 mWcm^{-2}, held at 20°C.

The light scattering of the PDLC samples is much improved, particularly in the central region of the droplets. The POM images in Figure 7.18b)ii) indicate a high density of LC droplets in the order of 1-2 μm in diameter.

The optimum curing intensity was found to be 34 mW/cm^2. Figure 7.18c shows microscopy and POM microscopy images of a 3x2 array of PDLC regimes each consisting of 20 consecutively printed droplets. As evident from Figure 7.18c)i), the increased UV-intensity and the larger volume of LC produces highly scattering PDLC pixels. The POM image in Figure 7.18c)ii) indicate LC droplets in the region of 1-1.5 μm in diameter.

The formation of lines and areas can be achieved using inkjet printing by depositing droplets at a distance such that they coalesce as the droplet wets the substrate. Figure 7.19 shows a bespoke PDLC pattern consisting of 80 droplets. The patterned PDLC was cured using the optimum intensity of 34 mW/cm^2. The pattern was designed to be a maze, however, there are three positions where the droplets unintentionally coalesced making the maze impossibly difficult. This is understandable given the spatial resolution achievable by the custom-made motorised stage described in §3.1.3. Nevertheless, the figure demonstrates the capability of producing bespoke array and film patterns.

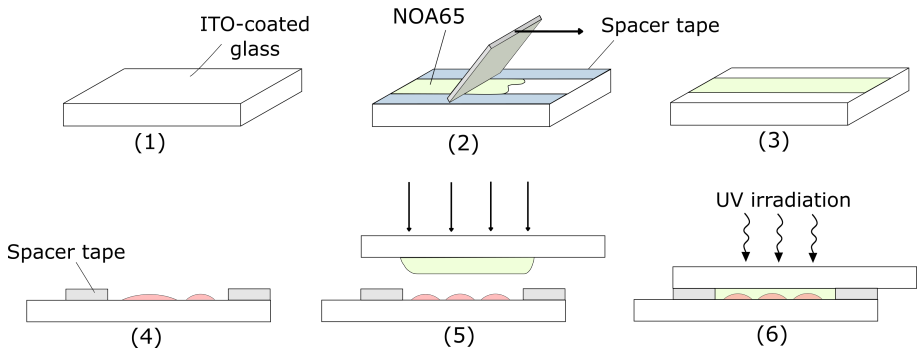

FIGURE 7.20: Illustration showing the procedure followed for fastening a top substrate for the inkjet printed PDLC films. (1) ITO-coated glass top substrate. (2) Spacer tape is applied to the top substrate and NOA65 is spread to create a thin-film. (3) The spacer tape is removed from the top substrate. (4) Spacer tape is applied to the either side of the microlens substrate. (5) The top substrate is fastened to the bottom substrate. (6) The cell is irradiated with UV-light.

7.3.3 Cell Preparation

The LC/prepolymer formulation was deposited directly onto ITO-coated glass. However, a top electrode must still be positioned in order to switch the PDLC regions to a transparent state. Ideally, this would be done in an all-printed manner thereby utilising the full benefits of inkjet printing. To test the switching capabilities of the printed PDLCs samples, a top substrate was fastened following the procedure illustrated in Figure 7.20.

A thin-film of NOA65 was first applied to an ITO-coated glass substrate, which would form the top substrate of the sample. Spacer tape was used to define the approximate film-thickness of the prepolymer, which was equivalent to the tape applied to the bottom substrate (Figure 7.20, step 4). The spacer tape was then carefully removed from the top substrate and it was placed over the bottom substrate containing the PDLC array. The substrates were clamped down using two clips to ensure an even pressure distribution. The cell was then irradiated with a UV-intensity of 34 mW/cm^2 for 30 minutes with the clips in place and a further 20 minutes once the clips had been removed.

Figure 7.21 shows microscopy and POM images of a PDLC array after the top substrate and been fastened and in-filled with NOA65 forming a 40 μm-thick cell. Comparing the images to Figure 7.18b, it is evident that the in-filling process did

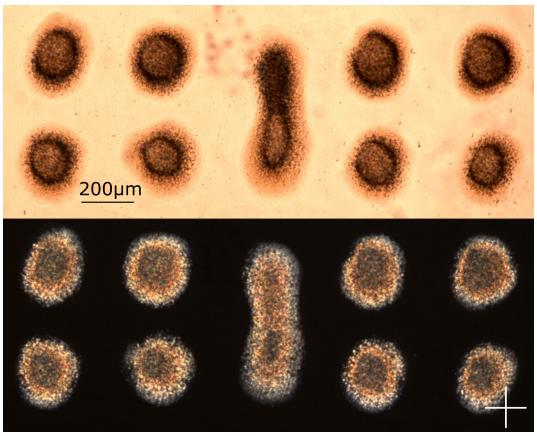

FIGURE 7.21: Microscopy and polarised microscopy image of the array shown in Figure 7.18b after the top substrate has been fastened and the cell has been photopolymerised.

not in any way effect the array pattern or the light scattering of the PDLC regions.

7.3.4 Electrical Switching

The cells were placed in a transmission-mode microscope and a waveform generator and amplifier used to supply a 1kHz sine wave to the PDLC sample. Microscope images were taken as the voltage was increased to observe the transparent state of the PDLC regions. Figure 7.22 shows the resulting microscope images over a range of voltages. The numbers in the top of each image is the field strength (E =$\mathrm{V}_{RMS}\mu\mathrm{m}^{-1}$). The sample shown in figure 7.22a consists of dots and hashes formed of 10 droplets. As seen in Figure 7.22a, the PDLC regions become almost indiscernible at 5.3 V. On the other hand, Figure 7.22b, where each PDLC region is composed of 20 droplets requires a higher field strength to switch. At 8.8 $\mathrm{V}_{RMS}\mu^{-1}$, both samples appear mostly clear in the microscope images. It is noted that when both samples were viewed using the microscope eyepiece (rather than the microscope camera), PDLC regions could not be discerned for fields above 7.07 $\mathrm{V}_{RMS}\mu\mathrm{m}^{-1}$.

Transmission

The optical arrangement shown in Figure 7.23a was used to quantify the optical transmission of the PDLC film. A Helium–neon laser (λ =632.8 nm) was used to illuminate a 1mm diameter circular region of the PDLC sample, which was

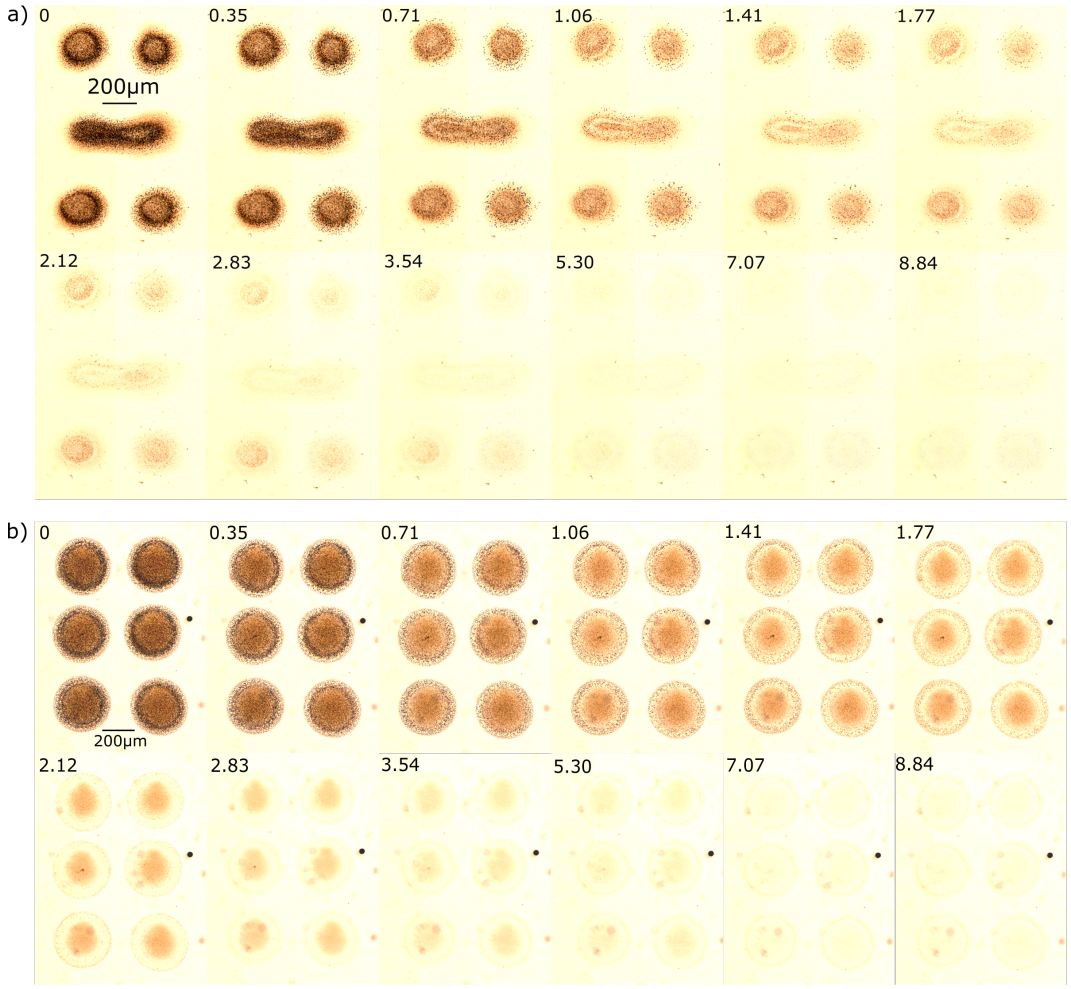

FIGURE 7.22: Microscopy images taken of the switching of two inkjet printed PDLC arrays: a) Sample presented in Figure 7.18b, cell thickness of 40 μm. b) Sample presented in Figure 7.18c, cell thickness of 80 μm. The numbers at the top of the images are the field strengths ($V_{RMS}\mu m^{-1}$). The switching waveform was a 1 kHz sine wave.

placed on an x-y-z translation stage. Initially, a lens and CCD camera was positioned in place of the photo-diode to form an image of the PDLC film. This was performed in order to assess the location of the centre of the laser relative to the PDLC pattern. The centre of the laser beam was positioned at the centre of the 3x2 PDLC sample, indicated by the blue cross in the inset of Figure 7.23a. A simple MATLAB program was then used to assess the 'coverage' of the laser beam (i.e. the proportion of the laser beam that is incident to PDLC regions, rather than just polymer). The CCD was then replaced with a photo-diode at a distance of 96mm from the PDLC film.

The voltage of the photodiode was measured as the amplitude of the voltage supplied to the cell was increased. The optical transmission was extracted by normalising the measured photo-diode voltage through the PDLC region to the voltage measured by the diode in the same configuration but with the laser beam passing through a region of the cell void of PDLC regions. Finally, the coverage of the laser beam by the PDLC regions was used to determine the transmission through the PDLC regions. The optical arrangement was placed in a box to minimise background light.

Figure 7.23b shows the resulting optical transmission through the sample shown in the inset of Figure 7.23a. In the off state, the transmission is 64% for λ=632.8 nm, which is comparable to PDLC films of similar thickness's and suitable for use as smart windows [207, 157]. The threshold field strength (E_{th}) and the saturation field strength (E_{sat}) are defined as the field strengths at which 10 and 90% of the possible transmission range is achieved, respectively. This corresponds to a E_{th} =0.3 $V_{RMS}\mu m^{-1}$ and V_{sat} =2.5 $V_{RMS}\mu m^{-1}$. The films show a high optical transmission of 95% in the ON-state. The good optical transmission is owed to the relatively low concentration of LC used and the excellent optical matching between the polymer and LC. Additionally, as transmission has been measured for longer wavelengths of visible light only, scattering due to LC domains smaller than ≈650 nm will be reduced.

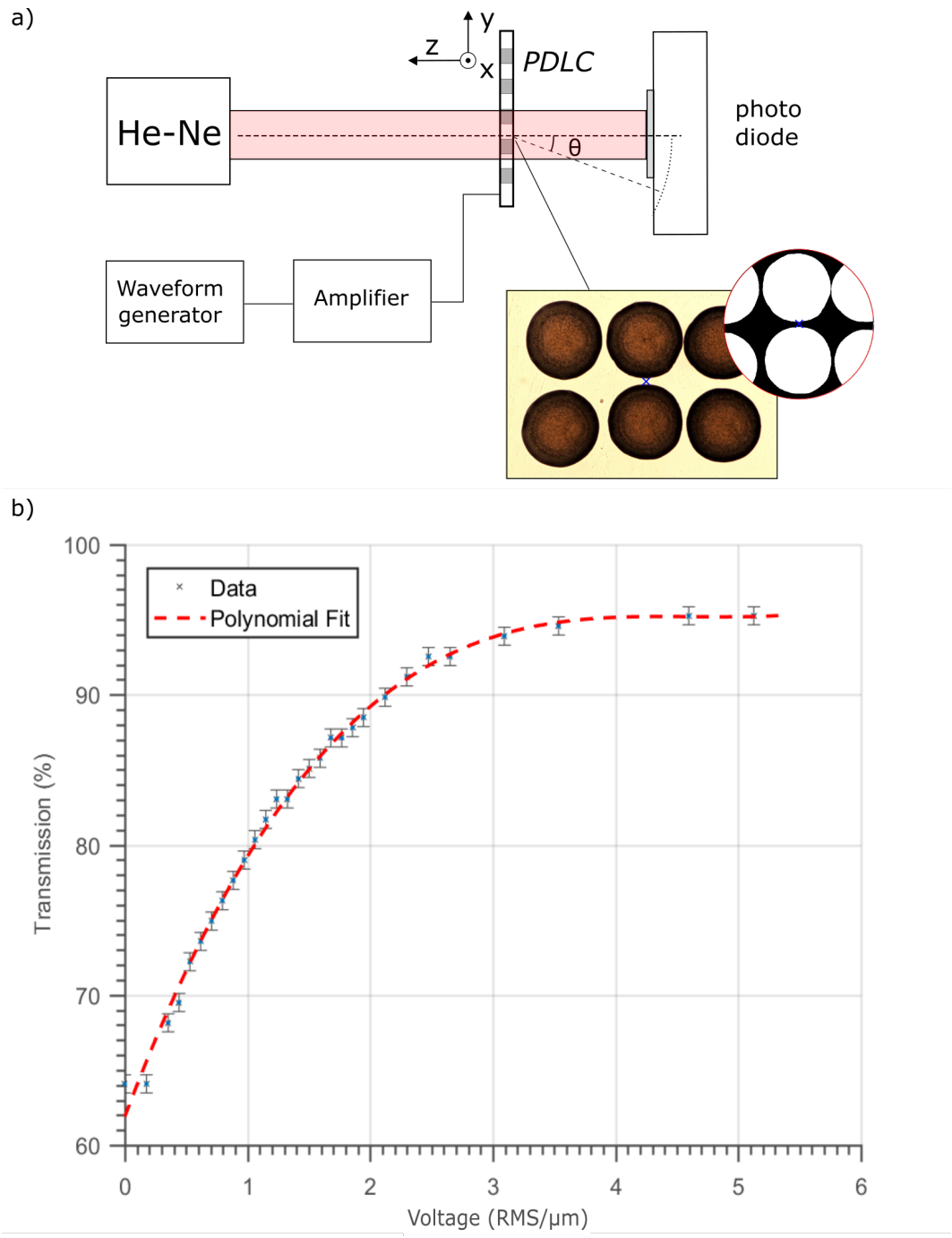

FIGURE 7.23: a) Optical arrangement used to determine the transmission of the IJP PDLC film and the off-angle scattering. The insert shows a microscopy image of the PDLC film used and the placement of the laser beam indicated by the blue cross. The binary image was used to calculate the area of the beam occupied by PDLC regions. b) Graph of the normalised optical transmission against the root-mean-squared voltage per micron. A 1 kHz sine wave was used to switch the PDLC film shown in the insert of (a).

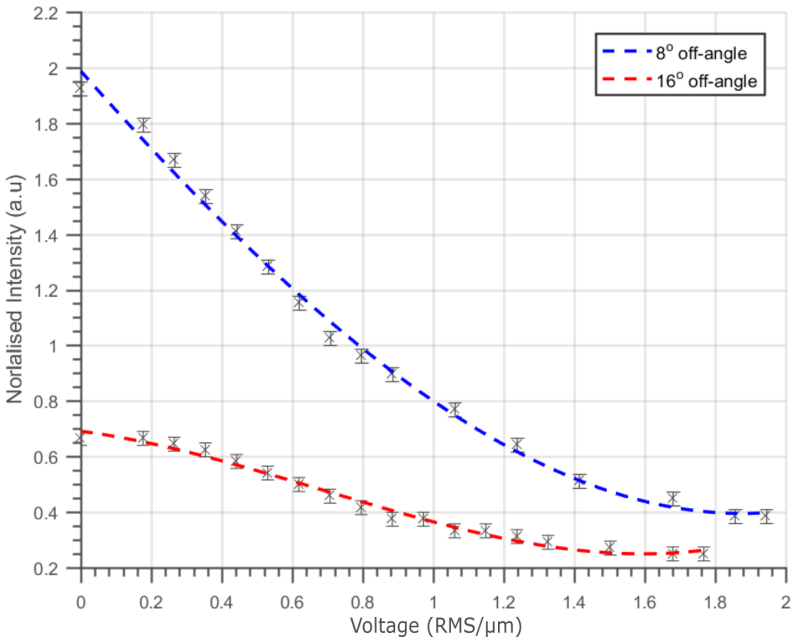

FIGURE 7.24: Graph of the off-angle scattering intensity measured using the optical arrangement in Figure 7.23a with the diode placed at 8 and 16°. The intensity has been normalised such that at 0 in the y-axis represents the scattering intensity measured with the beam positioned over a portion of the cell without any PDLC regions.

Scattering

The photo-diode in Figure 7.24a was positioned at two different angles of θ=8°and 16°C to measure the off-angle scattering. At these angles, the detector of the photodiode was outside the diameter of the unobstructed laser beam. At each angle, the intensity of scattered light was normalised against the background intensity, i.e. the intensity measured when the beam is directed onto a portion of the cell void of PDLC regions. The coverage was again used to determine the scattering of the beam due to PDLC regions only. The intensity was normalised such that 0 in the y-axis represents the background intensity, 1 represents double the background intensity, etc. After 2V, there was no further reduction in the intensity measured for both angles. This indicates there is some off-angle haze, an inherent problem with PDLC films. However, after 1.75 V (50% of V_{sat}), the intensity of scattered light drops to 20% (8°)and 40% (16°) of the background intensity.

Response Times

The response time was measured using the optical arrangement shown in Figure 7.25a. Two 5 Hz and 1 kHz square waves were generated using a dual-output waveform generator. The 5 Hz waveform was then used as an input to the waveform generator to modulate the 1 kHz waveform which was then amplified to 8.75V $_{RMS}\mu$m^{-1}. A photo-diode was attached to the microscope to measure transmitted light (halogen filament light bulb) through the PDLC sample.

Figure 7.25b shows the corresponding optical transmission. The driving waveform is high from 49-149 ms in the figure. The rise time (t_{rise}) and decay time (t_{decay}) are defined as the time taken for the transmittance to change from 10 to 90%, and 90 to 10% respectively. At this driving voltage, the rise time was 9 ms and the decay time was 60 ms. The relaxation time for a spherical droplet is analogous to that of a planar cell and can be used to estimate the decay time (see §2.4.3) [208]:

$$t_{decay} = \frac{\gamma_1 d^2}{\pi^2 K}, \tag{7.6}$$

where γ_1 is the rotational viscosity, d is the droplet diameter and K the average

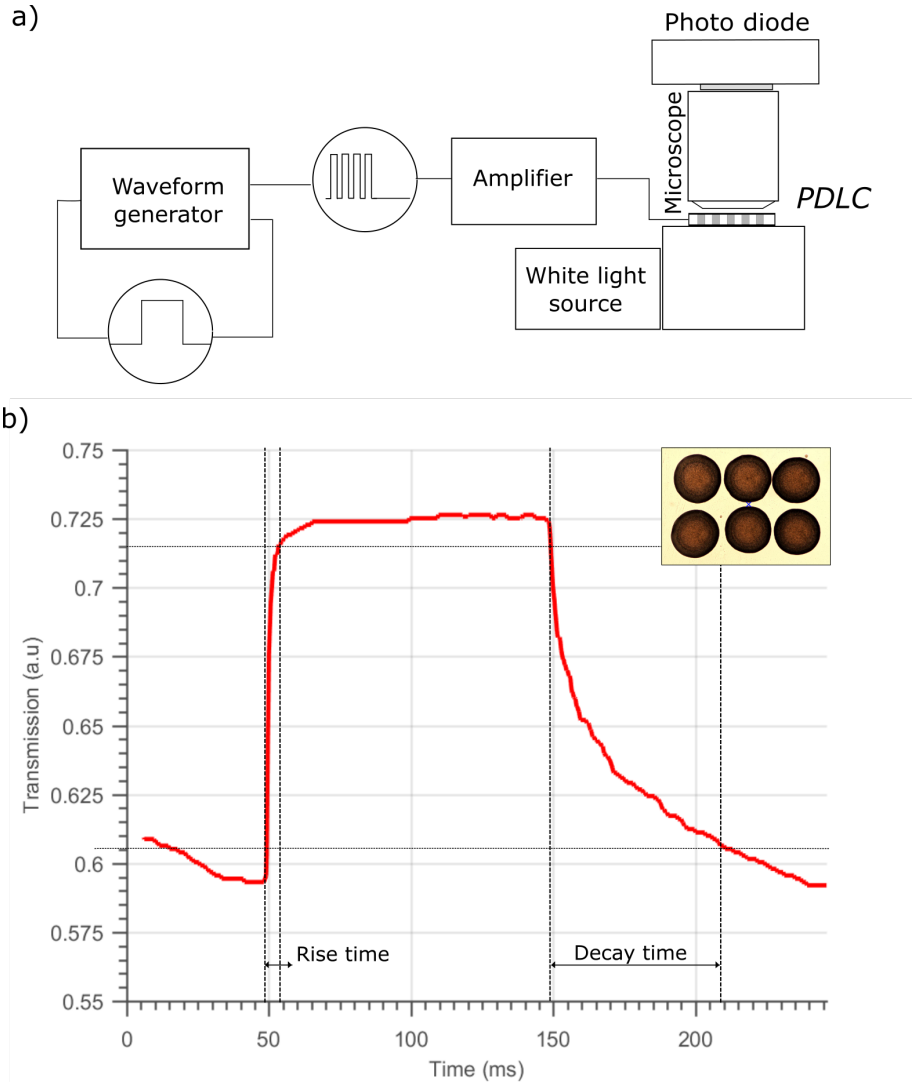

FIGURE 7.25: a) Optical arrangement used to determine the response times of the PDLC films. A 1 kHz output waveform was modulated by a 5 Hz square wave and amplified to produce a 8.75 V_{RMS}/μm pulsed driving waveform. b) Graph of the resulting response time of the inkjet printed PDLC sample shown in the insert.

elastic constant. Using γ_1 =253 mPas, K=10 pN (typical values for E7) and a decay time of 60 ms, this gives droplet diameters in the order of 4.8 μm. This droplet radius is a little larger than expected, as the POM images in Figure 7.18c, indicate LC regions in the order of 1-1.5 μm. However, given the exact morphology of PDLC is unknown this a reasonable discrepancy.

7.4 Conclusions

Investigating the deposition of the LC component separately on to a thin-film of prepolymer (Method 1), highlighted several important physical processes. Producing localised PDLC regions using this method required careful consideration of the mixing of the LC and prepolymer components, the concentration of the LC prior to photopolymerisation and the delay between droplet deposition and photopolymerisation.

Due to the high viscosity of the fluids used, mixing was attributed primarily to diffusion. For $T_{film} <\approx 0.6T_{mix}$, the LC did not sufficiently mix with the prepolymer and resulted in the the formation of surface waves. On the other hand, for $T_{film} \approx> 1.2T_{mix}$, the formation of PDLC regions was not observed which is attributed to fast diffusion of the LC droplet into the prepolymer film. The apparent ratio of LC prior to photopolymerisation proved to be critical for forming scattering PDLC regimes. The UV-delay offered a possible means of controlling the LC concentration as it effectively captures the system at a particular point in time.

The most promising patterned PDLC films were produced by depositing BL006 into a 70 μm-thick film of NOA65 held at 65°C. Additionally, using these conditions, the samples did not appear to be overly sensitive to the UV-delay. However, reliably forming PDLC regions using this method proved to be difficult given the number of variables and physical processes occurring simultaneously.

By depositing the PDLC formulation directly via inkjet printing, the successful formation of localised PDLC regions was demonstrated. Method 2 proved a reliable, replicable and simple way to produced patterned PDLC films. The formulation of E7 and NOA65 in a ratio of 40:60%wt formed a sufficiently homogeneous mixture that could be directly deposited using inkjet printing using a tailored bipolar actuation waveform and a printhead 60°C. There was no need to heat the substrate and samples could be left for several hours or longer after droplet deposition with no detrimental effect to the PDLC morphology after photopolymerisation.

The PDLC regions are highly localised and confined to the area of droplet deposition. Multiple droplets can be subsequently deposited to create larger PDLC regions which scatter more effectively. Additionally, droplets can be deposited adjacent to one another such that they coalesce, forming filled-in patterns and lines. The PDLCs are fully encapsulated after photopolymerisation. Although the surface is not flat at this stage, a top substrate and/or thin-film of an optically matched polymer can be used to homogeneous the film surface. In this study, this is achieved by fastening a top glass substrate via a subsequent process. However, it is feasible for the prepolymer to be deposited using IJP synchronous to the deposition of the PDLC formulation using multiple printheads.

The PDLC films show good light scattering properties, with clear, dark regimes where LC domains are present. In the passive state, they have an optical transmission of 60% ($\lambda = 632.9$ nm) which is suitable for smart-window and light-valve applications. The PDLC regions show good optical switching with an optical transmission of 95% in the voltage-on state ($\lambda = 632.9$ nm) and switching times and voltages equivocal to PDLC films deposited using other techniques.

The method of directly printing the LC/prepolymer formulation has proved to be a viable and effective means of fabricating PDLC films that is to-date, unreported in the literature. The technique offers an alternative method of producing PDLC films that leverages the advantages of inkjet printing, such as low-material wastage, scalable, large-area, non-contact and fast. In addition, it is a simple low-temperature, two-step, process to produce high-resolution patterned single-layer PDLC films. Single-layer films consisting of different LC formulations and dopants, such as dyes or surfactants, can be fabricated in a single process using a printing system comprising of multiple printheads. The work presented in this chapter has resulted in a patent and a publication that is currently in preparation. A possible promising application of this technology is the printing of large-area smart window films which could display aesthetic designs or logos.

Chapter 8

Conclusions and Future Work

This thesis has examined the role of inkjet printing in the fabrication of liquid crystalline-based thin-film optical elements. In order to thoroughly carry out this study, a bespoke printing rig was developed capable of depositing a range of different functional materials. A detailed examination of the inkjet printing of a nematic LC demonstrated how the printing conditions can be tailored to reliably deposit precise volumes of the fluid, despite its high viscosity and anisotropic properties. The effect of different substrates on printed LC droplets was studied, revealing valuable information regarding substrate selection. It was shown how the mechanisms of droplet impact and spreading can be leveraged to produce passive radially aligned droplet given certain substrate conditions. A study on the inkjet printing of nematic LC lenses was carried out showing inkjet printing a viable method of producing variable focus microlenses. Finally, two novel methods of produced inkjet printed PDLC films were investigated, resulting in the fabrication of a switchable, patterned PDLC film. The following sections draws the main conclusions and future directions of the work presented.

8.1 Inkjet Printing System

Without a robust and customisable printing system, none of studies presented could have been undertaken. Many of components forming the printer were either hobbyist, machined, laser-cut, or themselves printed using a 3D printer. A key takeaway from the design and build process was showing how it is possible to create effective, low-cost systems that can empower researchers. This is particularly pertinent to the printing of functional materials, which often have very

specific printing requirements and/or could damage equipment. The knowledge that equipment could be easily modified, fixed or replaced was a great benefit and allowed a more creative and explorative investigation of different materials and applications. In fact, it is for these reasons that the printing system will still be heavily used in the future, despite the recent purchase of an £70,000 commercial printing rig. Proof-of-concept, prototyping an exploration experimentation will be carried out on the custom-made system, before using the larger system once teething problems have been resolved.

The system was developed incrementally over time and as needs arose. As a result, there are certain aspects that could certainly do with improvement. Central to this is the minimum step resolution of 25 μm, coupled with the lack of designated motion control. In other words, missed steps was a problem. Although never designed to be a highly precise automated stage, improvements could be made by using encoded stepper motors with integrated motion controllers. This allows for monitoring and correction of missed steps and automatic acceleration and deceleration at higher speeds. In addition, a refactoring of the LabVIEW code in a language such as Python would be an advisable step to take. This would allow the program to leverage the huge number of high-quality libraries and API's available.

8.2 Inkjet Printing of Nematic Liquid Crystals

Generating droplets of a fluid was always the first hurdle to overcome in the printing of functional fluids. This is often overlooked in literature, or insufficient detail has been given to assessing whether replicable droplet generation has been achieved. An understanding of the physical processes underlying droplet actuation in a piezoelectric printhead is massively valuable when using functional and viscous fluids. Conducting the inkjet printing study of E7 highlighted the importance of the acoustic pressure wave and how it can be optimised to produce droplets even for highly viscous inks.

Carrying out a preliminary dimensionless analysis prior to printing, allows

one to predetermine the prohibiting factors likely to be encountered. When depositing viscous inks, the printing temperature is often the most convenient means to increase printability, and is particularly important for LCs due to their anisotropic nature. As described in §4.6.4, carrying out the case study of E7 (and many hours printing other fluids...), an intimate knowledge of the interplay between different different printing conditions and the fluid properties emerges. By observing the fluid jet produced at the nozzle whilst varying certain parameters, near-optimum printing conditions can be quickly determined. The conclusions drawn in this chapter laid the foundation to reliable droplet generation throughout the thesis and facilitated the inkjet printing of LC/prepolymer formulations previously unreported in the literature. Further work in this area may involve a compiling the results gathered in this chapter into a complete journal article the examines the use of LC inks in IJP.

8.3 The Role of Different Substrates on Printed Liquid Crystal Droplets

After droplet generation, the next process to be considered is the interaction with the substrate. Upon impact, LC droplets form the shape of a spherical cap, despite elastic deformation of the LC director. Uniquely to LC, not only must the wetting of the droplet be investigated, but also the alignment of the director in the bulk. Various models of the LC director were produced to predict the LC director configuration in different droplet configurations and show that radially aligned droplets can spontaneously form if the LC director is able to freely rotate in-plane at the substrate surface.

The quality of several different printing substrates was assessed by measuring the distribution of wetted droplet diameters. This revealed the excellent performance of the polymer coating which was then used in subsequent work on producing printed LC microlenses. An interesting method was developed for forming radially aligned droplets on untreated polymer substrates which exploits the impact and wetting processes inherent to inkjet printing. This method was

further investigated by assessing the effect of printing in high-humidity environments and pre-wetting the polymer substrates. A potential application of the radially aligned droplet is the formation of printed cholesteric reflectors, the preliminary study of which is outlined in Appendix §A.2.

The interesting phenomena of anisotropic wetting on certain planar-aligned substrates was observed. The fact that anisotropic wetting was not observed for an isotropic fluid (water) indicates that this is due to the alignment of the LC director at the substrate and merits further investigation. A more thorough investigation of different substrates with different surface energies and pre-tilt angles could lead to a better understanding of phenomena. In addition, the effect of the curved LC/air interface on the LC director could be investigated by depositing a LC material that aligns parallel to the air interface (such as S1461 Propyl 2-Cyanophenyl-Propyl cyclohexyl-Benzoate).

8.4 Inkjet Printing of Liquid Crystal Microlenses

The excellent droplet profile and uniform homeotropic alignment observed in Chapter 5 was exploited in the formation of drop-on-demand inkjet printed nematic LC microlenses. Already established in the manufacturing of fixed-focal length microlenses, inkjet printing is yet to be applied in the fabrication of variable focussing microlenses. It was demonstrated how a homeotropic aligned nematic droplet acts as plano-convex lens with inherent polarisation independent focussing properties for incident light that is normal to the substrate. Bespoke array of lenses can be efficiently produced and the diameter of lenses can be varied by depositing multiple droplets onto the same location. The thermal tuning of the lenses was demonstrated.

The chapter goes on to present important work on the formation of fully encapsulated lenses via the inkjet printing of a LC/prepolymer formulation. Printing conditions were found to deposit this formulation without the need to excessively heat the printhead. The UV-intensity and curing temperature was varied to find the optimum conditions to produce nano-sized LC domains. The cured

droplets showed no indication of the scattering of visible light and appeared birefringent under polarised optical microscopy.

The ability to deposit such formulations and form non-scattering PDLC droplets shows great promise in the fabrication of inkjet printed, electrically tunable, fast switching microlenses that have the potential to be deposited on curved and flexible substrates. Future work includes analysing the microstructure of PDLC droplets using AFM and electron microscopy techniques. The main goal is to demonstrate the variable focusing properties of the lenses and is described in further detail in Appendix §A.3.

8.5 Inkjet Printed Patterned Polymer-Dispersed Liquid Crystals

Inkjet printing is a popular tool in the fabrication of both small and large-area thin-films. However, uniquely to inkjet printing, the thin-films produced can vary in material composition. This chapter presents two novel methods of producing an inkjet printed patterned PDLC film. The objectives of the study was to demonstrate that highly localised regions of light-scattering, encapsulated PDLC regions can be formed in a single-layer film via inkjet printing.

The first method considers the inkjet printing of a LC droplet into a prepolymer film. In order to form PDLC regions, consideration of drop impact, spreading and dissolution processes must be considered. Observations of surface wave formation and excessive diffusion on the LC into the prepolymer were made and parameters identified to mitigate these effects. Certain critical temperature and concentration regimes were identified that partially meet the objectives of the study. Despite the difficulties in producing films using this method, a patterned PDLC film showing partial switching was demonstrated. However, the films produced in this manner possessed poor electro-optical properties and the results were difficult to replicate.

Building on the knowledge that LC/prepolymer mixtures can be deposited using inkjet printing, the second method explores the direct inkjet printing of

the PDLC formulation. This method proved a far more effective, robust and efficient way of forming inkjet printed PDLC films. After depositing the formulation, the substrates can be processed at low temperatures and left for long periods of time before curing, with no detrimental effect on the final optical properties. The curing conditions required to form effective light scattering PDLC regions were determined and the switching of the films demonstrated. The chapter concludes with an opto-electrical characterisation of a printed PDLC array.

Feature sizes in the region of 100-200 μm were demonstrated in this study. However, feature sizes as small as 50 μm, or less, should be achievable by using smaller nozzle diameters and a more hydrophobic printing substrate. Rather than attaching a glass substrate as a separate process, a fully printed PDLC film could be fabricated by inkjet printing an optically matched polymer in the same step as depositing the PDLC formulation. It would be interesting to further characterise the film produced. For example, the curved shape of the PDLC regions formed could potentially have an effect on the off-angle haze which is inherent to PDLC films.

Despite the rise of electrochromic smart windows, PDLC-based technologies still account for 15% of the market share. Given the suitability of inkjet printing to the manufacturing of large-area thin films, future work in this area should be focussed on showcasing the unique benefits of inkjet printing. For example, by using three different PLDC formulations, each doped with RGB azo-dichroic dyes, a large area patterned-PDLC film could be printed for aesthetic or advertisement purposes, which can switch to a transparent state upon application of an electric field.

Appendix A

Appendix

A.1 Drop-on-Drop Alignment Method

One of the main advantages of inkjet printing is its versatility, particularly the possibility to deposit LC arrays onto substrates which are arbitrary in shape, curved or flexible. However, this still requires the substrate to be treated to appropriately align the LC. This section introduces a novel technique that exploits the capability to deposit multiple fluids via multiple printheads. An illustration of the concept is shown in Figure A.1.

A droplet of PVA is initially deposited, on top of which, the LC drop is deposited. The LC droplet will interact only with the sessile PVA drop which, if much larger than the LC drop, is comparable to the interaction observed between a LC and PVA film discussed in §5.5. The objectives of the study is to demonstrate the drop-on-drop technique to produce radially-aligned nematic LC droplets that can be deposited onto a range of substrates and which do not require specific LC alignment treatments. The future aim is to use the findings from this study to develop printed chiral nematic LC reflectors introduced in Section A.2.

A.1.1 Custom-made Acrylic Printhead

The drop-on-drop method requires the non-trivial printing of a PVA solution. Due to the high viscosity of the PVA solution and the potential for it to dry, clog and damage the printhead, the commercial microfab nozzles could not be used. The custom-made acrylic printhead referenced in §3.1.1, was used to deposit the PVA. The printhead was designed and tested over several iterations.

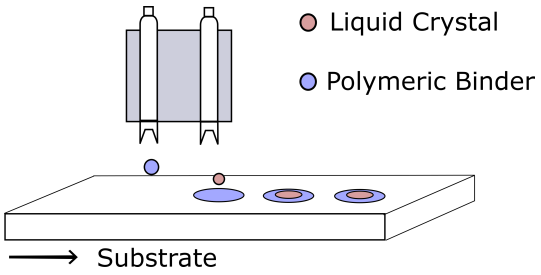

FIGURE A.1: Illustration of the drop-on-drop method showing two printheads depositing a LC droplet on top of a polymer droplet - in this case a solution of PVA.

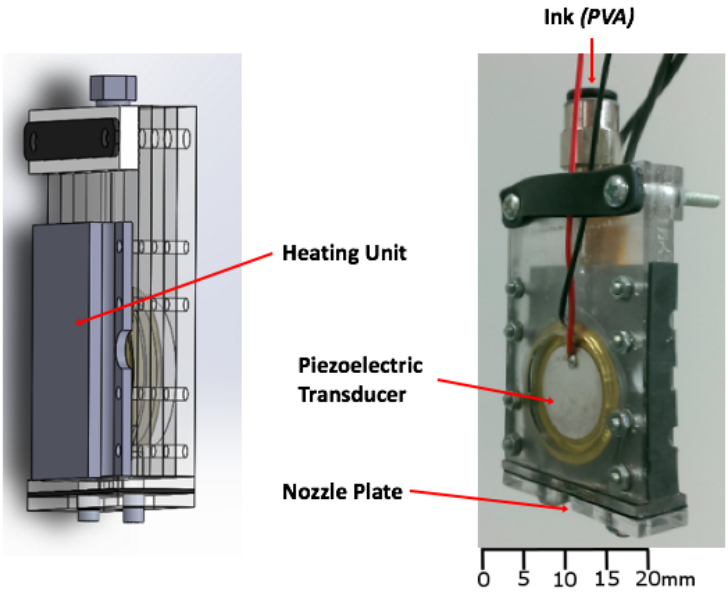

FIGURE A.2: A CAD model and actual image of the acrylic printhead used for jetting high-viscosity PVA solutions.

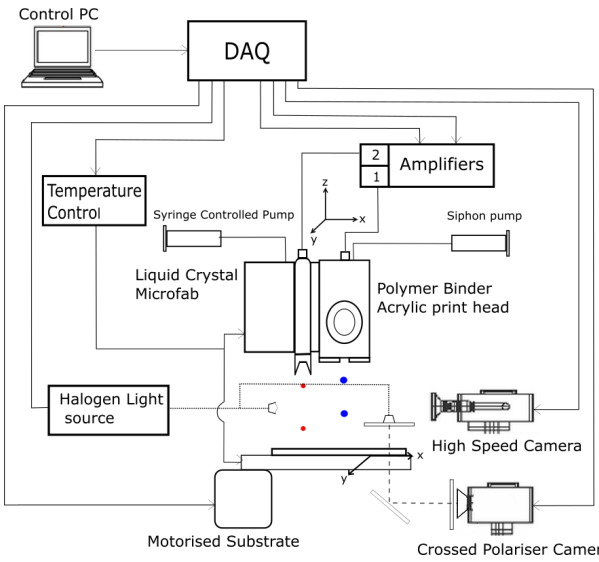

FIGURE A.3: Experimental schematic showing the set-up used for drop-on-drop printing.

A temperature controlled Microfab printhead can cost in the region of £4000 and, although offering superior printing performance, they are fragile and clog easily. The acrylic printheads cost less than £10 to manufacture. Figure A.2a shows a schematic of the acrylic printhead used in the drop-on-drop study. The printhead body consists of 2mm-thick acrylic sheets, that were laser cut and bonded together. A heating element (DBK HPOS-1/04/-24-20W) was fastened to one side of the printhead such that it it is in direct contact with the printhead chamber. Drop generation is achieved via a volume change of the printhead chamber due to deformation of the piezoelectric transducer (27mm diaphragm external piezo buzzer, RS). A 150μm-thick stainless steel sheet was laser etched to produce nozzles 220 and 300μm in diameter. Individual components, such as the nozzle plates can easily be interchanged if clogged or damaged, making the printheads suitable for use with with polymer solutions.

A.1.2 Experimental

The nematic LC E7 (Merck) was deposited using the 80μm microfab printhead. A solution of 10wt% PVA (80% hydrolysed, $9,000 - 10,000$MW, Sigma Aldrich) in deionised water was used as the PVA ink. The PVA ink was found to dry quickly and clog the nozzle orifice, making the solution very difficult to print.

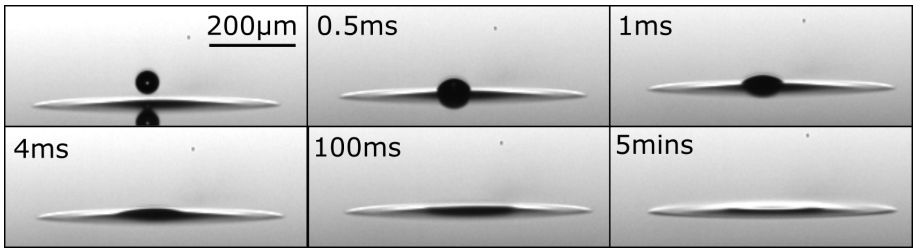

FIGURE A.4: a) High-speed images of a 80 μm droplet of E7 being printed on top of a droplet of PVA that deposited 3s earlier. b) Polarised microscopy image of the resulting droplet.

Dimethyl sulfoxide (DMSO) was added to the PVA formulation in a ration of 10%wt. DMSO is a solvent which gelates the PVA mixture and increases the drying time. With the addition of DMSO, the PVA solution could be effectively deposited using the acrylic nozzle. The drop-on-drop experimental set-up is shown in Figure A.3. In addition to the printing of a high-concentration PVA solution, the LC droplet must be positioned on top of the PVA droplet, requiring timing and positioning synchronisation (see §3.1).

Figure A.4 shows high-speed images of impact between a LC droplet and sessile droplet of PVA that was previously deposited onto a clean untreated glass substrate. There was ≈3s delay between the deposition of the PVA droplet and the sequences of images shown in the Figure, as the substrate needed to be moved to the required position to image with the high-speed camera. The time in the top right of each image is the from the point of impact between the two droplets. The diameter of the PVA droplet is approximately 400μm. Assuming a spherical cap, conservation of volume would suggest the contact angle should be around 25 °. However, the droplet appears to be flattened which is due to the volume shrinkage (1/3) of the droplet as it dries.

Figure A.5a shows various LC/PVA droplets that have been produced using the drop-on-drop method. The PVA droplet was printed onto an untreated glass substrate with ≈200ms delay before the LC droplet was deposited. The POM images show radial and twisted radial LC director configurations similar to droplets deposited onto a partially dry PVA substrate discussed in §5.5.4. Figure A.5 b and c are POM images where 5 drops of LC has been successively deposited onto the PVA drop.

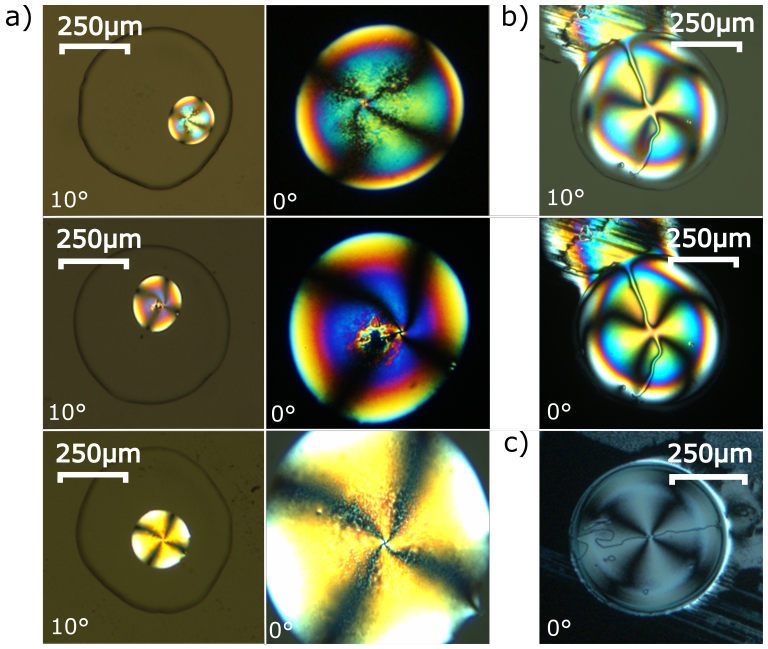

FIGURE A.5: a) Polarised microscopy images showing various nematic LC droplet configurations produced using the drop-on-drop method. b) Polarised microscopy images of the resulting configuration after successively depositing 10 LC drops on top of the PVA droplet.

Despite the addition of DMSO, the drying time of the PVA droplets were very fast due their small volume (≈3s), giving a narrow window of opportunity for passive radial alignment to occur. However, the method proved a viable method of radially aligning a LC droplet by pre-printing a droplet of polymer.

A.2 Printed Chiral Nematic Liquid Crystal Reflectors

A chiral nematic LC is formed of ordered quasi-nematic layers where the LC director $\hat{\boldsymbol{n}}$ rotates from one layer to the next. The helical axis is defined as the axis about which this rotation occurs. The pitch length P_o is defined as the distance over which the LC molecules undergo a full 2π rotation, though it is noted that the chiral nematic phase repeats itself every $P_o/2$ as $\hat{\boldsymbol{n}} \equiv -\hat{\boldsymbol{n}}$.

For light with a wavelength of the same order as the chiral pitch (P_o) and propagating in the direction of the the helical axis, the periodic change in refractive index between quasi-nematic layers induces selective Bragg reflection that is dependent on the chiral pitch and the angle of the incident light. In this case

the chiral nematic LC possesses a distinct pitch-dependent colour. Selective reflection results in a 1-D photonic band gap (PBG) for circularly polarised light of the same handedness as the helix, where the suppression (or reflection) band lies between $n_o P_o$ and $n_e P_o$. The central reflection wavelength (λ_c) is dependent on the average refractive index: $\lambda_c = P_o n_{avg} cos\theta$. Where θ is the off-axis viewing angle from the direction of the helical axis, and is responsible for the observed shift of the reflected light to shorter wavelengths as the off-axis viewing angle is increased. Chiral nematic LCs thus have the unique property of reflecting 50% of the incident non-polarised light of the same handedness as the helix, whilst the other 50% is transmitted through the sample.

The refractive indices are temperature dependent and thus the band edges and reflected colour will depend on the temperature. In addition, the helical pitch of a chiral nematic LC is also dependant on temperature, based on a theory describing thermodynamic vibration near a chiral nematic-smectic A* phase transition [209]. The result is a blue-shift in the PBG and reflected colour as the temperature is increased.

A.2.1 Experimental

The nematic mesogen BL006 was chosen as the LC ink as it has a higher clearing temperature than E7 ($T_c = 120$°c), giving it a larger operating temperature range. The chiral dopant R811 was added to BL006 in a ratio of 30:70%wt. This concentration of chiral dopant was selected to give a central reflection wavelength (λ_c) of 620nm. This wavelength gives the most optical sensitivity (to the human eye) to temperature as the reflected colour transitions from red to blue.

The temperature dependency of the reflected colour of the mixture was first tested by filling a 20μm thick planar cell. The transmission of the cell was analysed using a UV-vis spectrometer (Cary 8455 UV-Vis, Aligent Technologies) as the temperature was increased in 5°C intervals. The resulting spectra is shown in Figure A.6a. The the photonic band-gap (PBG) is seen to shift from 620 to 440nm over a temperature range 40°C. As shown in Figure A.6b, this gives a clear transition in reflected color from red to blue. At temperatures above 65°C, there was

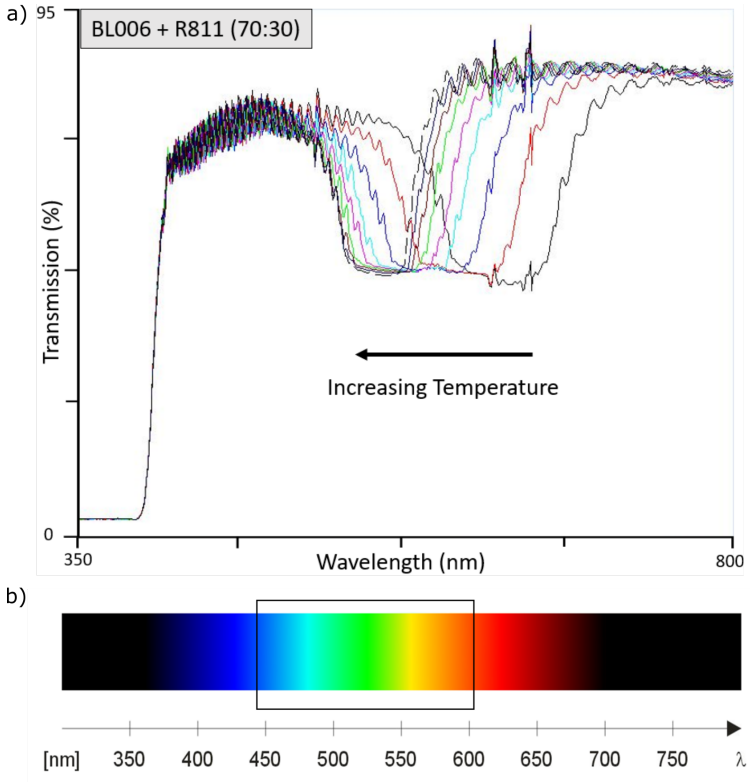

FIGURE A.6: a) UV-visible transmission spectra of a 20μm-thick cell filled with a mixture of BL006 and R811 (70:30%wt). The different curves show the transmission as the temperature is increased from 25°C (black line) to 65°C (dotted black line) in 5°C intervals. b) The visible reflected colour range of the chiral nematic mixture over a 20-65°C temperature range.

a significant narrowing and distortion of the PBG, effectively limiting the maximum temperature range to 60-70 °C.

In conventional LC cells, the formation of a chiral nematic LC with the helical axis oriented normal to the substrates is achieved using a planar aligned cell. However, the chiral reflectors produced in this study were produced by inkjet printing the LC formulation on to a partially dry PVA substrate, shown schematically in Figure A.7a (this method is described in detail in §5.5.4 and §5.5.5). Such an alignment surface should allow formation of a chiral LC droplet with the helical axis oriented normal the substrate, as illustrated by Figure A.7b. Depending on the chiral pitch, this would result in a droplet with a rotationally independent reflected colour. Further, the reflected color of the chiral nematic droplet will be temperature dependent allowing them to be used as printable optical temperature sensors.

The 120μm (MJ-ABP-01-120, Microfab) nozzle was used to deposit the chiral nematic mixture. This nozzle was selected to produce large sessile droplets that could be seen by the naked eye. The mixture was deposited using the waveform W5 given in Table A.1 and a printhead temperature of 64°C. A 70mum-thick PVA substrate was prepared as described in §5.5.4. The substrate was left for 50 minutes before depositing the chiral nematic mixture.

After printing, the sample was left for an additional hour to ensure the substrate had fully dried. Figure A.7c shows microscopy images, taken in reflection mode, of the deposited droplets at different substrate temperatures. As seen in the microscope images, the droplets show a strong observable color shift temperature dependent reflected colour. The printed chiral reflectors presented show promise as optical temperature sensors. If combined with the drop-on-drop method (§A.1), the sensors could be printed onto a wide-range of substrates that do not require specialist surface treatments.

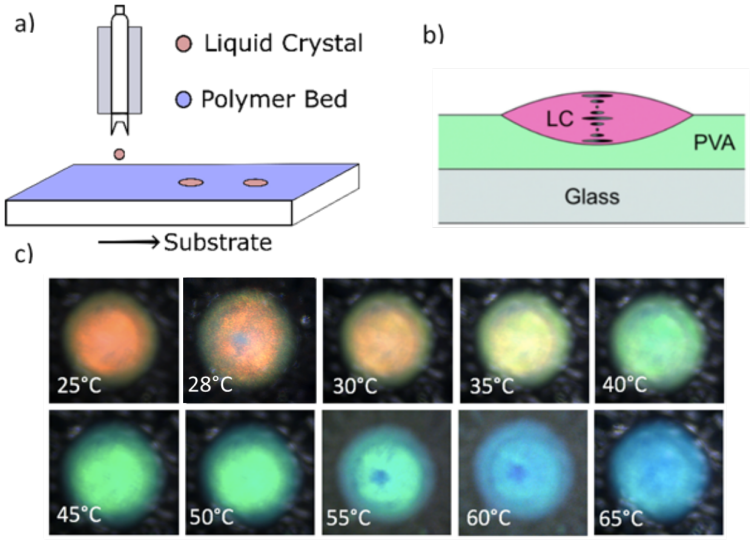

FIGURE A.7: a) Schematic illustration of the inkjet printing of chiral nematic reflectors. b) Illustration of the LC director configuration in a single droplet. c) Microscope images taken in reflection mode of droplets of chiral nematic LCs printed onto a partially dry PVA substrate over a temperature range.

A.3 Electronically tunable Nano-PDLC Microlenses

Optical Properties

The PDLC lenses presented in §6.4.4 show promise as encapsulated and fast switching variable-focus microlenses. In the body of the thesis, only the printing and photopolymerisation of the microlenses was considered. Unfortunately, the optical characterisation and electrical switching could not be carried and is a topic of future work being currently being undertaken. This section describes further work carried out on the nano-PDLC microlenses.

The focal length of the lenses after photo-polymerisation was approximated by measuring the distance of object/image formation using a microscope, as shown in Figure A.8a. The microlens substrate (750μm-thick) was placed on top of a 25μm grid etched into a microscope slide at a depth of ≈400μm. The microscope images in Figure A.8b and d, indicate a magnification of $M = -\frac{d_i}{n_2 d_o} \approx 0.18$. Using this equation, this gives an expected image distance of 1111μm, close to the value measured from the in-focus image (1150μm). Using the lens equation:

$$\frac{1}{f} = \frac{n_2}{d_o} + \frac{1}{d_i}, \tag{A.1}$$

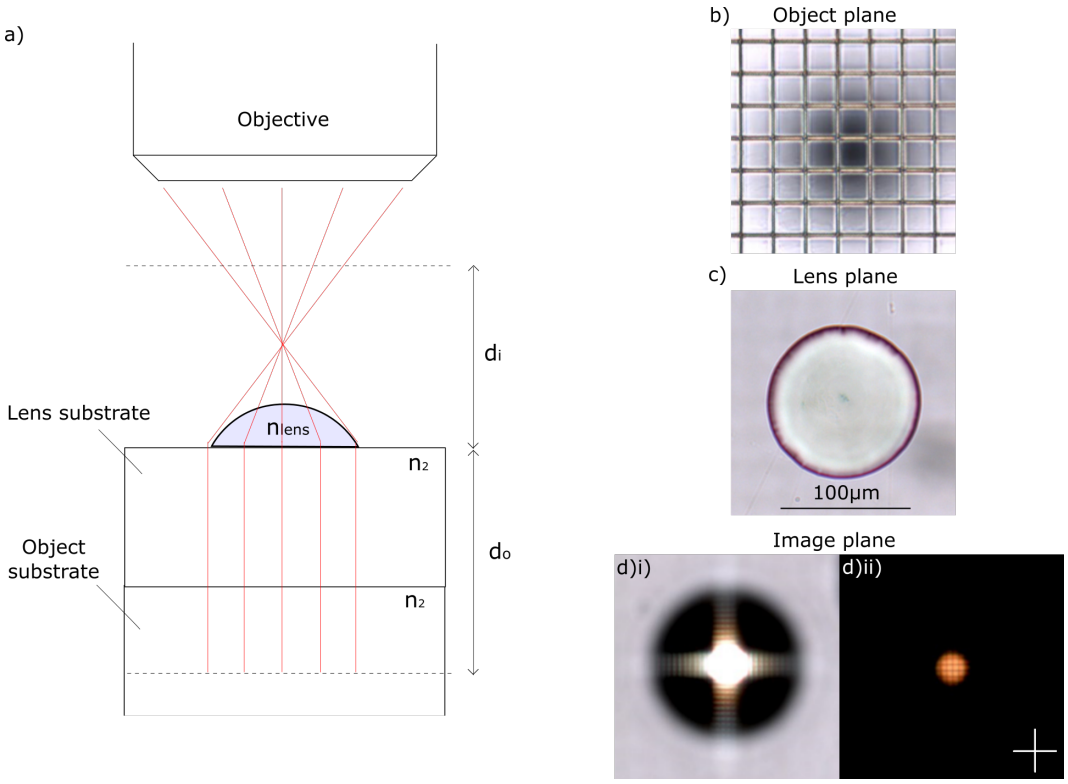

FIGURE A.8: a) Schematic illustration showing object and image formation using a microscope. b) A 25μm grid etched into a glass microscope slide used as the focussing object for the nano-PDLC microlenses. c) Microscopy image focussed at the lens plane ($\approx$1150μm from object plane). d)i) Microscopy image focussed at the image plane at a distance $\approx$300μm from the lens plane. d)ii) Polarised microscopy image with crossed polarisers focussed at the image plane.

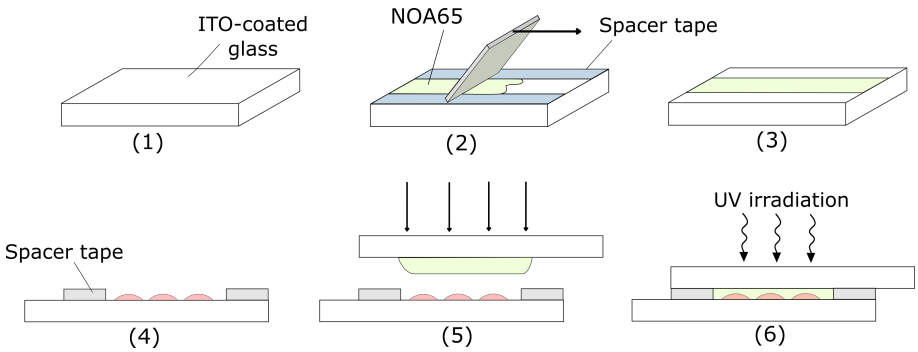

FIGURE A.9: Illustration showing the procedure followed for fastening a top substrate for electrical switching of the nano-PDLC lenses. (1) ITO-coated glass top substrate. (2) Spacer tape is applied to the top substrate and NOA65 is spread to create a thin-film. (3) The spacer tape is removed from the top substrate. (4) Spacer tape is applied to the either side of the microlens substrate. (5) The top substrate is fastened to the bottom substrate. (6) The cell is irradiated with UV-light.

gives a focal length of 215μm. This is close to the estimated focal length of 215μm, calculated using the equation for a thin spherical plano-convex lens and using $n_{lens} = 1.54$:

$$f = \frac{R}{n_{lens} - 1}\,. \tag{A.2}$$

A.3.1 Switching

In order to test the electrical switching, a top substrate must be fastened. This was achieved using the procedure illustrated in Figure A.9. The spacer tape for the top substrate and bottom substrate was approx 40μm. The resulting cell was 60μm, indicating the cell had not been fully compressed before photopolymeriasation. Figure A.10 shows microscopy images of the lenses after the top substrate had been applied.

A.4 Printing Waveforms

A.4.1 Refractive Indices

A.4.2 Optical Adhesive Transmission Spectra

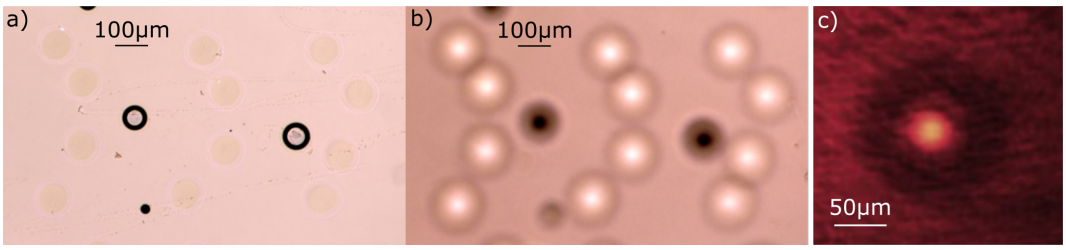

FIGURE A.10: a) Microscopy image of the same nano-PDLC array shown in Figure 6.19a but after a top substrate has been fastened. b) Microscopy image of (a) but with the microscope focussed at the focal plane of the lenses. c) CCD image taken at the focal plane using the set-up described in §6.3.1 on page 6.7.

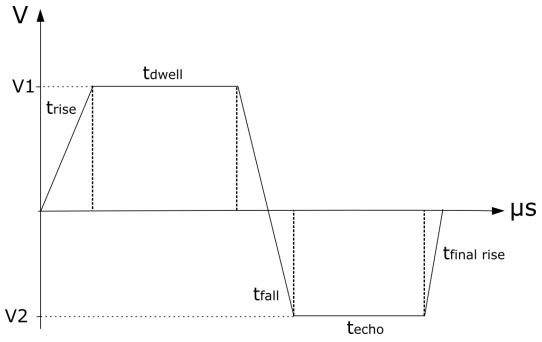

FIGURE A.11: Arbitrary actuation waveform showing the parameters listed in table A.1.

	λ (nm)											
T	450		486		546		589		633		656	
(°C)	n_e	n_o	n_e	n_o	n_e	n_o	n_e	n_o	n_e	n_o	n_e	n_o
15	1.817	1.5435	1.7921	1.536	1.7664	1.5273	1.7542	1.523	1.7446	1.5197	1.7407	1.5179
20	1.8084	1.5431	1.7847	1.5357	1.7589	1.5269	1.7466	1.5227	1.7378	1.5188	1.7338	1.5177
25	1.8005	1.5424	1.7763	1.5353	1.7512	1.5268	1.7394	1.5225	1.7305	1.5189	1.7263	1.5176
30	1.7909	1.543	1.7679	1.5357	1.7433	1.5271	1.7317	1.5226	1.7229	1.5189	1.719	1.5177
35	1.7811	1.5448	1.7581	1.5369	1.7344	1.5277	1.7231	1.5231	1.7142	1.5191	1.7102	1.5179
40	1.7695	1.547	1.7472	1.5383	1.7237	1.5287	1.7124	1.5239	1.7037	1.5205	1.7001	1.5189
45	1.7549	1.5491	1.7333	1.5406	1.7109	1.5308	1.7001	1.5261	1.6919	1.5221	1.6882	1.5206
50	1.7355	1.5538	1.7154	1.5449	1.6941	1.535	1.6837	1.5299	1.6761	1.526	1.6721	1.5246
55	1.6936	1.569	1.6779	1.5588	1.6601	1.5479	1.6511	1.5428	1.644	1.5377	1.6405	1.5353

FIGURE A.12: Refractive indices for the nematic LC E7 at different temperatures and wavelengths [210].

T	λ (nm)											
	450		486		546		589		633		656	
(°C)	n_e	n_o	n_e	n_o	n_e	n_o	n_e	n_o	n_e	n_o	n_e	n_o
15	1.8988	1.5478	1.8672	1.5438	1.8349	1.5348	1.8194	1.5304	1.8083	1.5266	1.8033	1.5257
20	1.8913	1.5516	1.8620	1.5434	1.8299	1.5339	1.8148	1.5296	1.8036	1.5259	1.7986	1.5244
25	1.8869	1.5505	1.8563	1.5421	1.8248	1.5331	1.8097	1.5285	1.7988	1.5249	1.7937	1.5236
30	1.8811	1.5479	1.8508	1.5414	1.8194	1.5323	1.8046	1.5275	1.7937	1.5239	1.7884	1.5224
35	1.8760	1.5482	1.8449	1.5405	1.8140	1.5312	1.7994	1.5266	1.7885	1.5229	1.7835	1.5215
40	1.8702	1.5472	1.8391	1.5399	1.8084	1.5306	1.7938	1.5257	1.7830	1.5221	1.7784	1.5206
45	1.8630	1.5454	1.8328	1.5387	1.8024	1.5294	1.7880	1.5249	1.7774	1.5211	1.7726	1.5200
50	1.8566	1.5447	1.8265	1.5382	1.7964	1.5292	1.7822	1.5245	1.7721	1.5204	1.7672	1.5192
55	1.8486	1.5441	1.8200	1.5377	1.7905	1.5286	1.7764	1.5238	1.7659	1.5199	1.7613	1.5181

FIGURE A.13: Refractive indices for the nematic LC BL006 at different temperatures and wavelengths[210].

n / λ (nm)						
T (°C)	450	486	546	589	633	656
20	1.5396	1.5352	1.5301	1.5275	1.5255	1.5243
25	1.5391	1.5347	1.5296	1.5270	1.5250	1.5239
30	1.5386	1.5343	1.5292	1.5266	1.5246	1.5235
35	1.5377	1.5335	1.5282	1.5254	1.5233	1.5225
40	1.5363	1.5324	1.5272	1.5245	1.5222	1.5214
45	1.5352	1.5311	1.5261	1.5235	1.5211	1.5204
50	1.5340	1.5305	1.5248	1.5223	1.5202	1.5192
55	1.5330	1.5298	1.5243	1.5217	1.5194	1.5187

FIGURE A.14: Refractive indices for the optical adhesive NOA65 at different temperatures and wavelengths[210].

TABLE A.1: Actuation waveforms for the different nozzles and inks used in this thesis, the times are in μs.

	Nozzle	**Ink**	t_{rise}	t_{dwell}	t_{fall}	t_{echo}	$t_{final\,rise}$	V_1	V_2
W1	80μm	E7/BL006	3	15	3	N/A	N/A	53V	0
W2	50μm	E7:NOA65	3	12	4	9	3	60V	-40V
W3	120μm	BL006	3	32	4	N/A	N/A	55V	0
W4	80μm	E7:NOA65	3	12	5	9	3	60V	-55V
W5	120μm	BL006:R811	3	32	4	N/A	N/A	60V	0

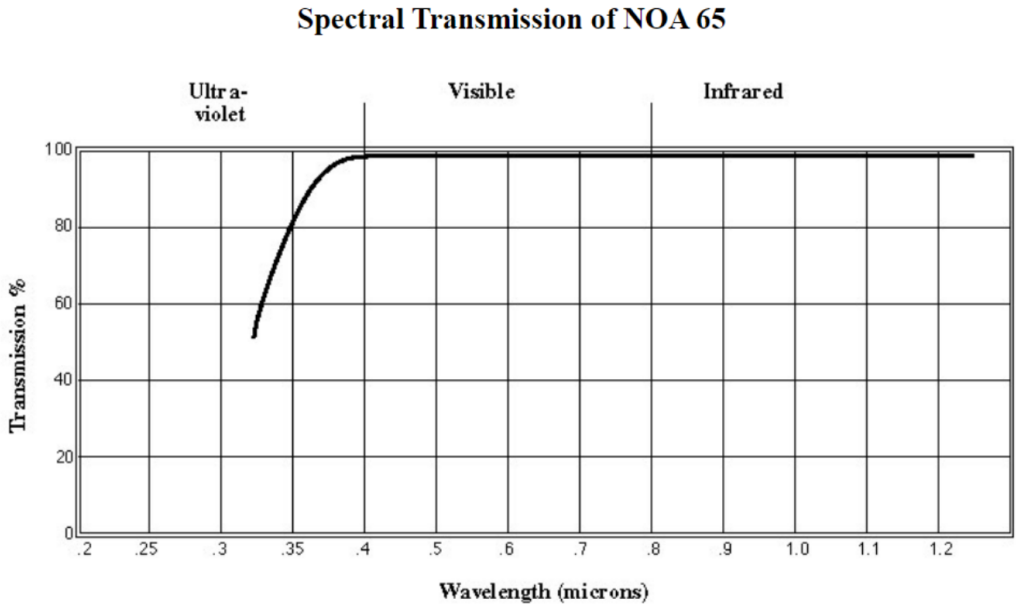

FIGURE A.15: Transmission spectra for NOA65 optical adhesive.

Bibliography

[1] E. Parry et al. “Drop-on-Demand Inkjet Printing of Thermally Tunable Liquid Crystal Microlenses”. In: *Advanced Engineering Materials* 20.3 (2018). ISSN: 14381656. DOI: 10.1002/adem.201700774.

[2] E. Parry et al. “Formation of Radial Aligned and Uniform Nematic Liquid Crystal Droplets via Drop-on-Demand Inkjet Printing into a Partially-Wet Polymer Layer”. In: *Optical Materials* 80 (2018), pp. 71–76. ISSN: 09253467. DOI: 10.1016/j.optmat.2018.04.038.

[3] M. Trainer. “The Patents of William Thomson (Lord Kelvin)”. In: *World Patent Information* 26.4 (2004), pp. 311–317. ISSN: 0172-2190. DOI: 10.1016/j.wpi.2004.05.003.

[4] L. Rayleigh. “On the Instability of Jets”. In: *Proceedings of the London Mathematical Society* s1-10.1 (1878), pp. 4–13. ISSN: 00246115. DOI: 10.1112/plms/s1-10.1.4.

[5] R. G. Sweet. “High Frequency Recording with Electrostatically Deflected Ink Jets”. In: *Review of Scientific Instruments* 36.2 (1965), pp. 131–136. ISSN: 00346748. DOI: 10.1063/1.1719502.

[6] S .N. Jayasinghe et al. “Electrohydrodynamic Jet Processing: An Advanced Electric-Field-Driven Jetting Phenomenon for Processing Living Cells”. In: *Small* 2.2 (2006), pp. 216–219. ISSN: 16136810. DOI: 10.1002/smll.200500291.

[7] J. R. Castrejón-Pita et al. “Future, Opportunities and Challenges of Inkjet Technologies”. In: *Atomization and Sprays* 23.6 (2013), pp. 571–595. ISSN: 10445110. DOI: 10.1615/AtomizSpr.2013007653.

[8] Q. Zheng et al. "Application of Inkjet Printing Technique for Biological Material Delivery and Antimicrobial Assays". In: *Analytical Biochemistry* 410.2 (2011), pp. 171–176. ISSN: 00032697. DOI: 10.1016/j.ab.2010.10.024.

[9] N. Scoutaris et al. "Inkjet Printing as a Novel Medicine Formulation Technique". In: *Journal of Controlled Release* 156.2 (2011), pp. 179–185. ISSN: 01683659. DOI: 10.1016/j.jconrel.2011.07.033.

[10] C. López-Iglesias et al. "From the Printer to the Lungs: Inkjet-Printed Aerogel Particles for Pulmonary Delivery". In: *Chemical Engineering Journal* 357 (2019), pp. 559–566. ISSN: 13858947. DOI: 10.1016/j.cej.2018.09.159.

[11] H. S. Kim et al. "Inkjet Printed Electronics for Multifunctional Composite Structure". In: *Composites Science and Technology* 69.7-8 (2009), pp. 1256–1264. DOI: 10.1016/j.compscitech.2009.02.034.

[12] X. Wang et al. "3D Printing of Polymer Matrix Composites: A Review and Prospective". In: *Composites Part B: Engineering* 110 (2017), pp. 442–458. ISSN: 13598368. DOI: 10.1016/j.compositesb.2016.11.034.

[13] J. Alamán et al. "Inkjet Printing of Functional Materials for Optical and Photonic Applications". In: *Materials* 9.11 (2016). ISSN: 19961944. DOI: 10.3390/ma9110910.

[14] Z. Zhan et al. "Inkjet-Printed Optoelectronics". In: *Nanoscale* 9.3 (2017), pp. 965–993. ISSN: 20403364. DOI: 10.1039/c6nr08220c.

[15] H.-S. Koo et al. "LCD-Based Color Filter Films Fabricated by a Pigment-Based Colorant Photo Resist Inks and Printing Technology". In: *Thin Solid Films* 515.3 (2006), pp. 896–901. ISSN: 00406090. DOI: 10.1016/j.tsf.2006.07.159.

[16] K. Abe et al. "Inkjet-Printed Microfluidic Multianalyte Chemical Sensing Paper". In: *Analytical Chemistry* 80.18 (2008), pp. 6928–6934. ISSN: 00032700. DOI: 10.1021/ac800604v.

[17] M. Singh et al. "Inkjet Printing-Process and Its Applications". In: *Advanced Materials* 22.6 (2010), pp. 673–685. ISSN: 09359648. DOI: 10.1002/adma.200901141.

[18] J. F. Dijksman et al. "Precision Ink Jet Printing of Polymer Light Emitting Displays". In: *J. Mater. Chem.* 17.6 (2007), pp. 511–522. DOI: 10.1039/B609204G.

[19] V. Wood et al. "Inkjet-Printed Quantum Dot-Polymer Composites for Full-Color AC-Driven Displays". In: *Advanced Materials* 21.21 (2009), pp. 2151–2155. ISSN: 09359648. DOI: 10.1002/adma.200803256.

[20] J. Han et al. "Toward High-Resolution, Inkjet-Printed, Quantum Dot Light-Emitting Diodes for next-Generation Displays". In: *Journal of the Society for Information Display* 24.9 (2016), pp. 545–551. ISSN: 10710922. DOI: 10.1002/jsid.467.

[21] R. Chesterfield et al. "Solution-Coating Technology for AMOLED Displays". In: *Information Display* 27.1 (2011), pp. 24–30.

[22] T. H. J. Van Osch et al. "Inkjet Printing of Narrow Conductive Tracks on Untreated Polymeric Substrates". In: *Advanced Materials* 20.2 (2008), pp. 343–345. ISSN: 09359648. DOI: 10.1002/adma.200701876.

[23] M. Y. Teo et al. "Direct Patterning of Highly Conductive PEDOT:PSS/Ionic Liquid Hydrogel via Microreactive Inkjet Printing". In: *ACS Applied Materials and Interfaces* 11.40 (2019), pp. 37069–37076. ISSN: 19448244. DOI: 10.1021/acsami.9b12069.

[24] S. Kirchmeyer and K. Reuter. "Scientific Importance, Properties and Growing Applications of Poly(3,4-Ethylenedioxythiophene)". In: *Journal of Materials Chemistry* 15.21 (2005), pp. 2077–2088. ISSN: 09599428. DOI: 10.1039/b417803n.

[25] S. H. Eom et al. "Polymer Solar Cells Based on Inkjet-Printed PEDOT:PSS Layer". In: *Organic Electronics* 10.3 (2009), pp. 536–542. ISSN: 15661199. DOI: 10.1016/j.orgel.2009.01.015.

[26] V. J. Aliño et al. "Inkjet Printing and Release of Monodisperse Liquid Crystal Droplets from Solid Surfaces". In: *Langmuir* 28.41 (Oct. 2012), pp. 14540–14546. ISSN: 0743-7463. DOI: 10.1021/la3028463.

[27] N. Herzer et al. "Printable Optical Sensors Based on H-Bonded Supramolecular Cholesteric Liquid Crystal Networks". In: *Journal of the American Chemical Society* 134.18 (2012), pp. 7608–7611. DOI: 10.1021/ja301845n. pmid: 22519954.

[28] D. J. D. Davies et al. "A Printable Optical Time-Temperature Integrator Based on Shape Memory in a Chiral Nematic Polymer Network". In: *Advanced Functional Materials* 23.21 (2013), pp. 2723–2727. ISSN: 1616301X. DOI: 10.1002/adfm.201202774.

[29] D. J. Gardiner et al. "Printed Photonic Arrays from Self-Organized Chiral Nematic Liquid Crystals". In: *Soft Matter* 8.39 (2012), pp. 9977–9980. DOI: 10.1039/C2SM26479J.

[30] C. L. Van Oosten et al. "Printed Artificial Cilia from Liquid-Crystal Network Actuators Modularly Driven by Light". In: *Nature Materials* 8.8 (2009), pp. 677–682. ISSN: 14761122. DOI: 10.1038/nmat2487.

[31] A. D. Auguste et al. "Enabling and Localizing Omnidirectional Nonlinear Deformation in Liquid Crystalline Elastomers". In: *Advanced Materials* 30.35 (2018). ISSN: 09359648. DOI: 10.1002/adma.201802438.

[32] J. Li et al. "Photoswitchable Fluorescent Liquid Crystal Nanoparticles and Their Inkjet-Printed Patterns for Information Encrypting and Anti-Counterfeiting". In: *Particle and Particle Systems Characterization* 36.10 (2019). ISSN: 09340866. DOI: 10.1002/ppsc.201900346.

[33] A. Hirai et al. "One Drop Filling for Liquid Crystal Display Panel Produced from Larger-Sized Mother Glass". In: *Hitachi Review* 57.3 (2008), pp. 144–148. ISSN: 0018277X.

[34] F. Reinitzer. "Beiträge Zur Kenntniss Des Cholesterins". In: *Monatshefte für Chemie* 9.1 (1888), pp. 421–441. DOI: 10.1007/BF01516710.

[35] O. Lehmann. "Über Fliessende Krystalle". In: *Z. Phys. Chem.* 4 (1889).

[36] Q. Zhong and L. Zhang. "Nanoparticles Fabricated from Bulk Solid Lipids: Preparation, Properties, and Potential Food Applications". In: *Advances in Colloid and Interface Science* 273 (2019). ISSN: 00018686. DOI: 10.1016/j.cis.2019.102033.

[37] P. Rastogi et al. "Exploration of Elastomeric and Polymeric Liquid Crystals with Photothermal Actuation: A Review". In: *European Polymer Journal* 121 (2019). ISSN: 00143057. DOI: 10.1016/j.eurpolymj.2019.109287.

[38] A. Ghosh and B. Norton. "Advances in Switchable and Highly Insulating Autonomous (Self-Powered) Glazing Systems for Adaptive Low Energy Buildings". In: *Renewable Energy* 126 (2018), pp. 1003–1031. ISSN: 09601481. DOI: 10.1016/j.renene.2018.04.038.

[39] A. P. C. Almeida et al. "Cellulose-Based Biomimetics and Their Applications". In: *Advanced Materials* 30.19 (2018). ISSN: 09359648. DOI: 10.1002/adma.201703655.

[40] V. N. Tsvetkov. "About the Molecular Order in the Anisotropic Liquid-Phase". In: *Acta Physicochim. URSS* 16.3 (1942).

[41] W. Maier and A. Saupe. In: *Z. Naturforsch.* 13 A (1958), pp. 564–566.

[42] D.-K. Yang and S.-T. Wu. *Fundamentals of Liquid Crystal Devices*. Vol. 9781118752005. Wiley Blackwell, 2014. 1-570. ISBN: 978-1-118-75199-2 978-1-118-75200-5. DOI: 10.1002/9781118751992.

[43] I. Haller et al. "Order-Related Properties of Some Nematic Liquids". In: *Journal of Physical Chemistry* 77.7 (1973), pp. 950–954. DOI: 10.1021/j100626a020.

[44] I. Haller. "Thermodynamic and Static Properties of Liquid Crystals". In: *Progress in Solid State Chemistry* 10 (PART 2 1975), pp. 103–118. DOI: 10.1016/0079-6786(75)90008-4.

[45] I. Chirtoc et al. "Determination of the Order Parameter and Its Critical Exponent for nCB (n = 5-8) Liquid Crystals from Refractive Index Data". In: *Liquid Crystals* 31.2 (2004), pp. 229–240. ISSN: 02678292. DOI: 10.1080/02678290310001642540.

[46] S. -T. Wu et al. "Refractive Index Dispersions of Liquid Crystals". In: *Optical Engineering* 32.8 (1993), pp. 1775–1780. ISSN: 00913286. DOI: 10.1117/12.143988.

[47] C. W. Oseen. "The Theory of Liquid Crystals". In: *Transactions of the Faraday Society* 29.140 (1933), pp. 883–899. DOI: 10.1039/tf9332900883.

[48] F. C. Frank. "I. Liquid Crystals: On the Theory of Liquid Crystals". In: *Discussions of the Faraday Society* 25 (1958), pp. 19–28. DOI: 10.1039/DF9582500019.

[49] R. K. Goyal and M. M. Denn. "Orientational Multiplicity and Transitions in Liquid Crystalline Droplets". In: *Physical Review E - Statistical, Nonlinear, and Soft Matter Physics* 75.2 (2007). DOI: 10.1103/PhysRevE.75.021704.

[50] T. Tixier et al. "Spontaneous Size Selection in Cholesteric and Nematic Emulsions". In: *Langmuir* 22.5 (2006), pp. 2365–2370. DOI: 10.1021/la0531953.

[51] D. W. Berreman. "Solid Surface Shape and the Alignment of an Adjacent Nematic Liquid Crystal". In: *Physical Review Letters* 28.26 (1972), pp. 1683–1686. DOI: 10.1103/PhysRevLett.28.1683.

[52] A. Rapini and M. Papoular. "Distortion d'une Lamelle Nematique Sous Champ Magnétic. Conditions d'Anchrage Aux Parois". In: *J. Phys. Colloq.* 30.C4 (1969), pp. 54–56.

[53] B. Jerome. "Surface Effects and Anchoring in Liquid Crystals". In: *Reports on Progress in Physics* 54.3 (1991), pp. 391–452. ISSN: 0034-4885. DOI: 10.1088/0034-4885/54/3/002.

[54] A. Sengupta et al. "Liquid Crystal Microfluidics: Surface, Elastic and Viscous Interactions at Microscales". In: *Liquid Crystals Reviews* 2.2 (2014), pp. 73–110. ISSN: 21680396. DOI: 10.1080/21680396.2014.963716.

[55] C. Loussert et al. "Manipulating the Orbital Angular Momentum of Light at the Micron Scale with Nematic Disclinations in a Liquid Crystal Film". In: *Physical Review Letters* 111.3 (2013). ISSN: 00319007. DOI: 10.1103/PhysRevLett.111.037802.

[56] J. P. F. Lagerwall and G. Scalia. "A New Era for Liquid Crystal Research: Applications of Liquid Crystals in Soft Matter Nano-, Bio- and Microtechnology". In: *Current Applied Physics* 12.6 (2012), pp. 1387–1412. ISSN: 15671739. DOI: 10.1016/j.cap.2012.03.019.

[57] J. H. Erdmann et al. "Configuration Transition in a Nematic Liquid Crystal Confined to a Small Spherical Cavity". In: *Physical Review Letters* 64.16 (1990), pp. 1907–1910. ISSN: 00319007. DOI: 10.1103/PhysRevLett.64.1907.

[58] R. Ondris-Crawford et al. "Microscope Textures of Nematic Droplets in Polymer Dispersed Liquid Crystals". In: *Journal of Applied Physics* 69.9 (1991), pp. 6380–6386. ISSN: 00218979. DOI: 10.1063/1.348840.

[59] A. V. Dubtsov et al. "Liquid Crystalline Droplets in Aqueous Environments: Electrostatic Effects". In: *Soft Matter* 14.47 (2018), pp. 9619–9630. ISSN: 1744683X. DOI: 10.1039/c8sm01529e.

[60] O. D. Lavrentovich. "Topological Defects in Dispersed Words and Worlds around Liquid Crystals, or Liquid Crystal Drops". In: *Liquid Crystals* 24.1 (1998), pp. 117–126. DOI: 10.1080/026782998207640.

[61] J. K. Gupta et al. "Size-Dependent Ordering of Liquid Crystals Observed in Polymeric Capsules with Micrometer and Smaller Diameters". In: *Angewandte Chemie - International Edition* 48.9 (2009), pp. 1652–1655. DOI: 10.1002/anie.200804500.

[62] M. Miesowicz. "The Three Coefficients of Viscosity of Anisotropic Liquids [14]". In: *Nature* 158.4001 (1946), p. 27. ISSN: 00280836. DOI: 10.1038/158027b0.

[63] J. L. Ericksen. "Anisotropic Fluids". In: *Archive for Rational Mechanics and Analysis* 4.1 (1959), pp. 231–237. ISSN: 00039527. DOI: 10.1007/BF00281389.

[64] F. M. Leslie. "Some Constitutive Equations for Anisotropic Fluids". In: *Quarterly Journal of Mechanics and Applied Mathematics* 19.3 (1966), pp. 357–370. DOI: 10.1093/qjmam/19.3.357.

[65] F. M. Leslie. "Some Constitutive Equations for Liquid Crystals". In: *Archive for Rational Mechanics and Analysis* 28.4 (1968), pp. 265–283. ISSN: 00039527. DOI: 10.1007/BF00251810.

[66] O. Parodi. "Stress Tensor for a Nematic Liquid Crystal". In: *J. Phys. (Paris)* 31 (1970), pp. 581–584.

[67] R. Orr and R. A. Pethrick. "Viscosity Coefficients of Nematic Liquid Crystals: I. Oscillating Plate Viscometer Measurements and Rotational Viscosity Measurements: K15†". In: *Liquid Crystals* 38.9 (2011), pp. 1169–1181. ISSN: 02678292. DOI: 10.1080/02678292.2011.602121.

[68] C. Gähwiller. "Temperature Dependence of Flow Alignment in Nematic Liquid Crystals". In: *Physical Review Letters* 28.24 (1972), pp. 1554–1556. DOI: 10.1103/PhysRevLett.28.1554.

[69] P. Pieranski and E. Guyon. "Two Shear-Flow Regimes in Nematic p-n-Hexyloxybenzilidene-P-Aminobenzonitrile". In: *Physical Review Letters* 32.17 (1974), pp. 924–926. DOI: 10.1103/PhysRevLett.32.924.

[70] R. Porter and J. Johnson. "The Rheology of Liquid Crystals". In: *Rheology* 4 (1967), pp. 317–345.

[71] H. Imura and K. Okano. "Temperature Dependence of the Viscosity Coefficients of Liquid Crystals". In: *Japanese Journal of Applied Physics* 11.10 (1972), pp. 1440–1445. ISSN: 00214922. DOI: 10.1143/JJAP.11.1440.

[72] P. S. Drzaic. "Reorientation Dynamics of Polymer Dispersed Nematic Liquid Crystal Films". In: *Liquid Crystals* 3.11 (1988), pp. 1543–1559. ISSN: 02678292. DOI: 10.1080/02678298808086694.

[73] Cooper, J. *Compositional Analysis of Merck E7 Liquid Crystal Intermediates Using UltraPerformance Convergence Chromatography (UPC2) with PDA Detection*. Waters Corporation, Oct. 2013.

[74] T. R. Cull et al. "Liquid Crystal Libraries - Ink-Jet Formulation and High-Throughput Analysis". In: *Advanced Materials* 19.17 (2007), pp. 2355–2359. ISSN: 09359648. DOI: 10.1002/adma.200602661.

[75] H. Coles and S. Morris. "Liquid-Crystal Lasers". In: *Nature Photonics* 4.10 (2010), pp. 676–685. ISSN: 17494885. DOI: 10.1038/nphoton.2010.184.

[76] C. Ohm et al. "Liquid Crystalline Elastomers as Actuators and Sensors". In: *Advanced Materials* 22.31 (2010), pp. 3366–3387. ISSN: 09359648. DOI: 10.1002/adma.200904059.

[77] A. Kotikian et al. "3D Printing of Liquid Crystal Elastomeric Actuators with Spatially Programed Nematic Order". In: *Advanced Materials* 30.10 (2018). ISSN: 09359648. DOI: 10.1002/adma.201706164.

[78] C .P. Ambulo et al. "Four-Dimensional Printing of Liquid Crystal Elastomers". In: *ACS Applied Materials and Interfaces* 9.42 (2017), pp. 37332–37339. ISSN: 19448244. DOI: 10.1021/acsami.7b11851.

[79] T. Takahashi. "Adaptability of Piezoelectric Inkjet Head". In: International Conference on Digital Printing Technologies. 2001, pp. 323–327.

[80] H. Wijshoff. "The Dynamics of the Piezo Inkjet Printhead Operation". In: *Physics Reports* 491.4 (2010), pp. 77–177. ISSN: 0370-1573. DOI: http://dx.doi.org/10.1016/j.physrep.2010.03.003.

[81] G. H McKinley and M. Renardy. "Wolfgang von Ohnesorge". In: *Physics of Fluids* 23.12 (Dec. 2011), p. 127101. ISSN: 1070-6631. DOI: 10.1063/1.3663616.

[82] S. D. Hoath. *Fundamentals of Inkjet Printing: The Science of Inkjet and Droplets*. Ed. by S. D. Hoath. Wiley-vch, 2015.

[83] N. Reis and B. Derby. "Ink Jet Deposition of Ceramic Suspensions: Modelling and Experiments of Droplet Formation". In: *Materials Research Society Symposium - Proceedings* 624 (2000). Ed. by Chrisey D.B., Gamota D.R., Helvajian H., Taylor D.P., pp. 65–70. ISSN: 02729172.

[84] D. Jang et al. "Influence of Fluid Physical Properties on Ink-Jet Printability". In: *Langmuir* 25.5 (2009), pp. 2629–2635. ISSN: 07437463. DOI: 10.1021/la900059m.

[85] B. Derby. "Inkjet Printing Ceramics: From Drops to Solid". In: *Journal of the European Ceramic Society* 31.14 (2011), pp. 2543–2550. ISSN: 09552219. DOI: 10.1016/j.jeurceramsoc.2011.01.016.

[86] P. C. Duineveld et al. "Ink-Jet Printing of Polymer Light-Emitting Devices". In: ed. by Kafafi Z.H. Vol. 4464. Proceedings of SPIE - The International Society for Optical Engineering. 2002, pp. 59–67. DOI: 10.1117/12.457460.

[87] B. W. Jo et al. "Evaluation of Jet Performance in Drop-on-Demand (DOD) Inkjet Printing". In: *Korean Journal of Chemical Engineering* 26.2 (2009), pp. 339–348. ISSN: 02561115. DOI: 10.1007/s11814-009-0057-2.

[88] H. Y. Gan et al. "Reduction of Droplet Volume by Controlling Actuating Waveforms in Inkjet Printing for Micro-Pattern Formation". In: *Journal of Micromechanics and Microengineering* 19.5 (2009). ISSN: 09601317. DOI: 10.1088/0960-1317/19/5/055010.

[89] F. Yang et al. "Homeotropic Polar Anchoring Energy of a Nematic Liquid Crystal Using the Fully Leaky Waveguide Technique". In: *Journal of Applied Physics* 88.11 (2000), pp. 6175–6182. ISSN: 00218979. DOI: 10.1063/1.1324695.

[90] K. Ichimura. "Photoalignment of Liquid-Crystal Systems". In: *Chemical Reviews* 100.5 (2000), pp. 1847–1873. ISSN: 00092665.

[91] C. Josserand and S.T. Thoroddsen. "Drop Impact on a Solid Surface". In: *Annual Review of Fluid Mechanics* 48.1 (2016), pp. 365–391. DOI: 10.1146/annurev-fluid-122414-034401. eprint: https://doi.org/10.1146/annurev-fluid-122414-034401.

[92] C. Josserand and S. Zaleski. "Droplet Splashing on a Thin Liquid Film". In: *Physics of Fluids* 15.6 (2003), pp. 1650–1657. DOI: 10.1063/1.1572815.

[93] T. Young. "III. An Essay on the Cohesion of Fluids". In: *Philosophical Transactions of the Royal Society of London* 95 (1805), pp. 65–87. DOI: 10.1098/rstl.1805.0005. eprint: https://royalsocietypublishing.org/doi/pdf/10.1098/rstl.1805.0005.

[94] P. G. De Gennes. "Wetting: Statics and Dynamics". In: *Reviews of Modern Physics* 57.3 (1985), pp. 827–863. ISSN: 00346861. DOI: 10.1103/RevModPhys.57.827.

[95] W. H. De Jeu. "Liquid Crystalline Materials: Physical Properties and Intermolecular Interacrions." In: ed. by C. Hilsum and E. P. Raynes. Royal Soc (First publ in Philosophical Transactions of the Royal Soc of London, Series A, v 309 n 1507), London, Engl, 1983, pp. 147–159. ISBN: 0-85403-210-X.

[96] W. Huang and G.F. Tuthill. "Structure and Shape of Nematic Liquid-Crystal Microdroplets". In: *Physical Review E* 49.1 (1994), pp. 570–574. ISSN: 1063651X. DOI: 10.1103/PhysRevE.49.570.

[97] *Detailed Explanation of the Finite Element Method (FEM)*. URL: https://uk.comsol.com/multiphysics/finite-element-method (visited on 07/17/2019).

[98] A. Kilian. "Computer Simulations of Nematic Droplets". In: *Liquid Crystals* 14.4 (1993), pp. 1189–1198. DOI: 10.1080/02678299308027827.

[99] O. O. Prishchepa et al. "Director Configurations in Nematic Droplets with Inhomogeneous Boundary Conditions". In: *Physical Review E - Statistical, Nonlinear, and Soft Matter Physics* 72.3 (2005). ISSN: 15393755. DOI: 10.1103/PhysRevE.72.031712.

[100] S. Kumar et al. "What Aligns Liquid Crystals on Solid Substrates? The Role of Surface Roughness Anisotropy". In: *Phys. Rev. Lett.* 94.7 (Feb. 2005), p. 077803. DOI: 10.1103/PhysRevLett.94.077803.

[101] I. Nys et al. "Surface-Mediated Alignment of Long Pitch Chiral Nematic Liquid Crystal Structures". In: *Advanced Optical Materials* 6.13 (2018). ISSN: 21951071. DOI: 10.1002/adom.201800070.

[102] B.R. Acharya et al. "Material-Independent Determination of Anchoring Properties on Rubbed Polyimide Surfaces". In: *Physical Review E - Statistical Physics, Plasmas, Fluids, and Related Interdisciplinary Topics* 60.6 (1999), pp. 6841–6846. ISSN: 1063651X. DOI: 10.1103/PhysRevE.60.6841.

[103] G. P. Bryan-Brown et al. "Weak Surface Anchoring of Liquid Crystals". In: *Nature* 399.6734 (1999), pp. 338–340. ISSN: 00280836. DOI: 10.1038/20646.

[104] E. Tan and S.T. Thoroddsen. "Marangoni Instability of Two Liquids Mixing at a Free Surface". In: *Physics of Fluids* 10.12 (1998), pp. 3038–3040. ISSN: 10706631. DOI: 10.1063/1.869831.

[105] X. Fanton and A.M. Cazabat. "Spreading and Instabilities Induced by a Solutal Marangoni Effect". In: *Langmuir* 14.9 (1998), pp. 2554–2561. ISSN: 07437463.

[106] S. -H. Hyon et al. "Preparation of Transparent Poly(Vinyl Alcohol) Hydrogel". In: *Polymer Bulletin* 22.2 (1989), pp. 119–122. ISSN: 01700839. DOI: 10.1007/BF00255200.

[107] H. Trieu and S. Qutubuddin. "Poly(Vinyl Alcohol) Hydrogels: 2. Effects of Processing Parameters on Structure and Properties". In: *Polymer* 36.13 (1995), pp. 2531–2539. ISSN: 00323861. DOI: 10.1016/0032-3861(95)91198-G.

[108] T. Hou et al. "Fabrication, Characterization, and Applications of Microlenses". In: *Appl. Opt.* 54.24 (Aug. 2015), pp. 7366–7376. DOI: 10.1364/AO.54.007366.

[109] J. Aizenberg and G. Hendler. "Designing Efficient Microlens Arrays: Lessons from Nature". In: *Journal of Materials Chemistry* 14.14 (2004), pp. 2066–2072. ISSN: 09599428. DOI: 10.1039/b402558j.

[110] C. Friese et al. "Materials, Effects and Components for Tunable Micro-Optics". In: *IEEJ Transactions on Electrical and Electronic Engineering* 2.3 (2007), pp. 232–248. ISSN: 19314973. DOI: 10.1002/tee.20138.

[111] R. Stevensa and T. Miyashita. "Review of Standards for Microlenses and Microlens Arrays". In: *Imaging Science Journal* 58.4 (2010), pp. 202–212. ISSN: 13682199. DOI: 10.1179/136821910X12651933390746.

[112] M.-H. Wu et al. "Fabrication of Arrays of Microlenses with Controlled Profiles Using Gray-Scale Microlens Projection Photolithography". In: *Langmuir* 18.24 (2002), pp. 9312–9318. DOI: 10.1021/la015735b.

[113] N. S. Ong et al. "Microlens Array Produced Using Hot Embossing Process". In: *Microelectronic Engineering* 60.3-4 (2002), pp. 365–379.

[114] D. Daly et al. "The Manufacture of Microlenses by Melting Photoresist". In: *Measurement Science and Technology* 1.8 (Aug. 1990), pp. 759–766. ISSN: 09570233. DOI: 10.1088/0957-0233/1/8/016.

[115] H. Becker and U. Heim. "Hot Embossing as a Method for the Fabrication of Polymer High Aspect Ratio Structures". In: *Sensors and Actuators, A: Physical* 83.1 (2000), pp. 130–135. ISSN: 09244247. DOI: 10.1016/S0924-4247(00)00296-X.

[116] Ph. Nussbaum et al. "Design, Fabrication and Testing of Microlens Arrays for Sensors and Microsystems". In: *Pure and Applied Optics (Print edition) (United Kingdom)* 6.6 (1997), pp. 617–636. ISSN: 09639659. DOI: 10.1088/0963-9659/6/6/004.

[117] A. Varshney et al. "Large Scale Arrays of Tunable Microlenses". In: *Lab on a Chip* 14.7 (2014), pp. 1330–1335. ISSN: 14730197. DOI: 10.1039/c3lc51170g.

[118] Y .-C. Chang et al. "High-Resistance Liquid-Crystal Lens Array for Rotatable 2D/3D Autostereoscopic Display". In: *Optics Express* 22.3 (2014), pp. 2714–2724. ISSN: 10944087. DOI: 10.1364/OE.22.002714.

[119] C. Monat et al. "Integrated Optofluidics: A New River of Light". In: *Nat Photon* 1.2 (Feb. 2007), pp. 106–114. ISSN: 1749-4885.

[120] J. Chen et al. "Variable-Focusing Microlens with Microfluidic Chip". In: *Journal of Micromechanics and Microengineering* 14.5 (2004), pp. 675–680. ISSN: 09601317. DOI: 10.1088/0960-1317/14/5/003.

[121] C. Li and H. Jiang. "Electrowetting-Driven Variable-Focus Microlens on Flexible Surfaces". In: *Applied Physics Letters* 100.23 (2012). ISSN: 00036951. DOI: 10.1063/1.4726038.

[122] T. Nose and S. Sato. "A Liquid Crystal Microlens Obtained with a Non-Uniform Electric Field". In: *Liquid Crystals* 5.5 (1989), pp. 1425–1433. DOI: 10.1080/02678298908027780. eprint: http://dx.doi.org/10.1080/02678298908027780.

[123] C. Lan et al. "Fast-Response Microlens Array Fabricated Using Polyvinyl Chloride Gel". In: *Journal of Molecular Liquids* 283 (2019), pp. 155–159. ISSN: 01677322. DOI: 10.1016/j.molliq.2019.03.050.

[124] S. Xu et al. "Fast-Response Liquid Crystal Microlens". In: *Micromachines* 5.2 (2014), pp. 300–324. ISSN: 2072-666X. DOI: 10.3390/mi5020300.

[125] S. Masuda et al. "Liquid-Crystal Microlens with a Beam-Steering Function". In: *Applied Optics* 36.20 (1997), pp. 4772–4778. ISSN: 1559128X. DOI: 10.1364/AO.36.004772.

[126] Y. Kao et al. "A New Low-Voltage-Driven GRIN Liquid Crystal Lens with Multiple Ring Electrodes in Unequal Widths". In: *osapublishing.org* 18.18 (2010), pp. 3467–3477. ISSN: 1094-4087. DOI: 10.1364/OE.18.018506. pmid: 20940742.

[127] A. F. Naumov et al. "Liquid-Crystal Adaptive Lenses with Modal Control". In: *Optics Letters* 23.13 (1998), p. 992. ISSN: 0146-9592. DOI: 10.1364/OL.23.000992. pmid: 18087406.

[128] L. Lu et al. "Surface Localized Polymer Aligned Liquid Crystal Lens". In: *Optics Express* 21.6 (2013), pp. 7133–7138. ISSN: 10944087. DOI: 10.1364/OE.21.007133.

[129] M. C. Tseng et al. "Tunable Lens by Spatially Varying Liquid Crystal Pretilt Angles". In: *Journal of Applied Physics* 109.8 (Apr. 2011), p. 083109. ISSN: 00218979. DOI: 10.1063/1.3567937.

[130] V. V. Presnyakov and T. V. Galstian. "Electrically Tunable Polymer Stabilized Liquid-Crystal Lens". In: *Journal of Applied Physics* 97.10 (2005). ISSN: 00218979. DOI: 10.1063/1.1896436.

[131] Y. Choi et al. "Fabrication of a Focal Length Variable Microlens Array Based on a Nematic Liquid Crystal". In: *Optical Materials* 21.1-3 (Jan. 2003), pp. 643–646. ISSN: 09253467. DOI: 10.1016/S0925-3467(02)00215-X.

[132] J. W. Goodman. *Introduction to Fourier Optics*. 3rd ed. 2005.

[133] Y. Liu et al. "Polarization-Independent Adaptive Lens with Two Different Blue-Phase Liquid-Crystal Layers". In: *Applied Optics* 52.14 (2013), pp. 3216–3220. DOI: 10.1364/AO.52.003216.

[134] J. Tan et al. "Blue Phase LC/Polymer Fresnel Lens Fabricated by Holographics". In: *IEEE/OSA Journal of Display Technology* 10.2 (2014), pp. 157–161. DOI: 10.1109/JDT.2013.2291068.

[135] Y. -H. Lin et al. "Polarization-Independent Liquid Crystal Phase Modulator Using a Thin Polymer-Separated Double-Layered Structure". In: *Optics Express* 13.22 (2005), pp. 8746–8752. DOI: 10.1364/OPEX.13.008746.

[136] A. Y.-G. Fuh et al. "Polarization-Independent Liquid Crystal Lens Based on Axially Symmetric Photoalignment". In: *Optics Express* 19.3 (2011), pp. 2294–2300. DOI: 10.1364/OE.19.002294.

[137] P. Calvert. "Inkjet Printing for Materials and Devices". In: *Chemistry of Materials* 13.10 (2001), pp. 3299–3305. ISSN: 08974756. DOI: 10.1021/cm0101632.

[138] D. L. MacFarlane et al. "Microjet Fabrication of Microlens Arrays". In: *IEEE Photonics Technology Letters* 6.9 (1994), pp. 1112–1114. ISSN: 10411135. DOI: 10.1109/68.324684.

[139] A. Voigt et al. "New Inks for the Direct Drop-on-Demand Fabrication of Polymer Lenses". In: *Microelectronic Engineering* 88.8 (2011), pp. 2174–2179. ISSN: 01679317. DOI: 10.1016/j.mee.2010.12.004.

[140] D. Xie et al. "Fabrication of Polymer Micro-Lens Array with Pneumatically Diaphragm-Driven Drop-Ondemand Inkjet Technology". In: *Optics Express* 20.14 (2012), pp. 15186–15195. ISSN: 10944087. DOI: 10.1364/OE.20.015186.

[141] C.-T Chen et al. "Self-Aligned Hemispherical Formation of Microlenses from Colloidal Droplets on Heterogeneous Surfaces". In: *Journal of Micromechanics and Microengineering* 19.2 (Jan. 2009), p. 025002. DOI: 10.1088/0960-1317/19/2/025002.

[142] W. Moench and H. Zappe. "Fabrication and Testing of Micro-Lens Arrays by All-Liquid Techniques". In: *Journal of Optics A: Pure and Applied Optics* 6.4 (Feb. 2004), pp. 330–337. DOI: 10.1088/1464-4258/6/4/007.

[143] S. Reichelt and H. Zappe. "Combined Twyman-Green and Mach-Zehnder Interferometer for Microlens Testing". In: *Applied Optics* 44.27 (2005), pp. 5786–5792. DOI: 10.1364/AO.44.005786.

[144] X. Huang et al. "Thermally Tunable Polymer Microlenses". In: *Applied Physics Letters* 92.25 (2008). ISSN: 00036951. DOI: 10.1063/1.2945646.

[145] H. Ren and S.-T. Wu. "Tunable-Focus Liquid Microlens Array Using Dielectrophoretic Effect". In: *Optics Express* 16.4 (2008), pp. 2646–2652. ISSN: 10944087. DOI: 10.1364/OE.16.002646.

[146] Y. Lu and S. Chen. "Direct Write of Microlens Array Using Digital Projection Photopolymerization". In: *Applied Physics Letters* 92.4 (2008). ISSN: 00036951. DOI: 10.1063/1.2838751.

[147] H. Ottevaere et al. "Comparing Glass and Plastic Refractive Microlenses Fabricated with Different Technologies". In: *Journal of Optics A: Pure and Applied Optics* 8.7 (2006), S407.

[148] G. P. Crawford. "Encapsulated Liquid Crystal Materials for Flexible Display Applications". In: *Flexible Flat Panel Displays*. John Wiley & Sons, Ltd, 2005, pp. 313–330. ISBN: 978-0-470-87050-1. eprint: https://onlinelibrary.wiley.com/doi/pdf/10.1002/0470870508.ch16.

[149] N. A. Vaz et al. "A Light Control Film Composed of Liquid Crystal Droplets Dispersed in a UV-Curable Polymer". In: *Molecular Crystals and Liquid Crystals* 146.1 (1987), pp. 1–15. DOI: 10.1080/00268948708071798. eprint: https://doi.org/10.1080/00268948708071798.

[150] L. Bouteiller and P. Lebarny. "Polymer-Dispersed Liquid Crystals: Preparation, Operation and Application". In: *Liquid Crystals* 21.2 (1996), pp. 157–174. ISSN: 02678292. DOI: 10.1080/02678299608032820.

[151] H. Ren et al. "Tunable-Focus Microlens Arrays Using Nanosized Polymer-Dispersed Liquid Crystal Droplets". In: *Optics Communications* 247.1-3 (2005), pp. 101–106. DOI: 10.1016/j.optcom.2004.11.033.

[152] I.-C. Khoo and S.-T. Wu. *Optics and Nonlinear Optics of Liquid Crystals*. WORLD SCIENTIFIC, 1993. DOI: 10.1142/1630. eprint: https://www.worldscientific.com/doi/pdf/10.1142/1630.

[153] D. Coates. "Polymer-Dispersed Liquid Crystals". In: *Journal of Materials Chemistry* 5.12 (1995), pp. 2063–2072. ISSN: 09599428. DOI: 10.1039/jm9950502063.

[154] A. J. Lovinger et al. "Morphological Investigation of UV-Curable Polymer-Dispersed Liquid-Crystal (PDLC) Materials". In: *Chemistry of Materials* 6.10 (1994), pp. 1726–1736. DOI: 10.1021/cm00046a027. eprint: https://doi.org/10.1021/cm00046a027.

[155] T. J. Bunning et al. "Holographic Polymer-Dispersed Liquid Crystals (H-PDLCs)". In: *Annual Review of Materials Science* 30 (2000), pp. 83–115. ISSN: 00846600. DOI: 10.1146/annurev.matsci.30.1.83.

[156] Y. Kim et al. "Optical Properties and Optimized Conditions for Polymer Dispersed Liquid Crystal Containing UV Curable Polymer and Nematic Liquid Crystal". In: *Current Applied Physics* 15.3 (2015), pp. 292–297. ISSN: 15671739. DOI: 10.1016/j.cap.2014.12.027.

[157] D. Cupelli et al. "Self-Adjusting Smart Windows Based on Polymer-Dispersed Liquid Crystals". In: *Solar Energy Materials and Solar Cells* 93.11 (2009), pp. 2008–2012. ISSN: 09270248. DOI: 10.1016/j.solmat.2009.08.002.

[158] A. Y.-G. Fuh et al. "Electrically Controllable Smart Window with Greyscale Based on Polymer-Stabilised Cholesteric Texture Films". In: *Liquid Crystals* 43.12 (2016), pp. 1784–1790. ISSN: 02678292. DOI: 10.1080/02678292.2016.1209700.

[159] P.S. Drzaic. In: *Liquid Crystal Dispersions* (1995).

[160] Y. J. Liu et al. "Polymer-Dispersed Liquid Crystals Light Shutter Driven by Surface Acoustic Wave". In: 16th International Solid-State Sensors, Actuators and Microsystems Conference, 2011, pp. 2554–2557. ISBN: 978-1-4577-0157-3. DOI: 10.1109/TRANSDUCERS.2011.5969772.

[161] M. Jamil et al. "Nanoparticle-Doped Polymer-Dispersed Liquid Crystal Display". In: *Current Science* 101.12 (2011), pp. 1544–1552. ISSN: 00113891.

[162] J. L. Fergason. "Polymer Encapsulated Nematic Liquid Crystals for Display and Light Control Applications". In: *SID Int. Symp. Dig. Tech. Pap.* 16 (1985), pp. 68–70.

[163] J. L. West. "Phase Separation of Liquid Crystals in Polymers". In: *Molecular Crystals and Liquid Crystals Incorporating Nonlinear Optics* 157.1 (1988), pp. 427–441. DOI: 10.1080/00268948808080247. eprint: https://doi.org/10.1080/00268948808080247.

[164] S. Zumer. *Liquid Crystals In Complex Geometries: Formed by Polymer And Porous Networks*. Taylor & Francis Group, 2014.

[165] M. Mucha. "Polymer as an Important Component of Blends and Composites with Liquid Crystals". In: *Progress in Polymer Science (Oxford)* 28.5 (2003), pp. 837–873. ISSN: 00796700. DOI: 10.1016/S0079-6700(02)00117-X.

[166] S. Bronnikov et al. "Polymer-Dispersed Liquid Crystals: Progress in Preparation, Investigation, and Application". In: *Journal of Macromolecular Science, Part B: Physics* 52.12 (2013), pp. 1718–1735. ISSN: 00222348. DOI: 10.1080/00222348.2013.808926.

[167] C. Serbutoviez et al. "Polymerization-Induced Phase Separation. 2. Morphology of Polymer-Dispersed Liquid Crystal Thin Films". In: *Macromolecules* 29.24 (1996), pp. 7690–7698. ISSN: 00249297. DOI: 10.1021/ma960293+.

[168] S. Mutlu Yanic et al. "Morphology and Preparation of Polymer Dispersed Liquid Crystals by Solvent-Induced Phase Separation Method". In: *Optoelectronics and Advanced Materials, Rapid Communications* 11.1-2 (2017), pp. 77–81. ISSN: 18426573.

[169] F. Ahmad et al. "New Developments in the Dye-Doped Polymer Dispersed Liquid Crystals Gratings: A Review". In: *International Journal of Polymer Analysis and Characterization* 22.8 (2017), pp. 659–668. ISSN: 1023666X. DOI: 10.1080/1023666X.2017.1363550.

[170] P. S. Drzaic. "Polymer Dispersed Liquid Crystals: A Look Back, a Look Ahead". In: *Liquid Crystals Today* 5.1 (1995), pp. 2–4. ISSN: 1358314X. DOI: 10.1080/13583149508047582.

[171] H. Hakemi. "Polymer-Dispersed Liquid Crystal Technology 'Industrial Evolution and Current Market Situation'". In: *Liquid Crystals Today* 26.3 (2017), pp. 70–73. ISSN: 1358314X. DOI: 10.1080/1358314X.2017.1359143. eprint: https://doi.org/10.1080/1358314X.2017.1359143.

[172] C.-C. Liao et al. "Design and Fabrication of a High-Bright Sunlight Readable Transparent Head-up Display for Automotive Application". In: vol. 2. Proceedings of the International Display Workshops. International Display Workshops, 2017, pp. 1461–1464. ISBN: 978-1-5108-5899-2.

[173] M. Casini. "Active Dynamic Windows for Buildings: A Review". In: *Renewable Energy* 119 (2018), pp. 923–934. ISSN: 09601481. DOI: 10.1016/j.renene.2017.12.049.

[174] Y. Alesanco et al. "All-in-One Gel-Based Electrochromic Devices: Strengths and Recent Developments". In: *Materials* 11.3 (2018). ISSN: 19961944. DOI: 10.3390/ma11030414.

[175] R. Baetens et al. "Properties, Requirements and Possibilities of Smart Windows for Dynamic Daylight and Solar Energy Control in Buildings: A State-of-the-Art Review". In: *Solar Energy Materials and Solar Cells* 94.2 (2010), pp. 87–105. ISSN: 09270248. DOI: 10.1016/j.solmat.2009.08.021.

[176] K. Kato et al. "Color Image Formation Using Polymer-Dispersed Cholesteric Liquid Crystal". In: *Japanese Journal of Applied Physics* 32 (10 R 1993), pp. 4600–4604. ISSN: 00214922. DOI: 10.1143/JJAP.32.4600.

[177] S. J. Woltman and G. P. Crawford. "Patterned Liquid-Crystal Laser Film for Multi-Dimensional Multi-Color Emissive Film Technology". In: *Journal*

of the Society for Information Display 15.8 (2007), pp. 559–564. ISSN: 10710922. DOI: 10.1889/1.2770855.

[178] T. Kyu and D. Nwabunma. "Simulations of Microlens Arrays Formed by Pattern-Photopolymerization-Induced Phase Separation of Liquid Crystal/Monomer Mixtures". In: *Macromolecules* 34.26 (2001), pp. 9168–9172. ISSN: 00249297. DOI: 10.1021/ma010567f.

[179] R. L. Sutherland et al. "Bragg Gratings in an Acrylate Polymer Consisting of Periodic Polymer-Dispersed Liquid-Crystal Planes". In: *Chemistry of Materials* 5.10 (1993), pp. 1533–1538. ISSN: 08974756. DOI: 10.1021/cm00034a025.

[180] L. V. Natarajan et al. "Switchable Holographic Polymer-Dispersed Liquid Crystal Reflection Gratings Based on Thiol-Ene Photopolymerization". In: *Chemistry of Materials* 15.12 (2003), pp. 2477–2484. ISSN: 08974756. DOI: 10.1021/cm021824d.

[181] J. Wang et al. "Phase Separation of Polymer-Dispersed Liquid Crystals on a Chemically Patterned Substrate". In: *Langmuir* 23.14 (2007), pp. 7411–7415. ISSN: 07437463. DOI: 10.1021/la700565w.

[182] J. Zou and J. Fang. "Adhesive Polymer-Dispersed Liquid Crystal Films". In: *Journal of Materials Chemistry* 21.25 (2011), pp. 9149–9153. ISSN: 09599428. DOI: 10.1039/c1jm10628g.

[183] E. Tekin et al. "Inkjet Printing as a Deposition and Patterning Tool for Polymers and Inorganic Particles". In: *Soft Matter* 4.4 (2008), pp. 703–713. ISSN: 1744683X. DOI: 10.1039/b711984d.

[184] N. Godard et al. "Direct Patterning of Piezoelectric Thin Films by Inkjet Printing". In: *Advanced Materials Technologies* 4.2 (2019). ISSN: 2365709X. DOI: 10.1002/admt.201800168.

[185] B. Derby. "Bioprinting: Inkjet Printing Proteins and Hybrid Cell-Containing Materials and Structures". In: *Journal of Materials Chemistry* 18.47 (2008), pp. 5717–5721. ISSN: 09599428. DOI: 10.1039/b807560c.

[186] J. A. Phillippi et al. "Microenvironments Engineered by Inkjet Bioprinting Spatially Direct Adult Stem Cells toward Muscle- and Bone-like Subpopulations". In: *Stem Cells* 26.1 (2008), pp. 127–134. ISSN: 10665099. DOI: 10.1634/stemcells.2007-0520.

[187] "Norland Optical Adhesives". In: (2019).

[188] G. W. Smith. "A Calorimetric Study of Phase Separation in Liquid Crystal/Matrix Systems: Determination of the Excess Specific Heat of Mixing". In: *Molecular Crystals and Liquid Crystals Science and Technology. Section A. Molecular Crystals and Liquid Crystals* 239.1 (1994), pp. 63–85. ISSN: 1058725X. DOI: 10.1080/10587259408047172.

[189] J. Whitehead et al. "Characterization of the Phase Separation of the E7 Liquid Crystal Component Mixtures in a Thiol-Ene Based Polymer". In: *Proceedings of SPIE - The International Society for Optical Engineering* 4107 (2000), pp. 189–197. ISSN: 0277786X. DOI: 10.1117/12.405323.

[190] H. Kittel and K. Herbert. *Thermal Physics*. 2nd ed. W. H. Freeman, 1980.

[191] G. W. Smith. "Cure Parameters and Phase Behavior of an Ultraviolet-Cured Polymer-Dispersed Liquid Crystal". In: *Mol. Cryst. Liq. Cryst.* 196 (1991).

[192] P. J. Flory. "Themodynamics of High Polymer Solutions". In: *The Journal of Chemical Physics* 10.1 (1942), pp. 51–61. DOI: 10.1063/1.1723621.

[193] M. Rein. "Phenomena of Liquid Drop Impact on Solid and Liquid Surfaces". In: *Fluid Dynamics Research* 12.2 (1993), pp. 61–93. DOI: 10.1016/0169-5983(93)90106-K.

[194] A. L. Yarin. "Drop Impact Dynamics: Splashing, Spreading, Receding, Bouncing.." In: *Annual Review of Fluid Mechanics* 38 (2006), pp. 159–192. DOI: 10.1146/annurev.fluid.38.050304.092144.

[195] N. P. van Hinsberg et al. "Dynamics of the Cavity and the Surface Film for Impingements of Single Drops on Liquid Films of Various Thicknesses". In: *Journal of Colloid and Interface Science* 350.1 (2010), pp. 336–343. DOI: 10.1016/j.jcis.2010.06.015.

[196] G. E. Cossali et al. "The Impact of a Single Drop on a Wetted Solid Surface". In: *Experiments in Fluids* 22.6 (1997), pp. 463–472. DOI: 10.1007/s003480050073.

[197] N. Chen et al. "Drop Impact onto a Thin Film: Miscibility Effect". In: *Physics of Fluids* 29.9 (2017). ISSN: 10706631. DOI: 10.1063/1.5001743.

[198] N. E. Ersoy and M. Eslamian. "Capillary Surface Wave Formation and Mixing of Miscible Liquids during Droplet Impact onto a Liquid Film". In: *Physics of Fluids* 31.1 (2019). ISSN: 10706631. DOI: 10.1063/1.5064640.

[199] S. M. Troian et al. "Fingering Instability in Thin Wetting Films". In: *Physical Review Letters* 62.13 (1989), pp. 1496–1499. ISSN: 00319007. DOI: 10.1103/PhysRevLett.62.1496.

[200] P. G. Smith et al. "The Transient Interfacial Tension between Two Miscible Fluids". In: *Journal of Colloid And Interface Science* 80.1 (1981), pp. 302–303. ISSN: 00219797. DOI: 10.1016/0021-9797(81)90186-7.

[201] M. A. Hack et al. "Printing Wet-on-Wet: Attraction and Repulsion of Drops on a Viscous Film". In: *Applied Physics Letters* 113.18 (2018). ISSN: 00036951. DOI: 10.1063/1.5048681.

[202] M. Santiago-Rosanne et al. "Dissolution of a Drop on a Liquid Surface Leading to Surface Waves and Interfacial Turbulence". In: *Journal of Colloid and Interface Science* 191.1 (1997), pp. 65–80. ISSN: 0021-9797. DOI: 10.1006/jcis.1997.4956.

[203] P.S. Drzaic. "Polymer Dispersed Nematic Liquid Crystal for Large Area Displays and Light Valves". In: *Journal of Applied Physics* 60.6 (1986), pp. 2142–2148. ISSN: 00218979. DOI: 10.1063/1.337167.

[204] G. P. Montgomery Jr. et al. "Light Scattering from Polymer-Dispersed Liquid Crystal Films: Droplet Size Effects". In: *Journal of Applied Physics* 69.3 (1991), pp. 1605–1612. ISSN: 00218979. DOI: 10.1063/1.347256.

[205] H. Minemawari et al. "Inkjet Printing of Single-Crystal Films". In: *Nature* 475.7356 (2011), pp. 364–367. ISSN: 00280836. DOI: 10.1038/nature10313.

[206] T. Juntunen et al. "Inkjet Printed Large-Area Flexible Few-Layer Graphene Thermoelectrics". In: *Advanced Functional Materials* 28.22 (2018), p. 1800480. DOI: 10.1002/adfm.201800480. eprint: https://onlinelibrary.wiley.com/doi/pdf/10.1002/adfm.201800480.

[207] U. Maschke et al. "Electro-Optical Properties of Polymer-Dispersed Liquid Crystals". In: *Macromolecular Rapid Communications* 23.3 (2002), pp. 159–170. ISSN: 10221336. DOI: 10.1002/1521-3927(20020201)23:3<159::AID-MARC159>3.0.CO;2-1.

[208] B.-G. Wu et al. "Response Times and Voltages for PDLC Light Shutters". In: *Liquid Crystals* 5.5 (1989), pp. 1453–1465. ISSN: 02678292. DOI: 10.1080/02678298908027783.

[209] P.-G. De Gennes et al. In: *Capillarity and Wetting Phenomena: Drops, Bubbles, Pearls, Waves* (2004).

[210] J. Li et al. "Refractive-Index Matching between Liquid Crystals and Photopolymers". In: *Journal of the Society for Information Display* 13.12 (2005), pp. 1017–1026. ISSN: 10710922. DOI: 10.1889/1.2150371.

[211] J. D. Bunning et al. "Frank Constants of Nematic 5CB at Atmospheric Pressure". In: *Journal de physique Paris* 42.8 (1981), pp. 1175–1182. DOI: 10.1051/jphys:019810042080117500.

[212] L. T. Creagh and A. R. Kmetz. "Mechanism of Surface Alignment in Nematic Liquic Crystals". In: *Mol Cryst Liq Cryst* 24.1-2 (1973), pp. 59–68. DOI: 10.1080/15421407308083389.

[213] P. G. De Gennes. "Short Range Order Effects in the Isotropic Phase of Nematics and Cholesterics". In: *Mol Cryst* 12.3 (1971), pp. 193–214.

[214] P. G. de Gennes and J. Prost. *The Physics of Liquid Crystals*. Clarendon Press, 1995. 597 pp. ISBN: 0-19-851785-8.

[215] A. C. Diogo and A. F. Martins. "Thermal Behaviour of the Twist Viscosity in a Series of Homologous Nematic Liquid Crystals". In: *Molecular crystals and liquid crystals* 66.1-4 (1980), pp. 133–145. ISSN: 00268941.

[216] J. E. Fromm. “Numerical Calculation of the Fluid Dynamics of Drop-On-Demand Jets”. In: *IBM Journal of Research and Development* 28.3 (1984), pp. 322–333. ISSN: 00188646. DOI: 10.1147/rd.283.0322.

[217] C. E. Hoyle et al. “Temperature Dependence of the Laser-Initiated Polymerization of a Thiol-Ene System”. In: *Journal of polymer science. Part A-1, Polymer chemistry* 22.8 (1984), pp. 1865–1873.

[218] R. Das; X. He; K. Ghaffarzadeh. *"Printed, Organic and Flexible Electronics 2020-2030: Forecasts, Technologies, Markets"*. IDTechEx, 2019.

[219] H. Mada and S. Kobayashi. “Wavelength and Voltage Dependencies of Refractive Indices of Nematic Liquid Crystals”. In: *Mol Cryst Liq Cryst* 33.1-2 (1976), pp. 47–53. DOI: 10.1080/15421407608083869.

[220] A. Saupe. “Disclinations and Properties of the Directorfield in Nematic and Cholesteric Liquid Crystals”. In: *Mol Cryst Liq Cryst* 21.3-4 (1973), pp. 211–238. DOI: 10.1080/15421407308083320.

[221] C. D. Stow et al. “An Experimental Investigation of Fluid Flow Resulting from the Impact of a Water Drop with an Unyielding Dry Surface”. In: *Proceedings of the Royal Society of London. A. Mathematical and Physical Sciences* 373 (1981).

[222] H. S. Subramhanyam et al. “Optical Anisotropy of Nematic Compounds”. In: *Mol Cryst Liq Cryst* 28.1-2 (1974), pp. 201–215. DOI: 10.1080/15421407408083165.

[223] D.-K. Yang and S.-T. Wu. *Fundamentals of Liquid Crystal Devices*. 2006. 1-378. DOI: 10.1002/0470032030.

b